WAVE PROPAGATION IN SPACE AND TIME MODULATED STRUCTURES

A Dissertation
Presented to
The Academic Faculty

By

Giuseppe Trainiti

In Partial Fulfillment
of the Requirements for the Degree
Doctor of Philosophy in the
School of Aerospace Engineering

Georgia Institute of Technology

May 2018

WAVE PROPAGATION IN SPACE AND TIME MODULATED STRUCTURES

Approved by:

Dr. Massimo Ruzzene, Advisor
School of Aerospace Engineering
Georgia Institute of Technology

Dr. Julian J. Rimoli
School of Aerospace Engineering
Georgia Institute of Technology

Dr. Graeme J. Kennedy
School of Aerospace Engineering
Georgia Institute of Technology

Dr. Claudio V. Di Leo
School of Aerospace Engineering
Georgia Institute of Technology

Dr. Karim G. Sabra
School of Mechanical Engineering
Georgia Institute of Technology

Dr. Alper Erturk
School of Mechanical Engineering
Georgia Institute of Technology

Date Approved: March 26, 2018

To Juliana

ACKNOWLEDGEMENTS

My first *grazie* goes to my advisor Dr. Massimo Ruzzene for his continued guidance and support. Your passion for research has been truly inspiring and motivating. The endless energy and resources you invested in me, shaping me as a scholar and as a person, will never be forgotten.

I would also like to thank my committee members Dr. Julian J. Rimoli, Dr. Graeme J. Kennedy, Dr. Claudio V. Di Leo, Dr. Karim G. Sabra, and Dr. Alper Erturk. Thank you for all your comments, the discussions and the knowledge you shared with me. You constantly guided my path at Tech and greatly contributed to my research.

I would like to thank all the present and past members of the Wave Lab, both the ones I met during my stay as visiting scholar, and the ones I spend my time with during my PhD. I am grateful I had the chance to work with Raj, Javier, Marshall and Yiwei, I learned a lot from each one of you and I had fun doing it. I would like to thank the undergraduate students I had the honor to mentor, Santiago and Michael, as well as the visiting students I worked with, Paolo and Jacopo. A special thanks goes to Matteo, you helped me immensely inside and outside the lab, you thought me to aim high and always set a good example. I would like to express my sincere gratitude to all the people I had the pleasure to interact with at both the School of Aerospace Engineering and at the School of Mechanical Engineering, including the fellow members of the Georgia Tech Chapter of the Acoustical Society of America, with whom I enjoyed working on the theremin project.

Finally, I would like to spend a few words for the two families I have, one for each side of the Atlantic Ocean. Amir, thank you. Your friendship is one of the most valuable experiences of my life, the sincere care and selflessness you showed me are unmatched and just priceless. Giovanni, friend and (ex)roommate, thank you for all

the fun we had together, including house sitting, dog sitting, scooter riding, wine tasting and pasta eating.

Juliana, thank you for having such a positive impact on my life. Your joy and happiness keep me focused on what really matters and give me a tremendous strength. Also, thanks for killing the bugs.

I would like to thank my mother, by brother, Giovanni and Rosetta for supporting my project. You motivated me beyond what I might have shown you.

TABLE OF CONTENTS

LIST OF FIGURES

SUMMARY

This thesis investigates structures with spatial and temporal modulation of the effective mechanical properties, contributing to the state-of-the-art of wave propagation control techniques and to advancements in metamaterials.

The first part of the dissertation investigates the effects of periodic geometric undulations on the dispersion properties of 1D and 2D elastic structures. Periodic undulations result from the spatial modulation of the curvature of beams and plates, which leads to the coupling of transverse and in-plane motion. Such coupling induces complete, modal and partial frequency band gaps, along with directional wave motion. Experimental illustration of the band gap behavior of undulated beams, and numerical simulations of wave motion in plates serve as partial validations of the analytical predictions, and as demonstrations of the potential application of the concept for the design of structural components and elastic waveguides with tailored band gap and directional properties. The analysis is extended to undulated square structural lattices, which are 2D reticulates obtained from the tessellation of the plane with curved beams. Periodic undulated structures, in which the undulation is uniform throughout the structure, as well as graded undulated patterns, in which the undulation gradually is varied within the lattice, inhibit wave motion within specified frequency ranges and in specific directions as a result of the undulation-induced anisotropy. The experimental characterization of wave motion in lattice structures is performed through a high speed digital image correlation technique for highly porous structures. Small displacements of the lattice nodes are tracked by centering image subsets about the lattice intersections. The transient response is recorded in the form of full wavefields, which are processed to characterize the properties of a hexagonal lattice. The described optical technique is then applied to experimentally demonstrate the elastic wave filtering properties of graded undulated lattices, which result

from the spatial variation of the curvature parameter.

The second part of the thesis focuses on periodic structures with time-varying mechanical properties. Specifically, longitudinal and transverse wave propagation in rods and beams with elastic properties that are periodically varying in space and time is first investigated. Spatio-temporal modulation of the elastic properties breaks mechanical reciprocity and leads to one-way wave propagation, which is signaled by directional band gaps in asymmetric dispersion diagrams. The investigation then considers discrete one-dimensional chains of resonators connected by springs with modulated stiffness. Finally, a broadband-to-narrowband elastic wave filter is presented that relies on time-modulation of the effective stiffness. For broadband waves impinging on the time-modulated domain of the system, narrowband reflected waves are induced due to the time periodic modulation of the effective stiffness. The experimental implementation of the stiffness modulation is achieved by using switchable negative capacitance shunts.

This work suggests new avenues for the design of structures with unique wave propagation properties, and it does so by providing both a theoretical framework and experimental validation of the proposed concepts.

CHAPTER 1
INTRODUCTION

1.1 Overview

This thesis investigates wave propagation in structures with a periodic spatial or temporal modulation of the effective mechanical properties. The systems under investigation are often referred to as metamaterials and are of interest due to their wave mitigation, insulation and filtering properties. The following section provides a background on periodic structures and metamaterials. The main focus of the section is on structures with emerging patterns due to load-induced geometry reconfiguration, which is a promising strategy for performance tunability, and systems with time-dependent material properties, which exhibit non-reciprocal behavior. The chapter then introduces the motivations and objectives of the thesis, followed by the research contributions. The chapter is closed by an outline of the thesis.

1.2 Background

1.2.1 Periodic structures

Periodic structures are systems that show spatial periodicity of one or more of their attributes, these being material properties, geometric features and boundary conditions [1]. While periodic structure have been used to model the fundamental properties of sound propagation as far back as Newton [2] and, more recently, to understand crystals' properties in condensed matter physics [3], only in the last few decades researchers recognized their potential in engineering. In electrodynamics and elastodynamics, for example, the appealing properties of periodic structures are associated to the control of wave propagation. Regardless of the nature of the waves, the interest

in periodic structures is motivated by two main properties. First, the existence of forbidden frequency ranges for wave propagation, called band gaps, that allow periodic structures to behave as filters, thus confining the energy associated to the waves within a certain domain. Second, frequency dependent directional wave propagation. Although these two properties might be seen in other systems, in periodic structures they can be achieved by a systematic design of the unit cell, the periodic structure's building block. The design of the unit cell and, ultimately, of the periodic structure's properties is guided by tools borrowed from condensed matter physics, usually in the form of dispersion diagrams, that relate frequency ω and wavenumber κ.

The remarkable properties of periodic structures arise from periodicity itself, and they can be shared by systems supporting waves of different nature. For this reason, periodic structures are of interest in many fields, such as electromagnetics, acoustics and mechanics. It is common that an idea introduced in one field, usually electromagnetics, inspires other fields, such as acoustics or mechanics. The "photonic crystals", first introduced in electromagnetics, later inspired investigation in acoustics and mechanics, leading to the term "phononic crystal" [4, 5]. Metamaterials provide another example, as they most frequently they consist of periodic arrangements of elementary units.

The suggested applications of periodic structures in acoustics and mechanics are numerous. Due to their filtering properties, periodic structures could be used for vibration isolation and mitigation [6], noise absorption and transmission reduction [7], wave localization through defect-engineering [8], as well wave demultiplexing, collimation, refraction and rectification [9, 10, 11, 12]. Also, thanks to their ability to guide elastic waves along preferential directions, it was suggested that periodic structures can be employed in energy harvesting applications [13] and in energy localization due to defects in a phononic crystals [14]. If the periodic repetition of the same unit cell is replaced by a smooth change of material properties or geometrical features along a

certain direction, graded configurations are obtained. In this regard, gradient-index phononic crystals (GRIN PCs) can be designed to provide a refractive index profile able to focus elastic energy, realizing acoustic lenses [15], with recent promising extensions to piezoelectric energy harvesting [16, 13].

1.2.2 Structural design exploiting spatial periodicity

In mechanical, civil and aerospace engineering, structures have often intrinsically periodic designs, such as many truss structures or frames. A deliberate use of periodicity to target specific dynamical properties is, instead, a recent approach. In his seminal work, D. J. Mead [17] studied the response of beams and plates with periodic supports in relation to aeronautical rib-skin structures [18, 19]. In the past few years, the interest in enriching the design tools of periodic structures benefited from the introduction of finite element-based techniques for dispersion analysis [20]. Also, optimization techniques have been used to design structures with targeted dynamic performance [21].

A notable example of structural design relying on spatial periodicity is given by structural lattices, which are obtained tessellating 2D and 3D space with slender beam elements. Structural lattices can be regarded as a special class of mechanical metamaterials, whose properties have been copiously investigated in recent years [3, 1, 22]. Demand of lightweight and high strength materials, driven by automotive and aerospace industries, has motivated the effort of populating previously forbidden regions of the material properties charts [23, 24]. In lattice materials stiffness, strength and fracture response have been shown to depend upon geometry and nodal connectivity, with behaviors ranging from bending-dominated in foams to stretching-dominated in highly connected cellular solids such as octet-truss lattices [23, 25, 26, 27]. Recent advancements in fabrication capabilities have further spurred on the interested in fully exploiting architected materials' potential, exploring nanometer-scale

lattices [28, 29, 30, 24] as well as hierarchical geometries [31, 32]. Structural metamaterials are perhaps even more appealing for their dynamic properties. Frequency-dependent forbidden elastic wave propagation and strongly directional behavior are the main features of structural lattices. As shown by Casadei and Rimoli [33], such properties become more and more evident by considering skew lattices with decreasing volume fraction, thus transitioning from a continuum material to a grid-like system. Fixing the volume fraction, the authors also shown how to design the anisotropy of both longitudinal and shear modes by varying a single geometric parameter, specifically the lattice skewness. Several others lattice topologies and geometries have been investigated [34, 35, 36], with possible applications in noise reduction, vibration control and stress wave mitigation [1]. Recently, enhanced functionality in lattices has been explored through nonlinearity to achieve amplitude-dependent response [37], tunable directivity with piezoelectric patches and shunted negative capacitance circuits [38], large deformations effects [39] and bistable magneto-elastic structures [40].

In several recent instances, considerable effort has been devoted to the development of periodic structures that adapt their mechanical properties to achieve targeted performance. An interesting approach to realize tunable periodic structures is given by load-induced instabilities. Examples of periodic patterns triggered by instabilities are seen in wrinkled suspended graphene sheets [41], Yoshimura-like patterns in thin-walled cylinders, which undergo buckling induced by a mandrel with prescribed annular gap [42], as well as in thin films on compliant substrates featuring periodic 1-D, hexagonal and herringbone patterns induced by swelling stresses [43]. Instabilities can also trigger a change of a pre-existing pattern. A relevant example of this behavior is given by a square array of circular holes in a soft material, which undergoes a pattern transformation due to a compressive load, resulting in an abrupt change of the system's periodicity, as shown by Bertoldi [44]. Since the wave propagation properties of a periodic structure depend on the unit cell, a change in the unit

cell's configuration induces a change in the way waves interact with the structure as a whole. From a structural point of view, the thin ligaments of the structure buckle due to the applied load, inducing a new pattern that can be further tuned by varying the applied load. The width and position of the band gaps of the porous soft material can be tuned by the applied load. Moreover, the same mechanics can be used to achieve tunable directional response [45].

1.2.3 Experimental investigation of wave properties

Although it was theoretically shown that structural metamaterials provide a landscape of wave propagation properties, experimental validation is scarcely documented, with most of tests performed to obtain transmissibility measures through a small number of sensors [46, 47]. When full wavefield measurement is required, 3D scanning laser Doppler vibrometry (SLDV) is commonly used [48, 49]. SLDVs provides measurement of the structure's transient response, which is then post-processed to extract the associated dispersion properties, especially wave directionality. SLDV is based on the Doppler frequency shift associated to the scattering of light by a moving surface [50]. The velocity of the surface is obtained in virtue of its proportionality to the measured Doppler frequency shift. In SLDVs the location of the probing laser beam is changed by typically using galvanometer mirrors, allowing to measure the wavefield of the structure in predefined grid locations. In 3D SLDV, three distinct laser beams are focused onto a single point and allow to obtain all three components of the wavefield, thus providing information on the in-plane and out-of-plane dynamics of the structure [51]. SLDVs find application in experimental modal analysis, structural health monitoring and characterization of Micro Electro-Mechanical Systems [50]. This approach, although mature, presents a number of shortcomings, mainly related to the cost of the experimental apparatus. In the context of lattice structures, the main challenge is focusing three laser beams onto the same measurement location,

task that can be problematic due to the highly porous nature of the structure, especially as the dimensions of the lattice and of the slender elements composing it is reduced. Thus alternative techniques to achieve similar objectives continue to be of interest.

1.2.4 Time-dependent systems and non-reciprocal behavior

Reciprocity is a fundamental principle of many wave phenomena and applies in electromagnetism [52], optics [53] and acoustics [54], to name a few. Rayleigh's provided the following statement about reciprocity [55]:

> If in a space filled with air which is partly bounded by finitely extended fixed bodies and is partly unbounded, sound waves be excited at any point A, the resulting velocity-potential at a second point B is the same both in magnitude and phase, as it would have been at A, had B been the source of the sound.

Asymmetric or one-way propagation violates reciprocity. In mechanical systems, weak non-reciprocal wave propagation occurs in rotating rings, in which the rotation introduces a mechanical bias that leads to different wavenumber and phase velocity values for waves propagating in opposite directions [56]. The mechanical bias is due to Coriolis forces [57], which are responsible for breaking reciprocity [58]. A similar non-reciprocal behavior is observed in systems subjected to a magnetic field [59]. Strong non-reciprocal effect are achieved by relaxing some of the assumptions of the Onsager-Casimir principle of microscopic reversibility [60], which states that reciprocity is not guaranteed when nonlinearity or time-dependent material properties are exploited [61].

Non-reciprocal devices are highly desirable in many technological applications. In acoustics, for instance, it might be required to protect a source from its echo or achieve full-duplex sound communication, *i.e.* simultaneously emitting and receiving on the

same frequency channel with the same transducer [61]. Furthermore, non-reciprocal devices can be used to realize directional filters, which behave as mechanical diodes by preventing propagation based on the direction of the waves [62, 61]. Among the suggested strategies to achieve non-reciprocal behavior, the ones involving nonlinearity or time-modulation of the media's properties are the most promising. Indeed, non-reciprocal transmission can be obtained in a 1D sytem by combining a nonlinear medium with a phononic crystal [63]. In this implementation, waves at frequency ω, or first harmonic, fall within one of the phononic crystal's band gaps thus are attenuated, while waves at frequency 2ω, or second harmonic, fall withing a pass band. Assuming that the waves impinge the phononic crystal first, they are almost completely attenuated by the phononic crystal when entering the nonlinear medium, hence the system behaves as an insulator. On the other hand, when the waves impinge on the nonlinear medium first, a non negligible fraction of the energy of the first harmonic is transferred to the second harmonic so, when entering the phononic crystal, is not attenuated and can pass through the system. Experimental evidence shows that the system behaves as an acoustic diode, although efficacy of such nonlinear devices depends on the amplitude of the input signal, which has to be large enough to trigger the second harmonic generation mechanism of the nonlinear medium [64]. In another implementation [65], which has the advantage of being more broadband than the previous one, the nonlinear medium is placed between a gain/loss pair. In this case, the non-reciprocal behavior of the system is determined by which element of the pair the wave interacts with first, so to be amplified or dissipated, before interacting with the nonlinear medium. Several recent studies have investigated the possibility of modifying in time the material properties of the system to achieve non-reciprocal behavior. For example, one-way acoustic isolation has been shown in graphene based nanoelectromechanical systems (NEMS)[66], acoustic waveguides [67], acoustic circulators [68] and time-dependent superlattices [69]. The common strategy in these

studies is to extend to the time domain the spatial-only periodic variation of material properties that in general is associated with metamaterials. This strategy thus exploits spatio-temporal modulated systems to manipulate wave propagation and achieve non-reciprocal propagation [70, 71, 72, 73]. Space and time modulation of the medium already gained the attention of the scientific community many decades ago. From a theoretical standpoint, Slater [74] studied the scattering of an electronic wave by a sinusoidal perturbation. In this problem, a particle is moving in a region with potential energy having the form of a traveling plane wave. The Schröedinger's equation for this particle, in the one dimensional case, reduces to a Mathieu's equation [3]. A perturbation approach is then employed to obtain the first three harmonics $n = 0, \pm 1$ of the wave function, under the assumption that the amplitude of modulation of the potential energy is small. Moreover, an approximate relation between the energy $\hbar\omega_0$ and the wavevector $\boldsymbol{\kappa}_0$ is derived, which is able to predict the first order stop-band or Bragg reflection, but fails at describing higher-order stop-bands. The solution to this problem, which uses a time-dependent Floquet representation, was later extended to other fields. Simon [75] and Hessel et al. [76] suggested a more general approach to study the wave propagation of an electromagnetic wave in a medium with sinusoidal dielectric constant. The wave equation for the electric field is solved by imposing a Floquet solution with space-time harmonics, which leads to a description of higher-order stop-bands by computing the dispersion relation given in the form of a rapidly convergent continued fraction. While many of these and others pioneering works focused mainly on the application of time-modulated systems to achieve traveling wave parametric amplification [77, 78] and the condition for stability of the system associated to frequency conversion effects [79, 80], the possibility of achieving one-way propagation in spatio-temporal modulated system was perhaps not properly recognized and described.

1.2.5 Time-modulation of mechanical properties

In mechanics, numerous studies focused on the theoretical aspects of time-dependent material properties, especially for their potential for interacting with elastic waves [81]. However, the practical implementation of time-dependent properties, such as dynamically changing stiffness or mass density, depends on the availability of effective strategies to appreciably change such properties. Obtaining a material or structure with time-varying stiffness or mass density still represents an open challenge. Among the approaches reported in the literature, it is shown that light can induce and control softening in Ge_xSe_{1-x} glasses [82], which suggests a way to vary the glass' stiffness with space and time [69]. A time-dependent moment of inertia can be obtained in a pendulum with a radially moving mass based on Coriolis-type effects [83]. More recently, several strategies have been specifically suggested for varying the effective mechanical properties of a structure in time and space, so to obtain non-reciprocal devices. A phononic crystal with spatio-temporal modulation of electrical boundary conditions in a stack of piezoelectric elements has been described [84]. Magnetoelastic media interacting with an external magnetic field [85] and magnetorheological fluids [86] are also solutions recently suggested to implement traveling-wave modulation.

1.3 Motivations and Objectives

While there is agreement on the role of undulation of buckled structural elements and periodic porous soft material in affecting wave propagation properties, little is known about the mechanism behind the radical change in the dispersion properties of the studied systems due to the onset of new patterns. A deeper understanding of such mechanism would not only inform the design of buckling soft materials, but also provide the chance to exploit the gained knowledge in the field of structural design.

Periodic curved structures, such as undulated beams and plates, could be considered as metamaterials with varying curvature as mechanism for modulating the effective material properties, avoiding designs with multiple materials. In this context, the curvature modulation associated to the undulation may be the result of an initial design for the structure. Furthermore, working with structural materials such as metals would prevent one of the main and inherent limitations of soft materials in effectively controlling wave propagation, namely high damping, in applications where the energy needs to be steered, rather than dissipated.

The systematic analysis of wave phenomena in periodic curved beams can shed light on the complex behavior of 2D reticulates of curved ligaments, or undulated lattice structures, which can be obtained by mimicking the bucking patters of porous soft materials, or by simply exploiting the numerous design that are not the result of instability-induced pattern reconfiguration. The key feature of undulated lattices would be that the required wave propagation properties could be engineered by choosing few geometrical parameters, such as undulation amplitude and spatial period, thus suggesting a simplified but effective design approach. By gradually changing few key parameters, such as thickness or curvature, along one direction of the undulated lattices, the analysis could exploit the role of undulation of the lattice ligaments in graded configurations, exploring the concept of GRIN PCs in lattice structures, enabling application such as wave focusing or structural mirrors [15].

Experimental validation is a crucial step in confirming the theoretical predictions on dispersion in undulated structural lattices. Due to the limitations of the current experimental approaches, discussed above, innovative techniques to study in-plane wave propagation in lattice structures would be highly desirable. The main attributes of an approach alternative to SLDV would be lower cost, higher spatial resolution and compatibility with highly porous structures and slender elements.

The recent surge of interest in non-reciprocal structures with time-modulated

properties calls for an extension of the analysis tools currently available for spatially periodic structures. A general approach to obtain the dispersion relation of space- and time-modulated systems would allow a quantitative study of the time-modulation parameters and their relation with the system's non-reciprocal behavior. On the other hand, it would be perhaps even more relevant an experimental implementation of time-modulation of mechanical material properties. The main requirements of such implementation would be a compact design, which can be easily integrated into structural designs, and with high range of frequency modulation, so to provide high performance tunability.

Given the motivations above, the objectives of the research are:

- To describe the dispersion properties of structural elements, such as beams and plates, with periodic variation of the curvature and provide guidance for their design by identifying relevant geometric parameters;

- To explore different periodic undulated lattice configurations obtained combining curved beams elements, with a focus on their filtering and directional behavior; also, to extend the findings on periodic undulated lattices to graded lattices, so to extend the concept of GRIN PCs to lattice structures.

- To introduce an innovative experimental approach for the measurement of in-plane wave propagation in lattice structures, providing an effective strategy for testing highly porous structures.

- To employ such novel experimental approach to study the filtering properties of undulated lattices.

- To investigate the effect of time-dependent material properties on the propagation of elastic waves.

- To implement a strategy to achieve time-dependent mechanical metamaterials.

1.4 Contributions

In reference to the objectives mentioned above, the thesis presents the following contributions:

- Analytic framework for the investigation of wave propagation in undulated beams and plates with a pre-existing curvature modulation. The existence of band gaps is shown in such structures, both complete and partial, resulting from the interaction of in-plane and transverse stress resultants. Moreover, the onset of frequency-dependent anisotropy is predicted in undulated plates by group velocity angular variations, which manifests itself through wave directionality. Finally, experimental validation of band gaps is presented for undulated beams.

- Extension of the wave propagation analysis to undulated graded and periodic structural lattices. Different undulation patters show radically different wave propagation properties, thus showing the importance of the geometric arrangement of the curved lattice ligaments, given the same value of curvature.

- Validation and improvement of an optical technique to measure in-plane elastic wave propagation in lattice structures based on digital image correlation (DIC).

- Experimental validation of the filtering properties of graded undulated structural lattices by means of the aforementioned optical technique.

- Analytic framework to study non-reciprocal wave propagation of spatio-temporal periodic structures. Methods for both continuous and discrete systems are presented. Analytic formulas relating the relevant modulation parameters and the induced non-reciprocal effect are obtained. Specifically, the condition to obtain full directional band gaps is discussed.

- Experimental implementation of a single-port system with selective frequency properties based on time-varying effective stiffness.

1.5 Work Organization

The work is organized in eight chapters, including this introduction. Chapter 2 presents the wave propagation characterization of periodically undulated beams and plates. The equations of motion of undulated beams are used to compute band diagrams by means of the plane wave expansion method. Numerical and experimental validations support the theoretical results. In Chapter 3, wave filtering and directionality of undulated structural lattices are studied by means of a FE-based Bloch analysis approach. Chapter 4 introduces an optical technique targeting the evaluation of in-plane wave propagation in structural lattices. A benchmark case involving a hexagonal lattice is discussed, then experimental validation of the filtering properties of graded undulated lattices is presented. Chapter 5 presents a theoretical study of spatiotemporally modulated structural elements, namely beams and plates, showing their non reciprocal behavior due to directional band gaps. Chapter 6 extends the approach to discrete one-dimensional chains of resonators. Chapter 7 discusses a practical implementation of effective stiffness modulation in time, which is obtained by means of piezoelectric patches and negative capacitance shunts. Finally, Chapter 8 summarizes the main findings of the present study and proposes directions for future investigations.

CHAPTER 2
UNDULATED STRUCTURAL ELEMENTS

2.1 Overview

In this chapter the equation governing the motion of curved beams and plates are first presented. These equations are then used to obtain dispersion properties for both classes of undulated structures by means of a plane wave expansion method. The dependence of such properties upon the relevant geometric parameters, namely undulation amplitude and thickness, is reported. It is shown that undulated beams behave as phononic crystal, displaying band gaps for nonzero undulation amplitude. The theoretical predictions are compared to finite element calculations and experimentally validated. In the undulated plates' case, modal band gaps are identified which are associated to the out-of-plane displacement components. Also, directionality is explored by plotting the in plane components of the group velocity, then compared to numerical simulations obtained through a finite element model.

2.2 Theoretical Background

2.2.1 Configurations and Geometry

Wave propagation behavior of plates and beams of the kind shown in Fig. 2.1 is investigated. The configuration of both structural components is fully described by prescribing the measure of local curvature, which varies periodically in space. The period of curvature undulations defines the unit cell [87], also highlighted in Fig. 2.1.

For plates, the location of a point P on the neutral surface $\mathcal{S}$ is identified by two

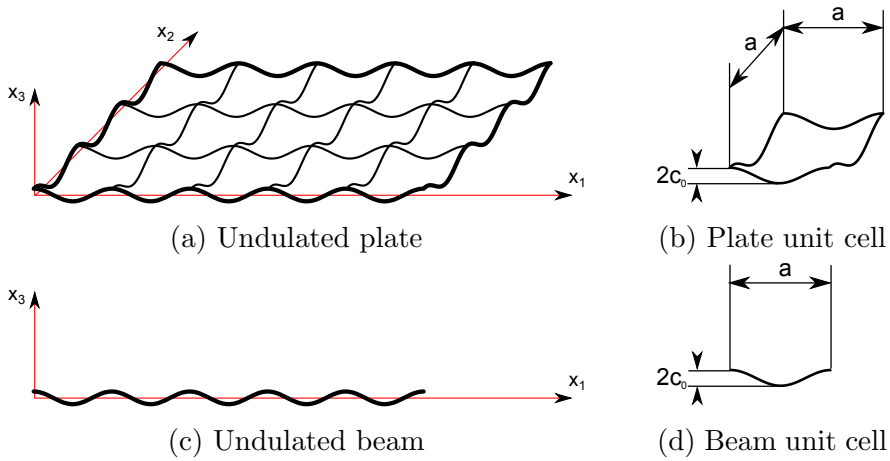

(a) Undulated plate (b) Plate unit cell

(c) Undulated beam (d) Beam unit cell

Figure 2.1: Periodically undulated plates and beams and corresponding unit cells.

surface coordinates α_1, α_2, so that the corresponding position vector $\mathbf{r}_P$ is given by:

$$\mathbf{r}_P(\alpha_1, \alpha_2) = f_1(\alpha_1, \alpha_2)\mathbf{e}_1 + f_2(\alpha_1, \alpha_2)\mathbf{e}_2 + f_3(\alpha_1, \alpha_2)\mathbf{e}_3 \tag{2.1}$$

where $\mathbf{e}_i$ is a triad associated with a Cartesian frame of reference. For convenience of formulation, the study is limited to configurations described by orthogonal curvilinear coordinates, aligned with the Cartesian frame, *i.e.*:

$$\alpha_1 = x_1,\ \alpha_2 = x_2 \tag{2.2}$$

The components of $\mathbf{r}_P(\alpha_1, \alpha_2) = \mathbf{r}_P(x_1, x_2)$ in Eq. (2.1) can be written as:

$$f_1(x_1, x_2) = x_1 \tag{2.3}$$

$$f_2(x_1, x_2) = x_2 \tag{2.4}$$

$$f_3(x_1, x_2) = c(x_1, x_2) \tag{2.5}$$

where $c(x_1, x_2)$ is a function that defines the spatial modulation of the neutral surface with the respect to the plane $x_3 = 0$. Orthogonal undulations of the neutral surface

are considered herein expressed as:

$$c(x_1, x_2) = c_0 \Big[\cos\left(\frac{2\pi}{a} x_1\right) + \cos\left(\frac{2\pi}{a} x_2\right) \Big] \tag{2.6}$$

where c_0 defines the undulation magnitude, with square unit cells of side a are considered as shown in Fig. 2.1. For $\frac{c_0}{a} << 1$ the lines of principal curvature are orthogonal to each other, and curvatures k_1 and k_2 can be expressed as:

$$k_2(x_1, x_2) = \frac{\partial^2 c}{\partial x_2^2} = -c_0 \Big(\frac{2\pi}{a}\Big)^2 \cos\left(\frac{2\pi}{a} x_2\right) \tag{2.7}$$

$$k_1(x_1, x_2) = \frac{\partial^2 c}{\partial x_1^2} = -c_0 \Big(\frac{2\pi}{a}\Big)^2 \cos\left(\frac{2\pi}{a} x_1\right) \tag{2.8}$$

The configuration for the beam (Fig. 2.1c,d) can be directly derived as a particular case of the plate geometry, whereby only one curvilinear coordinate x_1 and the curvature along the beam's axis $k_1(x_1)$ are utilized. The unit cell of the undulated beam is shown in Fig. 2.1d.

2.2.2 Governing Equations

For the configurations described above, equations of motion are expressed according to classical formulations for curved plates found for example in [88, 89]. The equations hold within the thin plate approximation, also upon neglecting rotary inertia and shear deformations through the thickness of the plate. Furthermore, the shells have uniform thickness h, which is small compared to curvature, and the neutral surface $\mathcal{S}$ is identified as being subject to membrane-type only stresses.

In the absence of external loading, the curved plate's equations of motion are:

$$\frac{\partial(N_{11}A_2)}{\partial\alpha_1}+\frac{\partial(N_{21}A_1)}{\partial\alpha_2}+N_{12}\frac{\partial A_1}{\partial\alpha_2}-N_{22}\frac{\partial A_2}{\partial\alpha_1}+A_1A_2\frac{Q_{13}}{R_1}=A_1A_2\rho h\ddot{u}_1 \tag{2.9}$$

$$\frac{\partial(N_{12}A_2)}{\partial\alpha_1}+\frac{\partial(N_{22}A_1)}{\partial\alpha_2}+N_{21}\frac{\partial A_2}{\partial\alpha_1}-N_{11}\frac{\partial A_1}{\partial\alpha_2}+A_1A_2\frac{Q_{23}}{R_2}=A_1A_2\rho h\ddot{u}_2 \tag{2.10}$$

$$\frac{\partial(Q_{13}A_2)}{\partial\alpha_1}+\frac{\partial(Q_{23}A_1)}{\partial\alpha_2}-A_1A_2\Big(\frac{N_{11}}{R_1}+\frac{N_{22}}{R_2}\Big)=A_1A_2\rho h\ddot{u}_3 \tag{2.11}$$

where ρ is the material density, u_i $(i=1,2,3)$ denotes the displacement component aligned with unit vector $\mathbf{e}_i$, while $R_i = R_i(\alpha_1,\alpha_2) = 1/k_i$ $(i=1,2)$ is the local radius of curvature. In Eq. (2.9), N_{ij}, Q_{ij} are generalized stress resultants which are depicted in the free body diagram of Fig. 2.2. Specifically, Q_{13} and Q_{23} are defined by the following expressions,

$$\frac{\partial(M_{11}A_2)}{\partial\alpha_1}+\frac{\partial(M_{21}A_1)}{\partial\alpha_2}+M_{12}\frac{\partial A_1}{\partial\alpha_2}-M_{22}\frac{\partial A_2}{\partial\alpha_1}-Q_{13}A_1A_2=0 \tag{2.12}$$

$$\frac{\partial(M_{12}A_2)}{\partial\alpha_1}+\frac{\partial(M_{22}A_1)}{\partial\alpha_2}+M_{21}\frac{\partial A_2}{\partial\alpha_1}-M_{11}\frac{\partial A_1}{\partial\alpha_2}-Q_{23}A_1A_2=0 \tag{2.13}$$

where, A_i $(i=1,2)$ is the fundamental form parameter, or Lamé parameter, which is defined as:

$$A_i=\left|\frac{\partial\mathbf{r}}{\partial\alpha_i}\right| \tag{2.14}$$

and M_{ij} are generalized stress moment resultants, as shown in Fig. 2.2.

A few manipulations, the enforcement of kinematic relations and Eq. (2.2) allows simplifying Eq. (2.9)-(2.13) which reduce to:

$$\frac{\partial N_{11}}{\partial x_1}+\frac{\partial N_{21}}{\partial x_2}+k_1\left[\frac{\partial M_{11}}{\partial x_1}+\frac{\partial M_{21}}{\partial x_2}\right]=\rho h\ddot{u}_1 \tag{2.15}$$

$$\frac{\partial N_{12}}{\partial x_1}+\frac{\partial N_{22}}{\partial x_2}+k_2\left[\frac{\partial M_{12}}{\partial x_1}+\frac{\partial M_{22}}{\partial x_2}\right]=\rho h\ddot{u}_2 \tag{2.16}$$

$$\frac{\partial^2 M_{11}}{\partial x_1^2}+2\frac{\partial^2 M_{12}}{\partial x_1\partial x_2}+\frac{\partial^2 M_{22}}{\partial x_2^2}-\left[k_1N_{11}+k_2N_{22}\right]=\rho h\ddot{u}_3 \tag{2.17}$$

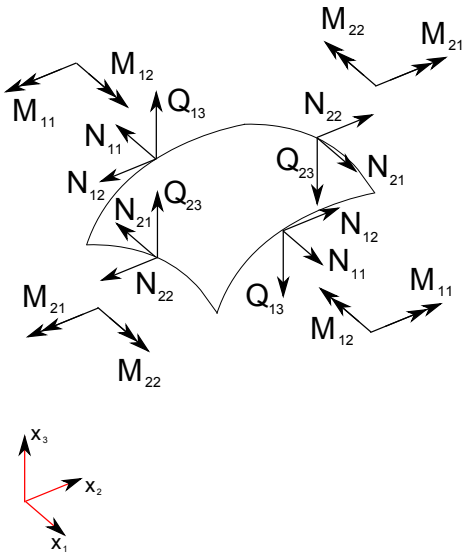

Figure 2.2: Free body diagram of a shell element. Standard arrows represent forces, while double-headed arrows represent moments.

For the sake of brevity, the expressions of generalized stress resultants in Eq.s (2.15)-(2.17) in terms of displacements are here omitted, but are reported in the Appendix for completeness.

It is important to note how the last three equations describe a system of coupled equations, which can be expressed in terms of the 3 displacement components. When both curvature terms are equal to zero, the equations reduce to two coupled equations and one decoupled equation, respectively governing the in-plane and transverse behavior of a flat plate. The latter specifically corresponds to the plate equation according to Kirchhoff Plate Theory, which is consistent with the assumptions made herein.

2.2.3 Particular Case: the Curved Beam

The curved beam governing equations can be obtained as particular cases of the general curved plate equations described above. For a beam, one assumes that all quantities vary only in terms of a single coordinate x_1, *i.e.* $\frac{\partial}{\partial x_2}\big(\,\cdot\,\big) = 0$, so that, for example, $k_1(x_1, x_2) = k_1(x_1)$, and that $k_2(x_1, x_2) = 0$. This, in addition to neglecting

all shear stress components and the displacements along the x_2 direction leads to:

$$N_{22} = 0 \tag{2.18}$$

$$M_{22} = 0 \tag{2.19}$$

$$N_{12} = N_{21} = 0 \tag{2.20}$$

$$M_{12} = M_{21} = 0 \tag{2.21}$$

Accordingly, Eq.s (2.15) and (2.17) reduce to:

$$\frac{\partial N_{11}}{\partial x_1} + k_1 \frac{\partial M_{11}}{\partial x_1} = \rho h \ddot{u}_1 \tag{2.22}$$

$$\frac{\partial^2 M_{11}}{\partial x_1^2} - k_1 N_{11} = \rho h \ddot{u}_3 \tag{2.23}$$

while Eq. (2.16) is identically zero. Based on these assumptions, the non-zero stress resultants can be expressed as:

$$N_{11} = K \left[\frac{\partial u_1}{\partial x_1} + k_1 u_3 \right] \tag{2.24}$$

$$M_{11} = D \left[\frac{\partial k_1}{\partial x_1} u_1 + k_1 \frac{\partial u_1}{\partial x_1} - \frac{\partial^2 u_3}{\partial x_1^2} \right] \tag{2.25}$$

where $K = Eh$ and $D = \frac{Eh^3}{12}$, if one assumes that $\nu \approx 0$, so that all lateral contractions are also neglected. Upon proper differentiation of Eq.s (2.24) and (2.25), Eq.s (2.22)

and (2.23) can be expressed in terms of displacements $u_1(x_1)$ and $u_3(x_1)$ only to give:

$$K\left[\frac{\partial^2 u_1}{\partial x_1^2}+\frac{\partial k_1}{\partial x_1}u_3+k_1\frac{\partial u_3}{\partial x_1}\right]+k_1 D\left[\frac{\partial^2 k_1}{\partial x_1^2}u_1+2\frac{\partial k_1}{\partial x_1}\frac{\partial u_1}{\partial x_1}+k_1\frac{\partial^2 u_1}{\partial x_1^2}-\frac{\partial^3 u_3}{\partial x_1^3}\right]=\rho h\ddot{u}_1 \tag{2.26}$$

$$D\left[\frac{\partial^3 k_1}{\partial x_1^3}u_1+3\frac{\partial^2 k_1}{\partial x_1^2}\frac{\partial u_1}{\partial x_1}+3\frac{\partial k_1}{\partial x_1}\frac{\partial^2 u_1}{\partial x_1^2}+k_1\frac{\partial^3 u_1}{\partial x_1^3}-\frac{\partial^4 u_3}{\partial x_1^4}\right]-k_1 K\left[\frac{\partial u_1}{\partial x_1}+k_1 u_3\right]=\rho h\ddot{u}_3 \tag{2.27}$$

which define a system of coupled partial differential equations, governing the axial and transverse displacement of the beam. The coupling of the equations is clearly associated with the curvature and its variation along the beam length, while letting $k_1(x_1) = 0$ produces the well known Euler-Bernoulli equations for the transverse displacement component, and the wave equation describing the longitudinal motion of the beam. In this case, within the limitations of beam theory, these two motions are completely decoupled and can be described independently of each other.

2.3 Band Diagram Calculations and Analysis of Dispersion

This section describes the approach employed for the investigation of the wave propagation properties of the periodic structures resulting from the periodic undulations. The approach employs the Plane Wave Expansion Method (PWEM) for analytical predictions of dispersion properties [90], along with a numerical procedure based on the Finite Element (FE) discretization of the unit cell [20]. Two methodologies are considered as, on the one end, they provide a relatively simple and computationally efficient framework for analysis, as in the case of the PWEM, while providing estimations that do not rely on a number of kinematic assumptions required to obtain governing equations, as in the case of FE. Comparisons validate the methods and allow the selection of one or the other technique based on convenience of formulation,

computational cost and the availability of tractable analytical forms of the governing equations.

2.3.1 The Plane Wave Expansion Method

The governing equations derived for the plate and beam case are natural candidates for the application of the Plane Wave Expansion Method (PWEM) which is in this case particularly interesting given the harmonic expression of the curvature spatial variation. Orthogonality of the Fourier basis functions with the expressions of the periodic coefficients in the governing equations related to curvature leads to an eigenvalue solution which includes a small number of coefficients, and therefore provides a convenient way to predict the dispersion properties of the medium under consideration.

First, the dispersion properties are studied imposing a time harmonic solution:

$$\ddot{u}_i(x_1, x_2, t) = -\omega^2 u_i(x_1, x_2) e^{j\omega t} \tag{2.28}$$

for $i = 1, 2, 3$, with $j = \sqrt{-1}$. Next, the periodic coefficients of the system are expressed as Fourier series in terms of the reciprocal lattice vectors [87]. Specifically, curvatures are expressed as:

$$k_i(x_1, x_2) = \sum_{m_1, m_2} \hat{k}_i(\mathbf{G}') e^{j\mathbf{G}'\cdot\mathbf{r}} \tag{2.29}$$

where $i = 1, 2$, while $\mathbf{r} = x_1\mathbf{e}_1 + x_2\mathbf{e}_2$ defines a generic location on the structure midplane. Also in (2.29), $\mathbf{G}' = m_1\mathbf{b}_1 + m_2\mathbf{b}_2$, with m_1, m_2 denoting a pair of integers, *i.e.* $m_1, m_2 \in \mathbb{Z}$, while $\mathbf{b}_1, \mathbf{b}_2$ are the reciprocal lattice vectors here defined as:

$$\mathbf{b}_1 = \frac{2\pi}{a}\mathbf{e}_1 \qquad \mathbf{b}_2 = \frac{2\pi}{a}\mathbf{e}_2 \tag{2.30}$$

The Fourier coefficients $\hat{k}_i(\mathbf{G}')$ in Eq. (2.29) are obtained through integration over the unit cell area of the curvature expressions weighted by the Fourier basis functions, *i.e.*:

$$\hat{k}_i(\mathbf{G}') = \frac{1}{A} \iint_A k_i(x_1, x_2) e^{-j\frac{2\pi m_1}{a}x_1} e^{-j\frac{2\pi m_2}{a}x_2} \, dA \tag{2.31}$$

where $A = a^2$ is the area of the unit cell. Considering the expressions for the curvatures k_1, k_2 in Eq.s (2.7)-(2.8), one can easily show that:

$$\hat{k}_1(\mathbf{G}') = -2c_0 \left(\frac{\pi}{a}\right)^2 \delta_{m_1,\pm 1} \delta_{m_2,0}, \tag{2.32}$$

$$\hat{k}_2(\mathbf{G}') = -2c_0 \left(\frac{\pi}{a}\right)^2 \delta_{m_1,0} \delta_{m_2,\pm 1}, \tag{2.33}$$

where δ_{m_1,m_2} is the Kronecker Delta. These expressions lead to compact representations of the periodic coefficients, which affect the solution of the system.

The solution in terms of displacement components $u_i(x_1, x_2)$, $i = 1, 2, 3$ are sought as plane waves comprising a cell periodic part and are of the following form:

$$u_i(x_1, x_2) = e^{j\boldsymbol{\kappa}\cdot\mathbf{r}} \sum_{n_1,n_2} \hat{u}_i(\mathbf{G}) e^{j\mathbf{G}\cdot\mathbf{r}} \tag{2.34}$$

where $\mathbf{G} = n_1\mathbf{b}_1 + n_2\mathbf{b}_2$, with $n_1, n_2 = -N, ..., +N \in \mathbb{Z}$, and $\boldsymbol{\kappa} = \kappa_1\mathbf{b}_1 + \kappa_2\mathbf{b}_2$ is the wave vector, whose component can be restricted to vary within the First Irreducible Brillouin Zone (IBZ)[87], *i.e* $\kappa_1, \kappa_2 \in [0, \frac{1}{2}]$.

Equations (2.29) and (2.34) are then substituted in Eq (2.15), (2.16) and (2.17). The resulting expressions, too lengthy to report, are however of similar form as those found in other applications of the PWEM which have investigated for example the effect of local resonators periodically located within a thin plate [91], or Lamb waves propagating in phononic plates [90].

The resulting equations are simplified by exploiting orthogonality of the Fourier basis, which requires multiplying both sides of the resulting equations by an orthog-

onal function $e^{-j\frac{2\pi s_1 x_1}{a}} e^{-j\frac{2\pi s_2 x_2}{a}}$ and integration over the unit cell area. A few manipulations lead to a system of equations of dimensions $3 \times (2N+1)^2$ of the following form:

$$\mathbf{P}\ \hat{\mathbf{U}} = \omega^2\ \hat{\mathbf{U}} \tag{2.35}$$

where the displacements vector writes:

$$\hat{\mathbf{U}} = \left[\hat{\mathbf{u}}_1,\ \hat{\mathbf{u}}_2,\ \hat{\mathbf{u}}_3\right]^T \tag{2.36}$$

with $\hat{\mathbf{u}}_i = [\hat{u_i}_{,-N}, ..., \hat{u_i}_{,+N}]^T$, where the following simplified notation is used $\hat{u_i}(\boldsymbol{G}_n) = \hat{u_i}_{,n}$. Also, $\mathbf{P} = \mathbf{P}(\boldsymbol{\kappa})$ is the wavevector dependent coefficients matrix.

Equation (2.35) is an eigenvalue problem (EVP) which is solved in terms of ω by letting $\boldsymbol{\kappa}$ vary in the IBZ, i.e. for $\kappa_{01}, \kappa_{02} \in [0, \frac{1}{2}]$. Once $\omega = \omega(\boldsymbol{\kappa})$ is known within the IBZ, band structure and directional properties of the system can be easily represented and analyzed.

2.3.2 PWEM Formulation for Beams

The PWEM formulation for undulated beams is here illustrated as a convenient simpler case that provides some insights into the coupling of axial and flexural wave motion. The m-th Fourier coefficients for undulated beams is obtained from the following expression:

$$\hat{k_1}_m = \frac{1}{a}\int_{-\frac{a}{2}}^{\frac{a}{2}} k_1(x_1) e^{-i\frac{2\pi m}{a}x_1}\, dx_1 = -2c_0\left(\frac{\pi}{a}\right)^2 \delta_{m,\pm 1} \tag{2.37}$$

where the following shorthand notation is applied $\hat{k_1}(\boldsymbol{G}'_m) = \hat{k_1}_m$.

The EVP that results from the PWEM is now dimensions $2 \times (2N+1)$ and can be expressed as:

$$\mathbf{B}\ \hat{\mathbf{U}} = \omega^2\ \hat{\mathbf{U}} \tag{2.38}$$

where the displacements vector is $\hat{\mathbf{U}} = \left[\hat{\mathbf{u_1}},\ \hat{\mathbf{u_3}}\right]^T$, while $\mathbf{B} = \mathbf{B}(\boldsymbol{\kappa})$ is the wavevector dependent coefficients matrix. The wave vector is expressed as $\boldsymbol{\kappa} = \kappa_1 \mathbf{b}_1$. A propagation constant may be also defined as $\mu = 2\pi k_1$ for convenience [1].

Band diagrams for the system are obtained by letting κ_1 vary in the IBZ, i.e. for $\kappa_1 \in [0, \frac{1}{2}]$, or letting $\mu \in [0, \pi]$, then solving the EVP in Eq. (2.38) in terms of ω. The n-th equation in the system expressed by Eq. (2.38) is the result of the substitution of the Fourier series in the beam governing equations (Eq.s (2.26) and (2.27)) and of the application of orthogonality, which lead to:

$$\begin{aligned} &K\left[\frac{2\pi}{a}\big(\kappa_1 + n\big)\right]^2 \hat{u_1}_n + D\sum_{m,r}\left[\frac{2\pi}{a}\big(\kappa_1 + n - m\big)\right]^2 \hat{k_1}_m \hat{k_1}_r \hat{u_1}_{n-m-r} \\ &-j\sum_m \left\{K\left[\frac{2\pi}{a}\big(\kappa_1 + n\big)\right] + D\left[\frac{2\pi}{a}\big(\kappa_1 + n - m\big)\right]^3\right\} \hat{k_1}_m \hat{u_3}_{n-m} = \rho h \omega^2 \hat{u_1}_n \end{aligned} \tag{2.39}$$

and

$$\begin{aligned} &D\left[\frac{2\pi}{a}\big(\kappa_1 + n\big)\right]^4 \hat{u_3}_n + K\sum_{m,r} \hat{k_1}_m \hat{k_1}_r \hat{u_3}_{n-m-r} \\ &+j\sum_m \left\{K\left[\frac{2\pi}{a}\big(\kappa_1 + n - m\big)\right] + D\left[\frac{2\pi}{a}\big(\kappa_1 + n\big)\right]^3\right\} \hat{k_1}_m \hat{u_1}_{n-m} = \rho h \omega^2 \hat{u_3}_n \end{aligned} \tag{2.40}$$

with $n, m, r = -N, ..., +N \in \mathbb{Z}$.

These equations can be further simplified by considering the simple expression of the curvature's Fourier coefficients in Eq. (2.37), which lead to very few terms in the summations in Eq.s (2.39) and (2.40). The number of plane waves $W_P(N) = 3(2N+1)^2$ and $W_B(N) = 2(2N+1)$ to be considered in the summations in the EVPs Eq. (2.35) and Eq. (2.38), respectively, is a critical analysis parameter to be conveniently chosen. In general, N must be large enough to guarantee convergence of the solution. However, N cannot be too large since the size of the EVP to be solved in each point of the IBZ increases linearly in Eq. (2.38) and with a quadratic

law in Eq. (2.35). Since the analysis targets the behavior of the structure in the low-frequency range, and given the considered harmonic expressions for the curvatures, it can be shown that the number of terms to be considered in the expansions of the Fourier series is $N = 3$ for the beam case.

2.4 Results for Undulated Beams

Results are presented for periodically undulated beams in terms of band diagrams and harmonic response of finite beams. The band diagram estimations are based on the PWEM formulation and the FE as in [20]. An aluminum beam (Young's modulus $E = 70$ GPa, mass density $\rho = 2700$ kg/m^3) of constant thickness h and assigned undulation magnitude c_0 and period a is considered. Studies are conducted by considering a fixed period $a = 0.1$, while varying thickness and undulation magnitude. For convenience, the following non-dimensional parameters are considered:

$$\zeta = \frac{c_0}{a}, \qquad \gamma = \frac{h}{a} \tag{2.41}$$

which normalize the undulation amplitude and beam thickness to the unit cell length a.

2.4.1 Band Diagrams

Band diagrams are obtained using the PWEM for a chosen suitable number of harmonic terms N included in the expansions. As explained in Sec 2.3.1, $N = 3$ represents a convenient choice for it guarantees convergence of the solution and minimizes the size of the EVP to be solved.

The governing equations employed for the beam formulation imply that the beam can be considered thin, which is here enforced by limiting the study to a thickness parameter $\gamma \in [0,\ 0.1]$. PWEM results are compared with FE predictions obtained

by following [20] and considering the unit cell shown in Fig. 2.1d, discretized using 100 $B21$ Abaqus 2-node linear beam elements. These elements account for shear deformation through the thickness of the beam, and are documented to provide accurate results when characteristic cross-sectional dimensions do not exceed 1/8 of the wavelength of the highest significant deformation mode [92]. This is certainly well within the range considered for the γ parameter.

Results are presented for four values of undulation, namely $\zeta = 0$ for the straight beam, $\zeta = 0.01$, $\zeta = 0.03$ and $\zeta = 0.05$. For each undulation value, the effect of beam thickness is considered by computing dispersion diagrams for $\gamma = 0.05$.

Band diagrams are presented in terms of a non-dimensional frequency Ω defined as:

$$\Omega = \frac{fa}{c_L} \tag{2.42}$$

where f is the frequency, expressed in Hz, a is the length of the unit cell and $c_L = \sqrt{E/\rho} = 5091.8\ \frac{m}{s}$ is the speed of longitudinal waves in a reference straight beam.

The first band diagram in Fig. 2.3a corresponds to the straight beam case, *i.e.* $\zeta = 0$, and is presented for reference purposes. In this diagram and in all the following diagrams, comparisons between PWEM and FE estimations are provided, and represented respectively as thick solid lines and green dotted lines. The straight beam case is still computed under the assumption of structural periodicity defined by a and this produces the folding of the dispersion branches at the edge of the IBZ corresponding to $\mu = \pi$. Two family of branches are easily recognized corresponding respectively to the longitudinal 'L' and flexural 'F' mode of propagation. Prior to folding, the curves obey the analytical expressions of the dispersion relations for a straight beam which are given by the well known expressions:

$$\omega_L(\kappa) = \sqrt{\frac{E}{\rho}}\kappa,\ \omega_F(\kappa) = \sqrt{\frac{EI}{A\rho}}\kappa^2 \tag{2.43}$$

In non-dimensional form, the two branches can be easily expressed as:

$$\Omega_L(\mu) = \frac{\mu}{2\pi},\ \Omega_F(\mu) = \frac{\gamma}{2\pi\sqrt{12}}\mu^2 \tag{2.44}$$

Also within a PWEM framework, one can easily show that the folded branches for both modes can be expressed as:

$$\Omega_L(\mu) = \frac{\mu + 2\pi n}{2\pi},\ \Omega_F(\mu) = \frac{\gamma}{2\pi\sqrt{12}}(\mu + 2\pi n)^2 \tag{2.45}$$

where $n = -N, .., +N$, with N defining the number of computed branches. With reference to Fig. 2.3a, the considered frequency range includes one axial branch corresponding to $n = 0$, and 3 flexural branches obtained for $n = 0, n = -1$ and $n = +1$ in Eq. (2.45). Of interest is the intersection between the axial branch corresponding to $n = 0$ and the folded flexural branch obtained for $n = -1$. This intersection occurs at frequency $\Omega \approx 0.08$ and suggests a condition where the existence of coupling may produce interesting wave phenomena. In the case of the straight beam, such coupling does not exist as the governing equations for axial and bending motion are completely decoupled. However, the introduction of even a small curvature couples the two behaviors, which leads to the occurrence of a band gap centered at the frequency of intersection of the two branches mentioned above, as shown in Fig.s 2.3. The identification of the intersecting frequency for the straight beam as the center of the band gap provides an interesting approach for design. Such center frequency can be obtained by imposing equal propagation constants in Eq.s (2.45) which gives the algebraic expression:

$$\Omega = \frac{2\pi}{\sqrt{12}}(\Omega - 1)^2\gamma \tag{2.46}$$

that can be solved in terms of Ω to define the center band gap frequency. As the explicit expression of such value is not particularly noteworthy and it is here omitted,

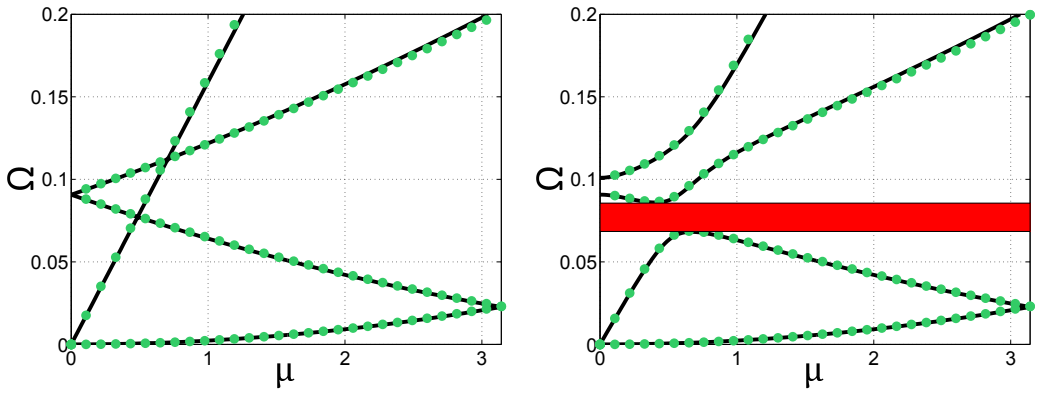

(a) $\zeta = 0$ (straight beam)

(b) $\zeta = 0.01$

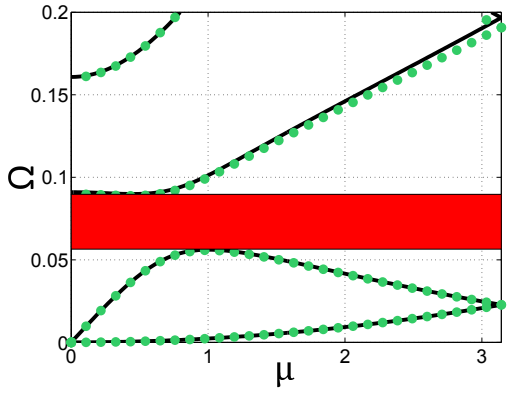

(c) $\zeta = 0.03$

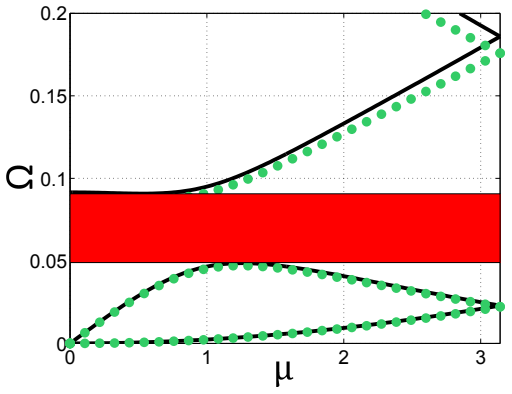

(d) $\zeta = 0.05$

Figure 2.3: Band diagram for undulated beams with $\gamma = 0.05$: PWEM (black solid line) vs. FEM (green dots). Band gap in red.

it is however interesting to show how the solution of Eq. (2.46) only depends on the thickness parameter γ, and the center frequency increases with γ. Further analysis of Fig.s 2.3 suggests that the width of the band gap is determined by the amplitude of the undulation as quantified by parameter ζ. Moreover, it is interesting to observe that another intersection occurs between the $n = 0$ axial branch and the $n = +1$ bending branch. The coupling does affect the dispersion near the intersection point, but it does not induce a second band gap within the range considered. In addition, it is interesting to note that increasing curvature amplitudes produces a shift of the third bending branch towards higher frequencies and reduces the P-wave speed below the gap. Coupling of axial and flexural polarizations effectively 'breaks' the longitudinal

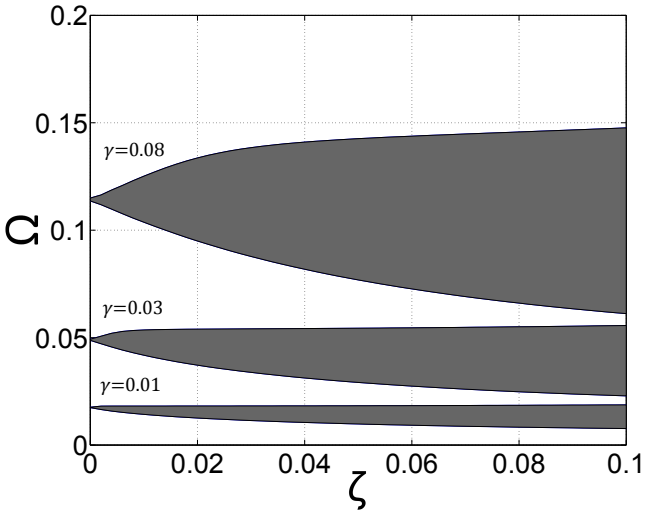

Figure 2.4: Complete band gap map in terms of curvature parameter ζ and thickness parameter γ.

branch into two branches for $\zeta \neq 0$, while the flexural branches are only slightly affected by the undulation. This essentially indicates that undulations do not allow pure longitudinal modes in favor of mixed longitudinal-flexural modes. Width and center frequency of the resulting band gap are affected by the two relevant parameter identified here, respectively γ and ζ. Their effect on band gap center frequency and width are summarized in the map of Fig. 2.4 which clearly shows how center frequency increases with γ, while width increases with the curvature parameter ζ.

The PWEM provides a faster and analytically valuable estimation of the dispersion properties, which can be exploited for parametric studies and eventually design purposes. On the other hand, the FE approach provides a general framework which is suitable for accounting for complex deformation characteristics such as the inclusion of shear deformations through the thickness of the beam and rotary inertia upon proper selection of the elements employed for discretization. The reasonable agreement between the two sets of predictions validates the two processes and provides a framework for their use based on needs and specific assumptions that may be allowed.

2.4.2 Experimental Illustration

An experimental illustration of the results given by the PWEM and FE is conducted on a finite beam including 10 unit cells. The beam is fabricated out of an aluminum plate using a water jet cutter, and it is shown in Fig. 2.5. The length of the beam is $L = 1$ m, for a period $a = 0.1$ m and is characterized by $\gamma = 0.127$ and $\zeta = 0.05$. A relatively thicker specimen was considered to facilitate the fabrication process which becomes challenging for thin sheets. The undulated beam was tested in a cantilever configuration under base excitation. The frequency response of the beam was recorded by a tip accelerometer over a relevant frequency range. A second accelerometer recorded the motion of the base so that an acceleration transmissibility could be evaluated according to the following definition:

$$\mathcal{T} = 20Log_{10}(\frac{A_{tip}}{A_{base}}) \tag{2.47}$$

The motion of the base is generated by an electrodynamic shaker connected to a sliding table on which the beam is mounted on. The experimental set-up is shown schematically in Fig. 2.6.

Results of the experiment are shown in Fig.2.7 in the form of transmission spectra. The experimental curve for the undulated beam is compared with the response predicted numerically through an Abaqus-FE model consisting of 10 unit cells of the kind used for the dispersion studies. A numerical curve for the equivalent straight beam is also obtained and plotted for the sake of completeness. Finally, the two vertical lines define the lower and upper limits of the complete band gap obtained from the dispersion analysis using the PWEM.

Numerical and experimental transmissibility are in reasonable agreement, in particular in the low-frequency range. They both display a drop in transmissibility of about 40 dB for $\Omega \in [0.12, 0.21]$, which indicates how in this range of frequencies the

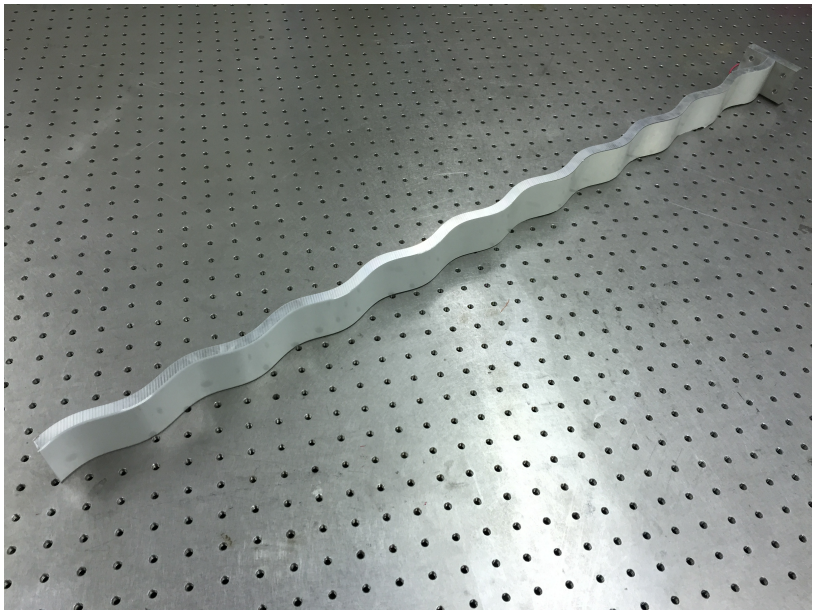

Figure 2.5: Aluminum undulated beam realized by using a water jet cutter.

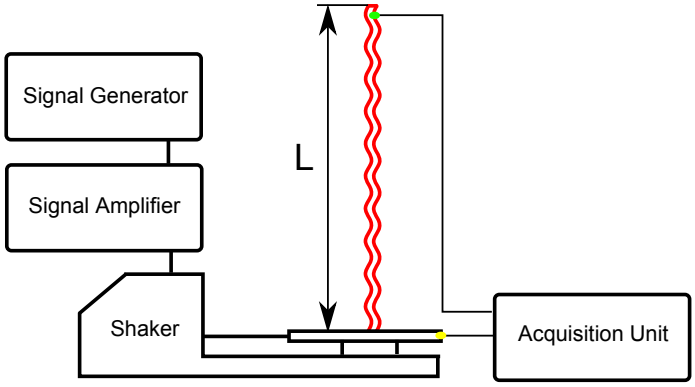

Figure 2.6: Undulated beam experiment schematics: reference accelerometer (yellow point), measurement accelerometer (green point).

transmission of mechanical energy from the excited base of the beam to the tip is negligible, and wave propagation is forbidden. A similar frequency range was predicted by the analytical model, as can be seen by comparing the two vertical lines, that correspond to the expected complete band gap, to the drop of transmission Fig.2.7. The analytical model then gives accurate predictions of the lower band gap, with the only exception represented by a peak around $\Omega = 0.18$, which is also predicted by the FE model. The origin of this peak is most likely related to the finite nature of the beam and to the presence of localized modes within the band gap. This is a point of current investigation. However, the results clearly highlight the occurrence of band gap in the predicted frequency range and confirm that the coupling of axial and flexural polarization leads to a reduction of the ability of the beam to propagate waves. Such reduced transmission characteristics are here highlighted by measuring the flexural motion of the beam.

2.5 Results for Undulated Plates

This section extends the previous analysis to the case of undulated plates. The considered plates are again made of aluminum (Young's modulus $E = 70$ GPa, Poisson's ratio $\nu = 0.33$ and mass density $\rho = 2700$ kg/m^3) and are considered thin, isotropic, and homogeneous. Dispersion relations are again computed using the PWEM and the FE approach. Forced harmonic response of a finite plate also assesses the effect of band gaps and anisotropy induced by undulations on the dynamic behavior of finite plates. These results serve as numerical experiments illustrating behaviors predicted by the dispersion studies.

2.5.1 Band Diagrams

Band diagrams are obtained by varying the wave vector components along the boundaries of the IBZ. Since the direct lattice unit cell is square of side a, the square re-

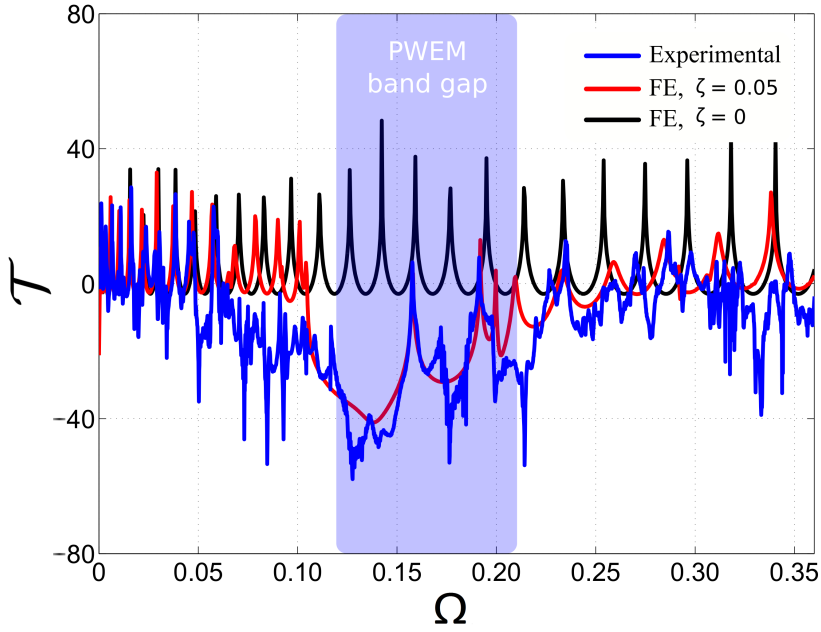

Figure 2.7: Transmission spectra: undulated beam, experimental (blue line); undulated beam, numerical (red line); straight beam, numerical (black line). The two vertical lines identify the range of the complete band gap defined by $\Omega \in [0.12, 0.21]$ computed analytically.

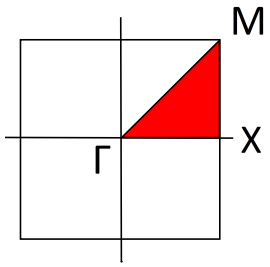

Figure 2.8: In red the Irreducible Brillouin Zone in the reciprocal lattice space of the undulated plate unit cell.

ciprocal lattice unit cell can be conveniently restricted to the IBZ shown in Fig. 2.8. The unit cells are considered square of side $a = 0.1$ cm, which is maintained fixed throughout the study. Undulation parameter ζ and thickness parameter γ are again varied to evaluated, their effect on the dispersion properties of the plate. Four sets of parameters were considered, depending on the value of ζ: flat plate, i.e. no undulation, for $\zeta = 0$, then $\zeta = 0.01$, $\zeta = 0.03$ and $\zeta = 0.05$. Each set presents, then, different values of the γ, namely $\gamma = 0.05$, $\gamma = 0.07$ and $\gamma = 0.1$.

Results are again presented in terms of a non-dimensional frequency Ω which is again defined as:

$$\Omega = \frac{fa}{c_L} \tag{2.48}$$

where c_L is the speed of longitudinal wave in the flat plate, given by:

$$c_L = \sqrt{\frac{E}{\rho(1-\nu^2)}}$$

which is equal to 5394 m/s in the considered case.

Band diagrams calculated for the considered set of parameters with both PWEM and FE are shown in Fig.s 2.9 through 2.11.

In using the PWE method, the truncation of the Fourier series was done imposing $N = 3$, as explained in Sec 2.3.1. The resulting EVP of dimension $3(2N+1)^2 = 147$ is solved in each point the IBZ is discretized by varying the value of κ_{01} and κ_{02} in

the range $[0, \frac{1}{2}]$.

The PWEM formulation was based on assumptions that neglect rotary inertia and shear deformations through the thickness of the plate. In contrast, the FE model employs Abaqus S4R 4-node general-purpose shell, reduced integration with hourglass control, finite membrane strains shell elements. These elements are able to model thick plates, where transverse shear deformations are not negligible, but they behave as discrete Kirchhoff plate elements when the thickness verifies the thin-plate assumption. A fine mesh was considered, each unit cell being discretized by 2500 S4R elements. The agreement of the predictions of the two methods in all cases considered show that the thin plate approximation is reasonable within this context, and that both methodologies accurately estimate dispersion for the case at hand.

As in the case of the beam, it is interesting to first analyze the dispersion diagrams for the flat plate shown in Fig.s 2.9a through 2.11a. Within the $\Gamma - X$ segment, one may recognize the branches obtained from the analytical solutions of the governing equations for the flat plate, which are given by the well known expressions:

$$\omega_L(\kappa) = \sqrt{\frac{E}{\rho(1-\nu^2)}}\kappa \tag{2.49}$$

$$\omega_S(\kappa) = \sqrt{\frac{E}{\rho}\frac{1}{2(1+\nu)}}\kappa = \sqrt{\frac{G}{\rho}}\kappa \tag{2.50}$$

$$\omega_F(\kappa) = \sqrt{\frac{D}{h\rho}}\kappa^2 \tag{2.51}$$

These are respectively associated with longitudinal 'L', in-plane shear 'S', and flexural 'F' wave polarizations. As in the case of the beam, it is instructive to provide the non-dimensional expressions for these branches which are:

$$\Omega_L(\mu) = \frac{\mu}{2\pi}, \tag{2.52}$$

$$\Omega_S(\mu) = \frac{\mu}{2\pi}\sqrt{\frac{1-\nu^2}{2(1+\nu)}}, \tag{2.53}$$

$$\Omega_F(\mu) = \frac{\gamma}{2\pi\sqrt{12}}\mu^2 \tag{2.54}$$

As in the case of the beam, the application of the PWEM to a unit cell of size a produces the folding of the branches, which causes the $n-1$ flexural branch to intersect the longitudinal and shear branches. This is where interactions are expected when undulation leads to coupled polarizations. The frequency where such intersection occurs can again be found from equations of the kind of Eq. (2.46), which identifies γ as the relevant parameter. Introducing undulation in the plates indeed alters the band structure primarily around this intersection frequency. As the undulation amplitude increases, one can observe the widening of a single-mode region, that eventually extends to the entire wavenumber range, thus producing a "modal" band gap that affects the propagation of longitudinal-flexural and shear-flexural modes in the plate. Within the modal band gap, highlighted by the shaded green region in the figures, the only allowed mode displays shear-dominated features along the $\Gamma - X$ direction, while the same mode has longitudinal-dominated features along the $\Gamma - M$ direction. Such a behavior has been described as "super anisotropy" in elastic metamaterials [93]. This can be observed as a general trend in Fig.s 2.9 through 2.11.

Further analysis of the results, suggests that for a fixed value of the thickness parameter γ, it is possible to define a critical value ζ_{cr} above which the modal band gap is produced. Dependence of ζ_{cr} on the thickness parameter γ is shown in Fig.2.12a, which illustrates how thicker plates require larger undulation parameters ζ in order to display a modal band gap. The evolution of the modal band gaps for increasing values of ζ is summarized in the map of Fig. 2.12b: the width of the modal band gap

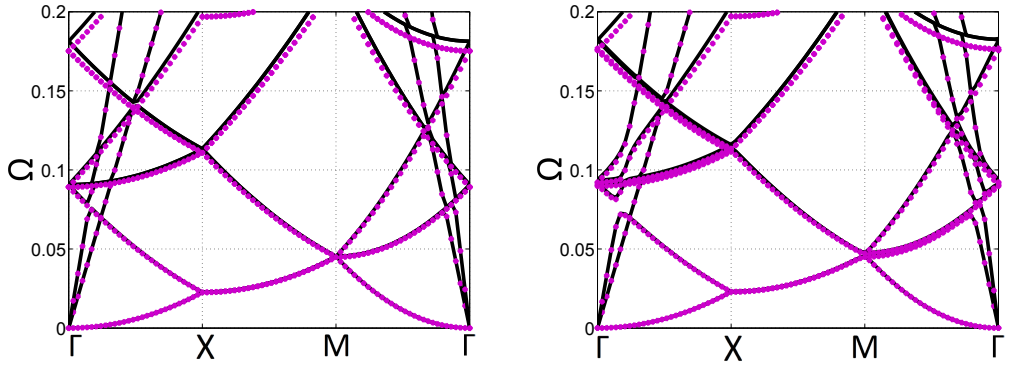

(a) $\zeta = 0$, i.e. flat plate

(b) $\zeta = 0.01$

(c) $\zeta = 0.03$

(d) $\zeta = 0.05$

Figure 2.9: Band diagram for undulated plates with $\gamma = 0.05$: PWEM (black solid line) vs. FEM (purple dots). Modal band gap in green.

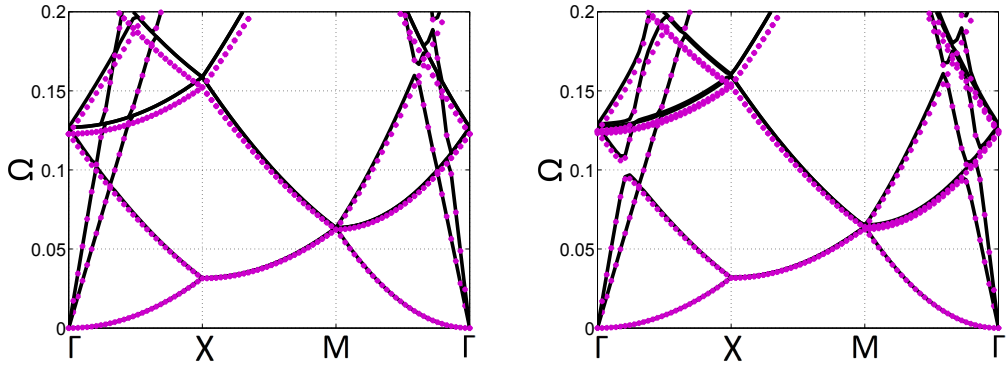

(a) $\zeta = 0$, i.e. flat plate

(b) $\zeta = 0.01$

(c) $\zeta = 0.03$

(d) $\zeta = 0.05$

Figure 2.10: Band diagram for undulated plates with $\gamma = 0.07$: PWEM (black solid line) vs. FEM (purple dots). Modal band gap in green.

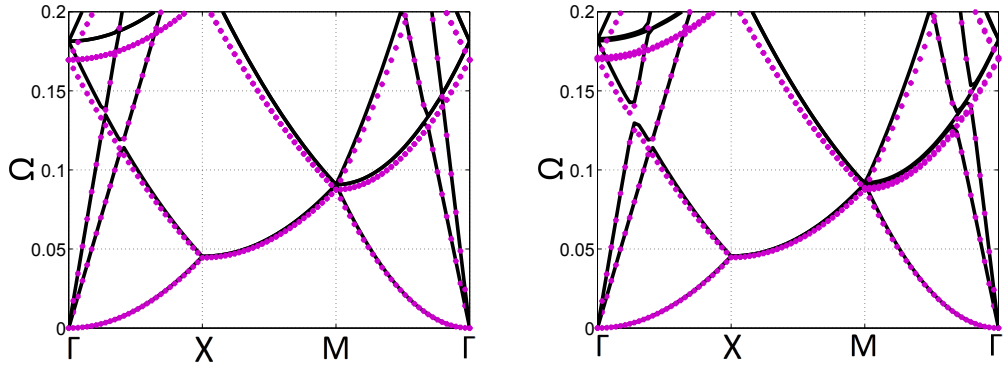

(a) $\zeta = 0$, i.e. flat plate

(b) $\zeta = 0.01$

(c) $\zeta = 0.03$

(d) $\zeta = 0.05$

Figure 2.11: Band diagram for undulated plates with $\gamma = 0.1$: PWEM (black solid line) vs. FEM (purple dots). Modal band gap in green.

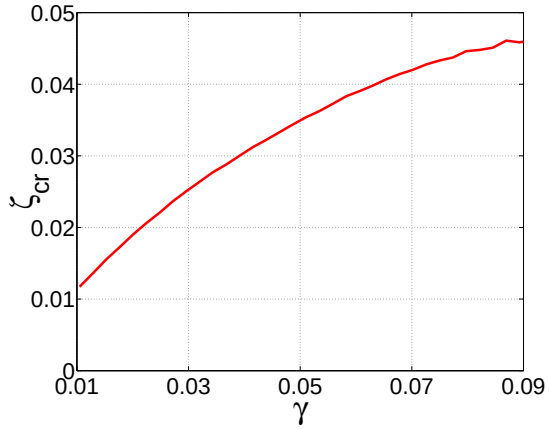

(a)

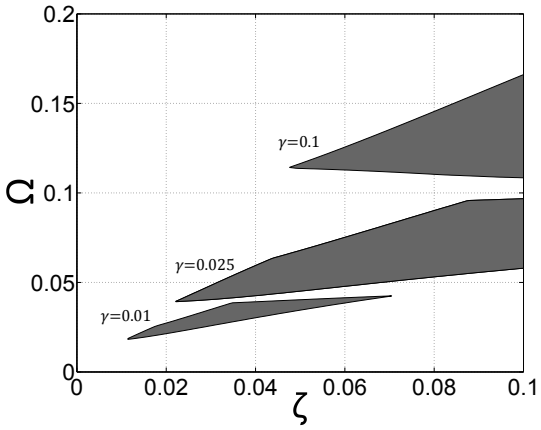

(b)

Figure 2.12: Critical value ζ_{cr} of the curvature parameter ζ as a function of the thickness parameter γ (a), and modal band gap variation in terms of ζ and γ (b).

is not constant for increasing values of ζ and it reaches a maximum before decreasing for higher values of ζ. Furthermore, it can be noted that the modal band gap is shifted towards higher frequencies when thicker plates are considered.

2.5.2 Frequency Response Analysis: Numerical Results

A 11×11 unit cells undulated aluminum (Young's modulus $E = 70$ GPa, Poisson's ratio $\nu = 0.33$ and density $\rho = 2700$ kg/m^3) plate is considered. The square unit cell of the plate has side of length $a = 0.1$ m, thickness parameter $\gamma = 0.05$ and curvature parameter $\zeta = 0.05$. The goal of the analysis is to compare the frequency

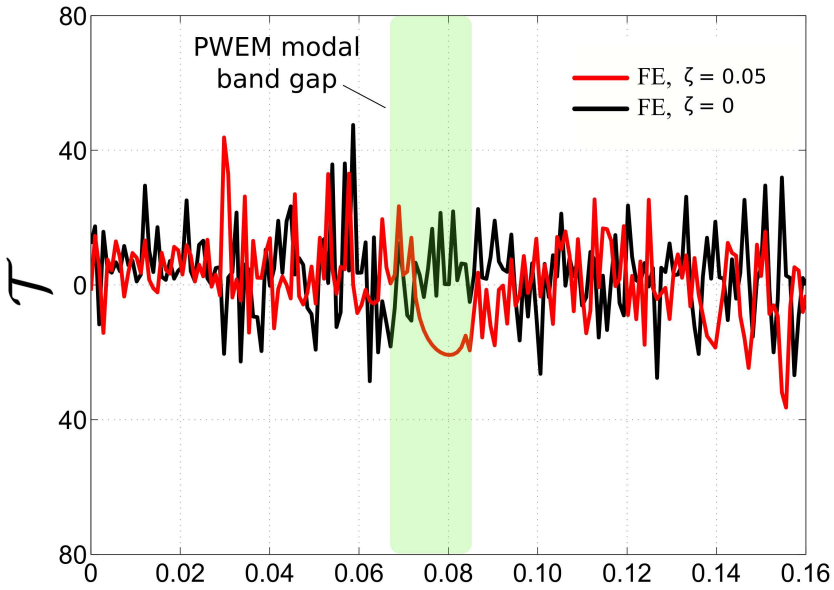

Figure 2.13: Frequency response diagrams: flat plate (black line) and undulated plate (red line) with $\gamma = 0.05$ and $\zeta = 0.05$. The two vertical lines identify the modal band gap range defined by $\Omega \in [0.068, 0.085]$ as computed by using the PWEM.

response diagrams for both the flat and the undulated plates by computing the steady state response to harmonic excitation at discrete excitation frequencies. The external excitation is enforced by imposing the displacement of the plates' central point along the x_3 direction. The plates are free at the boundaries. The response is collected at one of the plates' corner points. The plates are discretized with 9000 Abaqus S4R 4-node general-purpose shell, reduced integration with hourglass control, finite membrane strains shell elements. The frequency diagrams in Fig.2.13 relate $\mathcal{T} = 20Log_{10}(\frac{|U|}{|U|_{ref}})$ and the non-dimensional frequency parameter $\Omega = \frac{fa}{c_L}$, where $|U|$ and $|U|_{ref}$ are the magnitude of the displacement of the plate at the point where the response is collected and at the point where the excitation is imposed, respectively. The lower and the upper bounds of the modal band gap given by applying the PWEM is identified in the diagram by two vertical lines, corresponding to the $\Omega = 0.068$ and $\Omega = 0.085$. In this range, the value of $\mathcal{T}$ drops consistently as a result of the negligible contribution to the displacement magnitude $|U|$ given by the out-of-

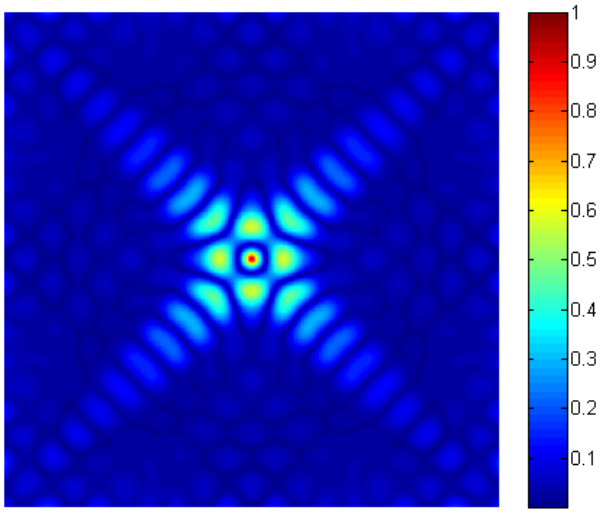

Figure 2.14: Normalized displacement magnitude $|U|$ at steady-state for harmonic excitation at $\Omega = 0.078$ in undulated plate with $\zeta = 0.05$ and $\gamma = 0.05$.

plane component U_3 As discussed above, the modal band gap in undulated plates is associated to a directionally shear-dominated and longitudinal-dominated mode, which are characterized by negligible displacements along the normal to the undulated surface. The steady state response of the undulated plate inside the modal band gap at $\Omega = 0.078$ is shown in Fig. 2.14, where the magnitude of the displacement, normalized to its maximum value, is plotted. The spatial amplitude decay of out-of-plane displacements is evident as produced by the modal band gap. It is also of interest that such decay does not occur uniformly in all directions, and that it is remarkably smaller along the plate diagonals. This suggests a form of directional response within a band gap that may deserve further investigations.

2.5.3 Wave directionality

Another step in the analysis of wave propagation in undulated plates studies how the energy flow in the structure is affected by the curvature modulations at different values of frequency. Wave propagation in isotropic flat plates is omnidirectional, meaning

that the mechanical energy propagates equally in all directions. Conversely, interference phenomena may arise when undulation is introduced, leading the mechanical energy associated with the propagating waves to be focused in specific directions. Directionality of wave propagation is studied by evaluating and analyzing the group velocity

$$\mathbf{c}_g = \nabla\omega(\kappa_{01}, \kappa_{02}) \tag{2.55}$$

where

$$\mathbf{c}_g = c_{g_1}\mathbf{e}_1 + c_{g_2}\mathbf{e}_2$$

The group velocity provides information about the direction of the energy flow throughout the structure. This information is conveniently represented by the polar representation of the vector $\mathbf{c}_g$. If waves propagate isotropically, then the group velocity plot is circular, while anisotropy is revealed if the polar plot ceases to be circular. These polar plots may also reveal preferential directions for the energy flow. The propagation of wave modes associated with longitudinal, transverse and flexural waves in the low-frequency range is of interest, namely prior to the formation of a band gap. This is the range that is mostly of interest in the formulation of equivalent continuum properties through structural geometry as in the case of metamaterials.

The effect of the undulation is investigated by considering the case of an undulated plates with $\gamma = 0.05$ and increasing values of ζ, namely $\zeta = 0$, $\zeta = 0.01$, $\zeta = 0.03$ at $\Omega = 0.056$. For convenience, group velocities are normalized as follows:

$$\tilde{c}_1 = \frac{c_{g_1}}{c_M} \qquad \tilde{c}_2 = \frac{c_{g_2}}{c_M} \tag{2.56}$$

where c_M is the wave speed of the considered mode in an equivalent flat plate ($\zeta = 0$) at the considered frequency. Results are presented in Fig.2.15, where the group velocity plots associated to the longitudinal, shear and flexural waves are shown separately.

For a flat plate, i.e. for $\zeta = 0$, the three velocities can be easily computed by means of Eq.s (2.49), (2.50) and (2.51). Longitudinal and shear modes are not dispersive, hence the group velocity does not depend on the frequency, while the group velocity related to flexural modes changes with the frequency, being the flexural mode dispersive. Nevertheless, wave propagation associated to longitudinal, transverse and flexural modes is isotropic, as shown by the circular polar velocity plots in Fig. 2.15a, Fig. 2.15b and Fig. 2.15c. In undulated plates, the mode-coupling due to the periodic undulation influences the dispersion properties of the structure by inducing a dispersive behavior in the longitudinal-dominated and transverse-dominated modes. As a result of that, the magnitude of the group velocities of the longitudinal-dominated and shear-dominated modes for $\zeta = 0.01$ slightly decreases with respect to the flat plate case, as shown in Fig. 2.15d and Fig. 2.15e, but isotropy of wave motion is mostly preserved. In constrast, the flexural mode starts displaying directionality for $\Omega = 0.056$, as shown in Fig.2.15f: lobes of different sizes protrude in the vertical and horizontal directions, as well as in the $\pm 45°$ directions, indicating directions of preferential wave propagation. Finally, for undulation $\zeta = 0.03$ the group velocity of longitudinal-dominated and shear-dominated modes shown in Fig.s 2.15g and 2.15h, respectively, decreases considerably if compared to the group velocity of the equivalent modes in a flat plate shown in Fig.s 2.15a and 2.15b. Furthermore, both longitudinal-dominated and shear-dominated modes display a directional behavior: the magnitude of the group velocity associated to the first mode is larger along the $\pm 45°$ directions, while the shear-dominated mode is characterized by cusps in the group velocity plot, called caustics, along the vertical and the horizontal directions. Caustics are due to interference phenomena involving the propagating waves that lead to strong energy focusing along specific directions, therefore it is possible to conclude that in the considered case longitudinal-type and transverse-type of waves focus along the $\pm 45°$ directions and along the vertical and the horizontal directions, respectively. As shown

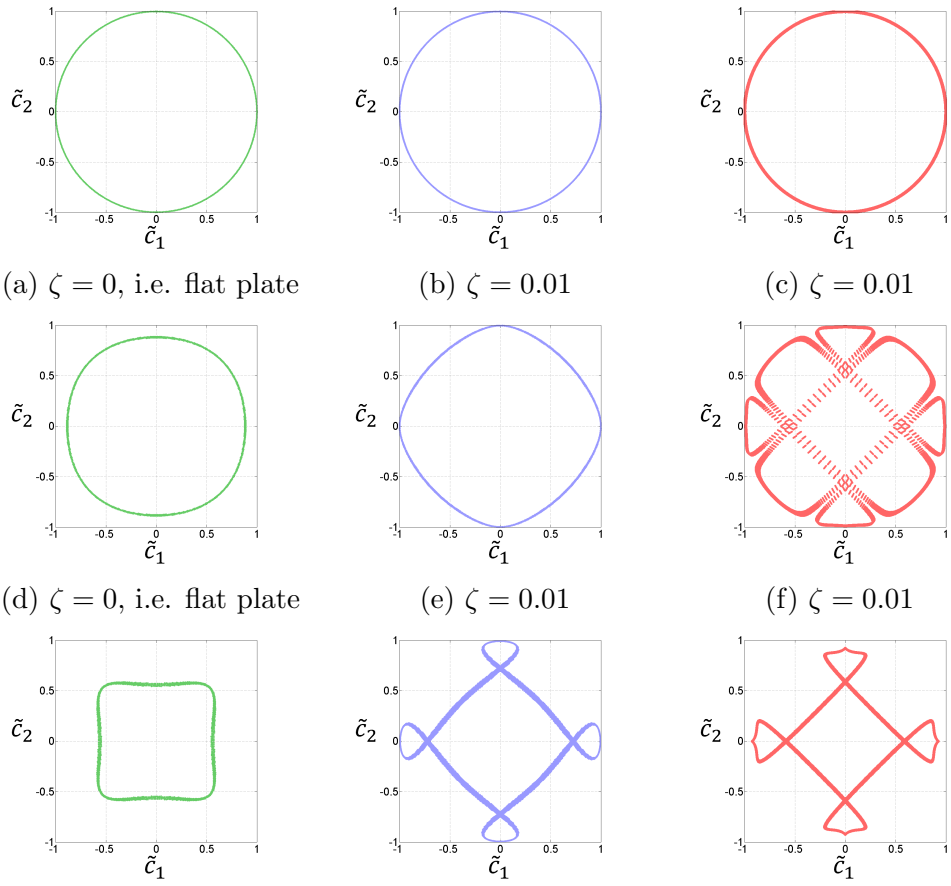

(a) $\zeta = 0$, i.e. flat plate (b) $\zeta = 0.01$ (c) $\zeta = 0.01$

(d) $\zeta = 0$, i.e. flat plate (e) $\zeta = 0.01$ (f) $\zeta = 0.01$

(g) $\zeta = 0$, i.e. flat plate (h) $\zeta = 0.01$ (i) $\zeta = 0.01$

Figure 2.15: Group velocity plots at $\Omega = 0.056$ for fixed $\gamma = 0.05$ and increasing values of the undulation ζ. The group velocity plots are presented for each of the investigated modes: longitudinal (L) mode, shear (S) mode and flexural (F) mode. Wave directionality introduced by the undulation is revealed by caustics along the horizontal and vertical directions in the transverse and the flexural modes.

in Fig. 2.15i, also the flexural mode shows caustics along the vertical and horizontal directions, suggesting the occurrence of directions of strong energy focusing.

In conclusion, undulation strongly affects wave directionality in plate structures: coupling of modes usually orthogonal to each other in flat plates affects wave propagation firstly by decreasing wave speeds associated to longitudinal-dominated and transverse-dominated waves, then by inducing anisotropic wave propagation behavior in flexural modes.

2.5.4 Transient Response Analysis: Numerical Results

Directionality as predicted by the group velocity plots is assessed through the evaluation of the transient response to harmonic excitation analysis of finite plates. Flat and undulated aluminum plates of side $L = 2.1\ m$ are considered. The undulated plate has unit cell of length $a = 0.1\ m$ and $\zeta = 0.03$, which corresponds to a 21×21 unit cells array. Both flat and undulated plates are characterized by thickness parameter $\gamma = 0.05$. The external excitation is applied as an imposed harmonic displacement along the x_3 (*i.e.* perpendicular to the plate plane) direction of the plates' central point. The frequency of excitation is $f = 3000\ Hz$, corresponding to $\Omega = 0.056$. The mesh used to discretize the plates comprises 193600 Abaqus S4R 4-node general-purpose shell, reduced integration with hourglass control, finite membrane strains shell elements. An implicit direct integration scheme was used in Abaqus/Standard.

Results are presented in Fig.2.16 in the form of the normalized displacement magnitude $|U|$ field at different time steps. The main contribution to $|U|$ is given by displacement components along the x_3 direction, being the displacement components along the x_1 and x_2 directions comparatively small. The flexural modes are then dominant in defining not only the flat plate displacement field, but also the undulated plate displacement field. For this reason it is useful to compare the displacement fields in Fig.2.16 with the group velocity plots at $\Omega = 0.056$ of the flat plate and the undulated plate with $\zeta = 0.03$ in Fig.2.15c and Fig.2.15i, respectively. As expected, perfectly isotropic flexural waves propagate from the excitation point in the flat plate, as can be seen in Fig.2.16a, before the reflections from the boundaries break the wave field circular symmetry, as shown in Fig.2.16c and Fig.2.16e. On the other hand, the wave front in the undulated plate displays anisotropy along the horizontal and vertical directions, as it is easily recognizable in Fig.2.16b being this consistent with the caustics in the group velocity plot shown in Fig.2.15i. It is interesting to note that as waves reach the boundaries of the structure and are reflected back, the energy

associated with the motion of the undulated plate is subjected to a channeling effect along the caustics horizontal and vertical directions.

The analysis of the group velocity and the study of the transient response of finite flat and undulated plates outline a rich design space for the tailoring of wave propagation. The configuration of these structures is such that directionality can be tailored not only by varying the excitation frequency, but also by increasing or decreasing the undulation of the structure, hence inducing a favorable modal coupling effect that effectively focuses the energy associated to the propagating waves along specific directions.

2.6 Conclusions

This chapter investigated complete and modal band gaps and wave propagation directionality in harmonically undulated plates and beams. For undulated beams, numerical analysis, performed by using PWEM and FEM in conjunction with the Bloch Theory, as well as experiments, illustrate such behaviors. Geometrical undulations is shown to be an effective design strategy that can be tailored to achieve desired the filtering properties. Directionality wave propagation characterize undulated plates, and its occurrence can be controlled through the design of undulation periodicity, amplitude and thickness.

In the next chapter, the concept of varying the local measure of curvature to obtain undulated patters is extended to square reticulates. The resulting undulated lattice show interesting filtering and wave directionality properties.

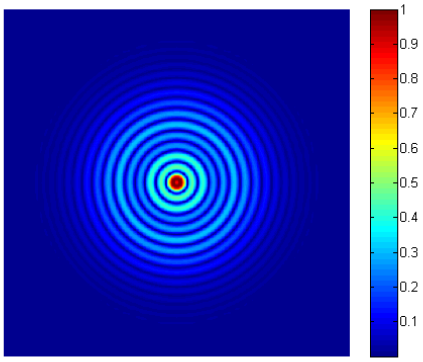

(a) Flat plate, $t = 8 \cdot 10^{-4}s$

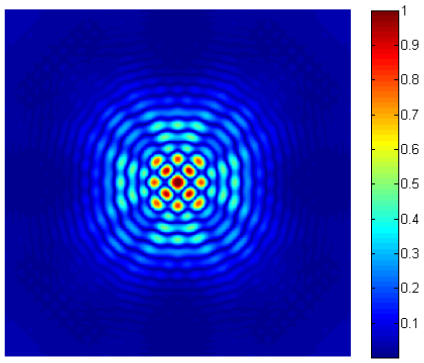

(b) Undulated plate, $t = 8 \cdot 10^{-4}s$

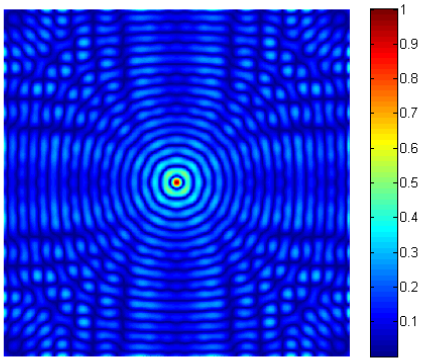

(c) Flat plate, $t = 2.4 \cdot 10^{-3}s$

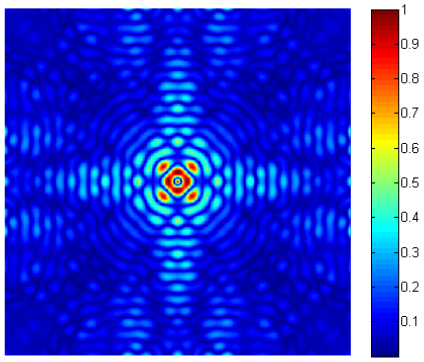

(d) Undulated plate, $t = 2.4 \cdot 10^{-3}s$

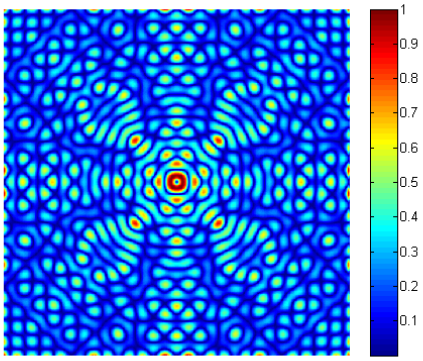

(e) Flat plate, $t = 4 \cdot 10^{-3}s$

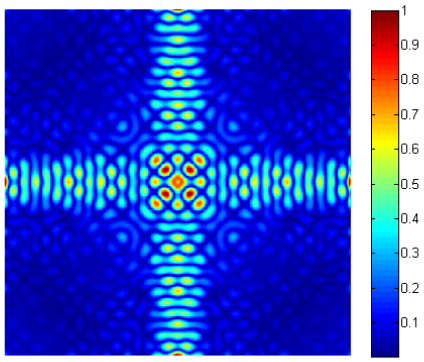

(f) Undulated plate, $t = 4 \cdot 10^{-3}s$

Figure 2.16: Transient response of a flat plate and undulated plate with $\zeta = 0.03$ to harmonic external excitation at $\Omega = 0.056$ for fixed $\gamma = 0.05$. The plots present the normalized magnitude of the displacement field $|U|$. Directionality along horizontal and vertical directions is a consequence of the periodic undulation of the plate.

CHAPTER 3
UNDULATED LATTICES

3.1 Overview

This chapter focuses on the behavior of 2D structures obtained by combining undulated beams in a lattice arrangement. As discussed in the previous chapter, undulation of beam elements is responsible for modal coupling phenomena leading to interesting wave propagation properties. When such beam elements are connected to form a 2D grid, the question arises if other factors influence wave phenomena in the resulting undulated lattices. Here, this question is addressed by first introducing the geometry of two different undulated lattice configurations. Both periodic and graded lattice configurations are considered, whereby graded configurations are obtained by gradually varying the lattice elements' curvature along a certain direction. Then, the dispersion properties of the periodic configurations are investigated by means of a numerical implementation of Bloch analysis. The two undulated configurations differ considerably at higher frequencies, both in terms of band gaps and wave directionality, as confirmed by time-domain numerical simulations. Finally, the properties of the graded configurations are considered based on the analysis of their periodic counterparts.

3.2 Geometry of undulated lattices

The considered lattices are obtained by modifying a straight, square array of beam elements joined together at the intersections, as shown in Fig. 3.1. All beams have square cross section of thickness h. Undulated lattice patterns are obtained by imposing an initial curvature to the beam elements. A harmonic undulation $c(x_i^l) = c \sin \pi x_i^l / a$

$(i = 1, 2)$ is defined by the maximum distance c between the centerlines of the undulated and the original straight configuration. The parameter c can be held constant throughout the lattice, thus maintaining the periodicity of the structure, or can be modulated in space, i.e. letting $c = c(x_1, x_2)$, to produce spatially graded configurations. Examples of graded configurations are given in Fig. 3.2a.

Undulation imposed to an originally straight square lattice breaks geometrical symmetries. It can be observed that, among others, straight lattices posses mirror symmetry with respect to $\pm 45°$ lines passing through the center of the unit cell. Similarly, undulated configuration 2 enjoys the same property, while undulated configuration 1 does not. The unit cell's symmetry plays an important role in determining the wave propagation properties of structural lattices [94].

3.3 Periodic Undulated Lattices

The following sections present results for periodic undulated lattices. All studies consider structures that are made of aluminum with Young's modulus $E = 73$ GPa, Poisson's ratio $\nu = 0.33$ and density $\rho = 2700\ \frac{kg}{m^3}$. Frequencies values are presented in terms of the normalized frequency Ω as defined in Eq. (2.48). Parametric studies investigate the effect of the undulation amplitude parameter ζ and the slenderness parameter γ on frequency band gaps and wave directionality produced by anisotropy.

The study of wave propagating in periodic undulated lattices is performed through implementation of the Bloch analysis as suggested in [20]. Each unit cell is discretized by 480 B21 beam elements. These elements allow for transverse shear deformation, which plays an important role for thick beam elements and when high frequency modes are considered. The sectional shear stiffness assumed in the analysis is $K = kGA$, with G shear modulus, A area of the cross section and $k = 0.85$ shear factor for the rectangular cross section [95].

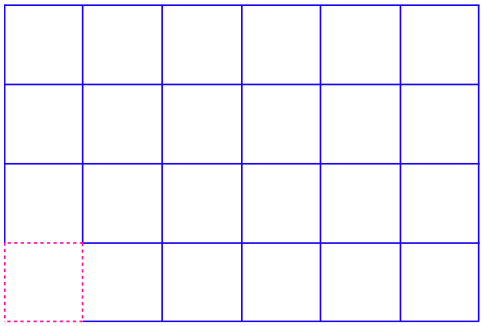

(a) Straight configuration

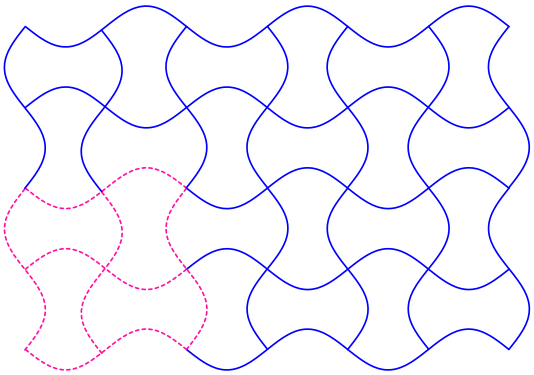

(b) Undulated configuration 1

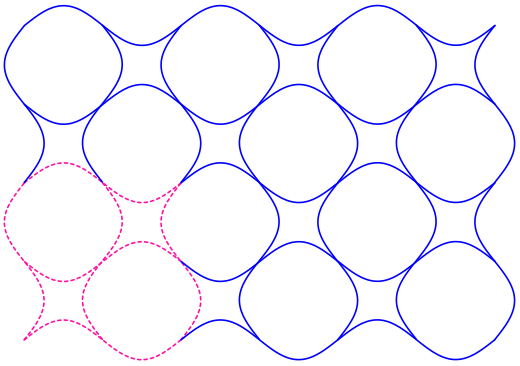

(c) Undulated configuration 2

Figure 3.1: Periodic straght and undulated lattice configurations 1 and 2 (left) with relative unit cells (right). The size of the undulated lattices unit cell is twice the size of the straight lattice unit cell.

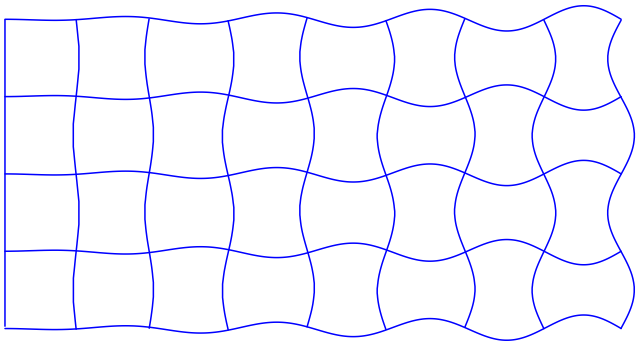

(a) Undulated configuration 1

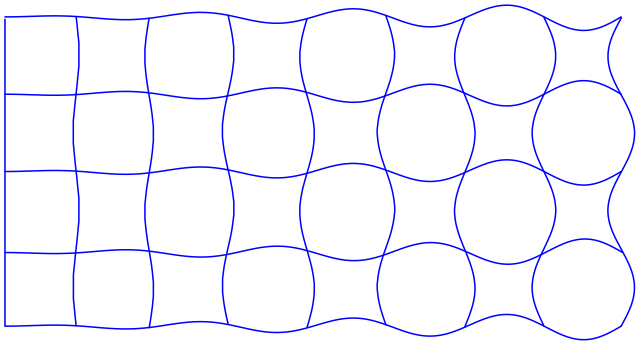

(b) Undulated configuration 2

Figure 3.2: Graded undulated lattice configurations 1 and 2.

3.3.1 Band diagrams

Band diagrams of undulated lattices are compared with that of the straight square lattice with $\gamma = 0.05$ shown in Fig. 3.3a. The reduced symmetry induced by the undulations requires considering an enlarged 2x2 unit cell with respect to the straight lattice (Fig. 3.1). A first set of observations is made on the low frequency range, $\Omega \to 0$, *i.e.* in the long wavelength limit. The two dispersion branches in the $\Gamma - X$ direction obey to the two analytical expressions in dimensional form:

$$\omega_l = c_l \kappa_l \qquad \omega_t = c_t \kappa_l \tag{3.1}$$

and are associated with longitudinal and transverse waves in the lattice. In this frequency/wavelength range, the velocities c_l and c_t for a square lattice are given by

[34, 96]:

$$c_l = \sqrt{\frac{E}{2\rho}} \qquad c_t = \gamma\sqrt{\frac{E}{\rho}} \tag{3.2}$$

where E is the Young's modulus and ρ is the density of the constituent material.

Striking differences between the straight and the undulated lattice configurations start to occur at higher frequencies. As already reported in [34], straight lattices do not display band gaps in a wide range of slenderness parameter values γ. When undulation is introduced, large band gaps are obtained, as it can be seen in Fig. 3.3b and Fig. 3.3c. Although both undulated configurations considered display band gaps, the frequency at which they occur, their width and their behavior at different values of undulation amplitude are distinctive of the specific undulated configuration. Information about band gaps for different values of the geometric parameters are provided by the band gap maps in Fig. 3.4. These maps are obtained for both configurations by holding constant the values of γ and a, and by varying the value of ζ within the range $[0, 0.1]$. The undulated configuration 1 is characterized by two main band gaps, one that is less wide but opens at a lower value of the undulation amplitude ζ and a wider one that opens at a higher value of ζ. For increasing ζ, the mean value of the wider band gap decreases, while its width first increases, then remains constant. For undulated lattices of increasing slenderness parameter γ, hence for increasingly thicker beam elements, the two band gaps open at a higher value of undulation amplitude ζ, also they are shifted at higher frequencies. On the other hand, band gaps for configuration 2 are less wide, and open and then close for increasing values of ζ. Also, for thicker beam elements, they vanish almost completely in the range of parameters considered. In general, for a given configuration, each set of geometric parameters and each band gap defines a critical value ζ_c of the undulation amplitude corresponding to which a band gap opens as clearly shown in Fig. 3.4.

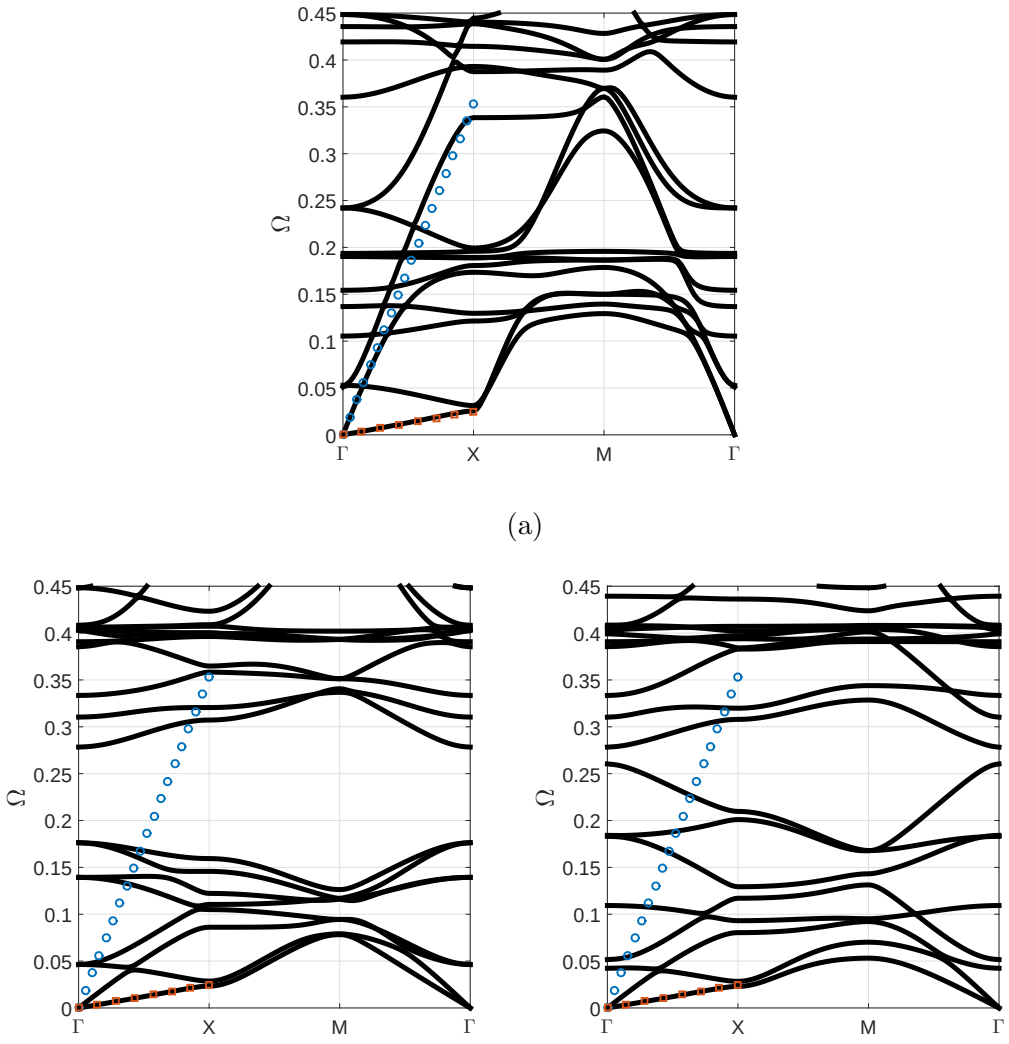

(a)

(b)

(c)

Figure 3.3: Band diagrams for straight lattice (a), undulated configuration 1 (b), and undulated configuration 2 (c) ($\zeta = 0.10$ and $\gamma = 0.05$). Circular and square marker lines are the dispersion relations for the longitudinal and transverse modes in the square lattice expressed by Eq. (3.2).

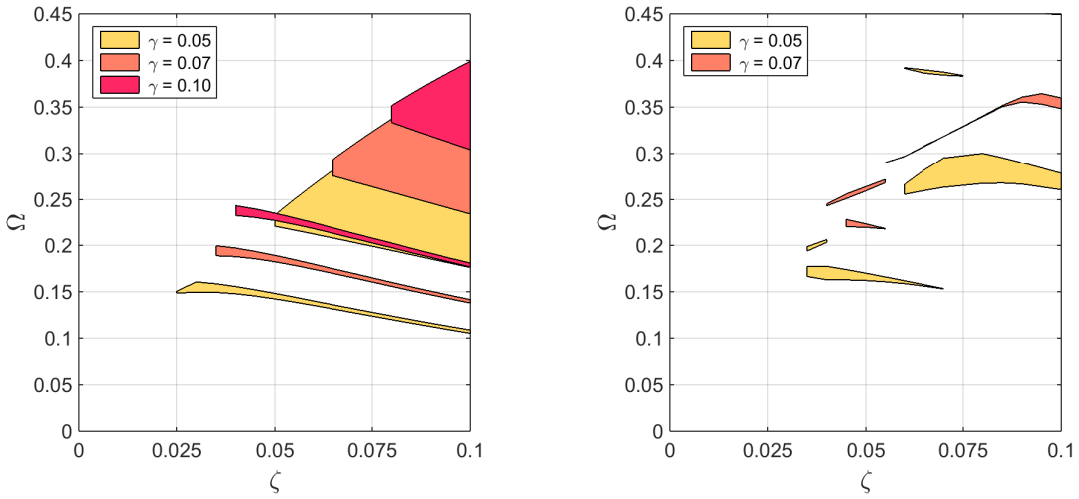

(a) Configuration 1.

(b) Configuration 2.

Figure 3.4: Band gap maps of configurations 1 and 2 as a function of ζ and γ.

3.3.2 Harmonic Response

A first verification of the analysis discussed so far is presented in the form of frequency response diagrams, which are obtained by calculating the steady-state dynamic response of finite 16x16 unit cell straight and undulated lattices. The responses are computed for harmonic excitation at different values of frequencies in the range $\Omega \in [0, 0.45]$. The excitation is enforced by imposing the displacement of a node of the boundary of the lattice along the $\hat{\mathbf{i}}_1$ direction, then collecting the magnitude of the response on the other side of the lattice, as shown in Fig. 3.5. Other than at the excitation point, all the remaining boundaries of the lattice are free. The frequency response diagrams are shown on the left column of Fig. 3.6 and 3.7.

The plots display the transmission coefficient T on the abscissa axis as a function of the non-dimensional frequency Ω on the ordinate axis. Transmission is computed as:

$$T = 20Log_{10}(\frac{|U|}{|U|_{ref}}) \tag{3.3}$$

where $|U|$ and $|U|_{ref}$ are the magnitude of the displacement vector at the point where

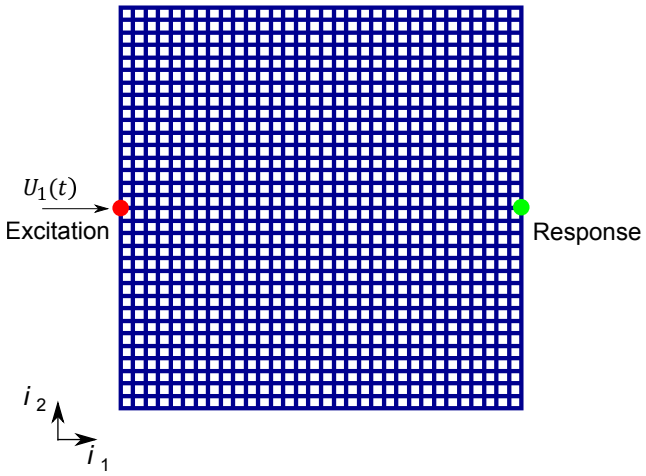

Figure 3.5: Schematics of a straight lattice subjected to imposed displacement $U_1(t)$ along the $\hat{\mathbf{i}}_1$ direction. The excitation is imposed at a node on the left side of the lattice's boundary, while the response is collected at a point located on the other side of the lattice.

the response is collected and at the point where the excitation is imposed, respectively. The coefficient T provides information on the frequencies at which waves are allowed to propagate throughout the structure: low values of T correspond to frequencies of forbidden wave propagation, since the perturbation applied locally remains local and decays quickly in the proximity of its point of application. Consistently with the information given by the band diagram in Fig. 3.3a, the values of the parameter T show that the straight lattice with $\gamma = 0.05$ allows wave propagation in all the considered frequency range. Conversely, in undulated lattices a significant drop of T is associated with frequencies corresponding to the band gaps represented by shaded areas in the diagrams of Fig. 3.6 and Fig. 3.7.

3.3.3 Directionality of Wave Propagation: Group Velocities and Anisotropy Index

The second step of the analysis characterizes the directionality of wave motion. Elastic energy propagates throughout the structure with different velocities depending on the direction of propagation. Information on wave propagation anisotropy of a structure

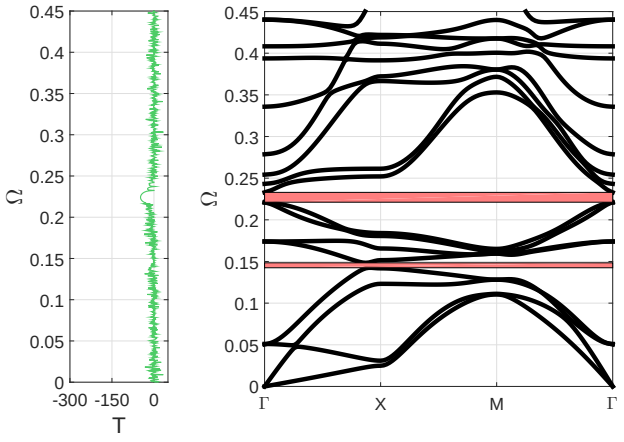

(a) $\zeta = 0.05$. (b) $\zeta = 0.05$.

(c) $\zeta = 0.07$. (d) $\zeta = 0.07$.

(e) $\zeta = 0.10$. (f) $\zeta = 0.10$.

Figure 3.6: Frequency response diagrams (left) vs. band diagrams (right) of the undulated lattice in configuration 1 for $\gamma = 0.05$ and increasing values of ζ. The shaded areas correspond to band gaps.

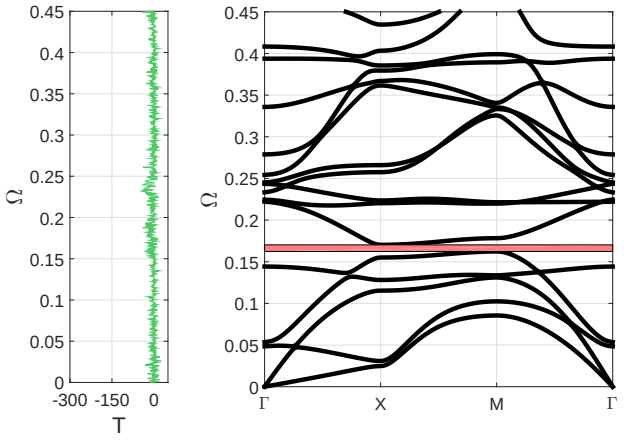

(a) $\zeta = 0.05$. (b) $\zeta = 0.05$.

(c) $\zeta = 0.07$. (d) $\zeta = 0.07$.

(e) $\zeta = 0.10$. (f) $\zeta = 0.10$.

Figure 3.7: Frequency response diagrams (left) vs. band diagrams (right) of the undulated lattice in configuration 2 for $\gamma = 0.05$ and increasing values of ζ.

can be obtained by plotting the components of the group velocity $\boldsymbol{c}_g$ associated to a certain value of frequency, which reveals the difference in velocity of propagation in different directions. When the components of $\boldsymbol{c}_g$ corresponding to a certain wave mode lead to a circular plot, no preferential direction for the energy is observed, and the structure is isotropic. In contrast, group velocity plots departing from circularity characterize non-isotropic behavior. A quantitative characterization of anisotropy relies on the evaluation of the angular dependence of the magnitude $c_g = |\boldsymbol{c}_g|$ of the group velocity in relation to its mean circumferential value. This leads to the formulation of the anisotropy index (AI), which is defined as [33]:

$$AI = \sqrt{\int_0^{2\pi} \left[\frac{c_g(\theta) - \bar{c}_g}{\bar{c}_g}\right]^2 d\theta} \tag{3.4}$$

where $c_g(\theta)$ denotes the magnitude of the group velocity relative to a certain mode as a function of the angular position θ, while $\bar{c}_g$ is the average value of $c_g(\theta)$ over the full 360° angular range, i.e.:

$$\bar{c}_g = \frac{1}{2\pi} \int_0^{2\pi} c_g(\theta) d\theta \tag{3.5}$$

From the definition of AI, it follows that $AI = 0$ defines isotropic assemblies, while a structure having $AI \neq 0$ is characterized by a certain degree of anisotropy.

It is known that square lattices, contrary to other lattice structures such as triangular, hexagonal honeycombs or Kagome lattices, are strongly anisotropic at low frequencies, with different degree of anisotropy for transverse modes (S-modes) and longitudinal modes (L-modes) [34, 33]. At higher frequencies, combinations of S-modes and L-modes generate complex wave propagation patterns. As shown by the band diagram of the straight square lattice in Fig. 3.3a wave propagation is always characterized by more than one mode at a certain frequency in the range $\Omega \in [0, 0.45]$. These modes are in general characterized by different degrees of anisotropy, which may

vary substantially from mode to mode [33]. In order to obtain a structure that effectively realizes complete directional wave propagation, it is desirable to have a single directional mode. This condition is realized in conveniently undulated lattices. The two undulated lattice configurations with $\gamma = 0.05$ and $\zeta = 0.1$ are considered. The dispersion branches that depart from the band gaps in Fig. 3.8a and Fig. 3.9a are studied. For undulated configuration 1, there is one branch displaying a stationary point of inflection at $\Omega = 0.3072$, while for undulated configuration 2 stationary points of inflection correspond to two different branches at $\Omega = 0.2097$ and $\Omega = 0.3079$. Stationary points of inflection are considered because they signal where the dispersion branches are locally flat, therefore where the group velocity associated to the mode is zero. In the case of the frequencies considered above, the modes are characterized by zero group velocity along $\Gamma - X$ and $X - M$, while the same branches have nonzero group velocity along $M - \Gamma$, therefore wave propagation is expected to occur mainly along $M - \Gamma$. Results shown in Fig. 3.8 and Fig. 3.9 are obtained by computing the group velocity for increasing values of the frequency parameter Ω, then evaluating the AI associated to the corresponding wave mode. The values of AI are normalized with respect to the peak value in each considered frequency range. Fig. 3.8b, 3.9b and 3.9c show that for both undulated configurations strong anistropic behavior is signaled by a peak in the value of AI. As expected, in the case of the undulated configuration 1, anisotropy has a maximum at $\Omega = 0.3072$, while in the case of undulated configuration 2 the maxima are reached at $\Omega = 0.2097$ and $\Omega = 0.3079$. Despite the fact that the two configurations display strong anisotropy at different frequencies, they are characterized by similar AI curves and group velocity plots which, for both configurations, show that the energy is focused along the $\pm 45^{\circ}$ directions.

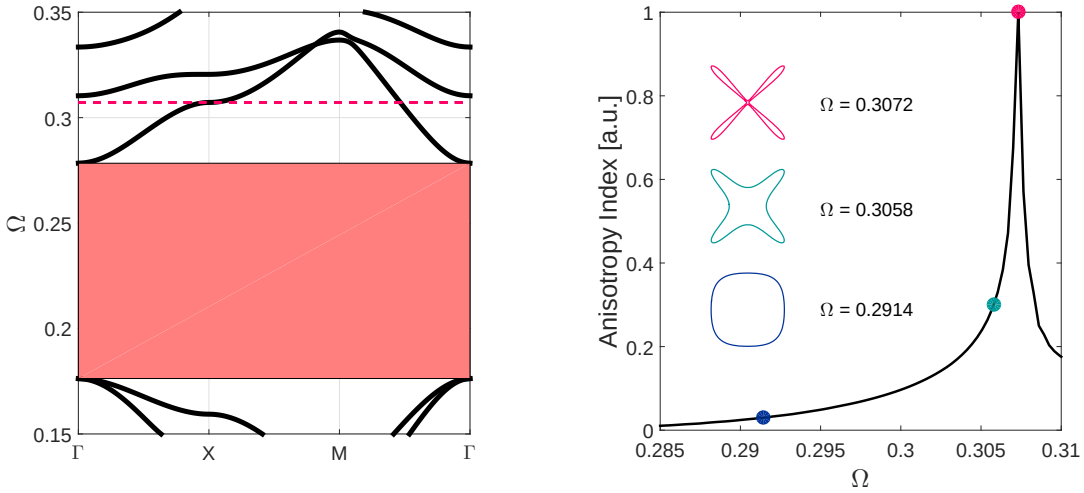

(a) (b)

Figure 3.8: Detail of the band diagram (a) and anisotropy index plot (b), in which group velocity plots are also displayed at selected frequencuies for configuration 1. Geometric parameters: $\gamma = 0.05$ and $\zeta = 0.1$. The group velocity plots are normalized.

3.3.4 Transient response to harmonic excitation

Transient responses are computed to illustrate the manifestation of directionality in finite lattices. Finite 16x16 unit cell lattices are excited by imposing the local rotation of the lattice at a point placed in the mid span of one of the lattice's edges. For both configuration 1 and 2, the geometric parameters are $\zeta = 0.1$ and $\gamma = 0.05$. The excitation has the form of a sine wave with frequency corresponding to a selected value of Ω, which in the case of configuration 1 is $\Omega = 0.3072$, while for configuration 2 it is $\Omega = 0.2097$. An equivalent square lattice is considered and its response is evaluated for the same excitation applied to the undulated configuration 1 in order to provide a reference. Figure 3.10 show snapshots of the magnitude of the displacement field for the square and both the configuration 1 and 2 lattices. The displacement in each plot is normalized to the maximum valued at the considered time instant. Consistently with the group velocity predictions, undulated lattices allow energy to propagate only along the $\pm 45°$ directions, while the energy propagates preferentially

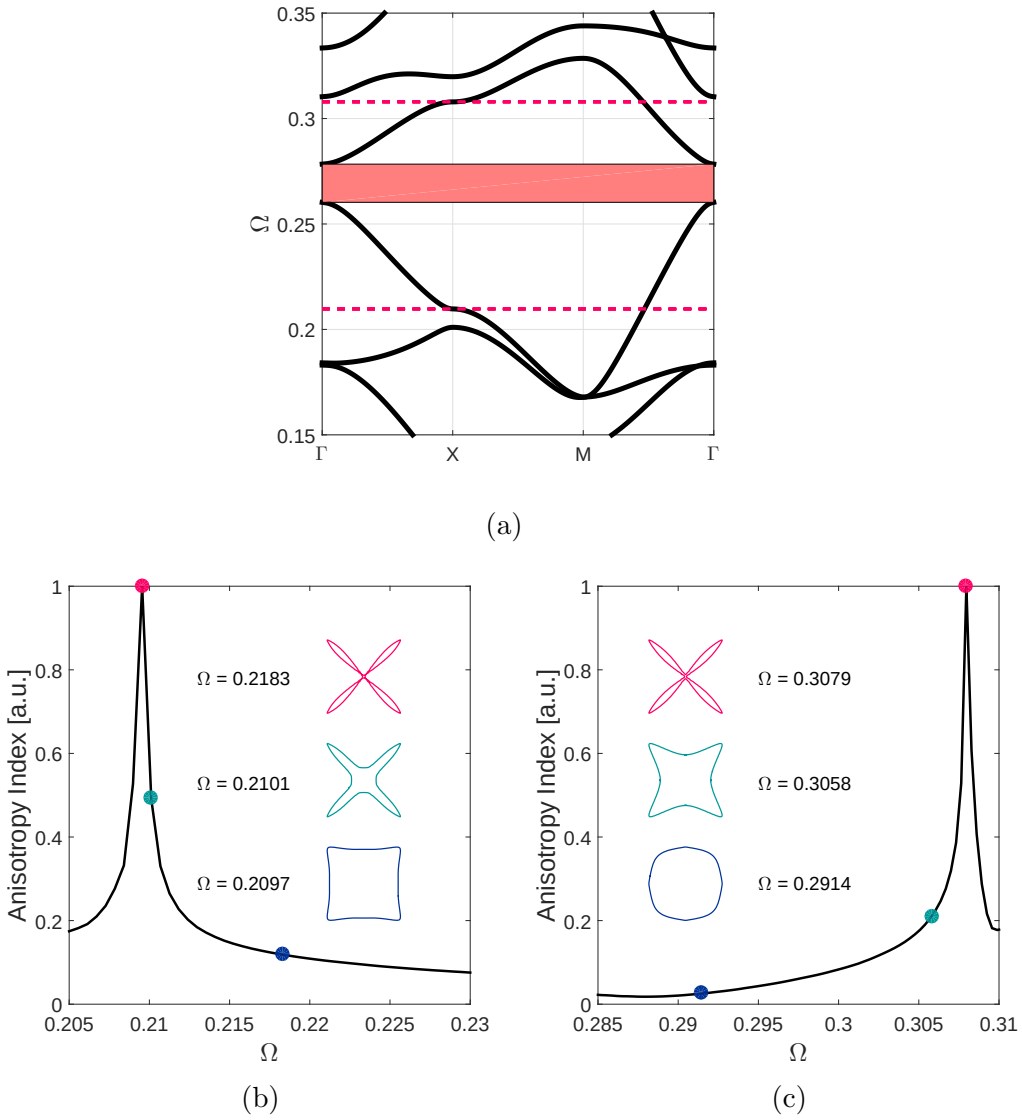

Figure 3.9: Detail of the band diagram (a) and anisotropy index plot (b-c), in which group velocity plots are also displayed at selected frequencuies for configuration 2. Geometric parameters: $\gamma = 0.05$ and $\zeta = 0.1$. The group velocity plots are normalized.

along the vertical and horizontal directions in the square lattice. Also, energy in undulated lattices travels at a lower speed compared to energy propagating in straight lattices.

3.4 Graded Undulated Lattices

Results developed in the previous sections can inform the design of structural lattices that are characterized by a spatial variation of the undulation parameter ζ. The resulting graded lattices are non-periodic, and combine properties of straight and undulated configurations by imposing selected variations $\zeta = \zeta(\mathbf{x}) = \zeta(x_1, x_2)$. Is is shown how graded lattices can be used to confine wave propagation within a certain region of a finite lattice.

3.4.1 Filtering properties

As a first example, two square graded lattices are considered, one for each of the two considered configurations, having size $L_1 = L_2 = L$ and $\gamma = 0.05$. The following undulation law is considered:

$$\zeta(x_1) = 0.1\frac{x_1}{L} \tag{3.6}$$

The band gap map in Fig. 3.4a shows that the critical undulation value ζ_c, as illustrated in 3.3.1, for configuration 1 is $\zeta_c \approx 0.05$ at $\Omega = 0.23$. Thus, an undulated lattice of configuration 1 having $\zeta_c > 0.05$ does not support the propagation of waves propagating at this frequency. Transient response to narrow band excitation at $\Omega = 0.23$ of a straight-to-undulated lattice is presented in Fig. 3.11. The simulation shows how the wave propagation is confined to the left part of the lattice, *i.e.* $0 < x_1/L < 0.5$, being the right part of the lattice forbidden to the wave. Similarly, the band gap map in Fig. 3.4b shows that the critical undulation value ζ_c for the undulated lattice configuration 2 at $\Omega = 0.27$ is approximately $\zeta_c = 0.07$. For this reason, the undulated

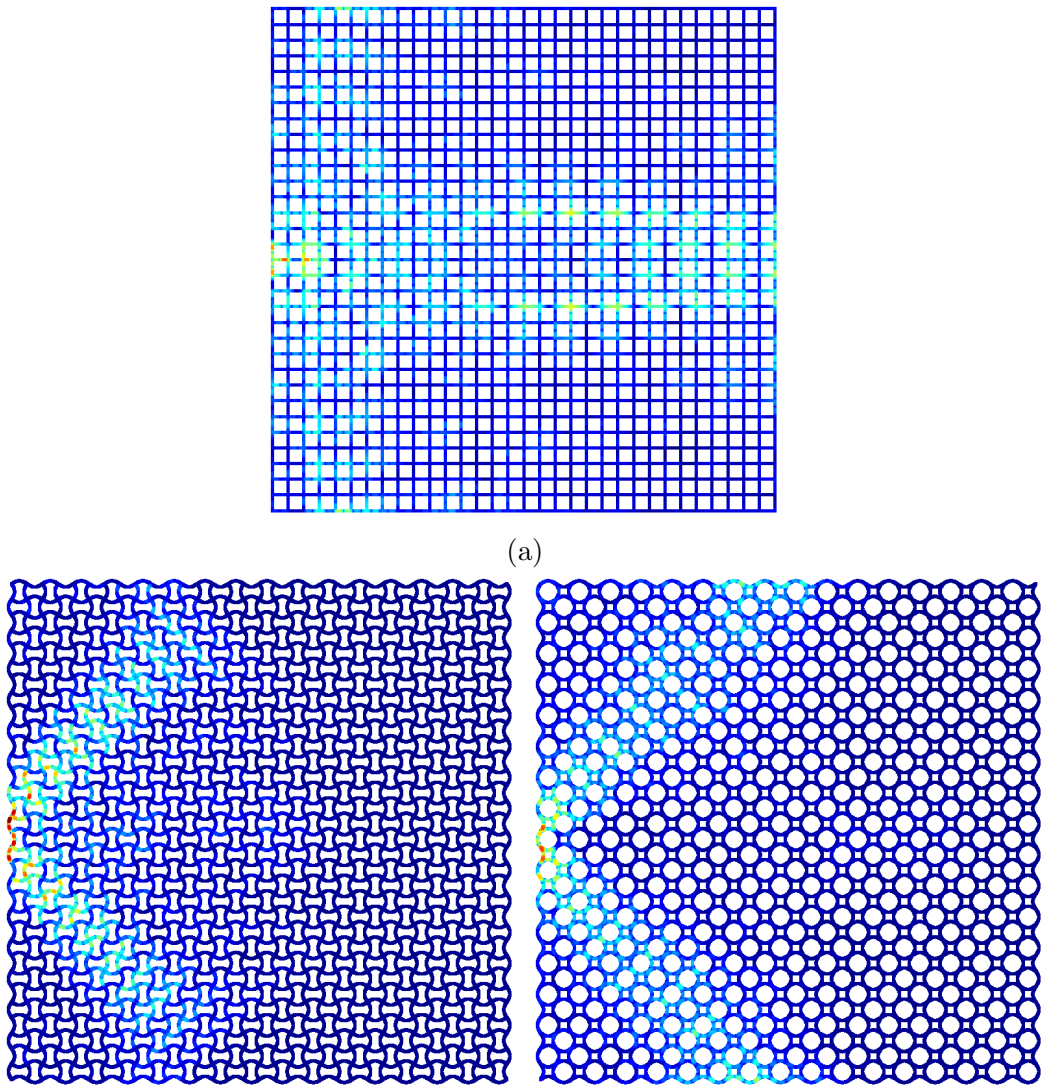

(a)

(b) (c)

Figure 3.10: Transient response to harmonic excitation for a square and undulated lattice of configuration 1, both at $\Omega = 0.3072$ (a,b), and for an undulated lattice of configuration 2 for $\Omega = 0.2097$ (c) ($\zeta = 0.1$ and $\gamma = 0.05$).

lattice with configuration 2 subject to a narrow band excitation at $\Omega = 0.27$, shown in Fig. 3.12, displays a wave that initially propagates and then remains confined in $0 < x_1/L < 0.7$.

As a second example, it is shown how graded lattices can be used to improve the filtering properties of undulated periodic lattices. Analysis of Fig. 3.13a, which shows the band gap map for the wider band gap of configuration 1, reveals that the position and the width of the band gap varies substantially with the undulation ζ and it ranges from about $\Omega = 0.175$ to $\Omega = 0.3$. Nevertheless, it is not possible to realize a periodic undulated lattice, *i.e.* with a fixed value of ζ, displaying a band gap in the range of frequency $[0.175, 0.3]$. Instead, it is possible to use a graded lattice with the following undulation law:

$$\zeta(x_1) = \zeta_1 + \big[\zeta_2 - \zeta_1\big]\frac{x_1}{L} \tag{3.7}$$

with $\zeta_1 = 0.05$, value at which the band gap starts to appear, and $\zeta_2 = 0.10$. In such a lattice, the variation of the undulation can be locally neglected and the filtering properties of the full lattice should combine the ones of the periodic undulated lattices with ζ in the range $[0.05, 0.10]$. This is verified by comparing the frequency response diagrams of a 16x16 unit cell graded configuration 1 lattice and two equivalent periodic undulated lattice with $\zeta = 0.07$ and $\zeta = 0.10$, all having size L and $\gamma = 0.05$. The diagrams, displayed in Fig. 3.13b, show that the graded lattice performs better than the undulated one with $\zeta = 0.07$ in the range $[0.175, 0.2]$. Similarly, the graded lattice performs better than the undulated one with $\zeta = 0.10$ in the range $[0.26, 0.3]$.

3.4.2 Wave directionality properties

Graded lattices can also be used to modify the directionality of wave motion. This is illustrated in a third example where two lattices for the two configurations, both

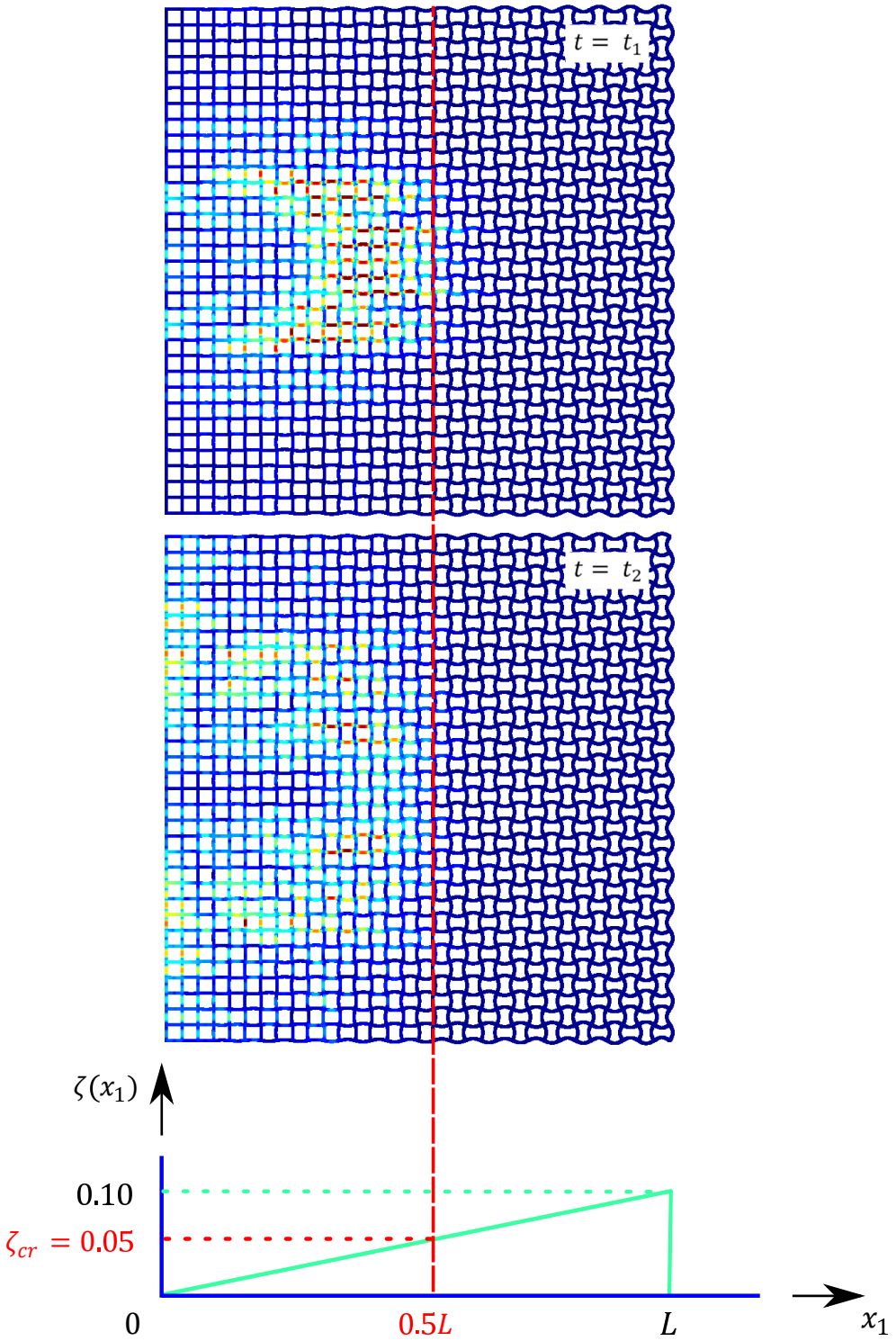

Figure 3.11: Finite straight-to-undulated lattice of configuration 1: two snapshots, with $t_2 > t_1$, of transient response for excitation at $\Omega = 0.23$ ($\gamma = 0.05$ and undulation law $\zeta = 0.1\frac{x_1}{L}$) show how wave propagation remains confined to the $0 < x_1/L < 0.5$ region.

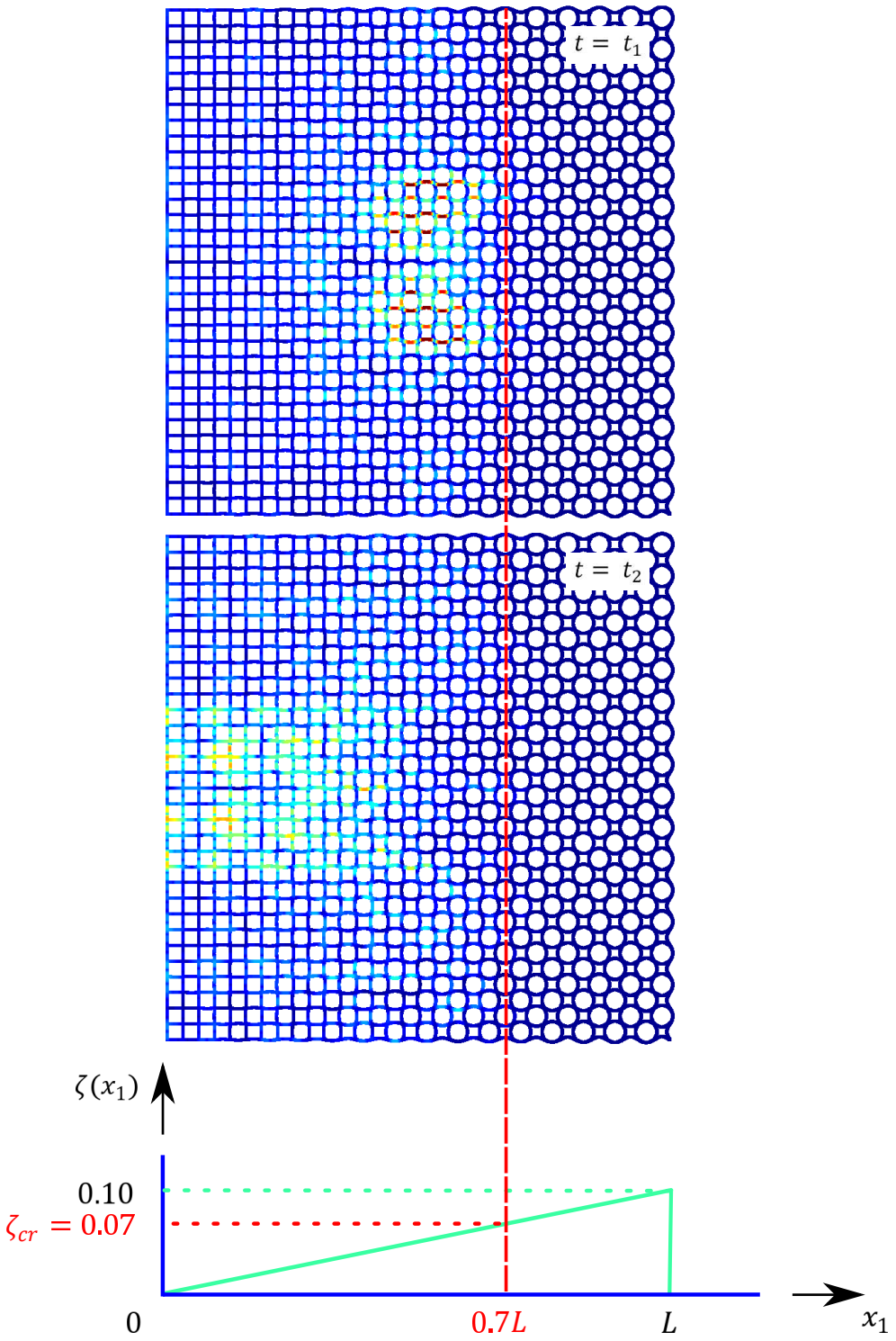

Figure 3.12: Finite straight-to-undulated lattice of configuration 2: two snapshots, with $t_2 > t_1$, of transient response for excitation at $\Omega = 0.27$ ($\gamma = 0.05$ and undulation law $\zeta = 0.1\frac{x_1}{L}$) show how wave propagation remains confined to the $0 < x_1/L < 0.7$ region.

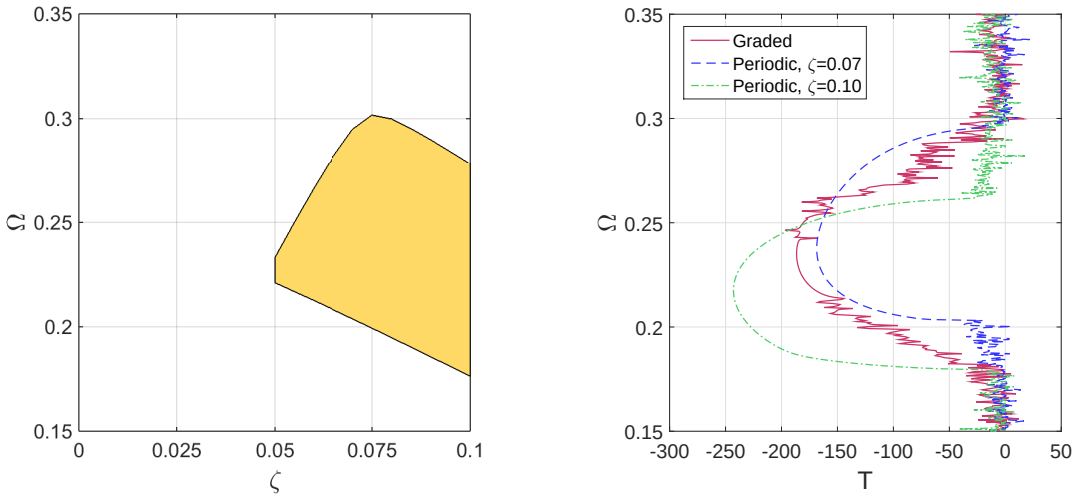

(a) (b)

Figure 3.13: Band gap map for undulated configuration 1 with $\gamma = 0.05$ and varying ζ (a); frequency response diagrams for configuration 1 graded lattice with ζ varying linearly in the range $[0.05, 0.10]$ and two equilvaent periodic undulated lattices with $\zeta = 0.07$ and $\zeta = 0.10$.

characterized by $\gamma = 0.05$, are considered. The undulation law is:

$$\zeta(x_1) = \begin{cases} 0.1\frac{x_1}{L} & \text{if } 0 < \frac{x}{L} < 1 \\ 0.1(1 - \frac{x_1}{2L}) & \text{if } 1 < \frac{x}{L} < 2 \end{cases} \tag{3.8}$$

Due to the imposed modulation of $\zeta = \zeta(x_1)$, the lattice goes from straight to undulated configuration, then from undulated to straight. Focus is placed on the low-frequency range, *i.e.* $\Omega \in [0, 0.05]$, where both configuration 1 and 2 lattices have an almost identical dynamic behavior, as it can be inferred from the band structures in Fig. 3.14. A closer look at the diagrams reveals that undulation creates a gap in the longitudinal mode at about $\Omega = 0.040$ along $\Gamma - X$. This observation is used to realize a smooth transition from a straight configuration to an undulated configuration, which allows purely longitudinal waves to be converted to waves displaying a transverse behavior. As a result of mode conversion, a change in the direction of propagation is achieved. In order to verify this claim, the transient response of

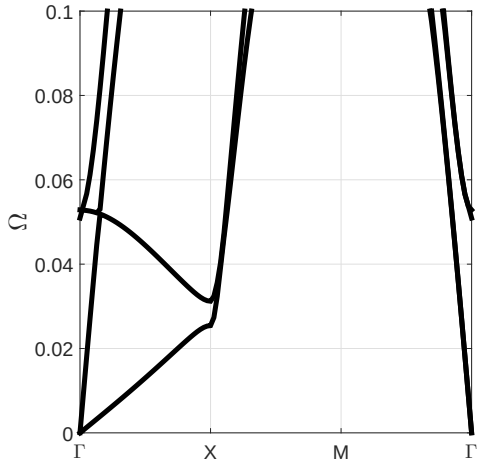

(a)

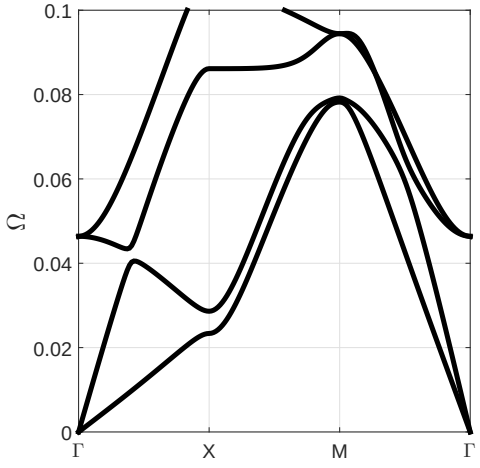

(b)

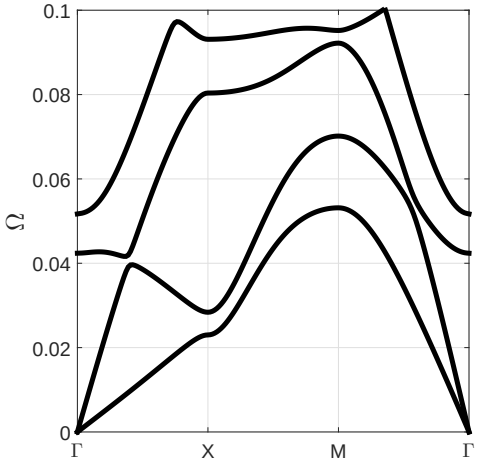

(c)

Figure 3.14: Band diagrams for straight lattice (a), configuration 1 undulated lattice (b) and configuration 2 undulated lattice (c). In all three cases, $\gamma = 0.05$, while for the undulated lattices $\zeta = 0.1$. Undulation breaks the longitudinal branch in two separate branches at about $\Omega = 0.040$ along $\Gamma - X$.

both graded lattices are computed by imposing a displacement varying harmonically at $\Omega = 0.040$ along the $\mathbf{i}_1$ direction, similarly to previous examples. As a result of the nature and direction of the excitation, a longitudinal wave is produced with a strong directional behavior along the $\hat{\mathbf{i}}_1$ direction. Then, for both configurations, the undulation is responsible for a bifurcation of the wave occurring approximately at $\frac{x}{L} = 0.4$ along $\pm 20°$ directions. This second example shows that undulation grading can be used to combine the different behaviors of undulated and straight lattices. This approach produces interesting effects not attainable with periodic structures and provides an additional design tool for structural lattices. Further investigation can be focused on the effects of different grading laws, not necessarily linear, along the finite structure. Moreover, is can be interesting to study lattices realized by combining more than one undulation pattern.

3.5 Conclusions

This chapter investigated wave propagation in square lattice structures with straight and undulated beam elements. Wave propagation properties are first studied numerically by applying Bloch analysis on the unit cell of the systems. Band diagrams and group velocity plots are made available for further analysis and verified through simulations of wave propagation in finite lattices. The results of the analysis show that undulated lattices, contrarily to straight lattices, display band gaps in the considered frequency range. The role of the geometric parameters on the amplitude of the band gaps is investigated and reported in the form of band gap maps, which unveil the drastically different dynamic behavior of the two undulated configurations in the high frequency range. When directionality of wave propagation is of interest, undulated lattices display single wave modes that tend to guide waves along specific directions. A quantitative representation of the directionality of selected wave-modes relies on the definition of an anisotropy index, which peaks at different frequency

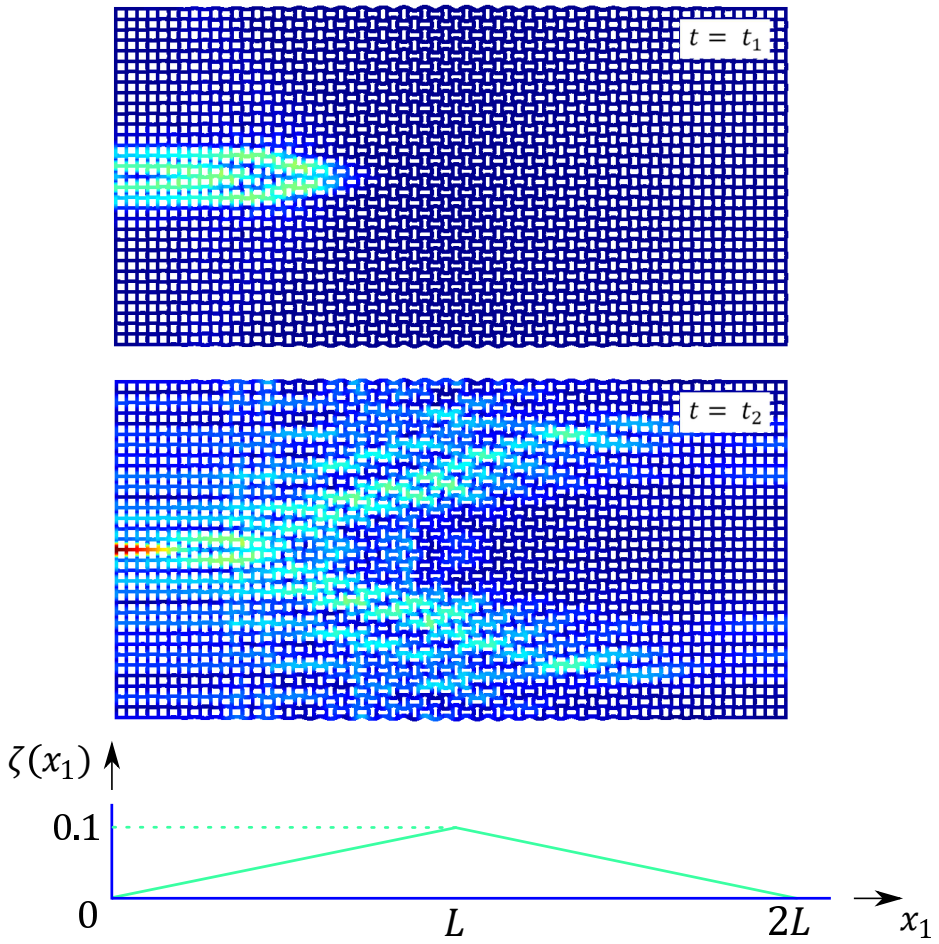

Figure 3.15: Finite straight-undulated-straight lattice of configuration 1: two snapshots, with $t_2 > t_1$, of transient response for excitation at $\Omega = 0.04$ ($\gamma = 0.05$ and linear undulation law) show bifurcation of wave propagation starting at approximately $x_1/L = 0.4$.

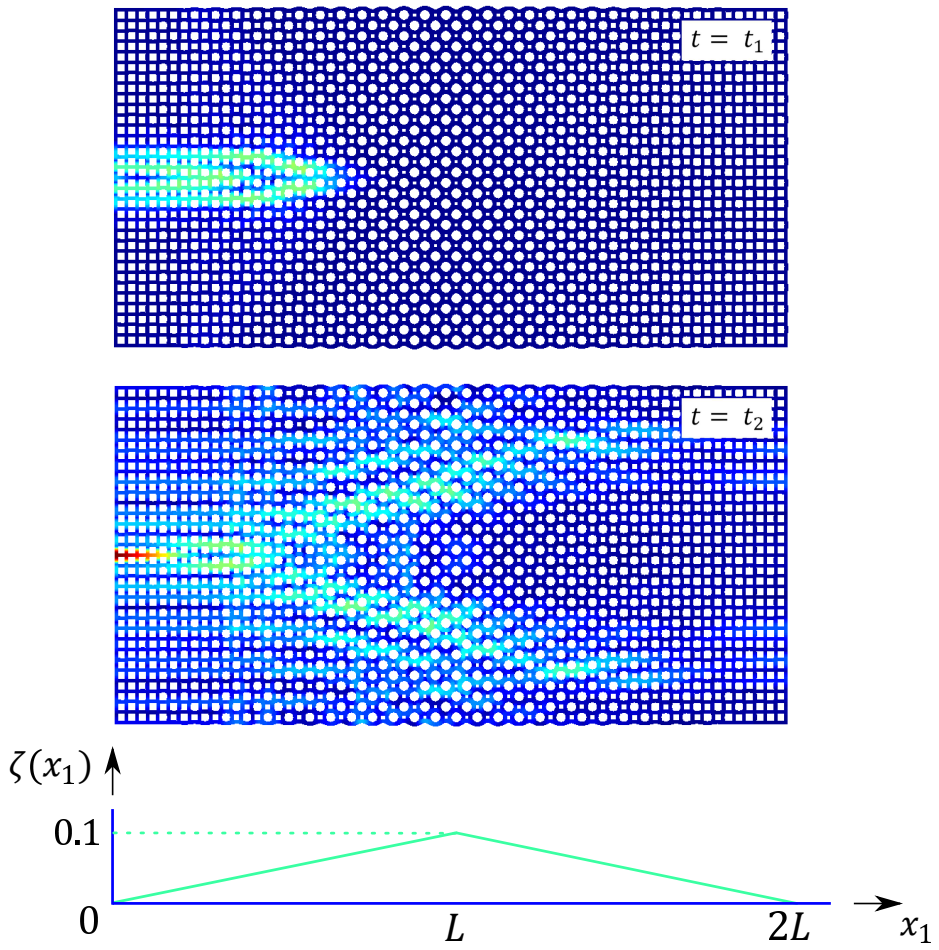

Figure 3.16: Finite straight-undulated-straight lattice of configuration 2: two snapshots, with $t_2 > t_1$, of transient response for excitation at $\Omega = 0.04$ ($\gamma = 0.05$ and linear undulation law) show bifurcation of wave propagation starting at approximately $x_1/L = 0.4$.

for the two configurations considered. Results have been numerically validated by computing the transient response to harmonic excitation of finite lattices. Finally, graded lattice configurations illustrate the possibility to conveniently modulate the structure's undulation to define areas of the lattice where wave propagation, and the energy associated with it, can be confined. Similarly, modulation of the undulation can be used to affect the directionality properties of the structure and induce, for example, wavefront splitting by means of mode conversion. The discussed results show how graded structural lattices have a great potential for wave propagation control, suggesting the possibility of broadband filtering by combining modulation of undulation and thickness.

The next chapter focused on experimentally evaluation of structural lattices's wave propagation properties by introducing an optical technique based on digital image correlation. First, a benchmark example is considered, then the filtering properties of graded undulated lattices are validated.

CHAPTER 4
DIGITAL IMAGE CORRELATION FOR WAVEFIELD MEASUREMENT

4.1 Overview

In this chapter a method for the measurement of the in-plane wavefield is presented for lattice structures. For reticulated or porous structural assemblies, such measurements are an open challenge. This stems from the limitations of currently employed approaches, that rely on 3D scanning laser Doppler vibrometry. Specifically, measurement of in-plane wavefields requires the three laser beams of the vibrometer to focus in one location, which might be problematic due to the limited available space in the structure. Celli and Gonella [48] addressed this issue by adding patches to the lattice's elements in order to increase the available space available at each measurement location. A Digital Image Correlation (DIC) approach is implemented that tracks small displacements of the lattice nodes by centering image subsets about the lattice intersections. A high speed camera records the motion of the points by properly interleaving subsequent frames thus artificially enhancing the available sampling rate. This, along with an imaging stitching procedure, enables the capturing of a field of view that is sufficiently large for subsequent processing. Results are first presented for a hexagonal lattice and show how it is possible to measure the transient response of the structure and identify both pressure (P) and shear (S) waves by applying Helmholtz decomposition. For both P and S waves, information on wave speed, wavenumber and directional behavior is collected and compared to theoretical predictions. Then, graded undulated lattices are studied. Results confirm the filtering properties induced by the gradual increase of the undulation along the structure.

DIC is employed to detect and track the motion of the lattice intersection points, which are identified through the search of corresponding clusters of pixels. The procedure is currently limited to the detection and monitoring of small displacements that do not cause significant changes in lattice topology and connectivity. The method should be extended to be applicable to investigate the dynamic behavior of structures that undergo large deformations [97], topological changes, and reconfigurations [98]. Challenges associated with the frame rates required for capturing wave motion are here addressed by employing a repetitive excitation that allows for implementing an image interleaving process that artificially enhances the sampling rate and that enables the stitching of sub-regions of the lattice recorded at subsequent times to enlarge the effective field of view. The obtained wavefield images can then be employed for the analysis of the wave motion in the lattice, specifically in terms of the dispersion characteristics of the in-plane wave modes and of the associated wave velocities.

4.2 Hexagonal Lattice

4.2.1 Lattice Fabrication

The technique described above is now applied to a hexagonal lattice. The hexagonal lattice is a simple lattice geometry that has been extensively studied, thus it is a good benchmark for experimental validation. The hexagonal honeycomb lattice, shown in Fig. 4.1, is manufactured out of polylactic acid (PLA) using fused deposition manufacturing (FDM). The lattice is characterized by 56x36 unit cells of dimensions $l = 3$ mm, $t = 0.8053$ mm (Fig. 4.2.a), and out-of-plane width $w = 10$ mm. The number of cells is maximized in relation to the overall area than can be fabricated by available machines. The beams comprising the hexagons have slenderness ratio $l/t \approx 3.725$ which leads to a fairly small material to void ratio. A reflective mirror spray paint is applied to the lattice, enhancing its ability to reflect the bright lights required for short camera exposures and protects the structure from overheating.

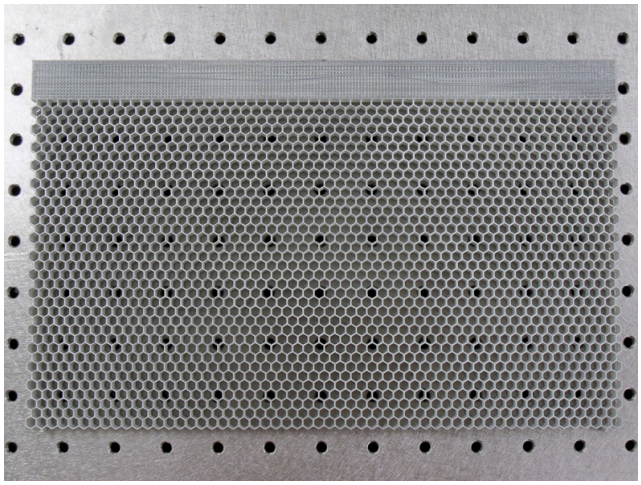

Figure 4.1: Picture of the 3D printed hexagonal lattice used for the test.

Before painting, the structure is sanded with 240 grit sandpaper to give more defined features for DIC to utilize.

4.2.2 Intersections Identification and Geometry Reconstruction

These intersections are identified by setting a brightness threshold to each black and white image of the kind in Fig. 4.3.a, which produces a binary representation of material and void as illustrated in Fig.s 4.3.c,d. Pixels with brightness above the threshold are denoted as "material pixels". A tolerance brightness level is applied to connect each material pixel to its neighbors whose brightness may fall just below the threshold, but are still part of the lattice material, which corrects for inaccuracies resulting from the non-uniform illumination of the lattice. The search for lattice intersections may be conducted using different strategies. The one used herein proceeds by counting the number of material points within a radius $r = t/\sqrt{3}$ from each material pixel, then estimating the candidate intersections as the material points which are surrounded by the largest number of other material points.

Once the intersections are evaluated, their connectivity is determined by looking for intersections which are approximately l apart. This results in the geometrical description of the lattice as an assembly of points connected by lines as shown in

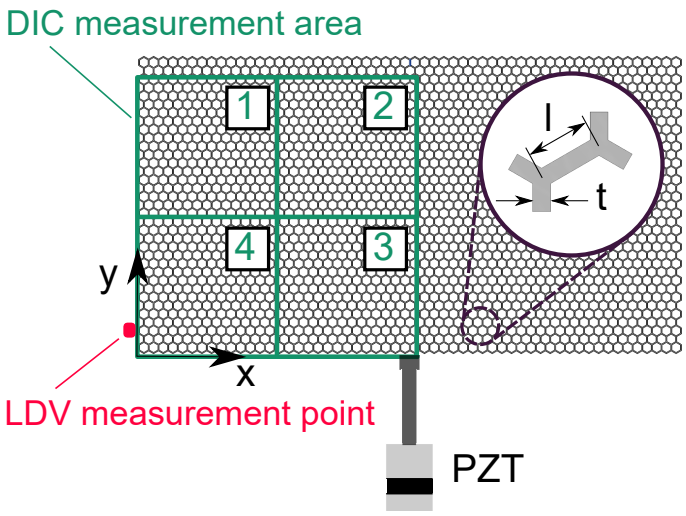

Figure 4.2: Schematic of monitored portion of surface area of the lattice, and subdivision into 4 tiles. The figure also illustrates the point of excitation as well as the location of the LDV measurements.

Fig. 4.3.e at the local level, and in Fig. 4.3.b for the lattice assembly. This simple procedure is limited to the specific lattice topology considered, and will require extension to handle a variety of topologies with complex connectivity and a variety of intersections characterized by different coordination numbers.

4.2.3 Procedure and Experimental Setup

As explained my Schaeffer in his Ph.D. thesis [99], the intersection identification process is applied to the first image recorded during the acquisition time, so that displacements can be evaluated through DIC [100, 101]. The DIC process in this work employs the open-source code by Eberl et al. [102], here adapted to track the intersection points. DIC applied to 19x19 pixel image subsets that are located at each lattice intersection, which provides a measure of the two in-plane displacement components relative to the initial reference lattice position. The recorded motion corresponds to the transient wave induced in the lattice by a piezoelectric (PZT) stacked disks assembly (APC 90-4060) designed to resonate at a specified frequency.

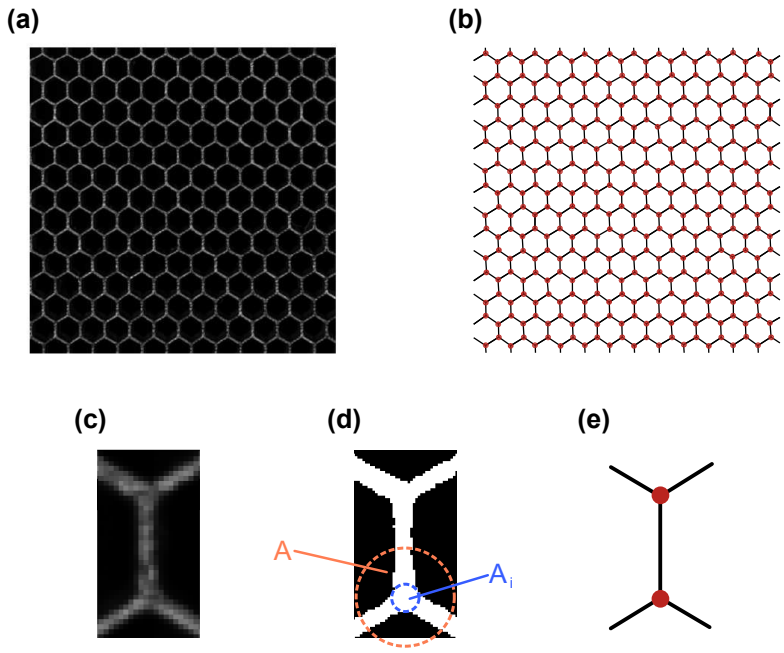

Figure 4.3: Picture of hexagonal lattice (a) and identified lattice geometry consisting of intersection points (red dots) connected by lines (black lines). Schematic of process followed for the identification of intersections and of lattice geometry (c-e).

The motion of the structure is recorded by a high-speed camera. A schematic of the experimental set-up is depicted in Fig. 4.5 and discussed later in the text. The excitation system is selected to provide repeatable forcing and, as a result, repeatable wave motion in the lattice. This has two main advantages. First, hardware limitations of the camera impose a trade-off between frame rate and image size, *i.e.* the number of pixels captured in each frame. To circumvent this, images from n recordings at a frame rate of f_s are interleaved to obtain an effective higher frame rate $f_{s,eff} = nf_s$. This is implemented by controlling the time delay between the beginning of a recording and the start of an excitation. The time delay corresponding to the i-th recording is given by:

$$t_d^{(i)} = \frac{1}{f_s}\frac{i-1}{n} \tag{4.1}$$

where $i \in 1, ..., n$, with n denoting is the number of the recordings. In this work, $n = 14$ delayed recordings are used to realize an effective $f_{s,eff} = 14 \times f_s$, where

$f_s = 5$ kHz is the frame rate provided by the video camera utilized. A schematic of the interleaving process is presented in Fig. 4.4. A second advantage is that it provides a wide effective field of view that allows capturing a sufficiently large portion of the surface area of the lattice. It was elected to capture the motion only of half of the lattice, invoking symmetry of geometry and loading configuration. The monitored half surface is further divided into 4 tiles as illustrated in Fig. 4.2. Recordings are first conducted on each of the tiles. A composite video is then obtained from the combination of the 4 tiles which is obtained by aligning the intersection locations in planned overlapping regions. The composite images are obtained by first rotating each tile's coordinate system so that the edges of the overlapping area align with the global coordinate axes. Then, each tile is translated so that the centroid of its overlap region matches that of its pairing neighbor. The PZT resonance frequency is the

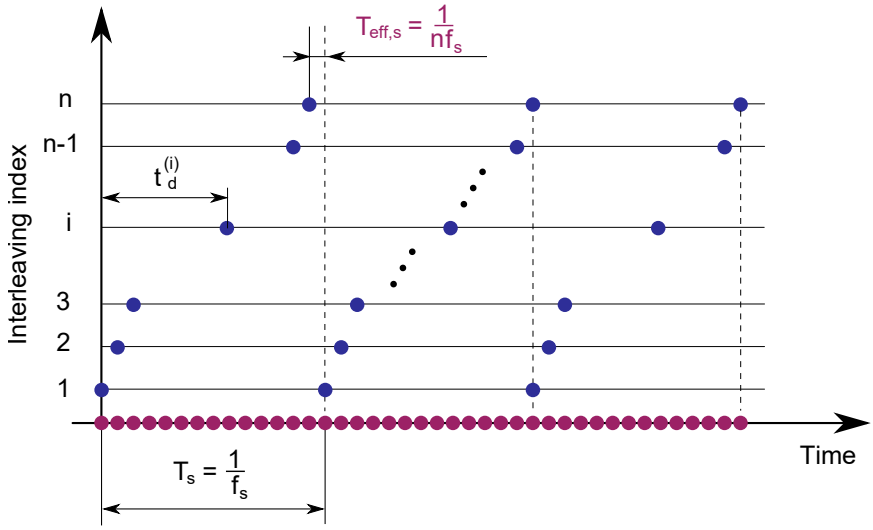

Figure 4.4: Schematic of interleaving process for enhancement of effective sampling rate.

considered excitation frequency $f_e = 16.74$ kHz. The excitation is applied in the form of a sinusoidal burst, with modulation being provided by an 11-cycle Tuckey window, as shown in Fig. 4.7.a. The motion of the structure is recorded by a high-speed camera (Photron Fastcam SA1.1) which is set to record images at a rate of $f_s = 5,000$ frames

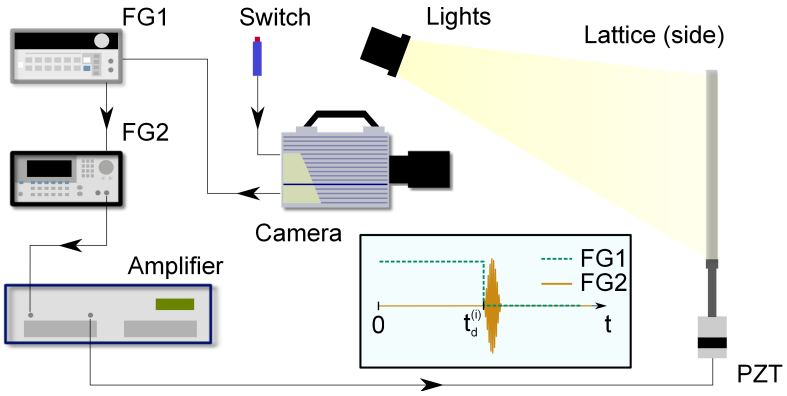

Figure 4.5: Schematic of experimental set-up.

per seconds. The interleaving process described above considers $n = 14$ properly delayed takes, so that the effective sampling frequency is $f_{s,eff} = nf_s = 70k$Hz. Each recording is repeated 16 times and averaged to minimize noise. Recording is started by a manual switch connected to the camera. Once the recording started, the camera triggers a first function generator (FG1 - Agilent 33120A), which produces a square wave. The falling edge of the square wave then triggers the excitation signal produced by second function generator (FG2 - Agilent 33220A). Imposing the frequency of the first signal generator allows us to enforce the time delay needed to achieve the effective sampling rate $f_{s,eff}$. The excitation signal is then fed to the PZT exciter through an amplified (E&I 1040L). The motion of one point of the lattice is also monitored through a Laser Doppler Vibrometer (LDV) (Polytec PDV 100). The location of the monitored point is shown also in Fig. 4.5. The LDV measurements are employed to verify the repeatability of the excitation and motion during various takes and excitation cycles, as well as to compare the time histories recorded at the monitored location with those extracted from the DIC procedure.

4.2.4 Analysis of the Measured Wavefield

The time snapshots of Fig.s 4.6 illustrate how the response of the lattice at the considered excitation frequency, equal to $f_e = 16.74$ kHz, is directional in space, i.e.

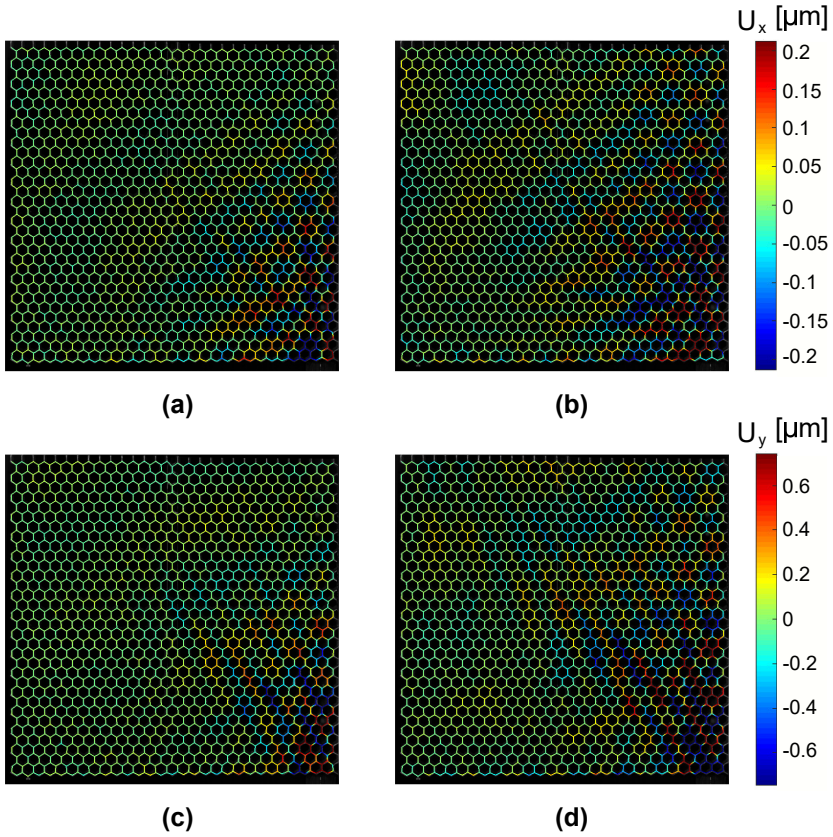

Figure 4.6: Time snapshots of the recorded wave motion in the lattice resulting from the DIC process presented at $t = 3.78$ ms (left) and $t = 3.99$ ms (right). Horizontal x component (a-b), vertical y component (c-d).

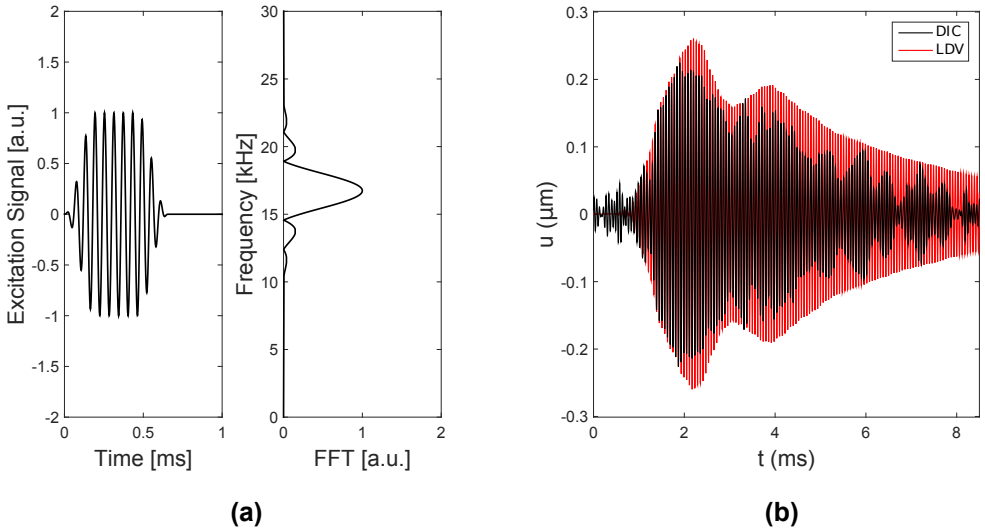

Figure 4.7: Time and frequency domain plot of the excitation signal generated by FG2 (a). Comparison of DIC time trace with LDV measurements recorded at the location shown in Fig. 4.2 (b).

wave motion occurs preferentially along the vertical (y) direction. This is the result of the anisotropy of this lattice which is documented for example in [103]. Such directionality can be predicted numerically by performing the dispersion analysis of the lattice as described for example in [104]. The experimental determination of the directional properties however is complicated by the fact that the recorded response is a superposition of the in-plane wave modes corresponding to longitudinal (P-mode) and transverse (S-mode) polarizations.

The availability of the in-plane displacement vector $\boldsymbol{u} = u\boldsymbol{i}+v\boldsymbol{j}$, with $\boldsymbol{i}, \boldsymbol{j}$ denoting the unit vectors aligned with the horizontal (x) and vertical (y) axes respectively, however affords the possibility to effectively separate the two modal contributions. This is achieved by employing Helmholtz decomposition to express the displacement $\boldsymbol{u}$ as a function of the scalar P-wave potential ϕ and the vector S-wave potential $\boldsymbol{\psi}$ [33]:

$$\boldsymbol{u} = \nabla\phi + \nabla \times \boldsymbol{\psi} \tag{4.2}$$

where the divergence $\nabla \cdot \boldsymbol{u} = \nabla^2\phi$ and the nonzero component of the curl $\nabla \times \boldsymbol{u} = -\nabla^2\psi$ of the wavefield, in this case directed along the out-of-plane direction z, separate P and S-wave contributions, respectively. The spatial derivatives required for the computation in Eq. 4.2 are computed by first interpolating the displacements of the hexagonal grid onto a 55x56 points rectangular grid. This is based on a natural neighbor interpolation routine available in the Matlab environment. Letting the bottom-most intersection define the position of the x-axis and letting the left-most intersection define the position of the y-axis, the square grid starts at coordinate $(\sqrt{3}/2l, \sqrt{3}/2l)$ and builds in the positive x and y directions with spacing $\sqrt{3}/2l$. Next, a central difference scheme is employed for the computation of derivatives. The time snapshots of $\mathcal{P}(x, y, t) = \nabla \cdot \boldsymbol{u}$ and of $\mathcal{S}(x, y, t) = \nabla \times \boldsymbol{u}|_z$ shown in Fig. 4.8 illustrate the differences in speed, wavelength and directionality between the two wave modes. In both figures, the color map is based on normalized data, with red

and blue respectively denoting maximum positive and negative values. Most notably, and as expected, the P-mode has a significantly larger wavelength and appears more isotropic than the S-mode, which is anisotropic with preferential propagation along the positive y direction and towards the top left corner of the structure. The maps of the separated modes also show that the S-mode dominates the overall response shown in Fig. 4.6. Directionality and wave speeds can be characterized and quantified by representing the two modal components $\mathcal{P}(x, y, t), \mathcal{S}(x, y, t)$ in the Fourier domain, i.e. $\hat{\mathcal{P}}(k_x, k_y, \omega), \hat{\mathcal{S}}(k_x, k_y, \omega)$ at a specific frequency. The contour plots of Figs. 4.9 correspond to the magnitudes $|\hat{\mathcal{P}}(k_x, k_y, \omega)|, |\hat{\mathcal{S}}(k_x, k_y, \omega)|$ at the excitation frequency $f_e = 16.74$ kHz and provide a distribution map of the energy content of the recorded response in the wavenumber domain. The maps also superimpose the iso-frequency contours of the theoretical dispersion surfaces for the lattice, which are represented by the solid black lines in both Fig.s 4.9. The theoretical dispersion relations are evaluated by applying established methods based on the Finite Element (FE) discretization of a unit cell, and the application of Bloch periodic conditions [104]. Both maps in Fig.s 4.9 show a good match between theoretical predictions and measured data, which demonstrates that the detected motion is descriptive of the wave properties of the lattice, and that the representation of the measured wavefields in the wavenumber space can be an effective tool for the estimation of the dispersion properties, and therefore the mechanical properties of a lattice under investigation. Of note is the fact that the iso-frequency contour has the form of a circle for the P-mode (Fig. 4.9.a), which matches the theoretical predictions well, while the S-mode reflects more predominantly the hexagonal geometry of the lattice and its six-fold symmetry (Fig. 4.9.b).

The theoretical predictions of dispersion can be further elaborated to obtain the group velocities for the two modes at designated frequencies. Theoretical group velocities for the two modes are shown in Fig. 4.10 illustrate their different anisotropy, and

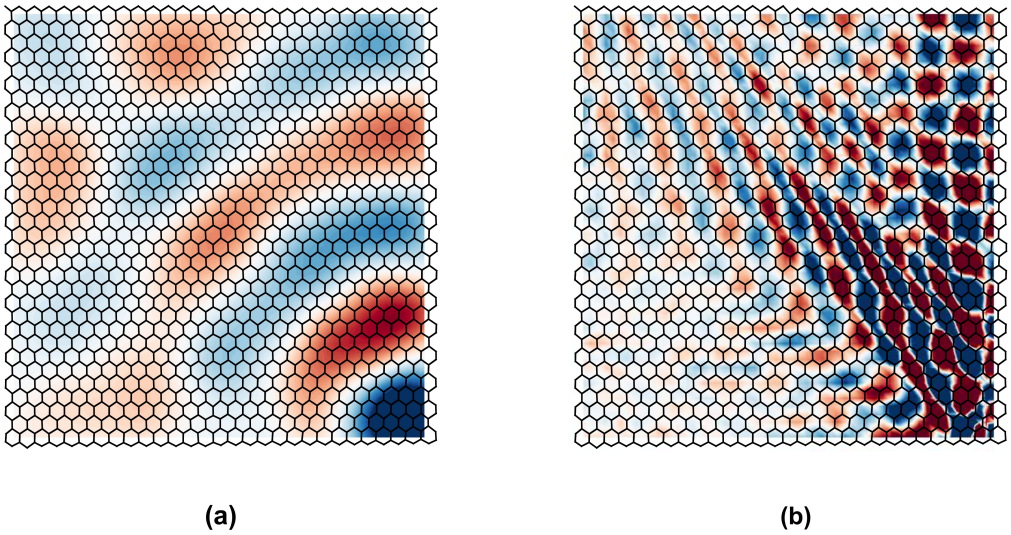

Figure 4.8: Snapshot of divergence $\mathcal{P}(x, y, t)$ (a) and curl $\mathcal{S}(x, y, t)$ (b) of the measured displacement field at $t = 3.78$ ms and $t = 4.14$ ms, respectively.

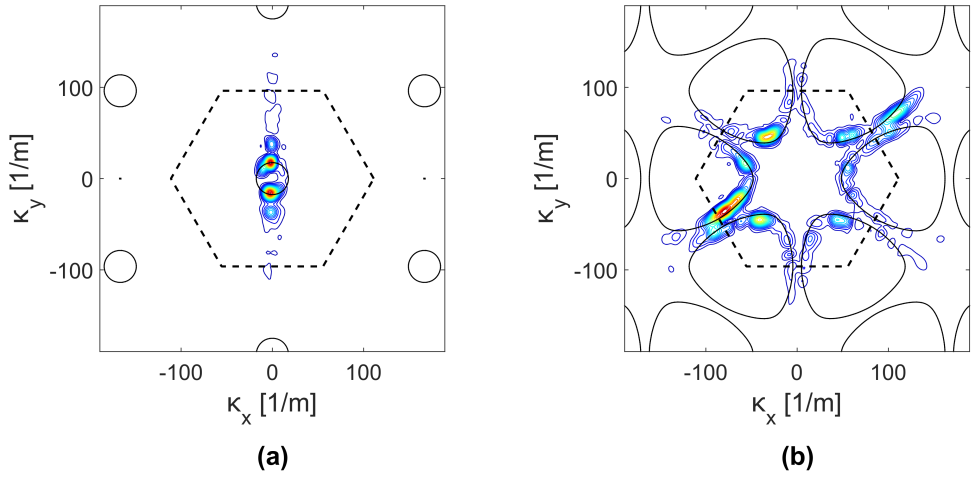

Figure 4.9: Wavenumber domain representation $|\hat{\mathcal{P}}(k_x, k_y, \omega)|$ (a), and $|\hat{\mathcal{S}}(k_x, k_y, \omega)|$ (b) at the excitation frequency and comparison with theoretical iso-frequency dispersion contours (solid black lines). The dashed black line outlines the First Brillouin Zone of the reciprocal space for the lattice [87].

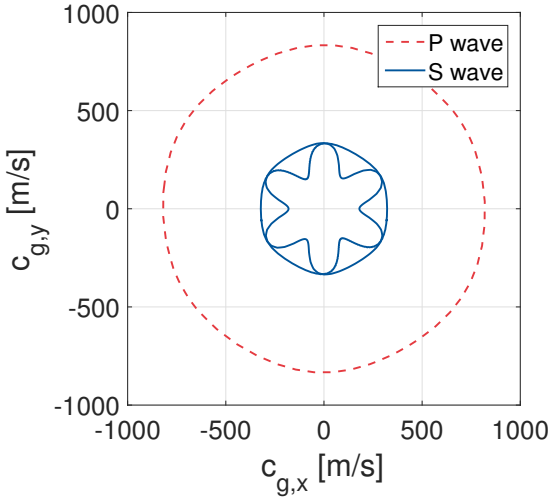

Figure 4.10: Direction variations of group velocity at the excitation frequency f_e = 16.74 kHz: S-mode: solid blue line, P-mode: dashed red line.

further highlight the directional properties of the S-mode in particular. The group velocity directional variations provide an estimate of the shape of the wave front corresponding to the propagation in the lattice of a wave packet. Thus, at a particular time, one may superimpose the predicted wavefront to the one actually measured to once again illustrate the capabilities of the method presented here along with the theoretical estimation of dispersion to investigate wave propagation characteristics in terms of both magnitude of group velocity and directional dependence. Specific to the results in Fig. 4.10, isotropy of the P-mode at f_e = 16.74 kHz is confirmed by the corresponding group velocity plot, which is almost a perfect circle, signaling that the energy carried by the P-mode spreads in all the direction, with about the same average speed approximately equal to 820 m/s. The "star" pattern shown in Fig. 4.9.b instead captures the anisotropic propagation of the S-waves, which is in good agreement with theoretical predictions showing directions along which the energy is focused by the S-wave with 6-fold symmetry, with faster components of the wave traveling at about 320 m/s.

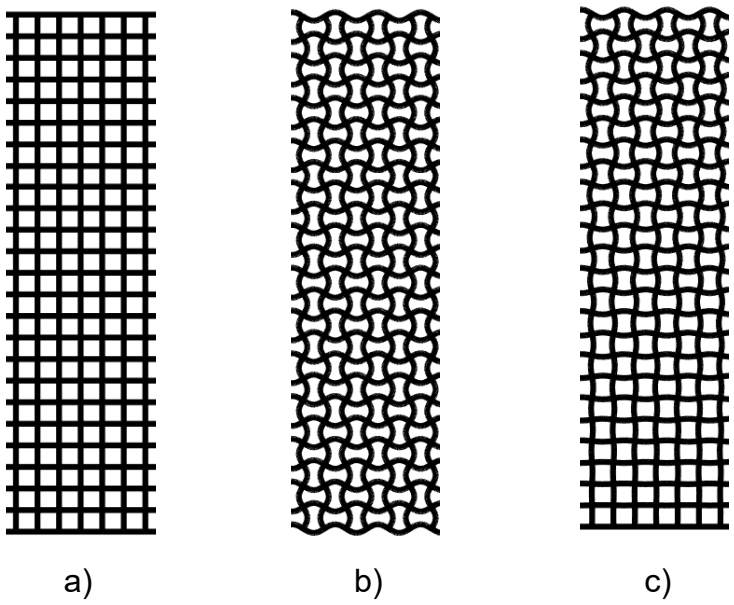

Figure 4.11: Different lattice configurations: straight (a), periodic undulated (b), graded undulated (c).

4.3 Undulated Lattice

This section report the experimental validation of the filtering properties of graded undulated lattices studied in chapter 3. The design of the graded structure relies on a numerical study of equivalent periodic undulated lattices, achieved by analyzing the band gaps of infinite periodic lattices as in chapter 3. For the experimental validation, scanning laser Doppler vibrometry (SLDV) is first used to obtain transmissibility maps. Such maps illustrate the cumulative effect of the increasing undulation along the structure, informing the design of graded structures. Next, the role of undulation grading in filtering elastic waves is illustrated through in-plane DIC wavefield measurements, according to the procedure presented above. Fig.4.11 illustrates the structural lattices considered in this study, *i.e.* configuration 1 presented in chapter 3. An infinite undulated periodic lattice is considered first, whose unit cell is represented in Fig. 4.12.

In this work, $a = 20.5$ mm and lattices with slender beams are targeted , therefore $h = 1$ mm is e considered. Also, intending to 3D print and test the lattice structures, the lattice's material is assumed to be ABSplus-P430 with tensile modulus $E = 2.2$ GPa and density $\rho = 1040$ kg/m^3. A dispersion analysis of the structure is performed by implementing a FE-based Bloch analysis [20] and modeling the unit cell with Abaqus C3D6 6-node linear triangular prism elements [92]. Wave attenuation due to material damping is expected in the 3D printed structures but not taken into account in the numerical model. However, the material damping is expected to induce the same attenuation in the different tested structures, thus any wave filtering effect is only imputable to the structure's undulated design. By sweeping the undulation amplitude c_0 from zero (straight lattice) to $c_{0,max} \approx 2$ mm, the band gap map of in-plane wave propagation is constructed and shown in Fig. 4.12. The map is obtained by identifying the width of the main band gap for each value of the considered c_0. The main band gap appears for $c_0 > c_{0,cr}$, with $c_{0,cr}$ a certain critical value which in general depends on the slenderness of the beam, thus on the ratio h/a. The widest band gap within the considered range of c_0 is obtained approximately for $c_0 \approx 1.6$ mm and it is about 5.5 kHz wide. In contrast, due the shape of the band gap region in Fig. 4.12, band gaps range from 15.7 kHz to 22.7 kHz, thus covering a wider 7 kHz frequency range. Therefore, one can speculate that a non-periodic structure with smooth graded undulation would benefit from the cumulative contributions of the local value of undulation, leading to an augmented elastic wave filtering capability compared to its periodic counterpart.

The lattices is fabricated with a total of $N_U = 12$ unit cells each using a Stratasys Fortus 250mc 3D printer. The value N_U is chosen in order to guarantee a smooth linear grading of the undulation in the range between 0 and 2 mm, given the manufacturing constraints in terms of available printing area (254×254 mm). During the fabrication process, the lattices were lying flat on the 3D printer building surface, so

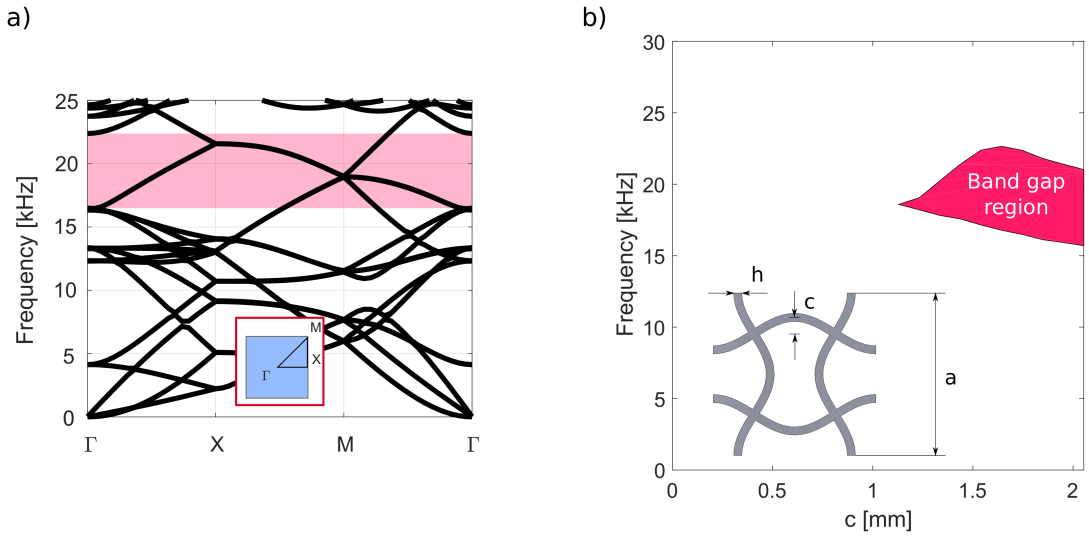

Figure 4.12: Band diagram corresponding to $c_0 = 1.75$ mm shows how the band gap (in red) is identified in the Brillouin zone (a). Band gap map of periodic undulated lattices for increasing c_0 with $h = 1$ mm (b), with inset on the bottom left showing the unit cell and its dimensions. The dispersion branches within the band gap are associated to out-of-plane modes which are not meaningful in an in-plane study.

to minimize induced anisotropy due to uneven material deposition, which would bias the lattice's in-plane dynamics. For the same reason, the highest degree of fill-to-void ratio was imposed.

4.3.1 Transmissibility maps

The experimental apparatus shown in Fig. 4.13 is used to measure the effect of the undulation grading on the wave propagation attenuation. The lattice is hanging from a frame hold by thin cables to approximate free boundary conditions. The excitation is provided by a piezoelectric disk glued to the lattices' edges. The piezoelectric disk generates a broadband signal, then the scanning head of the SLDV measures the transient response of the structure at different locations x along its edge, where x is a reference frame whose origin corresponds to the edge of the graded lattice with zero undulation. Due to the undulated edge's surface, a retroreflective tape is applied to improve the laser's signal quality. The response is recorded in the form of velocity,

with sampling rate of 256 kHz for 8 ms at each of 400 equally spaced locations from $x = 0$ to $x = L = 246$ mm. Define the transmissibility map $T(x, f)$, function of the frequency f and the space variable x, as the ratio:

$$T(x, f) = 20 \log_{10} \left[\frac{s(x, f)}{s(0, f)} \right] \tag{4.3}$$

where $s(x, f)$ is the Fourier transform of the signal recorded at the location x, and $s(0, f)$ is the Fourier transform of the reference signal recorded at $x = 0$. A comparison between the transmissibility maps of the straight and graded lattices is shown in Fig 4.14. The maps show that the graded lattice achieves a dramatic drop of transmissibility (between $\sim$ 40dB and $\sim$ 60dB) in the range between 20 kHz and 27.5 kHz at $x = L$, thus providing a 7.5 kHz wide wave attenuation range. Moreover, such drop in transmissibility is particularly visible at 20 kHz for $x > 150$ mm, the frequency at which the graded lattice is most effective in filtering elastic waves. In comparing the experimental and theoretical results, the analysis of the band gap map predicts wave attenuation in a 7 kHz wide range of frequencies, which is in excellent agreement with experimental validation. On the other hand, such range is shifted upwards in frequency, which might be explained partly by the uncertainty in material properties of the 3D printed material, especially the effective elastic modulus.

4.3.2 Analysis of the Measured Wavefield

Based on the information given by the transmissibility map for the graded lattice, a second experiment is designed to measure the in-plane wavefield. The response of the system is targeted at 20 kHz, frequency at which the drop of transmissibility is the largest. The experimental setup, shown in Fig. 4.15, employs a single high-speed camera (Photron Fastcam SA1.1) to record the motion of the structure. Adequate light is provided by two high intensity lights (Lowel Pro-light). Elastic waves are

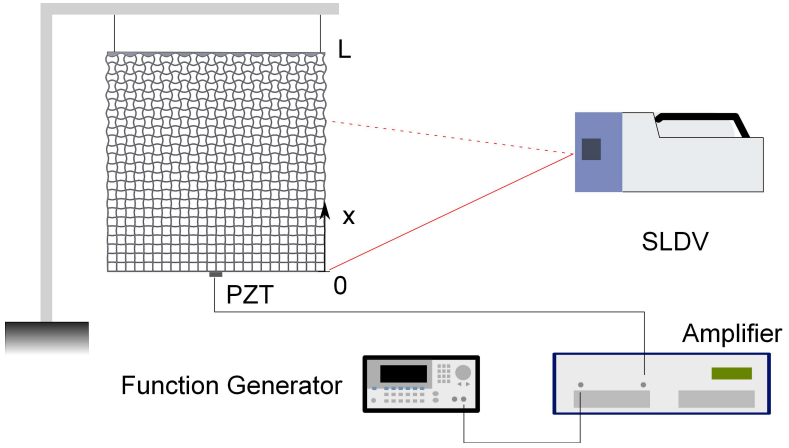

Figure 4.13: Experimental setup for the measurement of transmissibility maps $T(x, f)$.

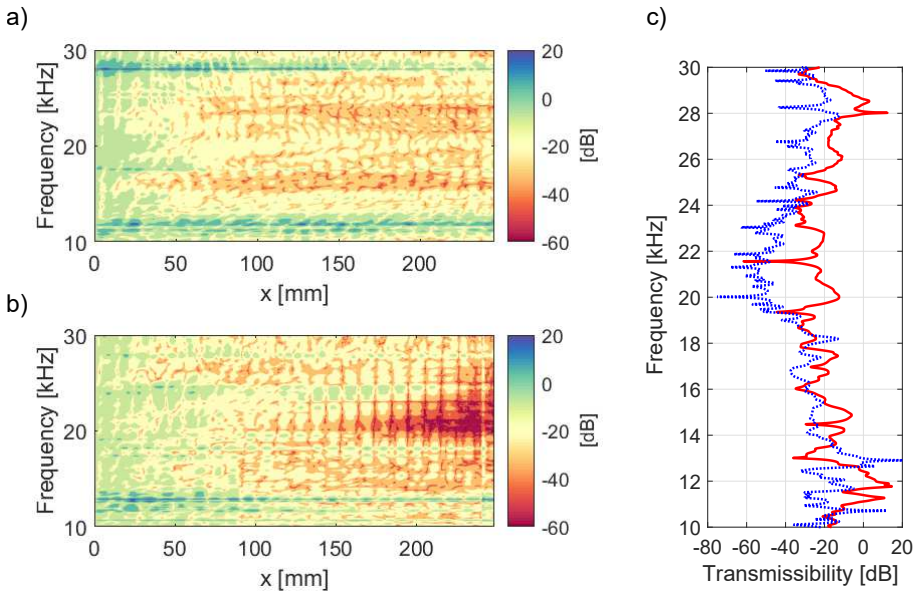

Figure 4.14: Transmissibility maps $T(x, f)$ for the straight (a) and graded (b) lattices. The graded configuration guarantees a wide transmissibility drop from 20 to 27.5 kHz. The difference in transmissibility between the straight (solid red line) and graded (dotted blue line) lattices is shown in detail in (c) for $x = 23.5$ mm.

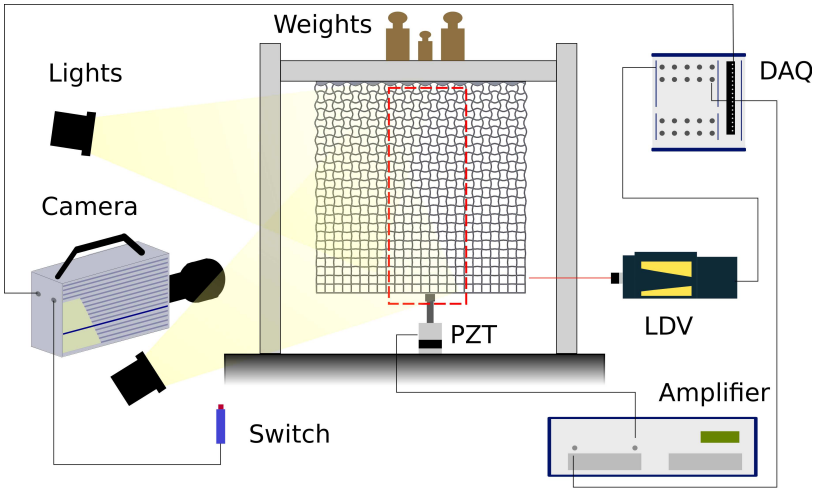

Figure 4.15: Experimental setup for optical in-plane wavefield measurement with high-speed camera. A switch initializes the camera's recording, then the camera triggers the acquisition unit (DAQ), which generates the excitation signal. This signal is first amplified, then sent to a piezoelectric actuator (PZT) placed at the bottom edge of the lattice. The lattice is preloaded to ensure firm contact with the actuator by means of weights sitting on a horizontal bar, which is free to slide vertically. A laser Doppler vibrometer (LDV) monitors the lateral displacement at a point of the lattice's edge.

excited by actuating an ultrasonic piezo-transducer (APC 90-4060) tuned to resonate at $f = 20$ kHz. In order to improve the coupling between the structure and the actuator, a 2.5 kg preload is imposed by using weights sitting on top of a horizontal bar, which is free to slide between two vertical guides. For each measurement, a manual switch triggers the recording, then the high-speed camera sends a signal to a data acquisition unit (DAQ, NI USB-6356). Upon receiving the signal from the high-speed camera, the DAQ generates the excitation signal, which is then sent to the amplifier and finally to the actuator. Concurrently, the DAQ records the voltage output from a laser Doppler vibrometer (LDV, Polytec PDV 100), which monitors the structure's response at one point on the lattice's side. In choosing the size of the measurement area, the high-speed camera's limitations in reading and storing the information while recording have to be considered. Higher sampling rates force us to reduce the frame size, thus the number of the recorded pixels within the same image,

while choosing larger frame sizes implies reducing the frame rate. This inverse relationship between frame rate and frame size would prevent us from measuring large enough wavefields with a sufficient temporal resolution. Nevertheless, such limitations are overcome by effectively increasing both spatial and temporal sampling, as discussed in our previous works [105, 106]. The measurement domain is divided into 23 tiles, each corresponding to an array of 2×14 lattice intersections. For each tile, the experiment is performed separately, then the data is stitched together to retrieve the full wavefield. 20 evenly spaced points between each intersection are tracked, which sums up to roughly 8600 measurement points for the total considered measurement area. The experiments are performed at sampling rate $f_s = 75$ kHz. An effective sampling rate $f_{s,eff} = 2f_s = 150$ kHz is realized by properly interleaving two different sets of measurements, which differ by a certain delay $t_d = 1/(2f_s)$ between the beginning of the camera measurement and onset of the excitation. The delay time t_d is imposed by conveniently programming the DAQ. For each set of measurement, 5 averages are considered which help improving the signal-to-noise ratio by reducing the uncorrelated noise. The behavior of the system to a narrowband excitation is targeted, thus the system is excited with a $11-$cycle tone-burst at 20 kHz. In order to obtain a sufficiently large excitation signal, the ultrasonic piezo transducer is coupled to a resonator to amplify its response. The piezo-resonator assembly is tuned to have its first resonant frequency at 20 kHz by properly selecting the resonator's length and conveniently preloading the assembly. The raw data, in the form of pixel intensity variations over the different frames, is collected and pre-processed by correlating the frame set, averaging and interleaving the two measurement sets [105]. The pre-processed data is then post-processed by filtering the data in the frequency domain around the excitation frequency to improve the signal-to-noise ratio. Owing to the highly discontinuous nature of the lattice structure, the results visualization is considerably improved by interpolating the data onto a rectangular 121×461 grid of points,

as shown in Fig. 4.16(a). Finally, a moving average filter is applied to the interpolated data to produce the plots shown in Fig. 4.16(b), which shows the wavefields in both straight and graded configurations, together with the original measurement points at different time instants. The wavefront is successfully tracked from the excitation location to the opposite side of the structure. It is important to remark on the strong directional nature of the wavefront, as expected for straight lattices. The wavefield of the graded lattice, on the other hand, starts differing quite remarkably from the one in the straight lattice already few intersections away from the excitation location, as the effect of the undulation gets strong enough. This effect becomes remarkable halfway through the lattice, preventing the energy carried by the elastic waves from propagating any further, effectively confining it to the first half of the structure.

4.4 Conclusions

In conclusion, the in-plane filtering properties of undulated lattices have been experimentally validated, showing that single-phase structural metamaterials can be conveniently designed in graded configurations by slowly varying the curvature of the lattice elements along one direction. The design of the graded lattice is informed by the dispersion analysis of infinite periodic undulated lattice, thorough inspection of the band gap map representing the relation between the band gap width and the beam element's curvature. Then, transmissibility maps are computed by measuring the velocity field at one edge of a graded and an equivalent straight lattice with an SLDV system, identifying a frequency range with transmission attenuation in the graded configuration. Finally, a high speed photography and digital image correlation is employed to measure the full wavefield for a narrowband excitation with frequency spectrum falling within the large attenuation frequency range in both lattices, tracking how in-plane elastic waves are attenuated in the graded one only due to the gradual change in geometry.

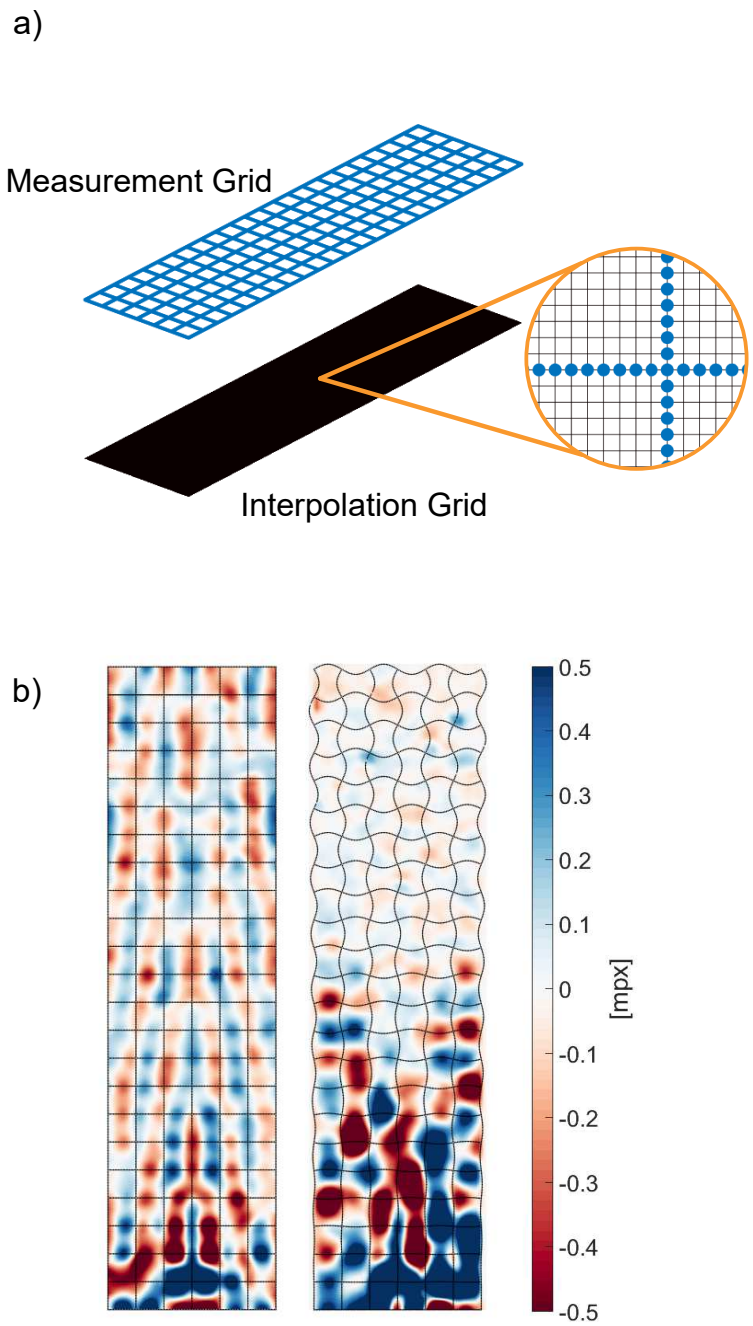

Figure 4.16: Measurement grid and interpolation grid (a). Interpolated wavefield in the straight and graded lattices show how waves are filtered by the increasing local curvature (b). Black lines represent the measurement locations. Elastic waves are attenuated by the undulation gradation.

CHAPTER 5
SPATIOTEMPORAL PERIODIC STRUCTURES: CONTINUUM CASE

5.1 Overivew

In this chapter, the properties of structures with space-time periodic material properties are investigated. Space-time periodicity represents a generalization of the concept of spatial periodicity seen in metamaterials and induces properties that are unique this new class of systems. This chapter presents an analysis of continuous systems, *i.e.* where mass and elasticity are continuously distributed. Both non-dispersive longitudinal motion and dispersive transverse motion in a beam. In the derivations, the Euler-Bernoulli beam theory assumptions are used. The dispersion diagrams are used to identify a new class of band gaps that allow wave propagation in one direction only. Such band gaps are thus referred to as non-reciprocal or directional band gaps. In one-dimensional systems, the directional band gaps signal and quantify the non-reciprocal behavior of the structure. It is shown that reciprocity is broken when a spatio-temporal modulation of the material properties of the structure, *i.e.* the Young's modulus E and ρ, is imposed in the form of a traveling wave.

In this case, a solution in the Floquet form with space-time harmonics is assumed, following the approach of [74]. The Floquet solution is substituted into the general equations of motion of beams with space and time varying material properties and leads to a Quadratic Eigenvalues Problem[107] (QEP) that can be solved for the frequency ω as a function of the wavenumber κ. This approach also provides approximate analytical relationships between the modulation parameters and the position and width of the directional band gaps for the simple case of harmonic modula-

tion. Moreover, the minimum speed at which the modulating traveling wave has to travel in order to maximize the non-reciprocal effect is computed. The shift of the First Brillouin Zone limits in the dispersion diagram is related to the spatio-temporal modulation.

Many recent works focused on the possibility to control wave propagation through active components, which can change dynamically the properties of the material they are coupled with. For instance, it is possible to obtain active acoustic metamaterials with varying density and bulk modulus by using water-filled cylinders coupled to piezoelectric elements [108]. By using the same piezoelectric effect, spatio-temporal piezoelectric beams could be obtained by properly switching the connection each piezoelectric patch has to an electric circuit [109], effectively achieving a time-varying equivalent stiffness.

The chapter first provides a description of the systems under investigation by presenting the equations of motion and the considered modulation strategies. Then, the methodology employed for the analysis is discussed. Results are presented and discussed for both longitudinal and transverse motion. Concluding remarks are presented in at the end of the chapter.

5.2 Theoretical background

5.2.1 Time-spatial periodic beams

Consider a beam with Young's modulus E and density ρ periodic functions of space and time. This periodic variation of the medium's characteristic in space and time is defined as modulation. Consider a periodic variation along the axial direction, so that the modulated Young's modulus E and density ρ can be expressed as:

$$E(x,t) = E(x+\lambda_m, t+T_m) \qquad \rho(x,t) = \rho(x+\lambda_m, t+T_m) \tag{5.1}$$

for any location x and at any instant t. Here λ_m and T_m define the spatial and time periodicity, respectively, while $\kappa_m = 2\pi/\lambda_m$ and $\omega_m = 2\pi/T_m$ are the wavenumber and the angular frequency associated to the properties of modulation. The periodic modulation pattern can be understood as a traveling wave with velocity $v_m = \omega_m/\kappa_m$. The analysis is limited to the case in which this pattern travels with constant velocity and v_m is defined as "modulation speed".

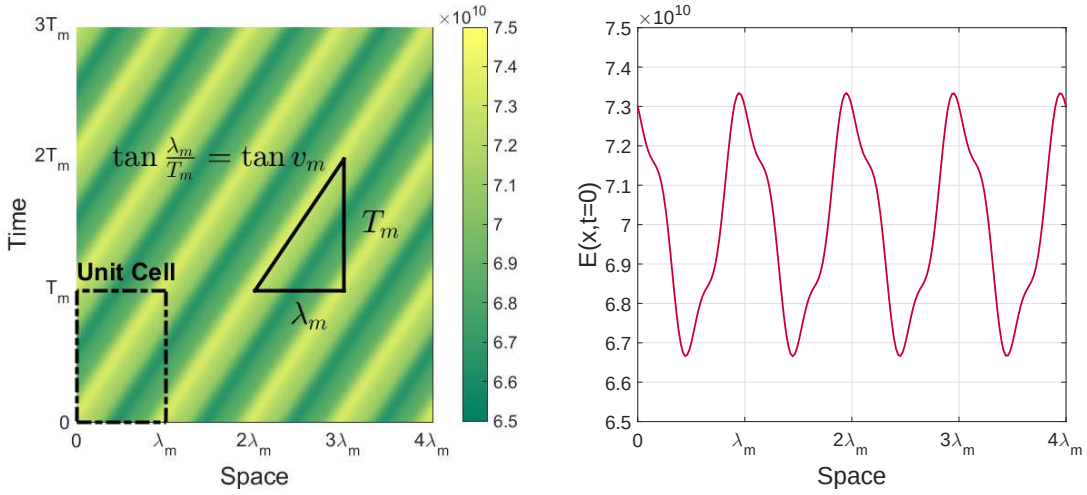

(a) (b)

Figure 5.1: Example of spatiotemporal periodic material with $E(x,t) = E_0 + E_m \cos(\omega_m t - \kappa_m x) + E_m/5 \cos\left[3(\omega_m t - \kappa_m x)\right]$, with $E_0 = 70$ GPa and $E_m = 3$ GPa: (a) spatio-temporal unit cell and its periodic space-time domain; (b) profile of the traveling modulation pattern as see at $t = 0$.

The behavior of spatial-only periodic structures can be fully characterized by studying a single unit cell, which represents the building block of the structure [3, 87]. For systems periodic both in space and time, the concept of unit cell has to be extended to account for periodicity both in the spatial and temporal domains. Therefore, this study focuses on the spatio-temporal unit cell in order to obtain the dispersion properties of the structure. The spatio-temporal unit cell is associated to λ_m and T_m, it travels with velocity v_m along the axial direction and coincides with the classically defined unit cell of spatial-only periodic structures for $v_m = 0$. An example of spatio-temporal unit cell is given in Fig. 5.1(a), in which a material with Young's

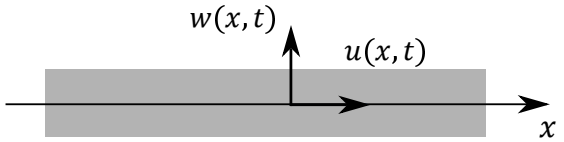

Figure 5.2: Schematic of a beam with longitudinal motion described by $u(x,t)$ and transverse motion described by $w(x,t)$.

modulus given by $E(x,t) = E_0 + E_m \cos(\omega_m t - \kappa_m x) + E_m/5 \cos\left[3(\omega_m t - \kappa_m x)\right]$ is considered, with $E_0 = 70$ GPa and $E_m = 3$ GPa. At $t = 0$, the stiffness of the structure is defined by the periodic function shown in Fig. 5.1.(b). While the spatio-temporal modulation can travel in both forward and backward directions, in the present study forward propagating modulation only is considered, since analogous considerations can be made for backward propagating modulation.

5.2.2 Analysis of dispersion

First, the equations of motions of beams with material properties that depend upon space and time are derived. Both longitudinal and transverse motion are considered. The study is restricted to the case of slender beams, in which shear deformation and rotational inertia are neglected [110]. Time-space periodic structures are then investigated by restricting the class of functions that describe the material properties to periodic functions in time and space only. As shown in Fig. 5.2, in the case of longitudinal motion $u = u(x,t)$ is assumed to be the longitudinal displacement of the beam along the axial direction. For transverse motion, the displacement is described by $w = w(x,t)$. The conservation of linear momentum is imposed along both axial and transverse direction and the constitute laws for the cross-section of the beam to get the following equation of motion for longitudinal motion:

$$\frac{\partial}{\partial x}\left[E(x,t)\frac{\partial u(x,t)}{\partial x}\right] - \frac{\partial}{\partial t}\left[\rho(x,t)\frac{\partial u(x,t)}{\partial t}\right] = 0 \tag{5.2}$$

and transverse motion:

$$R_g^2 \frac{\partial^2}{\partial x^2}\left[E(x,t)\frac{\partial^2 w(x,t)}{\partial x^2}\right] + \frac{\partial}{\partial t}\left[\rho(x,t)\frac{\partial w(x,t)}{\partial t}\right] = 0 \tag{5.3}$$

in which A is the cross-sectional area, I is the area moment of inertia and $R_g = \sqrt{I/A}$ is the radius of gyration of the beam. If $E(x,t) = E$ and $\rho(x,t) = \rho$ are constant in space and time, Eq. 5.2 and Eq. 7.1 reduce to the familiar equations of motion for uniform beams.

Wave propagation properties in time-spatial periodic structures are studied by computing and analyzing band diagrams for said structures. The approach followed in this work exploits the periodic nature of the considered modulation of the material properties functions $E(x,t)$ and $\rho(x,t)$. Both are periodic in the variables x and t with periodicity λ_m and T_m, respectively. It is then possible to express them by using the following Fourier series representations:

$$E(x,t) = \sum_{p=-\infty}^{+\infty} \hat{E}_p e^{ip(\omega_m t - \kappa_m x)} \tag{5.4}$$

$$\rho(x,t) = \sum_{p=-\infty}^{+\infty} \hat{\rho}_p e^{ip(\omega_m t - \kappa_m x)} \tag{5.5}$$

in which $\hat{E}_p$ and $\hat{\rho}_p$ are the Fourier coefficients of the series associated with the traveling harmonic terms $e^{ip(\omega_m t - \kappa_m x)}$. An explicit expression for these coefficients can be obtained by performing a double integration over the unit cell's spatial and time periods λ_m and T_m, respectively:

$$\hat{E}_p = \frac{1}{T_m}\frac{1}{\lambda_m}\int_{-T_m/2}^{+T_m/2}\int_{-\lambda_m/2}^{+\lambda_m/2} E(x,t)e^{-ip(\omega_m t - \kappa_m x)}dxdt \tag{5.6}$$

$$\hat{\rho}_p = \frac{1}{T_m}\frac{1}{\lambda_m}\int_{-T_m/2}^{+T_m/2}\int_{-\lambda_m/2}^{+\lambda_m/2} \rho(x,t)e^{-ip(\omega_m t - \kappa_m x)}dxdt \tag{5.7}$$

The solutions to Eq. 5.2 and Eq. 7.1 are chosen in the generalized Floquet form [74]

and write:

$$u(x,t) = e^{i(\omega t - \kappa x)} \sum_{n=-\infty}^{+\infty} \hat{u}_n e^{in(\omega_m t - \kappa_m x)} \tag{5.8}$$

$$w(x,t) = e^{i(\omega t - \kappa x)} \sum_{n=-\infty}^{+\infty} \hat{w}_n e^{in(\omega_m t - \kappa_m x)} \tag{5.9}$$

In a study on wave propagation in spatio-temporal periodic transmission lines [80], allowing solutions in the generalized Floquet form, the possibility of having time-growing waves for certain modulation parameters is discussed. These time-growing waves are associated to unstable interactions between the wave propagating in the system and the modulation wave. In the same study, the author discusses under which conditions the governing equations of the system are satisfied, for real wavenumbers, by complex frequencies only, leading to time-growing oscillations. Such instabilities occur when the modulation speed is greater than the wave speed in the uniform system. Although interesting, an analogous study of the stability conditions for wave propagation in modulated beams falls outside the scope of the present article. Nevertheless, knowing that non-periodic, time-growing solutions can arise for certain combinations of the modulation parameters ω_m, κ_m and $\hat{E}_p$, $\hat{\rho}_p$, stability is assumed to hold by imposing a modulation speed smaller than the wave speed in the uniform structure. Substituting Eq. 5.8 and Eq. 5.9 into Eq. 5.2 and Eq. 7.1, together with the expressions for the material properties in Eq. 5.4, leads to expressions that can be simplified by exploiting orthogonality of the Fourier basis in Eq.s 5.2-7.1. This gives:

$$\begin{aligned} \sum_{n=-\infty}^{+\infty} \Big[\big(\kappa + n\kappa_m\big)\big(\kappa + p\kappa_m\big) \Big] \hat{E}_{p-n} \hat{u}_n = \\ \sum_{n=-\infty}^{+\infty} \Big[\big(\omega + n\omega_m\big)\big(\omega + p\omega_m\big) \Big] \hat{\rho}_{p-n} \hat{u}_n \end{aligned} \tag{5.10}$$

$$\sum_{n=-\infty}^{+\infty} \Big[\big(\kappa + n\kappa_m\big)\big(\kappa + p\kappa_m\big) \Big]^2 \hat{E}_{p-n}\hat{w}_n = \frac{1}{R_g^2} \sum_{n=-\infty}^{+\infty} \Big[\big(\omega + n\omega_m\big)\big(\omega + p\omega_m\big) \Big] \hat{\rho}_{p-n}\hat{w}_n \tag{5.11}$$

which hold for the longitudinal and transverse motion of the beam, respectively. If a finite number N of terms is considered in Eq. 5.8 and 5.9, then Eq. 5.10 and 5.11 represent each a finite set of $2N + 1$ equations that can be cast in the form of a quadratic eigenvalue problem (QEP):

$$\big(\omega^2\hat{\mathbf{L}}_2 + \omega\hat{\mathbf{L}}_1 + \hat{\mathbf{L}}_0\big)\hat{\mathbf{u}} = \mathbf{0} \tag{5.12}$$

$$\big(\omega^2\hat{\mathbf{T}}_2 + \omega\hat{\mathbf{T}}_1 + \hat{\mathbf{T}}_0\big)\hat{\mathbf{w}} = \mathbf{0} \tag{5.13}$$

where $\hat{\mathbf{L}}_j = \hat{\mathbf{L}}_j(\kappa)$ and $\hat{\mathbf{T}}_j = \hat{\mathbf{T}}_j(\kappa)$, with $j = 0, 1, 2$, are coefficient matrices whose entries depend on the modulation parameters ω_m and κ_m, the Fourier coefficients $\hat{E}_p$ and $\hat{\rho}_p$ and the wavenumber κ. Moreover, $\hat{\mathbf{u}}$ and $\hat{\mathbf{w}}$ are the displacement coefficient vectors. The QEP in Eq.s 5.12-5.13 is solved in terms of ω by letting κ vary in a convenient range. For spatial-only periodic structure, this range is given by the Irreducible Brillouin Zone (IBZ) [3]. It is shown that spatio-temporal modulation challenges the classical definition of the IBZ, leading to a shift in the wavenumber range to be considered. The dispersion properties of the time-spatial periodic structure are then obtained by representing the relation $\omega = \omega(\kappa)$ in the form of band diagrams.

5.3 Band diagrams

The results are presented in the form of band diagrams for both longitudinal and transverse wave. Also, the proposed dispersion analysis is numerically verified through

a finite element study of the transient response to external excitation of beams with modulated properties. Two distinct modulation strategies of the Young's modulus E only are considered, *i.e.* harmonic and square traveling wave, while the density ρ is assumed to be constant. In discussing the results, the dimensionless frequency Ω and wavenumber μ are used:

$$\Omega = \frac{f\lambda_m}{c_0} \qquad \mu = \kappa\lambda_m \tag{5.14}$$

where f is the frequency and $c_0 = \sqrt{E_0/\rho_0}$ is the velocity of longitudinal waves in a non-modulated beam.

First, a harmonic modulation of the Young's modulus only is considered, thus assuming the following expressions for the material parameters:

$$E(x,t) = E_0 + E_m \cos(\omega_m t - \kappa_m x) \qquad \rho(x,t) = \rho_0 \tag{5.15}$$

where E_m is the amplitude of the modulation. For $E_m = 0$, the material is not

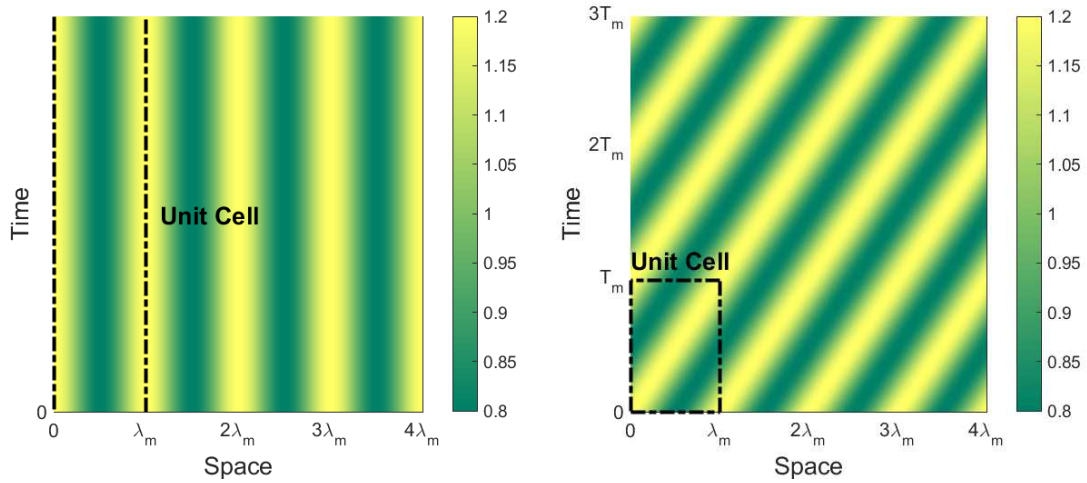

(a) (b)

Figure 5.3: For harmonic modulation, unit cells in the space-time domain given by the periodic change of the ratio $E(x,t)/E_0$, with $\alpha_m = 0.20$: (a) spatial-only modulation ($v_m = 0$, $T_m \to \infty$); (b) spatio-temporal modulation ($v_m \neq 0$).

modulated and the beam is uniform, while for $E_m \neq 0$ and $\omega_m \neq 0$, the value of the

Young's modulus can be described as the harmonic traveling wave defined in Eq. 5.15. The wave travels along the positive direction of the x axis with speed $v_m = \omega_m/\kappa_m$. Define the dimensionless modulation amplitude α_m and the dimensionless modulation velocity parameter ν_m:

$$\alpha_m = \frac{E_m}{E_0} \qquad \nu_m = \frac{v_m}{c_0} \tag{5.16}$$

An example of harmonic modulation is given in Fig. 5.3: spatial-only modulation is shown in Fig. 5.3a and corresponds to the case with $T_m \to \infty$, thus $\omega_m \to 0$ and $\nu_m \to 0$, while spatio-temporal modulation with $\alpha_m = 0.20$ and $\nu_m \neq 0$ is shown in Fig. 5.3b. The Fourier coefficients in Eq. 5.4 are given by Eq. 5.6 and write:

$$\hat{E}_p = \begin{cases} E_0 & \text{for } p = 0 \\ E_m/2 & \text{for } p = \pm 1 \end{cases} \tag{5.17}$$

while $\hat{\rho}_p = \rho_0 \delta_{p0}$, where δ_{p0} is the Kronecker delta.

Also, a square traveling wave of the Young's modulus only is considered with the following expressions:

$$E(x,t) = E_1 + (E_2 - E_1) H\big[\cos(\omega_m t - \kappa_m x)\big], \qquad \rho(x,t) = \rho_0, \tag{5.18}$$

in which H denotes the Heaviside function. The Young's modulus takes the two values E_1 and E_2, with $E_2 > E_1$. In this case, $E_m = E_2 - E_1$. The spatial and time periods of the modulation are $\lambda_m = 2\pi/\kappa_m$ and $T_m = 2\pi/\omega_m$, respectively. The modulation travels with velocity $v_m = \omega_m/\kappa_m$.

It can be shown that the Fourier coefficients for square wave modulation given by Eq. 5.6 write:

$$\hat{E}_p = E_2 \delta_p + \frac{E_1 - E_2}{2} sinc\Big[\frac{\pi p}{2}\Big] \tag{5.19}$$

in which $sinc(x) = sin(x)/x$ and $\hat{\rho}_p = \rho_0 \delta_{p0}$.

5.3.1 Harmonic modulation

The band diagrams shown in Fig. 5.4 and Fig. 5.5 are obtained by solving the QEP in Eq. 5.12 and Eq. 5.13 for longitudinal and transverse motion, respectively. For conventional periodic system with spatial-only modulation, the dispersion diagrams are periodic in the wavenumber domain, therefore the calculation of the dispersion diagrams can be restricted to one period, known as First Brillouin Zone (FBZ), where the dimensionless wavenumber μ ranges in $[-\pi, \pi]$. Moreover, it is customary to further restrict the domain of the computation by considering just half of the period, called Irreducible Brillouin Zone (IBZ), with μ ranging in $[0, \pi]$. This approach is justified by an important property of conventional periodic structures, namely that their dispersion relation satisfies the relation $\Omega(\mu) = \Omega(-\mu)$. Such property is due to the fact that the structure can support both backward propagating waves and forward propagating waves, and the behavior of the waves is the same no matter which direction they are propagating to. It is also understood that the relation $\Omega(\mu) = \Omega(-\mu)$ implies symmetry of the dispersion diagrams with respect to the frequency axis, allowing the analysis to be restricted on the IBZ [3]. For spatio-temporal modulation of the material properties $\Omega(\mu) \neq \Omega(-\mu)$, the band diagrams are not symmetric with respect to the frequency axis. For this reason, a sufficiently broad range for the values of the wavenumber needs to be considered. In our analysis, μ is imposed to range in $[-3/2\pi, 3/2\pi]$. In all the computations, the focus is on the two lowest dispersion branches where a band gap opens for $\alpha_m \neq 0$, so it is possible to truncate the series expressing the solution imposing $N = 3$. Increasing the truncation order does not provide any additional advantage, while the CPU time needed to solve the QEP increases quickly. Therefore, the matrices $\hat{\mathbf{L}}_j$ and $\hat{\mathbf{T}}_j$, with $j = 0, 1, 2$, in the QEP are square matrices of order $2 \cdot 3 + 1 = 7$. Both for longitudinal and transverse motion in absence of modulation, thus for $\alpha_m = 0$ and $\nu_m = 0$, the beam does not display any band gap (Fig. 5.4a and 5.5a). The only dispersion branches

having physical meaning are the ones departing from the origin, which are associated to the two $0-$th order harmonics, one associated to the backward-propagating wave, the other associated to the forward-propagating wave. On the contrary, when space-only modulation is applied, in our example for $\alpha_m = 0.40$ and $\nu_m = 0$, the system displays a complete band gap for Ω in the range $[0.43, 0.53]$ for longitudinal motion and $[0.0197, 0.0244]$ for transverse motion, in which both backward-propagating waves and forward-propagating waves are not supported by the structure, as shown in Fig. 5.4b and Fig. 5.5b. Due to spatial periodic modulation of the medium, higher spatial-only harmonics in the solutions expressed by Eq. 5.8 and Eq. 5.9 have nonzero amplitude and coupling between the associated modes leads to dispersive behavior and band gaps of Bragg type at the edge of the FBZ. The band diagram is periodic with period 2π, with FBZ ranging from $\mu = -\pi$ to $\mu = \pi$. When modulation in space *and* time is introduced, symmetry of the dispersion diagram with respect to Ω and μ is broken, as shown in Fig. 5.4c and Fig. 5.5c, which are obtained respectively for $\alpha_m = 0.40$ and $\nu_m = 0.05$ for longitudinal motion, and for $\alpha_m = 0.40$ and $\nu_m = 0.002$ for transverse motion. The band diagrams for spatiotemporal periodic structures clearly show that, within certain frequency ranges, only modes propagating in one direction are allowed. For longitudinal motion, a closer look at Fig. 5.4c reveals that waves propagating with Ω in the range $[0.41, 0.46]$ have positive group velocity only, therefore forward propagating waves only are allowed to propagate, while backward-propagating longitudinal waves only are supported by the structure for Ω in the range $[0.51, 0.56]$. Such frequency ranges are then associated to one-way propagation, thus they can be called "directional band gaps". By comparing the band diagrams for longitudinal motion in Fig. 5.4c and 5.4d, it is also observed that for $\alpha_m = 0.40$ and $\nu_m = 0.05$ the structure displays a complete band gap for Ω in the range $[0.46, 0.51]$ together with the two directional band gaps for Ω in the ranges $[0.41, 0.46]$ and $[0.51, 0.56]$, while for $\alpha_m = 0.40$ and $\nu_m = 0.20$ the structure

exhibit just two wider directional band gaps. Analogous considerations can be done for transverse motion by analyzing the dispersion diagrams in Fig. 5.5. Furthermore, Fig. 5.4c and Fig. 5.4d reveal that when $\nu_m \neq 0$, the local maxima of the dispersion branches do not coincide with the limits of the classically defined FBZ $\mu = \pm\pi$, instead they are shifted in the direction of positive wavenumbers κ for forward propagating modulation. Similar considerations hold in the case of transverse motion, as shown in Fig. 5.5c and 5.5d. In other words, spatiotemporal modulation of the material properties introduces shifts in the position of the band gaps, breaking symmetry of the dispersion diagrams and leading to directional band gaps. In addition, spatiotemporal modulation also challenges the classic definition of the FBZ and its limits, as already observed by Cassedy [79, 111].

5.3.2 Square modulation

For square modulation one can also compute the band diagrams for both longitudinal and transverse motion and compare the cases of spatial-only modulation and spatiotemporal modulation. Values $\alpha = 3$ and $\nu_m = 0.15$ are considered for the beam in longitudinal motion, while for transverse motion the values $\alpha = 3$ and $\nu_m = 0.015$ are considered. The focus is on the first two band gaps only. $N = 5$ is assumed to be a good compromise between quality of the approximation and time required for the computation. As shown in Fig. 5.6a and Fig. 5.6c, the spatial-only modulation, thus for $\nu_m = 0$, induces multiple band gaps in the structure. From Fig. 5.6b and Fig. 5.6d, it can be seen that when spatiotemporal modulation is considered, in this case for $\nu_m \neq 0$, the band gaps are shifted upwards or downwards depending on the direction of propagation, hence they become directional band gaps and inform on the non-reciprocal behavior of the structure.

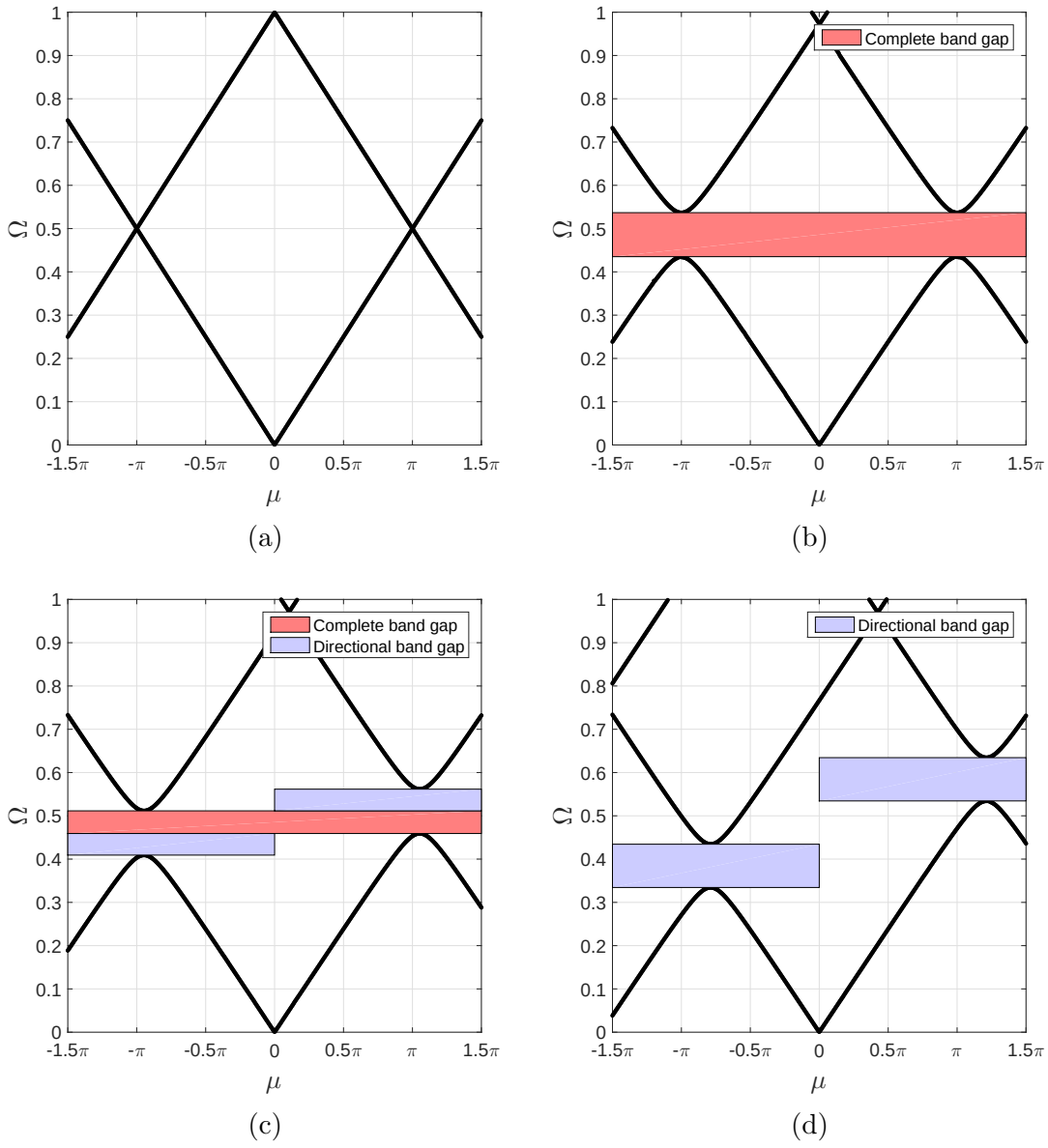

Figure 5.4: Band diagrams for beam in longitudinal motion and harmonic modulation: (a) non-modulated beam with $\alpha_m = 0$ and $\nu_m = 0$, (b) space modulated only beam with $\alpha_m = 0.40$ and $\nu_m = 0$, (c) space-time modulated beam with $\alpha_m = 0.40$ and $\nu_m = 0.05$, (d) space-time modulated beam with $\alpha_m = 0.40$ and $\nu_m = 0.20$. For $\alpha_m \neq 0$ and $\nu_m \neq 0$ the mirror symmetry with respect to the frequency axis is relaxed, leading to directional band gaps which signal the possibility of one-way propagation.

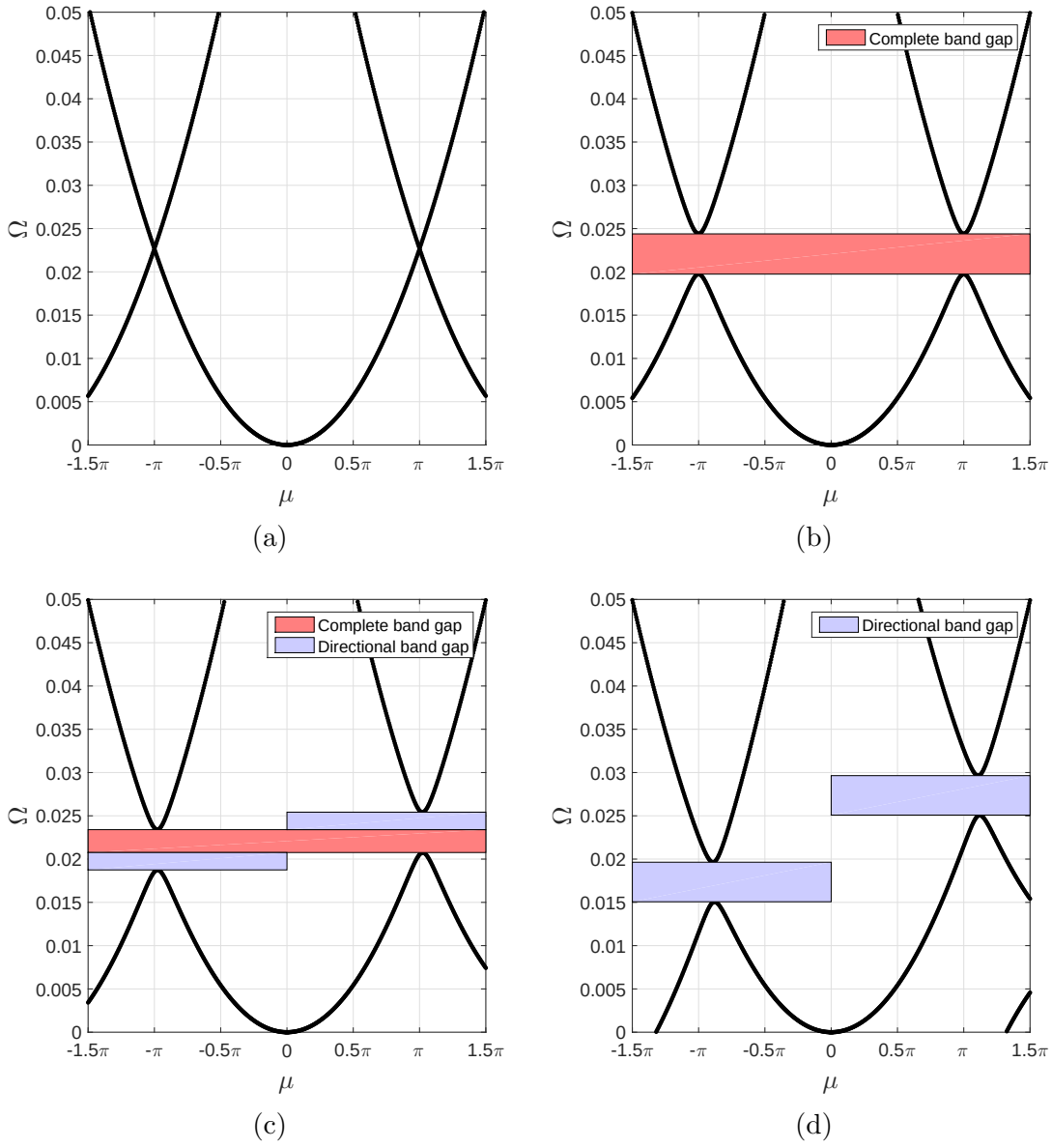

Figure 5.5: Band diagrams for beam in transverse motion and harmonic modulation: (a) non-modulated beam with $\alpha_m = 0$ and $\nu_m = 0$, (b) space modulated only beam with $\alpha_m = 0.40$ and $\nu_m = 0$, (c) space-time modulated beam with $\alpha_m = 0.40$ and $\nu_m = 0.002$, (d) space-time modulated beam with $\alpha_m = 0.40$ and $\nu_m = 0.01$. For $\alpha_m \neq 0$ and $\nu_m \neq 0$ the mirror symmetry is lost and directional band gaps are obtained.

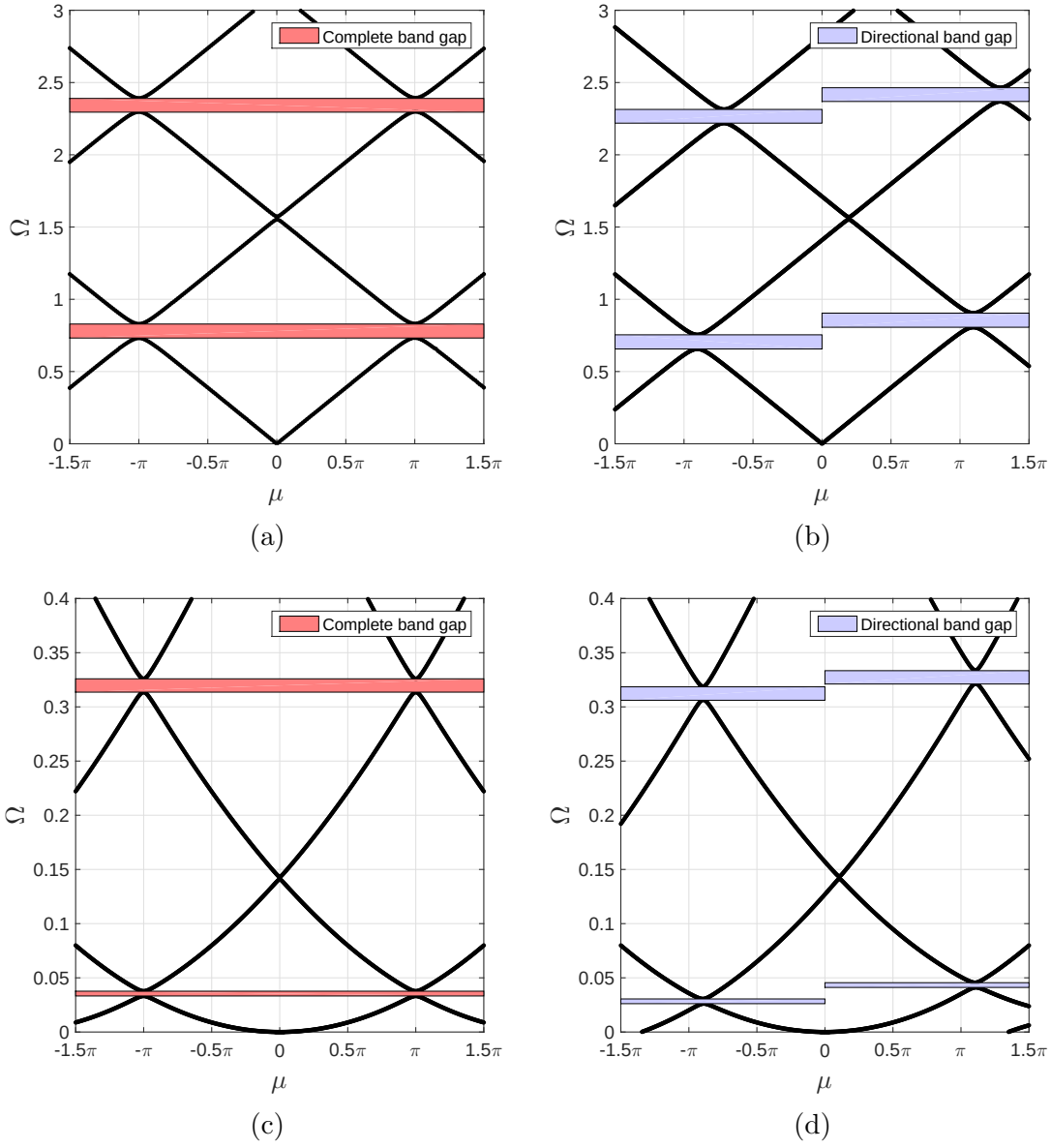

Figure 5.6: Band diagrams for beam in longitudinal (a,b) and transverse (c,d) motion and square modulation. For longitudinal motion: (a) space modulated only beam with $\alpha_m = 3$ and $\nu_m = 0$, (b) space-time modulated with $\alpha_m = 3$ and $\nu_m = 0.15$. Similarly for transverse motion: (c) space modulated only beam with $\alpha_m = 3$ and $\nu_m = 0$, (d) space-time modulated with $\alpha_m = 3$ and $\nu_m = 0.015$. The structure is non-reciprocal for $\alpha_m \neq 0$ and $\nu_m \neq 0$ in multiple frequency ranges.

5.3.3 Analysis of the modulation parameters

Now an analytical characterization of the effect of the modulation parameters on the dispersion properties of the beam is performed. A reduced version of the QEP used to compute the band diagrams in Fig. 5.4 and Fig. 5.5 is used to obtain approximate analytical expressions for the dispersion branches of spatio-temporal modulated beams. Such expressions allow us to quantify the effect of the modulation parameters α_m and ν_m not only on the position and width of the directional band gaps, but also on the shift of the limits of the FBZ. The analysis is confined to the harmonic modulation only. The longitudinal motion case is considered first by investigating the values of the FBZ limits induced by the modulation. Fig. 5.7 shows a detail of the regions of the band diagram associated with the directional band gaps. The plot presents different cases of modulation, each corresponding to the same value $\nu_m = 0.10$ and increasingly smaller values of α_m. In Fig. 5.7b and 5.7c it can be observed that for $\alpha_m \to 0$, the band gaps close and two dispersion branches intersect at the point (μ_F, Ω_F) for forward propagating waves, with $\mu_F \neq \pi$, and at the point (μ_B, Ω_B) for backward propagating waves, with $\mu_B \neq -\pi$. In the limit of zero modulation, the dispersion branches departing from the origin and associated to the 0-th order harmonic in Eq. 5.8 are the only having physical reality, as discussed by Cassedy [79]. Analytic expressions for μ_B, Ω_B and μ_F, Ω_F are sought by truncating the series expressing the solution in Eq. 5.8 to the first order, then Eq. 5.12 reduces to:

$$\begin{bmatrix} L_{11} & L_{12} & L_{13} \\ L_{21} & L_{22} & L_{23} \\ L_{31} & L_{32} & L_{33} \end{bmatrix} \begin{bmatrix} \hat{u}_{-1} \\ \hat{u}_0 \\ \hat{u}_{+1} \end{bmatrix} = \begin{bmatrix} 0 \\ 0 \\ 0 \end{bmatrix} \tag{5.20}$$

where the coefficients can be found in the C. First the analysis focuses on the directional band gap for forward propagating waves. In this case, the band gap is

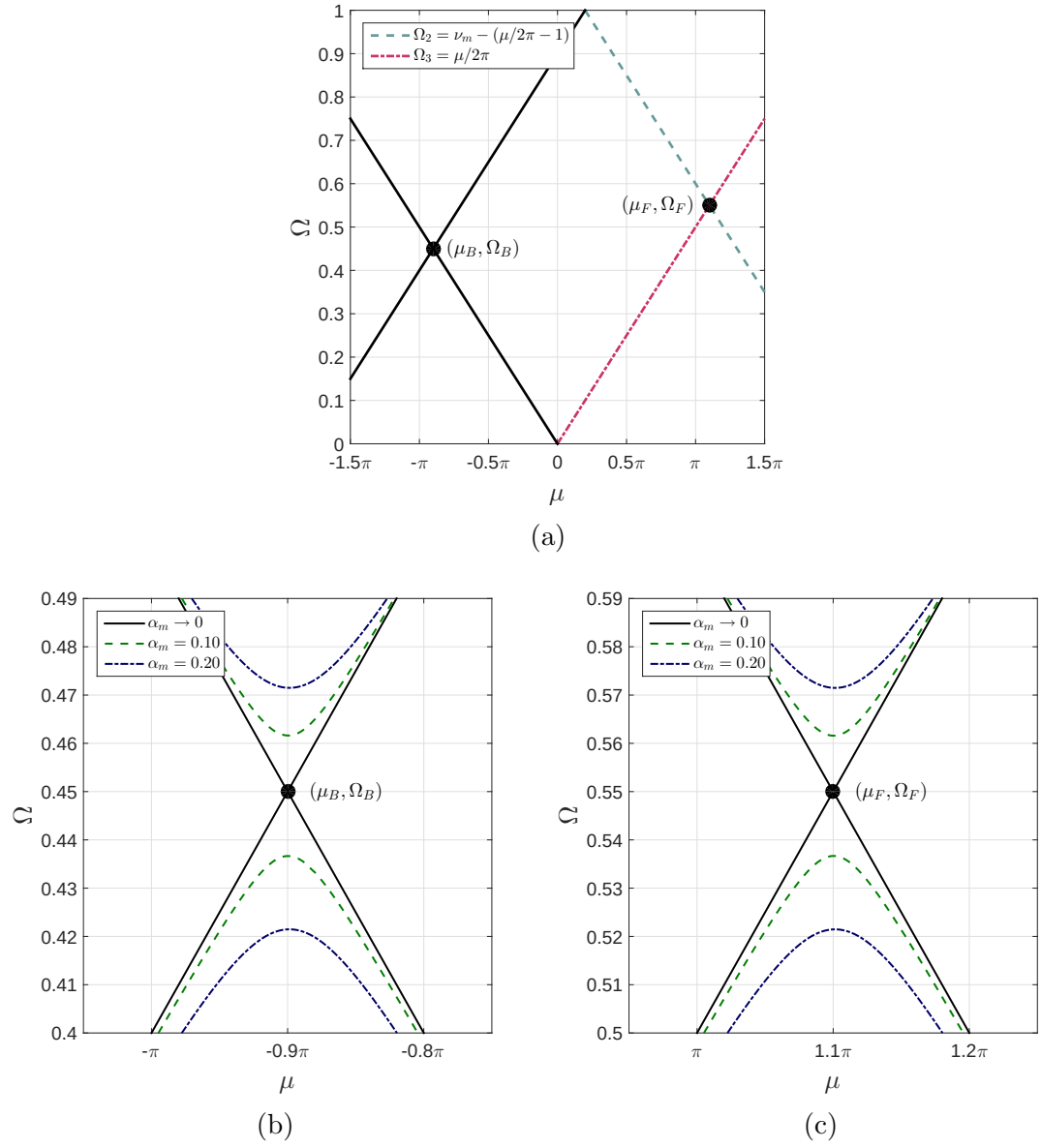

Figure 5.7: Band diagrams for longitudinal motion with $\nu_m = 0.10$ and different values of α_m. For $\alpha_m \to 0$ (a), the first two dispersion branches intersect at (μ_B, Ω_B) and (μ_F, Ω_F) for backward and forward propagating waves, respectively. Specifically, the point (μ_F, Ω_F) is the intersection of the branch Ω_2 in Eq. 5.23 with the branch Ω_3 in Eq. 5.24. Comparison with the case in which $\alpha_m \neq 0$ is given in (b) for backward propagating waves and in (c) forward propagating waves.

generated by the interaction of the forward 0-th order harmonic wave with frequency ω and the backward (or folded) first order harmonic wave with frequency $\omega - \omega_m$. Therefore, the first order harmonic wave with frequency $\omega + \omega_m$ can be neglected and it is possible to further simplify Eq. 5.20 by solving the problem for the coefficients $\hat{u}_{-1}$ and $\hat{u}_0$ only to obtain:

$$\begin{bmatrix} L_{11} & L_{12} \\ L_{21} & L_{22} \end{bmatrix} \begin{bmatrix} \hat{u}_{-1} \\ \hat{u}_0 \end{bmatrix} = \begin{bmatrix} 0 \\ 0 \end{bmatrix} \tag{5.21}$$

A compact solution to this QEP is obtained by observing that for $\alpha_m \to 0$, then $L_{12}, L_{21} \to 0$. The characteristic equation for Eq. 5.21 reduces to:

$$L_{11}L_{22} = \left\{\Omega^2 - 2\nu_m\Omega - \left[\left(\frac{\mu}{2\pi} - 1\right)^2 - \nu_m^2\right]\right\}\left\{\Omega^2 - \left(\frac{\mu}{2\pi}\right)^2\right\} = 0 \tag{5.22}$$

whose solutions are:

$$\Omega_{1,2} = \nu_m \pm \left(\frac{\mu}{2\pi} - 1\right) \tag{5.23}$$

$$\Omega_{3,4} = \pm\frac{\mu}{2\pi} \tag{5.24}$$

Each of these four roots is associated to a different dispersion branch. In general these roots are distinct, but at $\mu = \mu_F$ Eq. 5.21 allows double roots for $\alpha_m \to 0$. Two of the dispersion branches intersect at the point (μ_F, Ω_F), which can be obtained by imposing:

$$\frac{\mu_F}{2\pi} = \nu_m - \left(\frac{\mu_F}{2\pi} - 1\right) \tag{5.25}$$

to get:

$$\mu_F = \pi(1 + \nu_m) \qquad \Omega_F = \frac{1}{2}(1 + \nu_m) \tag{5.26}$$

These expressions show that the right limit of the FBZ is given by $\mu = \pi$ only if $\nu_m = 0$, otherwise the limit of the FBZ between the first and the second dispersion branches is shifted by the value $\Delta\mu = \nu_m\pi$, which in first approximation depends upon the modulation speed only. As already recognized by Cassedy [79], when spatio-temporal modulation is introduced, the dispersion diagrams present a peculiar skew representation in the frequency-wavenumber plane, with repetition of the unit cell along a line of slope dependent on the modulation frequency, rather than repetition along the wavenumber axis, as customary in spatially modulated only systems. Therefore, in the context of spatio-temporally modulated systems, it is not possible to apply the concept of FBZ as defined for spatially modulated systems only. For this reason, Cassedy talks about generalized Brillouin diagrams. If the dimensionless modulation amplitude is small but different from zero, $\alpha_m << 1$, the characteristic equation for Eq. 5.21 is a quartic and does not allow double roots at $\mu_F = \pi(1+\nu_m)$. Instead, it allows four distinct solutions, two of which lie in a neighborhood of Ω_F. In a neighborhood of the point (μ_F, Ω_F), it can be written $\mu = \mu_F + \delta\mu$ and $\Omega = \Omega_F + \delta\Omega$, with $\delta\mu, \delta\Omega << 1$. Substituting the assumed μ and Ω into $L_{11} - L_{22}$, this quantity is expressed as a function of the small quantities $\delta\mu, \delta\Omega$ only, hence they can be neglected leading to:

$$L_{11} - L_{22} \approx 0 \tag{5.27}$$

for $\mu = \mu_F = \pi(1 + \nu_m)$, in which equality holds for $\alpha_m \to 0$. The latter key approximation allows us to study two simple problems:

$$L_{11}^2 - L_{12}^2 = 0 \qquad \to (L_{11} - L_{12})(L_{11} + L_{12}) = 0 \tag{5.28}$$

$$L_{22}^2 - L_{12}^2 = 0 \qquad \to (L_{22} - L_{12})(L_{22} + L_{12}) = 0 \tag{5.29}$$

both representing an approximation of the original problem expressed by the characteristic equation given by solving Eq. 5.21 in a neighborhood of (μ_F,Ω_F). The

solutions of Eq. 5.28 write:

$$\Omega_r^I = \nu_m \pm \frac{1-\nu_m}{2}\sqrt{1 \pm \frac{\alpha_m}{2}\frac{1+\nu_m}{1-\nu_m}} \tag{5.30}$$

while the solutions of Eq. 5.29 write:

$$\Omega_r^{II} = \pm\frac{1+\nu_m}{2}\sqrt{1 \pm \frac{\alpha_m}{2}\frac{1-\nu_m}{1+\nu_m}} \tag{5.31}$$

with $r = 1, 2, 3, 4$. For both of the approximate problems, only the two positive values of frequency in a neighborhood of Ω_F are considered, which approximate of the upper and lower limits of the directional band gap. By properly averaging such frequencies, one can define:

$$\Omega_F^{top} = \frac{1}{2}\left[\nu_m + \frac{1-\nu_m}{2}\sqrt{1 + \frac{\alpha_m}{2}\frac{1+\nu_m}{1-\nu_m}} + \frac{1+\nu_m}{2}\sqrt{1 + \frac{\alpha_m}{2}\frac{1-\nu_m}{1+\nu_m}}\right] \tag{5.32}$$

$$\Omega_F^{bot} = \frac{1}{2}\left[\nu_m + \frac{1-\nu_m}{2}\sqrt{1 - \frac{\alpha_m}{2}\frac{1+\nu_m}{1-\nu_m}} + \frac{1+\nu_m}{2}\sqrt{1 - \frac{\alpha_m}{2}\frac{1-\nu_m}{1+\nu_m}}\right] \tag{5.33}$$

where Ω_F^{top} and Ω_F^{bot} are the upper and the lower limits of the directional band gap for the forward propagating waves, respectively.

Since $\alpha_m << 1$, linearized expressions can be obtained by using the Taylor series of $\sqrt{1+x} = 1 + 1/2x + O(x^2)$, thus Eq. 5.32 rewrites as:

$$\Omega_{F,lin}^{top} = +\frac{\alpha_m}{8} + \frac{1}{2}\Big(1+\nu_m\Big) \tag{5.34}$$

$$\Omega_{F,lin}^{bot} = -\frac{\alpha_m}{8} + \frac{1}{2}\Big(1+\nu_m\Big) \tag{5.35}$$

The dependency of the directional band gap width on the modulation parameters α_m and μ_m is given by the following expression:

$$\Delta\Omega_{F,lim} = \Omega_{F,lin}^{top} - \Omega_{F,lin}^{bot} = \frac{\alpha_m}{4} \tag{5.36}$$

A similar approach can be used to study the directional band gap associated to the backward propagating waves. In this case, the terms $\hat{u}_0$ and $\hat{u}_{+1}$ are retained in Eq. 5.20 to give:

$$\begin{bmatrix} L_{22} & L_{23} \\ L_{32} & L_{33} \end{bmatrix} \begin{bmatrix} \hat{u}_0 \\ \hat{u}_{+1} \end{bmatrix} = \begin{bmatrix} 0 \\ 0 \end{bmatrix} \tag{5.37}$$

It can be shown that modulation induces a shift of the left edge of the FBZ, thus the following relations hold:

$$\mu_B = -\pi(1-\nu_m) \qquad\qquad \Omega_B = \frac{1}{2}(1-\nu_m) \tag{5.38}$$

Moreover the expression for the upper and lower limits of the directional band gaps for backward propagating waves are:

$$\Omega_B^{top} = \frac{1}{2}\Bigg[-\nu_m + \frac{1+\nu_m}{2}\sqrt{1+\frac{\alpha_m}{2}\frac{1-\nu_m}{1+\nu_m}} + \frac{1-\nu_m}{2}\sqrt{1+\frac{\alpha_m}{2}\frac{1+\nu_m}{1-\nu_m}}\Bigg] \tag{5.39}$$

$$\Omega_B^{bot} = \frac{1}{2}\Bigg[-\nu_m + \frac{1+\nu_m}{2}\sqrt{1-\frac{\alpha_m}{2}\frac{1-\nu_m}{1+\nu_m}} + \frac{1-\nu_m}{2}\sqrt{1-\frac{\alpha_m}{2}\frac{1+\nu_m}{1-\nu_m}}\Bigg] \tag{5.40}$$

while the corresponding linearized expressions write:

$$\Omega_{B,lin}^{top} = +\frac{\alpha_m}{8} + \frac{1}{2}\Big(1-\nu_m\Big) \tag{5.41}$$

$$\Omega_{B,lin}^{bot} = -\frac{\alpha_m}{8} + \frac{1}{2}\Big(1-\nu_m\Big) \tag{5.42}$$

The linearized expression for the backward directional band gap width is given by:

$$\Delta\Omega_{B,lim} = \Omega_{B,lin}^{top} - \Omega_{B,lin}^{bot} = \frac{\alpha_m}{4} \tag{5.43}$$

hence:

$$\Delta\Omega_{F,lim} = \Delta\Omega_{B,lim} = \frac{\alpha_m}{4} \tag{5.44}$$

both backward and forward directional band gap widths have the same value, which depends on the modulation amplitude α_m only. One can also determine the minimum value of the modulation velocity parameter ν_m^{cr} such that, for $\alpha_m \neq 0$, the beam shows two distinct directional band gaps, one associated to the backward propagating waves, the other one associated to the forward propagating waves. In order to obtain an expression for ν_m^{cr}, let:

$$\Omega_{B,lim}^{top} = \Omega_{F,lim}^{bot} \tag{5.45}$$

which, solved for ν_m gives:

$$\nu_m^{cr} = \frac{\alpha_m}{4} \tag{5.46}$$

This results shows that, for smalls values of α_m, the modulation velocity parameter ν_m determines a shift Ω_{shift} in the location of the band gaps that writes $\Omega_{shift} = \nu_m$ for forward propagating waves and $\Omega_{shift} = -\nu_m$ for backward propagating waves, thus breaking the mirror symmetry of the band diagram about the Ω axis.

Following the same procedure outlined in the case of longitudinal motion, backward and forward wave propagation are characterized in the case of transverse motion through approximate analytic expressions for the directional band gaps. The following QEP is studied:

$$\begin{bmatrix} T_{11} & T_{12} & T_{13} \\ T_{21} & T_{22} & T_{23} \\ T_{31} & T_{32} & T_{33} \end{bmatrix} \begin{bmatrix} \hat{w}_{-1} \\ \hat{w}_0 \\ \hat{w}_{+1} \end{bmatrix} = \begin{bmatrix} 0 \\ 0 \\ 0 \end{bmatrix} \tag{5.47}$$

which can be obtained from Eq. 5.13 by retaining the 0-th and first order harmonics in Eq. 5.9. The dimensionless expressions for the coefficients in Eq. 5.47 can be found in A.. For forward wave propagation, Fig. 5.8 shows that for $\nu_m = 0.005$, the right edge of the FBZ between the first and the second dispersion branch is shifted due to modulation. Similarly to the case of longitudinal motion, in the limit of

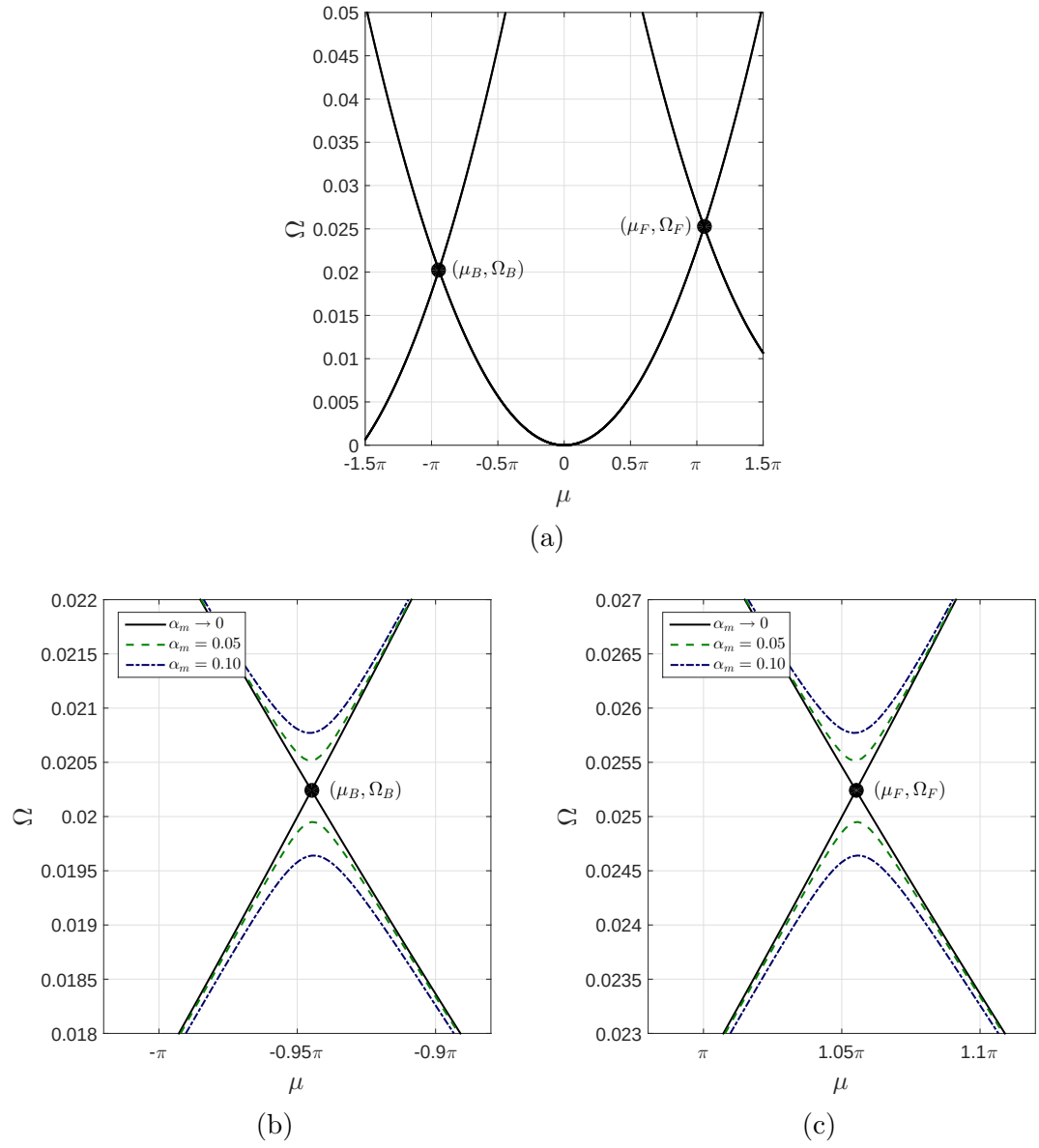

Figure 5.8: Band diagrams for transverse motion with $\nu_m = 0.005$ and different values of α_m. For $\alpha_m \to 0$ (a), the first two dispersion branches intersect at (μ_B, Ω_B) and (μ_F, Ω_F) for backward and forward propagating waves, respectively. Comparison with the case in which $\alpha_m \neq 0$ is given in (b) for backward propagating waves and in (c) forward propagating waves.

zero modulation, the only dispersion branches having physical reality are the ones departing from the origin and associated to the 0-th order harmonic in Eq. 5.9. Also, as $\alpha_m \to 0$, the band gap closes and the dispersion branches intersect at the point corresponding to the following dimensionless wavenumber and frequency:

$$\mu_F = \pi\Big(1 + \frac{\nu_m}{\chi}\Big) \qquad\qquad \Omega_F = \frac{1}{4}\Big(1 + \frac{\nu_m}{\chi}\Big)^2 \chi. \tag{5.48}$$

in which one can define $\chi = R_g \kappa_m$. Also, one can observe that $\mu_F \to \pi$ and $\Omega_F \to \chi/4$ as $\nu_m \to 0$, hence when no temporal modulation is applied. The limits of the directional band gaps write:

$$\begin{aligned}\Omega_F^{top} = \frac{1}{2}\Bigg[\nu_m + &\frac{1}{4}\left(1 - \frac{\nu_m}{\chi}\right)^2 \chi \sqrt{1 + \frac{\alpha_m}{2}\left(\frac{1 + \frac{\nu_m}{\chi}}{1 - \frac{\nu_m}{\chi}}\right)^2} \\ &+ \frac{1}{4}\left(1 + \frac{\nu_m}{\chi}\right)^2 \chi \sqrt{1 + \frac{\alpha_m}{2}\left(\frac{1 - \frac{\nu_m}{\chi}}{1 + \frac{\nu_m}{\chi}}\right)^2}\Bigg]\end{aligned} \tag{5.49}$$

$$\begin{aligned}\Omega_F^{bot} = \frac{1}{2}\Bigg[\nu_m + &\frac{1}{4}\left(1 - \frac{\nu_m}{\chi}\right)^2 \chi \sqrt{1 - \frac{\alpha_m}{2}\left(\frac{1 + \frac{\nu_m}{\chi}}{1 - \frac{\nu_m}{\chi}}\right)^2} \\ &+ \frac{1}{4}\left(1 + \frac{\nu_m}{\chi}\right)^2 \chi \sqrt{1 - \frac{\alpha_m}{2}\left(\frac{1 - \frac{\nu_m}{\chi}}{1 + \frac{\nu_m}{\chi}}\right)^2}\Bigg]\end{aligned} \tag{5.50}$$

The radical in the previous expression can be linearized to get:

$$\Omega_{F,lin}^{top} = \frac{1}{2}\left[\nu_m + \frac{1}{2}\left(1 + \frac{\alpha_m}{4}\right)\chi\right] \tag{5.51}$$

$$\Omega_{F,lin}^{bot} = \frac{1}{2}\left[\nu_m + \frac{1}{2}\left(1 - \frac{\alpha_m}{4}\right)\chi\right] \tag{5.52}$$

in which it is assumed that $(\nu_m/\chi)^2 << 1$. The linearized expression for the band gap width writes:

$$\Delta\Omega_{F,lim} = \Omega_{F,lin}^{top} - \Omega_{F,lin}^{bot} = \frac{\alpha_m}{8}\chi \tag{5.53}$$

.

For waves traveling backward, one can show that, for the first band gap with $\alpha_m \to 0$, the modulation shifts the left edge of the FBZ leading to the following values:

$$\mu_B = -\pi\Big(1 - \frac{\nu_m}{\chi}\Big) \qquad\qquad \Omega_B = \frac{1}{4}\Big(1 - \frac{\nu_m}{\chi}\Big)^2 \chi. \tag{5.54}$$

For $\alpha_m << 1$ but different from zero, directional band gaps open and their limiting frequencies can be obtained as functions of the modulation parameters and written as follows:

$$\begin{aligned}\Omega_B^{top} = \frac{1}{2}\Bigg[-\nu_m + \frac{1}{4}\Big(1 + \frac{\nu_m}{\chi}\Big)^2 \chi \sqrt{1 + \frac{\alpha_m}{2}\Bigg(\frac{1 - \frac{\nu_m}{\chi}}{1 + \frac{\nu_m}{\chi}}\Bigg)^2} \\ + \frac{1}{4}\Big(1 - \frac{\nu_m}{\chi}\Big)^2 \chi \sqrt{1 + \frac{\alpha_m}{2}\Bigg(\frac{1 + \frac{\nu_m}{\chi}}{1 - \frac{\nu_m}{\chi}}\Bigg)^2}\Bigg]\end{aligned} \tag{5.55}$$

$$\begin{aligned}\Omega_B^{bot} = \frac{1}{2}\Bigg[-\nu_m + \frac{1}{4}\Big(1 + \frac{\nu_m}{\chi}\Big)^2 \chi \sqrt{1 - \frac{\alpha_m}{2}\Bigg(\frac{1 - \frac{\nu_m}{\chi}}{1 + \frac{\nu_m}{\chi}}\Bigg)^2} \\ + \frac{1}{4}\Big(1 - \frac{\nu_m}{\chi}\Big)^2 \chi \sqrt{1 - \frac{\alpha_m}{2}\Bigg(\frac{1 + \frac{\nu_m}{\chi}}{1 - \frac{\nu_m}{\chi}}\Bigg)^2}\Bigg]\end{aligned} \tag{5.56}$$

Linearized expressions can be obtained and write:

$$\Omega_{B,lin}^{top} = \frac{1}{2}\Bigg[-\nu_m + \frac{1}{2}\Big(1 + \frac{\alpha_m}{4}\Big)\chi\Bigg] \tag{5.57}$$

$$\Omega_{B,lin}^{bot} = \frac{1}{2}\Bigg[-\nu_m + \frac{1}{2}\Big(1 - \frac{\alpha_m}{4}\Big)\chi\Bigg] \tag{5.58}$$

therefore the band gap width has the following expression:

$$\Delta\Omega_{B,lim} = \Omega_{B,lin}^{top} - \Omega_{B,lin}^{bot} = \frac{\alpha_m}{8}\chi = \Delta\Omega_{F,lim} \tag{5.59}$$

hence also for beams in transverse motion, the directional band gaps width has the

same expression both for backward and forward propagating waves. Moreover the gap width does not depend on the modulation velocity parameter ν_m, similarly to the case of longitudinal motion. Instead, the gap width depends on the modulation amplitude α_m and on the parameter χ. One can compute the critical modulation velocity to get:

$$\nu_m^{cr} = \frac{\alpha_m}{8}\chi \tag{5.60}$$

The validity of the approximate relations discussed above is assessed by comparing the band gaps given by the full solution of the QEP with $N = 3$ and by the analytic expression valid for $\alpha_m << 1$. Results are presented in Fig.5.9 for both longitudinal and transverse motion. The gap amplitude is tracked as a function of α_m for the two cases $\nu_m = 0$ and $\nu_m \neq 0$, *i.e.* with zero and nonzero modulation velocity parameter, respectively. For $\nu_m = 0$ the system shows complete band gaps originating from the same value of frequency Ω as $\alpha_m \to 0$, thus symmetry with respect to backward and forward propagation holds. On the contrary, for $\nu_m \neq 0$ symmetry is broken, directional band gaps appear that originate from different values of frequency Ω as $\alpha_m \to 0$. The analytic formulae for the band gaps not only represent an excellent approximation for $\alpha_m << 1$, but they also appear to give accurate estimates when α_m is not small compared to unity.

5.4 Numerical resutls

Numerical simulations are performed to verify the non-reciprocal behavior of the beams when an external excitation is imposed. Specifically, the transient response of the structure to narrow-band excitation is computed, then the displacement field is analyzed. The computation are performed by using the commercial finite element code COMSOL Multiphysics. Consider a $2L$ long beam, with $L = 70\lambda_m$ and a total of 140 unit cells. In the presented model, each unit cell is discretized by 20 quadrilateral

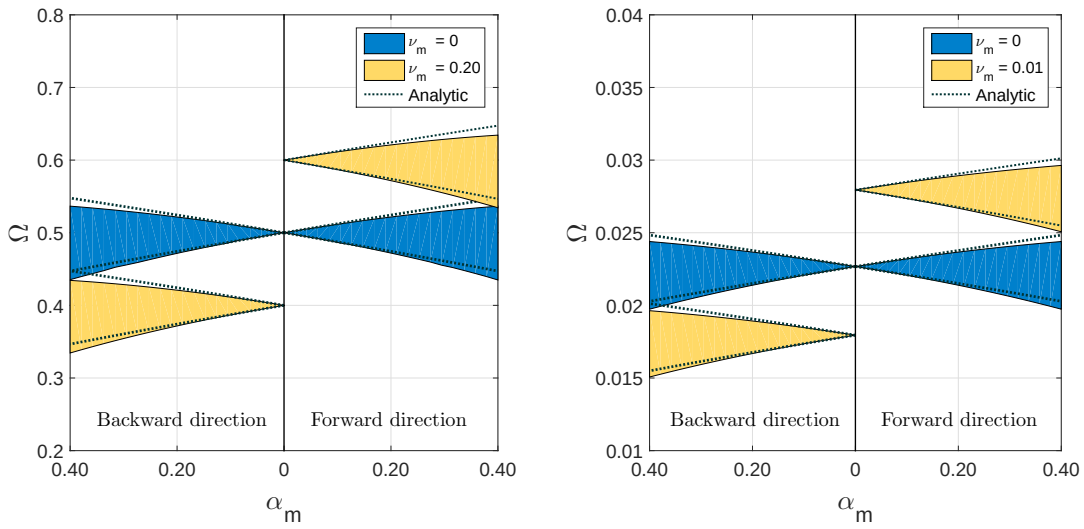

Figure 5.9: Band gap maps for beam in longitudinal (a) and transverse (b) motion. The gap amplitude is plotted as a function of the increasing modulation amplitude parameter α_m for the two cases $\nu_m = 0$ and $\nu_m \neq 0$, *i.e.* with zero and nonzero modulation velocity parameter, respectively. The colored regions represent the band gap evolution as computed solving the full QEP, while the approximate analytic expression, valid for $\alpha_m << 1$, are represented by the dashed lines.

elements, therefore 2800 elements for the whole structure are considered. In this section $\chi = 0.0144$ is assumed. The excitation is imposed halfway through the length of the structures at $x = 0$ as a point load, so that both backward and forward propagating waves are excited. The load acts along the x direction when longitudinal motion is targeted, while it acts normally to the x direction for transverse motion. The dimensionless time τ is introduced as:

$$\tau = \frac{c_0 t}{\lambda_m} \tag{5.61}$$

which represents the number of unit cells of length λ_m that a longitudinal wave, traveling at the speed c_0 in a uniform beam, covers in the time t. Results are presented in Fig. 5.11 and Fig. 5.12 in the form of waterfall plots, that allow us to track how the waves propagate throughout the system. A non-modulated beam, in which $\alpha_m = 0$,

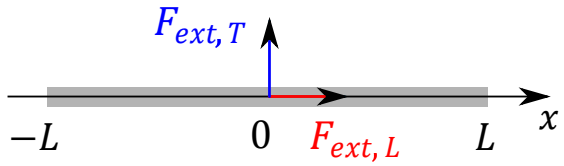

Figure 5.10: Schematic of a $2L$ long beam loaded in its mid span. Longitudinal and transverse motion are excited by the horizontal force $F_{ext,L}$ and the transverse force $F_{ext,T}$, respectively.

$\nu_m = 0$ are considered, is compared with a spatio-temporal modulated beam with $\alpha_m = 0.40$ and $\nu_m = 0.20$ for longitudinal motion and with $\alpha_m = 0.40$ and $\nu_m = 0.01$ for transverse motion. The results can be better interpreted when compared to the band diagrams of the corresponding system in Fig. 5.4a and Fig. 5.5a for the non-modulated beam and Fig. 5.4d and Fig. 5.5d for the modulated beams, respectively. When no modulation is applied, the system is perfectly reciprocal and waves propagate symmetrically in the backward and forward directions, as shown in Fig. 5.11a and Fig. 5.12a, with excitation centered at $\Omega = 0.485$ and $\Omega = 0.0225$ for longitudinal and transverse motion, respectively. When the same excitation is applied but the properties of the beam are modulated, the systems still behaves in a reciprocal fashion since the excitation is centered in a pass band, as shown in band diagram in Fig. 5.4d. The waterfall plots for this case are shown in Fig. 5.11b and Fig. 5.12b for longitudinal and transverse motion, respectively. Conversely, strong one-directional wave propagation is achieved when the excitation is centered in a directional band gap. Forward-only propagation is recognized in Fig. 5.11c and Fig. 5.12c, being the modulated structure excited with a narrow band signal centered at $\Omega = 0.3844$ and $\Omega = 0.0175$, for longitudinal and transverse motion, respectively. Instead, backward-only propagation can be observed in Fig. 5.11d and Fig. 5.12d for longitudinal and transverse motion when the excitation is centered at $\Omega = 0.5844$ and $\Omega = 0.0275$, respectively.

Another numerical approach to characterize the dispersion properties of a beam

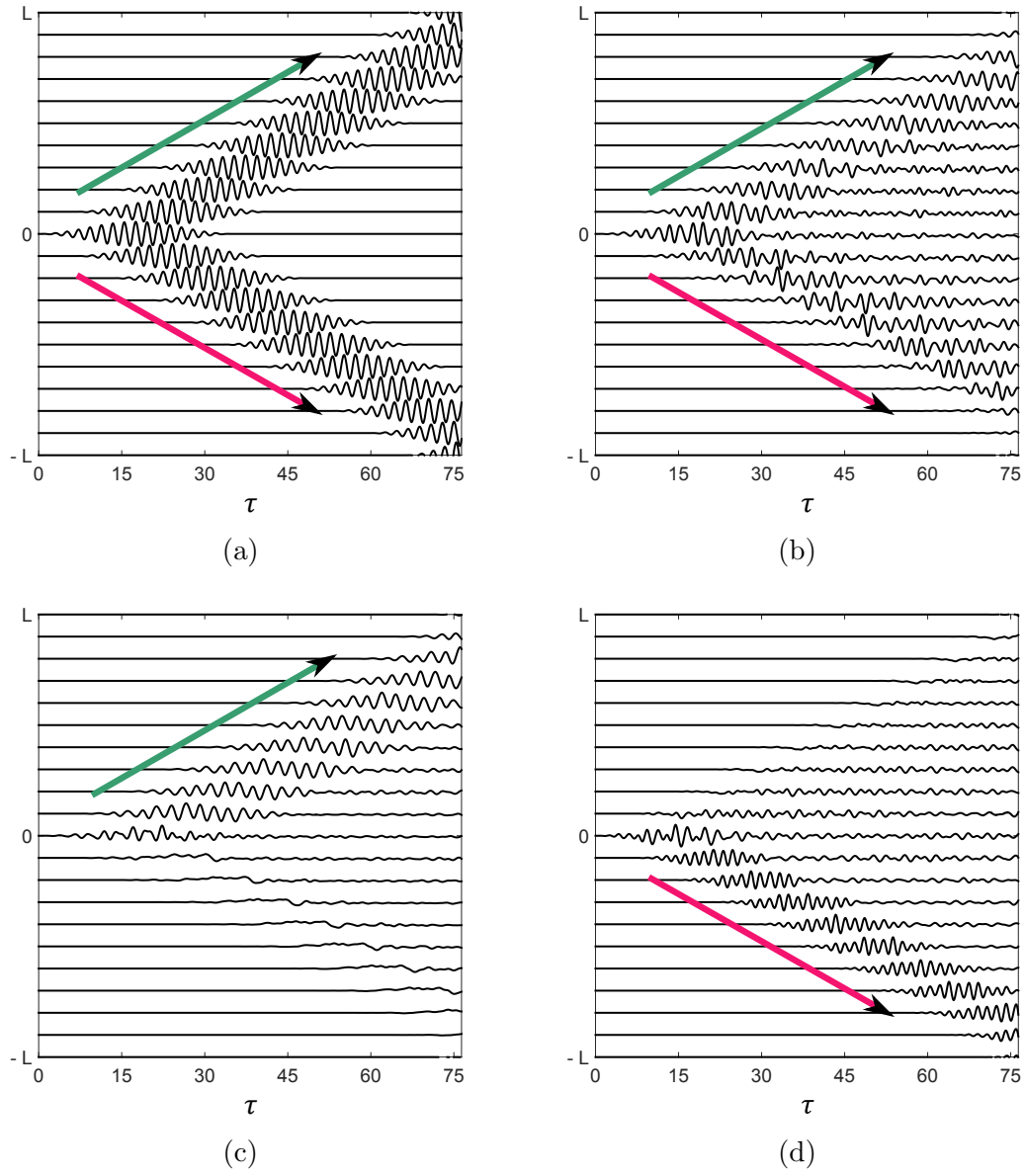

Figure 5.11: Waterfall plots representing the transient response of a $2L$ long beam in longitudinal motion to narrow band external excitation loaded at its mid span. In (a), both forward and backward waves in a non-modulated beam are excited around $\Omega_{ext} = 0.485$; in (b), modulation is imposed with $\alpha_m = 0.40$ and $\nu_m = 0.20$ and same excitation, waves in both directions propagate; in (c), the same modulated beam is excited in a directional band gap at frequency centered at $\Omega_{ext} = 0.3844$, thus forward-propagating waves only propagate; in (d), with excitation centered at $\Omega_{ext} = 0.5844$, backward-propagating waves only are allowed.

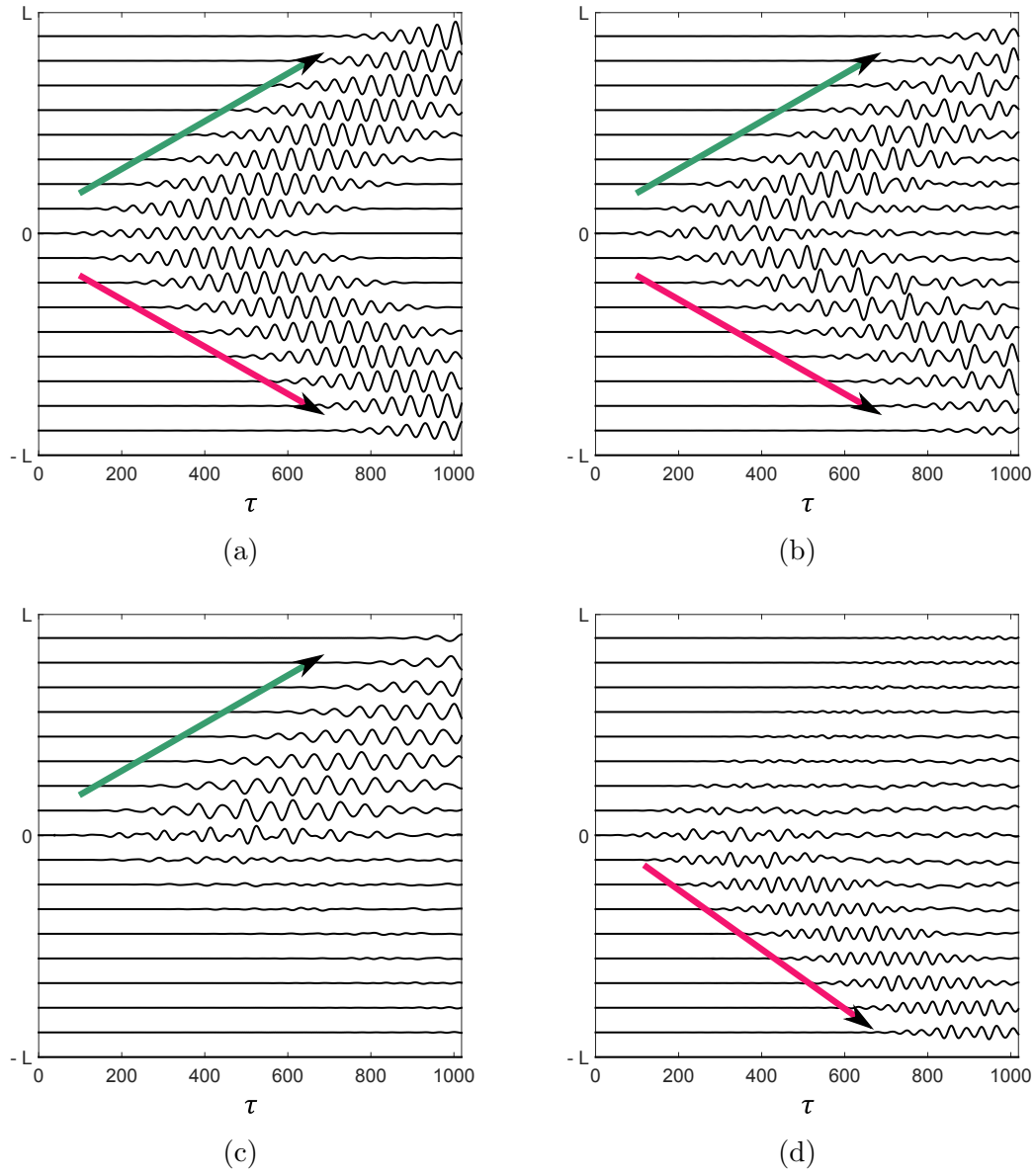

Figure 5.12: Waterfall plots representing the transient response of a $2L$ long beam in transverse motion to narrow band external excitation loaded at its mid span, with $\chi = 0.0144$. In (a) wave excited at $\Omega_{ext} = 0.0225$ propagate in both directions, as no modulation is applied; in (b), the same excitation is applied to a modulated beam with $\alpha_m = 0.40$ and $\nu_m = 0.01$, but waves still propagation in both directions; in (c), the same modulated beam is excited with frequency centered at $\Omega_{ext} = 0.0175$, which falls within a directional band gap, thus forward-propagation only is allowed; in (d), for $\Omega_{ext} = 0.0275$, backward-propagation only is allowed.

consists in exciting the structure and computing the two-dimensional Fourier transform (2DFT) of the recorded displacement fields $u(x,t)$ and $w(x,t)$:

$$U(\kappa,\omega) = \int_{-\infty}^{\infty}\int_{-\infty}^{\infty} u(x,t)e^{-i(\omega t-\kappa x)}dx\,dt \tag{5.62}$$

$$W(\kappa,\omega) = \int_{-\infty}^{\infty}\int_{-\infty}^{\infty} w(x,t)e^{-i(\omega t-\kappa x)}dx\,dt \tag{5.63}$$

The transformation allows one to describe the response of the beam in the wavenumber/frequency domain, effectively obtaining a band diagram for the structure. This technique is successfully applied in experimental validations as well [112]. The band diagrams given by plotting the magnitude $|U(\kappa,\omega)|$ and $|W(\kappa,\omega)|$ of the complex quantities defined by Eq. 5.62 and 5.63, in the form of contour lines, are compared with the band diagrams that are given by the method discussed in the previous sections.

The results are presented in Fig. 5.13b and Fig. 5.13c for longitudinal motion of respectively a uniform and modulated beam with $\alpha_m = 0.40$ and $\nu_m = 0.20$. Similarly, Fig. 5.14b and Fig. 5.14c show the results for transverse motion of a uniform and modulated beam with $\alpha_m = 0.40$ and $\nu_m = 0.005$, respectively. When longitudinal waves are concerned, the structure is excited with a load characterized by a broadband signal centered at $\Omega = 0.485$ and acting along the x direction as shown in Fig. 5.13a, while for transverse waves a vertical load centered at $\Omega = 0.0225$ is used. The broadband signal is now required in order to excite the structure within the frequency range of interest, which in this case has to be wide enough to obtain the band diagram. The contour lines used to plot both $|U(\kappa,\omega)|$ and $|W(\kappa,\omega)|$ overlap with the dispersion branches given by the proposed method, thus verifying the validity of the methodology for the calculation of the dispersion diagrams of spatio-temporal structures. For comparison, Fig. 5.13 and 5.14 show also the case in which the modulation is spatial only, hence for $\nu_m = 0$.

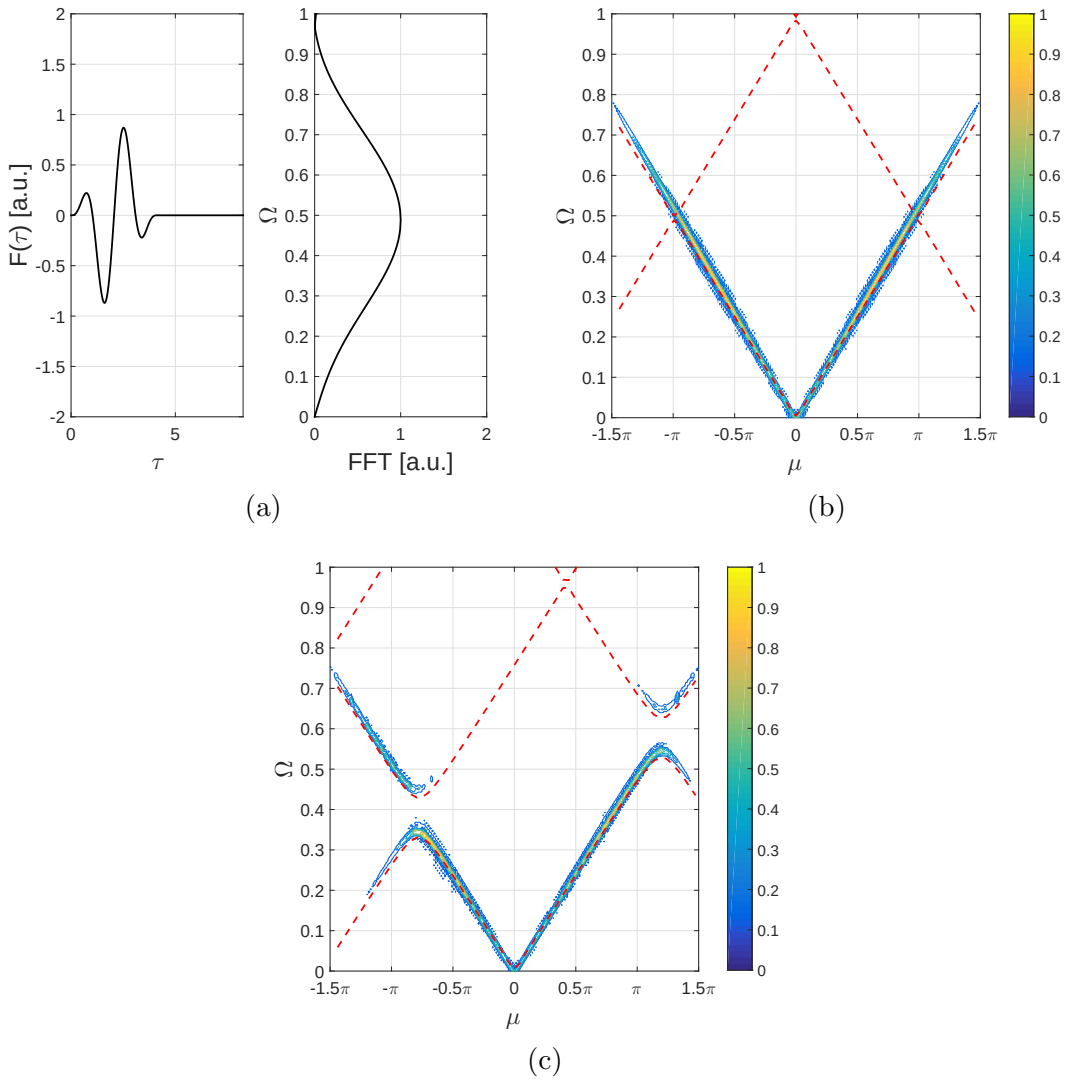

Figure 5.13: For longitudinal motion of $2L$ long beam excited at its mid span, comparison between the band diagram obtained solving the QEP (dashed lines) and through the normalized magnitude $|U(\kappa,\omega)|$ of the 2DFT of the displacement field (contour lines): (a) excitation signal and its frequency spectrum; (b) band diagram for uniform beam ($\alpha_m = 0$ and $\nu_m = 0$); (c) band diagram for modulated beam ($\alpha_m = 0.40$ and $\nu_m = 0.20$).

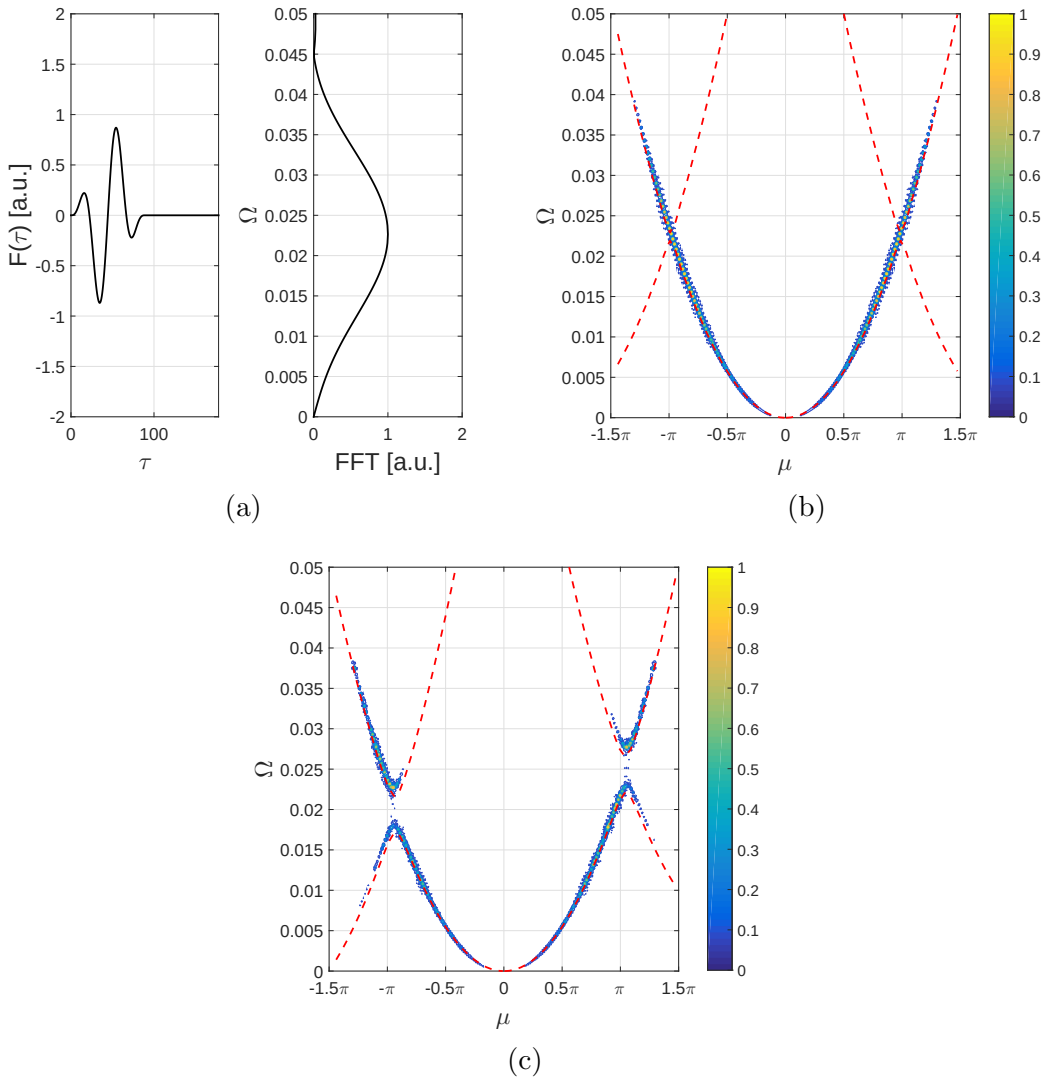

Figure 5.14: For transverse motion of $2L$ long beam excited at its mid span, comparison between the band diagram obtained solving the QEP (dashed lines) and through the normalized magnitude $|W(\kappa, \omega)|$ of the 2DFT of the displacement field (contour lines): (a) excitation signal and its frequency spectrum; (b) band diagram for uniform beam ($\alpha_m = 0$ and $\nu_m = 0$); (c) band diagram for modulated beam ($\alpha_m = 0.40$ and $\nu_m = 0.005$).

5.5 Conclusions

In summary, the dispersion properties of spatio-temporal periodic beams in longitudinal and transverse motion are characterized. By employing a solution in the Floquet form with space and time harmonics, it is shown how to compute the dispersion diagrams for such structures by solving a quadratic eigenvalue problem. The analysis of the dispersion diagrams, limited by the 1D beam modeling assumptions to the low-frequency range, allows to describe the unique features that spatio-temporal modulation induces on the wave propagation properties of the structure, such as symmetry breaking of the dispersion relation and the relative dispersion diagrams. Specifically, the signature of one-way propagation is identified as directional band gaps. Such band gaps clearly describe in which frequency ranges forward-propagating or backward-propagating waves only are supported by the structure. The key finding of the chapter is the analytical relation between the modulation parameters and the position and width of the directional band diagrams, which allows to compute the minimum modulation speed required in order to have a fully non-reciprocal wave propagation for harmonic modulation. Finally, the theoretical predictions are verified with numerical simulations.

Nonreciprocal systems are the object of an emerging field of study and promise to deeply impact the way once can control wave propagation, enriching the design space for technological applications in acoustics, phononics and photonics, to name a few. For this reason, when spatio-temporal periodic structures are used to achieve one-way prorogation, is it important to be able to properly describe and characterize their non-reciprocal behavior, correctly predicting the influence of the modulation parameters. The proposed methodology was exposed in the context of elastic waves propagating in an elastic solid, but it could be applied to other one-dimensional wave propagation problems with a similar mathematical structure and involving a periodic

variation of the medium characteristics in both space and time. Further investigation should be devoted in understanding the role of frequency conversion phenomena in spatio-temporal modulated structures in relation to their use in manipulating and controlling elastic waves, similarly to what has been done in the study of traveling-wave parametric circuits and parametric amplification of electromagnetic waves, possible applications being one-directional vibration insulators or directional spatial filters.

Another major challenge is the practical implementation of time-modulated mechanical systems. This aspect of the problem will be considered in chapter 7.

CHAPTER 6

SPATIO-TEMPORAL PERIODIC STRUCTURES: DISCRETE CASE

6.1 Overview

In this chapter, the analysis the dispersion properties of spatio-temporal periodic structures, presented for continuous systems in the previous chapter, is extended to discrete systems. Most of the studies that investigate wave phenomena in discrete time-dependent structures rely on numerical simulations [69], which are time consuming, particularly for higher dimensional structures and are not convenient for design and optimization studies. A systematic procedure for obtaining dispersion information of lattices with periodic time-varying properties is therefore of interest for design and analysis of time-varying systems. In this chapter, a technique for obtaining the dispersion diagrams of discretized linear elastic media with space-time stiffness variability is presented. The method consists of four steps: the appropriate selection of an extended unit cell, a suitable choice of the solution ansatz, the application of Bloch wave analysis and filtering of the obtained eigen-solutions to identify the frequencies associated with the fundamental plane wave solution. The developed procedure for computing the dispersion diagram for spring-mass chains with periodic time varying stiffness is first introduced. Then, its implementation is illustrates by analyzing three distinct systems, and the results are validated with numerical solutions. It is shown how the dispersion diagrams predict the broken time-reversal behavior of infinite and finite time-varying systems. Final remarks close the chapter.

6.2 Theoretical background

6.2.1 Time varying periodic lattice configuration

A one-dimensional (1D) structure characterized by periodically modulated properties is considered. The structure is governed by linear interactions, defined by stiffness coefficients that vary in time, and by constant inertia coefficients. The stiffness modulation is expressed as a traveling wave propagating with velocity $v_m = \lambda_m/T_m$, where λ_m and T_m respectively denote the spatial wavelength and temporal period of the modulation. Thus, at any given instant of time, it is possible to describe the structure as the assembly of unit cells that are identified by one spatial modulation period λ_m. Based on this description, and the assumption that the structure has been discretized through a Finite Element procedure, one can express the generalized equation of motion for the n-th cell of the assembly as

$$\mathbf{M}\ddot{\mathbf{u}}_n + \mathbf{K}^{(l)}(t)\mathbf{u}_{n-1} + \mathbf{K}(t)\mathbf{u}_n + \mathbf{K}^{(r)}(t)\mathbf{u}_{n+1} = \mathbf{0}. \tag{6.1}$$

where $\mathbf{M}, \mathbf{K}$ and $\mathbf{u}_n$ denote the mass, stiffness matrices and a vector of degrees of freedom of the unit cell n, while $\mathbf{K}^{(l)}, \mathbf{K}^{(r)}$ describe the interactions of this unit cell with its neighboring unit cells. For simplicity of notation, but without loss of generality, it is assumed that the mass is lumped so that there is no inertial coupling across the cells.

The stiffness matrices are all expressed as a periodic functions of time with period T_m so that the following relation holds

$$\mathbf{K}(t) = \mathbf{K}(t + T_m). \tag{6.2}$$

Accordingly, each of the matrices in Eq. (6.1) can be expanded in terms of their

Fourier series and expressed as

$$\mathbf{K}^{(l)}(t) = \sum_{q=-\infty}^{\infty} \mathrm{e}^{\mathrm{i}q\omega_m t}\mathbf{K}_q^{(l)}, \tag{6.3a}$$

$$\mathbf{K}(t) = \sum_{q=-\infty}^{\infty} \mathrm{e}^{\mathrm{i}q\omega_m t}\mathbf{K}_q, \tag{6.3b}$$

$$\mathbf{K}^{(r)}(t) = \sum_{q=-\infty}^{\infty} \mathrm{e}^{\mathrm{i}q\omega_m t}\mathbf{K}_q^{(r)} \tag{6.3c}$$

where $\mathbf{K}_q$, $\mathbf{K}_q^{(l)}$ and $\mathbf{K}_q^{(r)}$ are the corresponding matrix coefficients and $\omega_m = 2\pi/T_m$ is the frequency associated with the temporal modulation.

6.2.2 Spatio-temporal plane wave expansion for the estimation of dispersion

The dispersion relations for the considered time-varying structure can be estimated, following the Hill-determinant method [113], by seeking for a plane wave solution with modulated amplitude, which is expressed as

$$\mathbf{u}_n(t) = \mathbf{a}(t)\mathrm{e}^{\mathrm{i}(n\kappa\lambda_m+\omega t)}, \tag{6.4}$$

where κ is the wavenumber and $\mathbf{a}(t) = \mathbf{a}(t+T_m)$ is a periodic amplitude function in time. The frequencies in the displacement amplitude $\mathbf{a}(t)$ depend on the stiffness modulation frequency $\omega_m = 2\pi/T_m$ and it can be expressed as a Fourier series in the form

$$\mathbf{a}(t) = \sum_{p=-\infty}^{\infty} \mathbf{a}_p \mathrm{e}^{\mathrm{i}p\omega_m t}. \tag{6.5}$$

Based on the solution form expressed by Eq. (6.4), the following relations hold

$$\mathbf{u}_{n-1}(t) = \mathrm{e}^{-\mathrm{i}\mu}\mathbf{u}_n(t), \qquad \mathbf{u}_{n+1}(t) = \mathrm{e}^{\mathrm{i}\mu}\mathbf{u}_n(t), \tag{6.6}$$

where $\mu = \kappa\lambda_m$ is the non-dimensional wavenumber. Substituting into Eq. (6.1) gives

$$\mathbf{M}\ddot{\mathbf{u}}_n(t) + \left(\mathbf{K}^{(l)}(t)\mathrm{e}^{-\mathrm{i}\mu} + \mathbf{K}(t) + \mathbf{K}^{(r)}(t)\mathrm{e}^{\mathrm{i}\mu}\right)\mathbf{u}_n(t) = \mathbf{0},$$

which may be written as

$$\mathbf{M}\ddot{\mathbf{u}}_n(t) + \hat{\mathbf{K}}(\mu, t)\mathbf{u}_n(t) = \mathbf{0}. \tag{6.7}$$

with

$$\hat{\mathbf{K}}(\mu, t) = \mathbf{K}^{(l)}(t)\mathrm{e}^{-\mathrm{i}\mu} + \mathbf{K}(t) + \mathbf{K}^{(r)}(t)\mathrm{e}^{\mathrm{i}\mu}. \tag{6.8}$$

Next, substituting Eq. (6.5) into Eq. (6.7) and performing harmonic balance, by collecting the terms with frequency $\omega + p\omega_m$ one obtains

$$-(\omega + p\omega_m)^2\mathbf{M}\mathbf{a}_p + \sum_{q=-\infty}^{\infty}\hat{\mathbf{K}}_q(\mu)\mathbf{a}_{p-q} = \mathbf{0}, \qquad \forall p. \tag{6.9}$$

Choosing a truncation order P for the displacement amplitude $\mathbf{a}(t)$, i.e., $\mathbf{a}_p = \mathbf{0}$ for $|p| \leq P$, Eq. (6.9) reduces to a system of $(2P+1)R$ equations, with R being the number of degrees of freedom in a unit cell. This system of equations defines a quadratic eigenvalue problem that can be solved in terms of frequency ω for assigned values of μ. Specifically, μ spans the reciprocal lattice space, limited to $\mu \in [-\pi, \ +\pi]$ which defines the First Brillouin zone. It is here considered instructive to analyze the structure of the infinite eigenvalue problem in Eq. (6.9). By doing a change of variable $p \to \hat{p} + s$, the resulting expression may be written as $-((\omega + s\omega_m) + \hat{p}\omega_m)^2\mathbf{M}\hat{\mathbf{a}}_{\hat{p}} + \sum_{q=-\infty}^{\infty}\hat{\mathbf{K}}_q(\mu)\hat{\mathbf{a}}_{\hat{p}-q} = \mathbf{0}$, where $\hat{\mathbf{a}}_{\hat{p}} = \mathbf{a}_p$. Comparing it with Eq. (6.9), it can be observed that if $(\omega, \mathbf{a}_p)$ is an eigensolution of the infinite dimensional eigenvalue problem, then $(\omega + s\omega_m, \mathbf{a}_{p+s})$ is also a solution.

The solution of the following quadratic eigenvalue problem with truncated terms

$$-(\omega + p\omega_m)^2 \mathbf{M}\mathbf{a}_p + \sum_{q=-P+p}^{P+p} \hat{\mathbf{K}}_q(\mu)\mathbf{a}_{p-q} = \mathbf{0}.$$

thus leads to $R \times (2P+1)$ eigenvalues that are of the general form

$$\lambda_{r,p} = \omega_r + p\omega_m \tag{6.10}$$

with $r = 1, .., R$ and $p = -P, ..., +P$. The associated eigenvectors $\boldsymbol{\alpha}_{r,p}$ can be expressed as

$$\boldsymbol{\alpha}_{r,p} = [\mathbf{a}_{-P}^{(p)}, ... \, , \mathbf{a}_0^{(p)}, \ ..., \mathbf{a}_{+P}^{(p)}]_r^T.$$

Equation (6.10) shows how the eigenvalues are clustered into R groups of $2P+1$ values centered at frequencies ω_r and separated by integer multiples of the modulation frequency ω_m. Thus, the solution approach introduces the challenge of identifying the R dispersion branches associated with the sought plane wave solution from the $R(2P+1)$ frequencies obtained from the eigenvalue problem. This challenge is here addressed through a procedure that identifies the plane wave branches based on a weighting factor corresponding to the magnitude of the eigenvector components associated with the fundamental plane wave term.

To illustrate the rationale of this weighting procedure, the plane wave solution imposed in Eqs. (6.4) and (6.5) is considered. The r-th family of solutions ($2P+1$ solutions) associated with this plane wave may be expressed as

$$\mathbf{u}_n^{(r)}(t) = \mathrm{e}^{\mathrm{i}n\mu} \sum_{p=-P}^{+P} \left(\sum_{q=-P}^{+P} \mathbf{a}_q^{(p)}|_r \mathrm{e}^{\mathrm{i}(\omega_r + q\omega_m)t} \right) \mathrm{e}^{\mathrm{i}p\omega_m t} \tag{6.11}$$

where $a_q^{(p)}|_r$ is the q part of eigenvector $\boldsymbol{\alpha}_{r,p}$. Last equation can be re-organized to

read

$$\mathbf{u}_n^{(r)}(t) = \mathrm{e}^{\mathrm{i}(n\mu+\omega_r t)} \sum_{p=-P}^{+P} \left(\sum_{q=-P}^{+P} \mathbf{a}_q^{(p)}|_r \mathrm{e}^{\mathrm{i}(p+q)\omega_m t} \right) \tag{6.12}$$

Thus, the fundamental plane wave term has a magnitude that is identified for $p+q = 0$. It is reasonable to expect that such fundamental is the leading term in the expansion such that

$$\mathbf{u}_n^{(r)}(t) \approx \mathrm{e}^{\mathrm{i}(n\mu+\omega_r t)} \sum_{p=-P}^{+P} \left(\sum_{q=-P}^{+P} \mathbf{a}_q^{(p)}|_r \delta_{p+q,0} \right) \tag{6.13}$$

where $\delta_{p+q,0}$ is the Kronecker delta, i.e. $\delta_{i,j} = 1$ if $i = j$, or $\delta_{i,j} = 0$ if $i \neq j$. According to the above equation, the dispersion branch corresponding to the fundamental plane wave can be effectively obtained weighting each branch by the magnitude of the fundamental component and applying a thresholding value which filters the branches, thereby avoiding their plotting if the associated eigenvector magnitude is low compared to that of the fundamental. The effectiveness of this procedure in tracking the branch corresponding to the plane wave of interest is illustrated through the examples presented in the next section.

6.2.3 Spectral energy density method

The spectral energy density method, oftern used for obtaining the dispersion diagrams in time-periodic systems [114], is now briefly described. as used by other studies. In this method, displacements are obtained by numerical integration. Full numerical simulations of the system velocity field under a range of excitation frequencies are needed, and the results are used to construct the dispersion diagrams.

Consider a finite lattice having R degrees of freedom per unit cell and a total length of N unit cells, i.e. a total of RxN degrees of freedom. For the algorithm, first the velocity field of each simulation $\dot{\mathbf{u}}(n,t)$ is projected into the orthogonal Fourier basis $\mathrm{e}^{\mathrm{i}(\mu n-\omega t)}$

$$\dot{\mathbf{u}}(n,t) = \sum_{\omega} \sum_{\mu} \mathbf{c}^{(\omega,\mu)} \mathrm{e}^{\mathrm{i}(\mu n-\omega t)}. \tag{6.14}$$

$$\mathbf{c}^{(\omega,\mu)} = \left\langle \dot{\mathbf{u}}(n,t), \mathrm{e}^{\mathrm{i}(\mu n - \omega t)} \right\rangle = \frac{1}{TN} \int_0^T \sum_{n=1}^{N} \dot{\mathbf{u}}(n,t) \mathrm{e}^{\mathrm{i}(\mu n - \omega t)} dt. \tag{6.15}$$

where T is the total integration time. The spectral energy density is a measure of the energy content of the each plane wave with specific frequency ω and wavenumber μ, by considering the kinetic energy of the masses, $(1/2)m\|\mathbf{c}^{(\omega,\mu)}\|^2$. Given Eq. (6.14), the SED $\Phi(\omega,\mu)$ is obtained as

$$\Phi(\omega,\mu) = \sum_{r=1}^{R} \frac{1}{2} m \left(c_r^{(\omega,\mu)}\right)^2 = \frac{m}{2(TN)^2} \sum_{r=1}^{R} \left| \int_0^T \sum_{n=1}^{N} \dot{u}_r(n,t) \mathrm{e}^{\mathrm{i}(\mu n - \omega t)} dt \right|^2 \tag{6.16}$$

where r is the position of the particle within the unit cell. Time integration is performed numerically using the trapezoidal rule

$$\Phi(\omega,\mu) = \frac{m}{2(TN)^2} \sum_{r=1}^{R} \left| \Delta t \sum_{j=0}^{T/\Delta t} \sum_{n=1}^{N} \dot{u}_r(n, j\Delta t) \mathrm{e}^{\mathrm{i}(\mu n - \omega j \Delta t)} \right|^2 \tag{6.17}$$

where Δt is the grid spacing of the numerical integration.

Last, Eq. (6.17) is evaluated for each (ω,κ) pair and the result is a contour plot. The dispersion diagrams are given by the high contour values of Φ, indicating the allowance of plane waves with that specified frequency/wavenumber pair.

6.3 Dispersion analysis of spring-mass lattices

The procedure explained in Section 6.2 is illustrated for the case of the spring-mass lattice shown in Fig. 6.1. The masses of the lattice are considered constant in time, and are all equal to m. The masses are connected to their adjacent neighbors by springs of time-modulated constant $k_r(t) = k_0 + k_m \Gamma_r(t)$, and to the ground by springs that may be also time-modulated, *i.e.* $k_{g,r}(t) = k_{g_0} + k_{g_m} \Gamma_{g,r}(t)$. According to the derivations in the previous section, the procedure considers periodic time modulations, so that the two functions $\Gamma(t), \Gamma_m(t)$ are both periodic of period T_m, *i.e.* $\Gamma_r(t) =$

$\Gamma_r(t+T_m), \Gamma_{g,r}(t) = \Gamma_{g,r}(t+T_m)$.

The equation of motion for the r-th mass is

$$m\ddot{u}_r + k_{r-1}(t)(u_r - u_{r-1}) + k_r(t)(u_r - u_{r+1}) + k_{g,r}(t)u_r = 0. \tag{6.18}$$

A characteristic frequency $\omega_0^2 = k_0/m$ is introduced, so that Eq. (6.18) can be rewritten in non-dimensional form as follows

$$\ddot{u}_r + \omega_0^2(1+\beta_m\Gamma_{r-1}(t))(u_r - u_{r-1}) + \omega_0^2(1+\beta_m\Gamma_r(t))(u_r - u_{r+1}) + \omega_0^2\gamma_g(1+\beta_{g,m}\Gamma_{g,r}(t))u_r = 0. \tag{6.19}$$

where

$$\beta_m = \frac{k_m}{k_0},\ \beta_{g,m} = \frac{k_{g,m}}{k_g},\ \gamma_g = \frac{k_g}{k_0}$$

Note that the above expression corresponds to a system of Mathieu-Hill equations, whose stability with respect to the modulation parameters has been extensively investigated [113]. The method presented here applies when the parameters lie in the stable regions. In the presented examples, the modulation properties are small compared to the constant order terms and it can be assumed that solutions lie within the stable regions.

Three examples of stiffness modulated systems are studied. In the first two examples, the dispersion of one-dimensional lattices having a harmonic modulation of their properties in space and time is analyzed. In the last example, a spring-mass chain with a traveling square-wave modulation is studied, thereby demonstrating the applicability of the method when there are multiple modulation frequencies.

6.3.1 Harmonic stiffness modulation

A first example considers a stiffness modulation that is imposed along the length of the chain with spatial wavelength $\lambda_m = Ra$, where a is the distance between

neighboring masses, while R denotes the number of masses in a spatial modulation wavelength λ_m. Figure 6.1 displays a schematic of the chain along with the spring stiffness modulation.

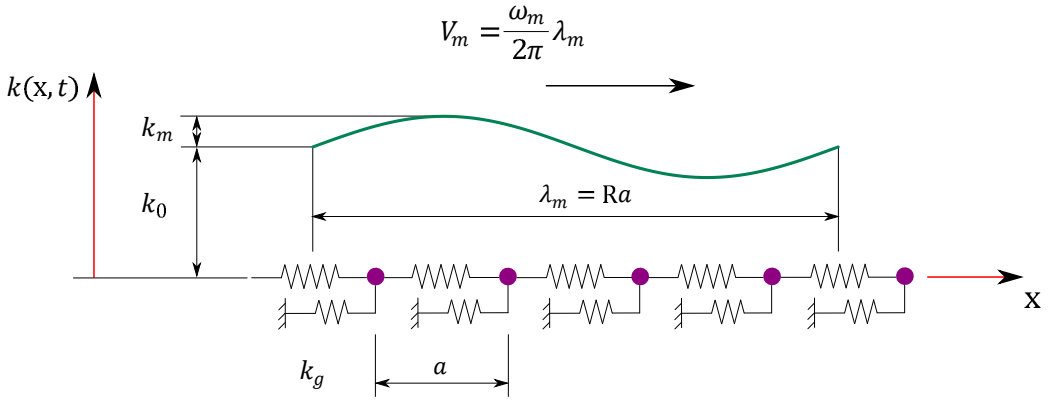

Figure 6.1: Schematic of a chain of resonators with harmonic modulation of the first-neighbor interaction springs. The modulation pattern travels with velocity $V_m = \omega_m \lambda_m / 2\pi$.

Consider a periodic modulation of the springs between adjacent masses, so that the stiffness of the r-th spring is

$$k_r(t) = k_0(1 + \beta_m \cos(\omega_m t + \phi_r)), \tag{6.20}$$

where $\phi_r = 2\pi r/R$ is the spatial phase shift related to the position r of the considered spring. Also, the ground stiffnesses are considered constant in time, therefore in Eq. (6.19) $\beta_{g,m} = 0$. A unit cell is identified that contains R degrees of freedom, whose behavior is governed by a system of equations of the kind of Eq. (6.1), subsequently transformed into Eq. (6.9), with $\mathbf{M} = \mathbf{I}$, where $\mathbf{I} \in \mathbb{R}^{R\times R}$ is the identity matrix, while

$$\hat{\mathbf{K}}_q(\mu) = \gamma_g\omega_0^2\mathbf{I}\delta_{q,0} + \omega_0^2 \begin{bmatrix} 2 & -1 & 0 & 0 & \dots & -\mathrm{e}^{-\mathrm{i}\mu} \\ -1 & 2 & -1 & 0 & \dots & 0 \\ 0 & -1 & 2 & -1 & \dots & 0 \\ \vdots & \vdots & \vdots & \vdots & \ddots & \vdots \\ -\mathrm{e}^{\mathrm{i}\mu} & 0 & 0 & 0 & \dots & 2 \end{bmatrix} \delta_{q,0}$$
$$+\omega_0^2\frac{\beta_m}{2} \begin{bmatrix} \mathrm{e}^{\mathrm{i}q\phi_R} + \mathrm{e}^{\mathrm{i}q\phi_1} & -\mathrm{e}^{\mathrm{i}q\phi_1} & 0 & \dots & -\mathrm{e}^{-\mathrm{i}q\phi_R}\mathrm{e}^{-\mathrm{i}\mu} \\ -\mathrm{e}^{\mathrm{i}q\phi_1} & \mathrm{e}^{\mathrm{i}q\phi_1} + \mathrm{e}^{\mathrm{i}q\phi_2} & -\mathrm{e}^{\mathrm{i}q\phi_2} & \dots & 0 \\ 0 & -\mathrm{e}^{\mathrm{i}q\phi_2} & \mathrm{e}^{\mathrm{i}q\phi_2} + \mathrm{e}^{\mathrm{i}q\phi_3} & \dots & 0 \\ \vdots & \vdots & \vdots & \ddots & \vdots \\ -\mathrm{e}^{-\mathrm{i}q\phi_R}\mathrm{e}^{\mathrm{i}\mu} & 0 & 0 & \dots & \mathrm{e}^{\mathrm{i}q\phi_{R-1}} + \mathrm{e}^{\mathrm{i}q\phi_R} \end{bmatrix} \delta_{q,\pm1} \tag{6.21}$$

A chain with modulation wavelength $\lambda_m = 3a$ ($R = 3$ masses in each unit cell) is considered, and its dispersion properties estimated from the solution of Eq. (6.9). Given the considered form of modulation, which is harmonic, the solution is conducted by considering $P = 1$ terms, which is found to lead to results that are in agreement with those estimated through numerical simulations and for higher order expansions. Results are presented for the following set of parameters $\Omega_m = \omega_m/\omega_0 = 0.2$, $\beta_m = 0.15$, $\gamma_g = 1$.

The solution is conducted by imposing $\mu \in [-\pi,\ \pi]$ which provides $R\times(2P+1) = 9$ frequency branches. These branches are plotted in terms of the non-dimensional frequency $\Omega = \omega/\omega_0$ in Fig. 6.2a. Figure 6.2a displays 3 families of curves that appear parallel and separated by Ω_m. These branches cross for certain wavenumber values and fold at the boundaries of the first Brillouin zone. The dispersion diagram corresponds to the branch associated with the fundamental plane wave component among the 3 families of curves. To identify this branch, the filtering method described

in the last paragraph of section 6.2.2 is applied, whereby the plotting of each curve is based on a weighting parameter defined by the amplitude of the eigenvector parts corresponding to the fundamental frequency Ω and a thresholding procedure. The result of this process is shown in Fig. 6.2b, which shows only the single fundamental branch. As expected the lattice is characterized by a high-pass cut-off at $\Omega = 1$ for $\mu = 0$ which is defined by the ground spring stiffness, and by a low-pass cut off for $\mu = \pm\pi$. Of significance is the asymmetry about the $\mu = 0$ axis, which is generated by the modulation. This leads to asymmetric band gaps seen in Fig. 6.2b, which result in the ability of the lattice to support one directional wave motion. For frequencies within one of these band gaps, frequency is only defined for either a positive or negative wavenumber value which corresponds to waves propagating in the forward or backward direction only. For example, for $\Omega \in [2.05, 2.15]$ the band diagram displays only a branch with negative slope, i.e., negative group velocity and thus excitation of the lattice within this frequency range will result in a wave propagating only in the $-x$ direction. Thus, lattices with periodic time-varying properties are characterized by non-reciprocal behavior for frequencies belonging to non-symmetric bandgaps.

The dispersion curves obtained using our Bloch based procedure are compared with the dispersion data extracted from explicit numerical simulations using the SED method. The SED results are obtained by computing the transient response of the system to harmonic excitation at frequency Ω, which is imposed as a prescribed displacement on one of the masses. The dispersion diagram is obtained through the excitation over a range of frequencies with each frequency excited individually. The velocity field obtained in each simulation is then used to compute the spectral energy density $\Phi(\Omega, \mu)$, which is shown as a contour plot to trace the dispersion diagram. The reported calculation considered a closed system consisting of 70 unit cells, whereby Born-Karman boundary conditions are enforced to avoid edge reflections [115]. The

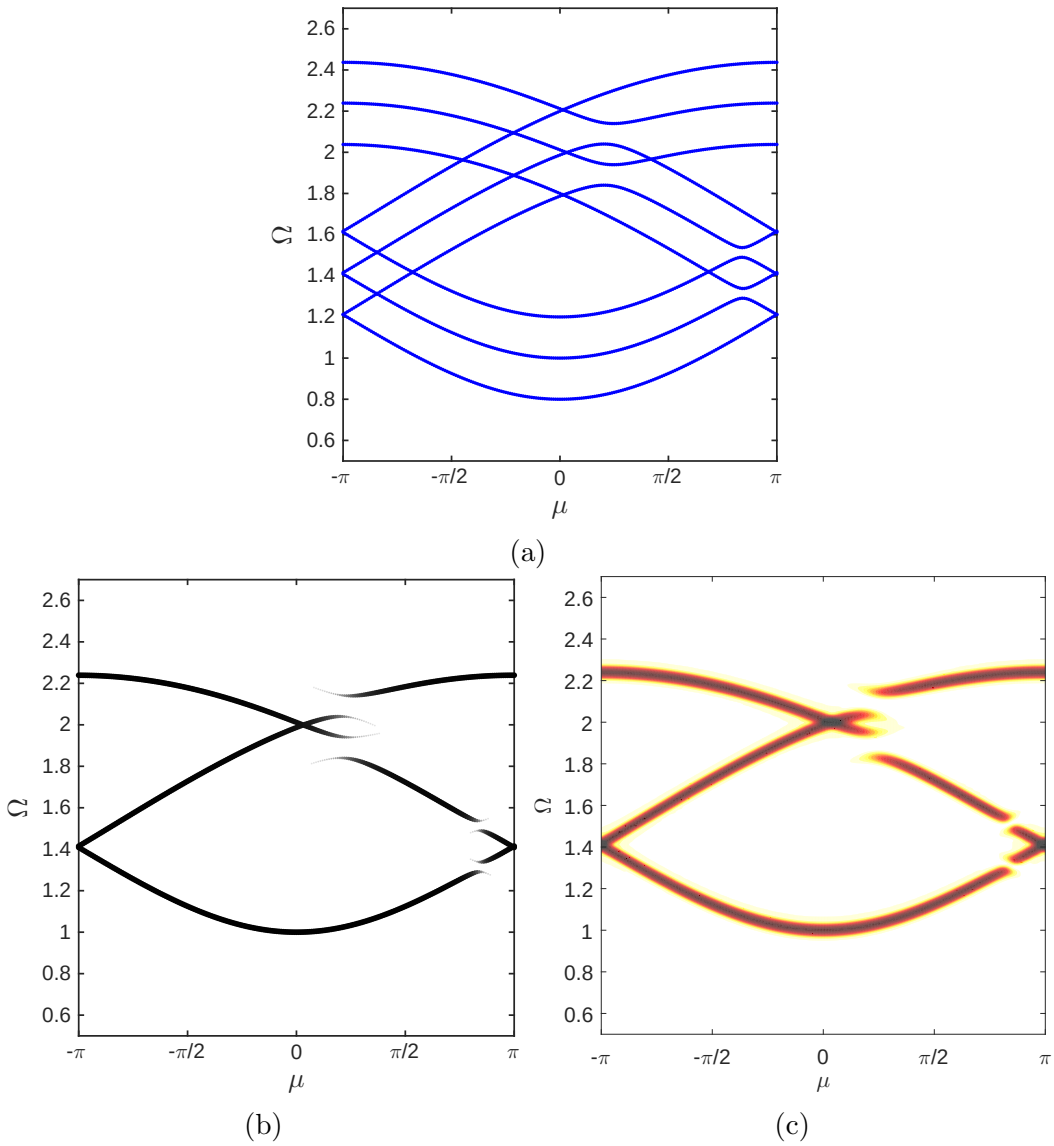

Figure 6.2: Branches resulting from the solution of the eigenvalue problem in Eq. (6.9) for $R = 3$ and assigned $\mu \in [-\pi, +\pi]$ (a). Fundamental branch obtained through weighting and thresholding process (b) illustrating the presence of asymmetric band gaps as a result of the harmonic spatio-temporal modulation of the stiffness constants. Dispersion diagram obtained with the SED method shows excellent agreement with the predicted fundamental dispersion branches (c).

results, displayed in Fig. 6.2, show the excellent agreement between the SED method and the procedure presented in this paper.

The next example considers the modulation of the ground stiffness, which is expressed as

$$k_{g,r}(t) = k_{g,0}(1 + \beta_{g,m} \cos(\omega_m t + \phi_r)), \tag{6.22}$$

while the inter-mass stiffnesses are kept constant in time, *i.e.* $\beta_m = 0$. The corresponding stiffness coefficients are given by

$$\begin{aligned}
\hat{\mathbf{K}}_q(\mu) &= \omega_0^2 \begin{bmatrix} 2 & -1 & 0 & 0 & \dots & -\mathrm{e}^{-\mathrm{i}\mu} \\ -1 & 2 & -1 & 0 & \dots & 0 \\ 0 & -1 & 2 & -1 & \dots & 0 \\ \vdots & \vdots & \vdots & \vdots & \ddots & \vdots \\ -\mathrm{e}^{\mathrm{i}\mu} & 0 & 0 & 0 & \dots & 2 \end{bmatrix} \delta_{q,0} + \gamma_g \omega_0^2 \mathbf{I} \delta_{q,0} \\
&+ \gamma_g \omega_0^2 \frac{\beta_{g,m}}{2} \begin{bmatrix} \mathrm{e}^{\mathrm{i}q\phi_1} & 0 & 0 & 0 & \dots & 0 \\ 0 & \mathrm{e}^{\mathrm{i}q\phi_2} & 0 & 0 & \dots & 0 \\ 0 & 0 & \mathrm{e}^{\mathrm{i}q\phi_3} & 0 & \dots & 0 \\ \vdots & \vdots & \vdots & \vdots & \ddots & \vdots \\ 0 & 0 & 0 & 0 & \dots & \mathrm{e}^{\mathrm{i}q\phi_R} \end{bmatrix} \delta_{q,\pm 1}
\end{aligned} \tag{6.23}$$

The considered lattice consists of unit cells with $R = 3$ masses. Results are obtained for $\Omega_m = 0.2$, $\beta_{g,m} = 0.15$, $\gamma_g = 2$. For this set of parameters, the obtained dispersion branches are shown in Fig. 6.3a, while the results obtained with the SED method are presented in Fig. 6.3b. The results, displayed in Fig. 6.3, show the excellent agreement between the SED method and the procedure presented in this paper.

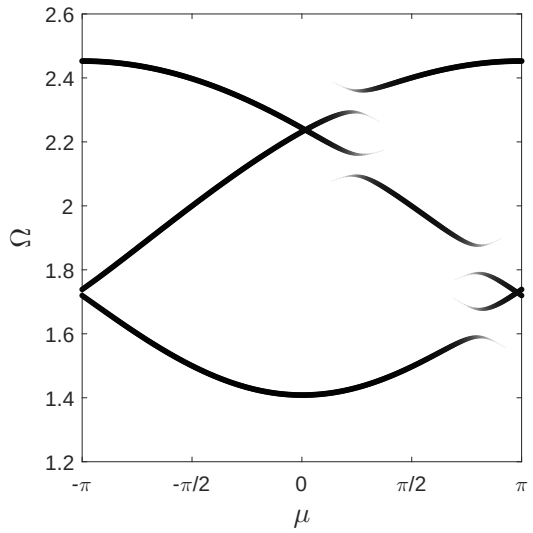

(a)

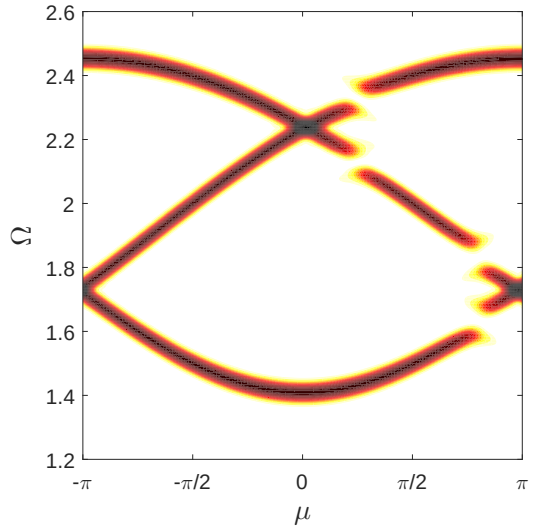

(b)

Figure 6.3: Dispersion diagrams for spring-mass lattice with modulated ground springs: fundamental branch evaluated through the procedure presented in this paper (a), and results from the application of the SED method (b).

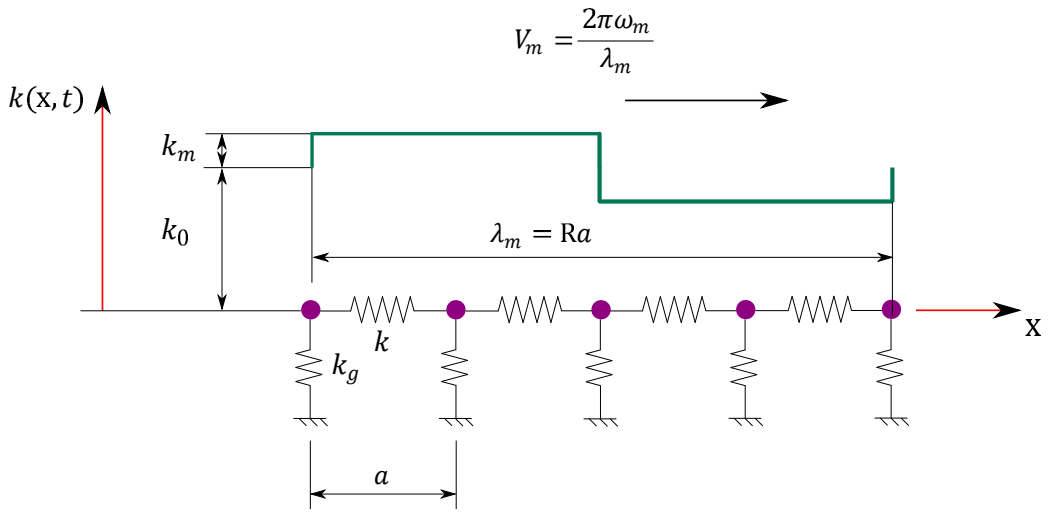

Figure 6.4: Schematic of a chain of resonators with a traveling square wave stiffness modulation.

6.3.2 Square stiffness modulation

Having demonstrated the effectiveness of our procedure in predicting dispersion diagrams for chains with harmonic modulation of stiffness, a more complex example is presented where the modulation is a traveling square wave and is thus composed of multiple harmonic components. The case of stiffness modulation imposed on the inter-mass springs is investigated for illustration purposes. The spring constant of the s-th spring is expressed as

$$k_r(t) = k_0(1 + \beta_m\{2H[\cos(\omega_m t + \phi_s)] - 1\}), \tag{6.24}$$

where H is the Heaviside function. A schematic of the modulated spring-mass chain is shown in Fig. 6.4. Similar to the harmonic modulation, the stiffness modulation square wave travels with phase velocity $V_m = \omega_m\lambda_m/2\pi$. The stiffness coefficients in

Eq. (6.9) are now given by

$$\hat{\mathbf{K}}_q(\mu) = \gamma_g\omega_0^2\mathbf{I}\delta_{q,0} + \omega_0^2 \begin{bmatrix} 2 & -1 & 0 & 0 & \dots & -\mathrm{e}^{-\mathrm{i}\mu} \\ -1 & 2 & -1 & 0 & \dots & 0 \\ 0 & -1 & 2 & -1 & \dots & 0 \\ \vdots & \vdots & \vdots & \vdots & \ddots & \vdots \\ -\mathrm{e}^{\mathrm{i}\mu} & 0 & 0 & 0 & \dots & 2 \end{bmatrix} \delta_{q,0}$$

$$+ \omega_0^2\beta_m \begin{bmatrix} \mathrm{e}^{\mathrm{i}q\phi_R} + \mathrm{e}^{\mathrm{i}q\phi_1} & -\mathrm{e}^{\mathrm{i}q\phi_1} & 0 & \dots & \mathrm{e}^{\mathrm{i}q\phi_R}\mathrm{e}^{-\mathrm{i}\mu} \\ -\mathrm{e}^{\mathrm{i}q\phi_1} & \mathrm{e}^{\mathrm{i}q\phi_1} + \mathrm{e}^{\mathrm{i}q\phi_2} & -\mathrm{e}^{\mathrm{i}q\phi_2} & \dots & 0 \\ 0 & -\mathrm{e}^{\mathrm{i}q\phi_2} & \mathrm{e}^{\mathrm{i}q\phi_2} + \mathrm{e}^{\mathrm{i}q\phi_3} & \dots & 0 \\ \vdots & \vdots & \vdots & \ddots & \vdots \\ -\mathrm{e}^{\mathrm{i}q\phi_R}\mathrm{e}^{\mathrm{i}\mu} & 0 & 0 & \dots & \mathrm{e}^{\mathrm{i}q\phi_{R-1}} + \mathrm{e}^{\mathrm{i}q\phi_R} \end{bmatrix} c_q \tag{6.25}$$

where

$$c_q = \begin{cases} \frac{2}{|q|\pi}, & \text{for } q \text{ odd} \\ 0, & \text{for } q \text{ even} \end{cases} \tag{6.26}$$

The dispersion diagram of a lattice with modulation wavelength $\lambda_m = 3a$ ($R = 3$) and stiffness parameters $\Omega_m = 0.25$, $\beta_m = 0.05$, $\gamma_g = 1$ is shown in Fig. 6.5a, while the SED calculation is presented in Fig. 6.5b. The number of terms used in the series expressing the stiffness modulation of the structure in Eq. (6.26) is $2P + 1 = 31$ ($P = 15$). Since the square wave is a superposition of multiple frequencies, a larger number of terms than in the harmonic stiffness modulation case are required to obtain an accurate dispersion diagram for this system. The convergence rate of the Fourier series with respect to the number of terms is slow due to the Gibbs phenomenon when representing the square wave function in the Fourier basis.

The square-wave modulated system also exhibits asymmetric dispersion behavior illustrating that the system violates time reversal symmetry. Note that the dispersion

diagram is different from the harmonically modulated chain and displays several gaps in each branch instead of one due to the presence of multiple frequencies in the modulation. A comparison of Figs. 6.5a and 6.5b shows that the proposed method predicts the gaps associated with stiffness modulation accurately. Finally, it can be noted that the weighting process shows some traces of branches at low frequencies and low wavenumbers. There are two parallel branches to the actual dispersion curve and these arise due to the corresponding components of the eigenvector having a non-negligible amplitude. These additional branches may filtered out through a more aggressive threshold, which would need to be adapted in the case of multiple component modulations. Despite these minor traces, good agreement in Fig. 6.5 indicates that the Bloch-based analysis accurately predicts the dispersion diagrams where the modulation involves multiple frequencies.

6.4 Non-reciprocal behavior of time-modulated lattices

Upon observation of the time reversal symmetry breaking properties of modulated lattices, the implications on wave motion and dynamic response of both infinite and finite lattices are illustrated. The discussion first illustrates the effects of the modulation parameters on the observed asymmetric gaps and relates them to the bandgaps observed in space-periodic, time-invariant systems. Next, numerical simulation of the transient response of modulated lattices illustrate the one-directional wave properties of this class of lattices, which are predicted by the analysis of dispersion. Finally, the study of a finite lattice shows how frequency modulation leads to the non-reciprocal steady-state response, which can be also predicted from observations made on the dispersion diagrams.

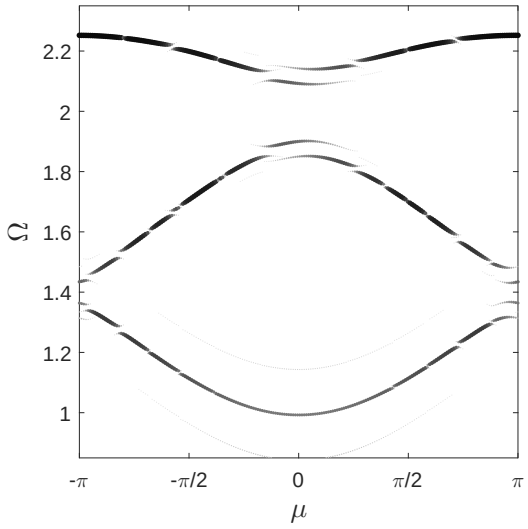

(a)

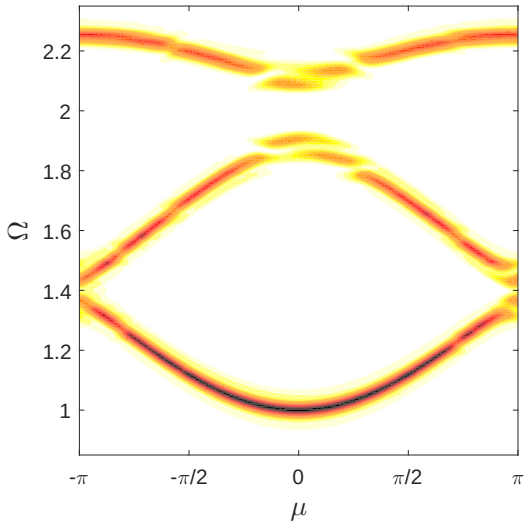

(b)

Figure 6.5: Dispersion diagrams of the square-wave stiffness modulated lattice: dispersion diagram obtained with $2P+1=31$ coefficients (a), and SED method results (b).

6.4.1 Analysis of symmetry and asymmetry of the dispersion diagram

The analysis of symmetries and their lack of thereof in the dispersion diagram due to spatio-temporal modulations is conducted with reference to the spring-mass lattice with harmonic ground stiffness modulation, whose parameters and stiffness properties are described in Section 6.3 and Eq. (6.22). For reference purposes, the case where only spatial modulation exists is considered first, *i.e.* when $\Omega_m = 0$. This leads to a time-invariant periodic system, which is known to feature a series of band gaps whose frequency location and width are defined by the amplitude and period of the modulation. In this case, the period is $\lambda_m = 3a$, while the modulation amplitude is $\beta_m = 0.2$. The dispersion diagram for this lattice, shown in Fig. 6.6a, shows the presence of two band gaps, shaded in red and blue for visualization purposes, which are commonly expected to occur for a system with periodic spatial variations in mechanical properties. The diagrams are plotted over an extended wavenumber range, $\mu \in [-3\pi, +3\pi]$, to illustrate its periodicity as well as to highlight its symmetry with respect to the $\mu = 0$ axis. In the presence of a modulation that occurs both in space and in time, defined in this case by a modulation frequency $\Omega_m = 0.2$, the symmetry of the dispersion diagrams is broken as shown in Figure 6.6b. Two asymmetric gaps occur at different frequencies for waves traveling to the left or to the right. The difference in the central frequency of the gaps, $\Delta\Omega = \Omega_m = 0.2$, is thus exactly equal to the value of the modulation frequency. This statement, which was proven analytically in [104] for continuous media, can be explained intuitively by observing that the impedance mismatch encountered by the propagating wave travels at velocity $v_m = \omega_m/\kappa_m$, so the rate at which the same wave perceives it is different when the wave travels to the left or to the right, by a difference that is the velocity of the modulation wave. Another perspective to this observation is to apply a change in variable $\bar{x} = x - (\omega_m/\kappa_m)t$ to the space-time modulated lattice, which recovers a space-only modulated lattice, but in the new coordinate system where the frequency

of any traveling wave is shifted by a quantity ω_m. One interesting observation is that the impedance mismatch remains the same, therefore the gaps have the same width, but occur at shifted frequencies. Similar observations are reported by Cassedy and Oliner [116] in continuous systems subjected to space-time periodic modulation, where a proportional relation between the difference in frequency in the gaps ($\Delta\Omega$) and the phase velocity of the modulation wave v_m was also derived.

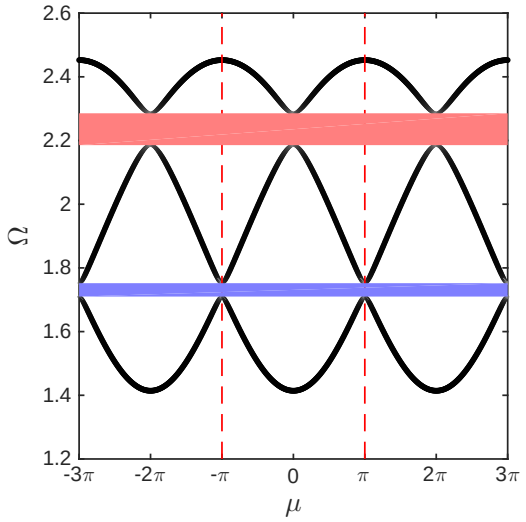

(a)

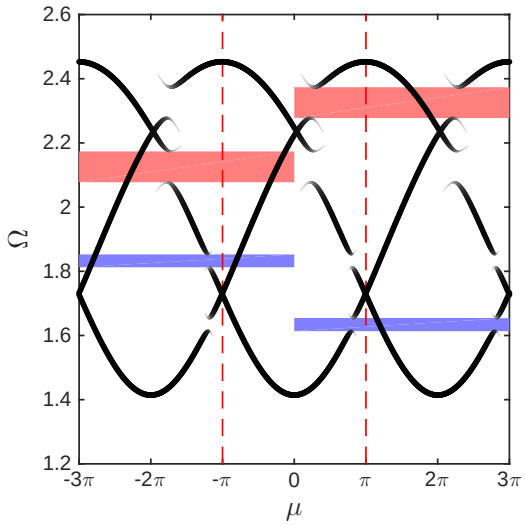

(b)

Figure 6.6: Dispersion diagrams for (a) space modulated and (b) space-time modulated ($\lambda_m = 3a$) systems having 3 identical masses in a unit cell. Space-time modulation produces asymmetric shift in the bandgaps.

6.4.2 One-directional wave motion

The implications of asymmetric dispersion properties in terms of wave motion can be illustrated through numerical simulations conducted on lattices with the considered spatio-temporal modulations. These lattices violate mechanical reciprocity by allowing one-directional wave propagation. Consider a lattice with harmonic modulation of the first-neighbor interaction springs as discussed in Sec. 6.3.1, having the properties $\Omega_m = 0.2$, $\beta_m = 0.15$, $\gamma_g = 1$. The dispersion diagram of this lattice exhibits an asymmetric band gap in the branch with positive slope for $\Omega \in [2.05, 2.15]$, see Fig. 6.2b. At frequencies in this band gap, only modes with negative group velocities are allowed, which means that the lattice allows propagation in the $-x$ direction. The response of the lattice is evaluated for transient excitation over one mass at a frequency inside this band gap, $\Omega = 2.1$. For the numerical simulations, a lattice with 70 unit cells and a modulation period $\lambda_m = 3a$ is considered, which corresponds to a total of 210 masses. Reflections at the edges are avoided by applying Born-Karman boundary conditions. Figure 6.7 displays the evolution of displacement along the chain against the normalized time $\tau = \omega_0 t$. In the simulations, the center mass is excited for a duration of $\omega_0 t = 200$. The total simulation time is $\omega_0 t = 600$. For the integration, the Verlet algorithm [117] is used with a time step $\Delta t = 2 \times 10^{-8}$. The resulting displacement field is strongly asymmetric, as most of the energy of wave motion is supported by waves that travel along the $-x$ direction. Some waves with frequency different from ω are also excited and they travel in both directions with group velocities different from the primary wave. Their amplitude is small compared to the primary wave, as can be observed in Fig. 6.7. Note that the dispersion diagrams only predict the wavenumbers and group velocities of waves traveling with the excitation frequency ω and the transient response of the chain is indeed consistent with the dispersion analysis.

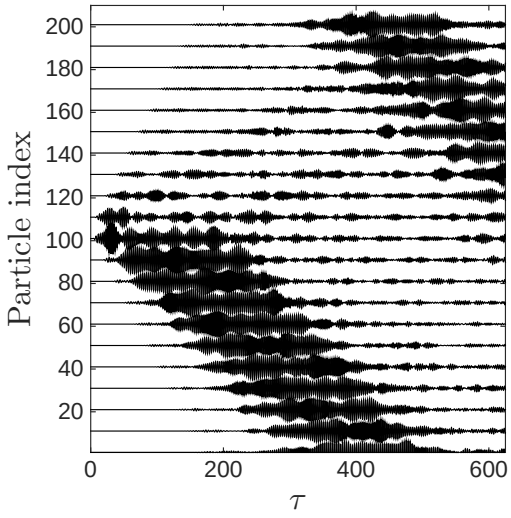

Figure 6.7: Contours of displacement magnitude for transient response to harmonic excitation of a stiffness modulated lattice. The waves propagate primarily in $-x$ direction, as predicted by the dispersion analysis.

6.4.3 Steady state response of a finite modulated lattice: mechanical circulator

Finally, the free out-of-plane vibration response of a three mass system arranged in a circle as illustrated in Fig. 6.8 is considered. The masses are all identical and equal to m. Without loss of generality, the ground spring stiffness is set to $k_g = 0$.

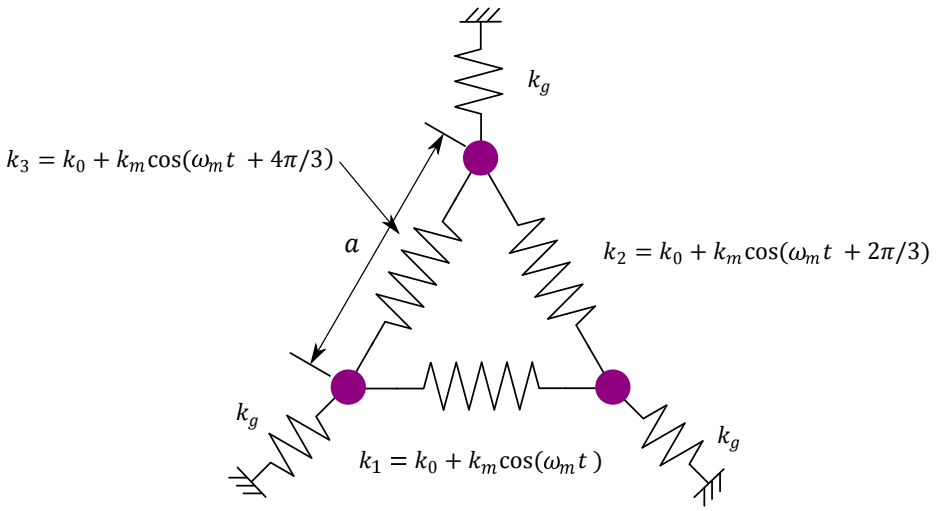

Figure 6.8: Schematic of a three mass system, with a stiffness modulation corresponding to a traveling wave applied on the springs.

The spring stiffness has two components: a constant part and a time varying

modulation component. A traveling wave modulation of frequency ω_m and amplitude k_m is applied to the springs connecting the masses and their stiffness is $k_r = k_0 + k_m \cos(\omega_m t + 2\pi r/3)$. The governing equations of this system read $\mathbf{M}\ddot{\mathbf{u}} + \hat{\mathbf{K}}\mathbf{u} = \mathbf{0}$. They can be written in dimensionless form as $\ddot{\mathbf{u}} + \mathbf{K}\mathbf{u} = \mathbf{0}$, where the stiffness matrix $\mathbf{K}$ is

$$\mathbf{K} = {\omega_0}^2 \begin{bmatrix} 2 & -1 & -1 \\ -1 & 2 & -1 \\ -1 & -1 & 2 \end{bmatrix} - {\omega_0}^2 \frac{\beta_m}{2} \left(\begin{bmatrix} 1 & \mathrm{e}^{\mathrm{i}2\pi/3} & \mathrm{e}^{\mathrm{i}4\pi/3} \\ \mathrm{e}^{\mathrm{i}2\pi/3} & \mathrm{e}^{\mathrm{i}4\pi/3} & 1 \\ \mathrm{e}^{\mathrm{i}4\pi/3} & 1 & \mathrm{e}^{\mathrm{i}2\pi/3} \end{bmatrix} \mathrm{e}^{\mathrm{i}\omega_m t} + \text{c.c.} \right), \quad (6.27)$$

and c.c. stands for complex conjugate. To solve the system of equations, a procedure similar to that proposed by Alù et al. [118] is followed. The following change of variables is introduced to diagonalize the above system

$$\begin{bmatrix} u_1 \\ u_2 \\ u_3 \end{bmatrix} = \frac{1}{\sqrt{3}} \begin{bmatrix} 1 & 1 & 1 \\ 1 & \mathrm{e}^{\mathrm{i}2\pi/3} & \mathrm{e}^{\mathrm{i}4\pi/3} \\ 1 & \mathrm{e}^{\mathrm{i}4\pi/3} & \mathrm{e}^{\mathrm{i}2\pi/3} \end{bmatrix} \begin{bmatrix} a_1 \\ a_2 \\ a_3 \end{bmatrix} \quad (6.28)$$

Note that a basis that is not orthogonal is chosen because, as demonstrated below, the solution is expressed conveniently in the above basis in the presence of modulation. Using the transformation in Eq. (6.28) leads to the following equation for $\mathbf{a} = [a_1\ a_2\ a_3]^T$

$$\ddot{\mathbf{a}} + {\omega_0}^2 \left(\mathbf{K}_0 + \frac{\beta_m}{2} \mathbf{K}_1 \right) \mathbf{a} = \mathbf{0} \quad (6.29)$$

where

$$\mathbf{K}_0 = \begin{bmatrix} 0 & 0 & 0 \\ 0 & 3 & 0 \\ 0 & 0 & 3 \end{bmatrix}, \quad \mathbf{K}_1 = \begin{bmatrix} 0 & 0 & 0 \\ 0 & 0 & 3\mathrm{e}^{-\mathrm{i}(\omega_m t + 2\pi/3)} \\ 0 & 3\mathrm{e}^{-\mathrm{i}(\omega_m t + 2\pi/3)} & 0 \end{bmatrix}. \quad (6.30)$$

Note that the a_1 mode becomes uncoupled from the a_2 and a_3 modes. To solve for these modes, a solution of the form is assumed

$$a_2 = A_2 \mathrm{e}^{-\mathrm{i}(\omega+\omega_m/2)t}, \;\; a_3 = A_3 \mathrm{e}^{-\mathrm{i}(\omega-\omega_m/2)t},$$

where ω is an unknown frequency and A_2, A_3 are scalar constants. Substituting the above equation into the system of equations (6.29) results in a homogeneous system of equations and the condition for the existence of non-trivial solutions leads to

$$\det \begin{pmatrix} 3-(\Omega+\Omega_m/2)^2 & (3\beta_m/2)\mathrm{e}^{\mathrm{i}2\pi/3} \\ (3\beta_m/2)\mathrm{e}^{-\mathrm{i}2\pi/3} & 3-(\Omega-\Omega_m/2)^2 \end{pmatrix} = 0. \tag{6.31}$$

Solving the above system leads to the frequencies

$$\Omega_{1,2} = \left(\frac{\Omega_m^2}{4} + 3 \pm \sqrt{3\Omega_m^2 + \frac{9\beta_m^2}{4}} \right)^{1/2}. \tag{6.32}$$

Substituting values $\beta_m = 0.09$ and $\Omega_m = 0.5$ for the modulation parameters, it is found that $A_2 \gg A_3$ for the mode Ω_1 and $A_3 \gg A_2$ for the other mode Ω_2. Thus transforming back to the original displacement basis using the inverse of the transform in Eq. (6.28), and considering only the term dominant between A_2 and A_3 in each of the modes, the solution is expressed as

$$\mathbf{u} = A_2 \mathrm{e}^{\mathrm{i}(\Omega_1+\Omega_m/2)\tau} \begin{bmatrix} 1 \\ \mathrm{e}^{\mathrm{i}2\pi/3} \\ \mathrm{e}^{\mathrm{i}4\pi/3} \end{bmatrix} + A_3 \mathrm{e}^{\mathrm{i}(\Omega_2-\Omega_m/2)\tau} \begin{bmatrix} 1 \\ \mathrm{e}^{-\mathrm{i}2\pi/3} \\ \mathrm{e}^{-\mathrm{i}4\pi/3} \end{bmatrix}. \tag{6.33}$$

Note that the frequencies split as a consequence of modulation from $\Omega = \sqrt{3}$ and the a_2 and a_3 modes are called clockwise and counter-clockwise propagating modes, respectively, based on the sign of the group velocity.

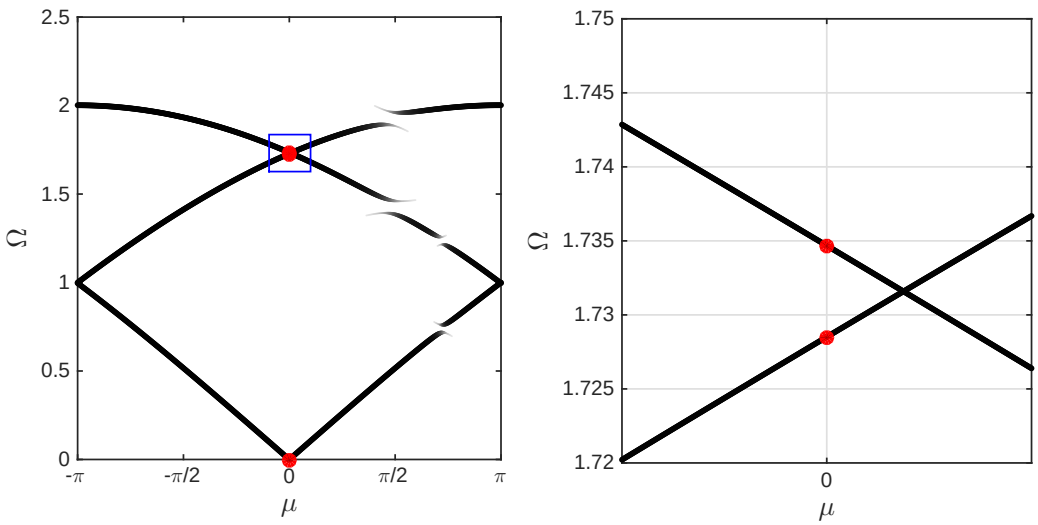

(a) (b)

Figure 6.9: (a) Dispersion diagram for a chain subjected to stiffness modulation showing loss of symmetry. (b) Zoomed in view of the dispersion diagram showing frequency splitting at $\mu = 0$. The left and right propagating waves have different frequencies and match with the frequencies obtained from steady state solution.

It is possible to now interpret the above results using the dispersion analysis of an infinite chain of masses subjected to the same modulation. The normalized modulation stiffness β_m and frequency Ω_m are set to 0.09 and 0.5, respectively. Figure 6.9a displays the dispersion diagram for a chain having a modulation wavelength $\lambda_m = 3a$. Similar to the previous case, there are 3 branches in the dispersion diagram as a unit cell has three degrees of freedom. Also, the presence of modulation breaks the symmetry about the $\mu = 0$ axis, where $\mu = 3a\kappa$. Figure 6.9b displays a zoomed-in view of the dispersion diagram where the two branches intersect close to $\mu = 0$. It is observed that the branches do not intersect at $\mu = 0$ as a result of modulation.

The steady state free vibration response corresponds to a constraint $u_i = u_{i+3}$ imposed on an infinite chain. This constraint is satisfied for wavenumbers μ which have $e^{i\mu} = 1$. This condition is equivalent to $\mu/2\pi = n$, where n is an integer and is equivalent to $\mu = 0$ in the First Brillouin zone. Figure 6.9 displays that there are 3 values of frequency Ω at wavenumber $\mu = 0$. One frequency is $\Omega = 0$, while there

are two non-zero frequencies. In the absence of modulation, these frequencies would be $\Omega = \sqrt{3}$. Modulation results in a split of frequencies, and the two frequencies are derived in Eq. (6.32). From the dispersion diagram, one can infer that the wave with frequency $\Omega_2 - \Omega_m/2 = 1.7285$ is a right traveling wave while the wave with frequency $\Omega_1 + \Omega_m/2 = 1.7347$ is a left traveling wave. The dispersion analysis thus predicts accurately the frequency splitting due to stiffness modulation in a 3-mass system. This frequency splitting is the basis for designing non-reciprocal acoustic circulators. When the system is excited at the frequency $\Omega = 1.7315$, the combination of the a_2 and a_3 modes results in small ratio A_3/A_2, as demonstrated by Alu and coworkers [118], see frequency response function in Fig. 6.10 (damping coefficient was set to c=0.01). This phenomena can be exploited to build a nonreciprocal mechanical 3-port device.

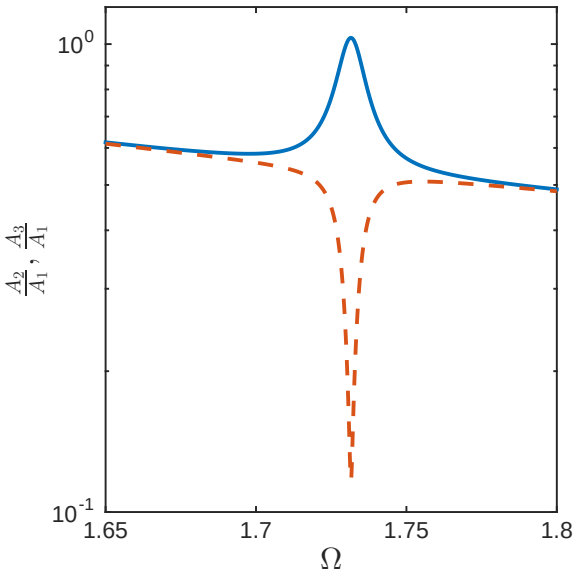

Figure 6.10: Frequency response function when particle 1 is excited. Amplitudes ratio A_2/A_1, A_3/A_1 in a blue solid and a red dashed line respectively. At excitation frequency $\Omega = 1.7315$ the amplitude of particle 3 response is much smaller than the other two.

6.5 Conclusions

The chapter presented a Bloch-based method to study the dispersion properties of systems with periodic time-varying coefficients. The method provides the dispersion diagram of the lattice by formulating and solving a quadratic eigenvalue problem over a unit cell whose length depends upon the spatial and time modulation wavelength. The method extends the traditional Bloch approach for spatially modulated systems to provide a general framework that is applicable to cases where the coefficients of the governing equations vary periodically in time. Although the method is here illustrated for simple, low-dimensional lattices, it is applicable to a general class of systems whose dynamic behavior is described by a system of ordinary differential equations, and could be implemented as a post-processing step in Finite Element-based analysis. This is considered as the main contribution of the work.

The applicability of the proposed method is demonstrated for both harmonic modulation and modulation having multiple frequencies, and it is validated with dispersion diagrams obtained from numerical simulations using the SED method. Excellent agreement with the dispersion diagrams obtained from full numerical simulations for all the considered cases is shown, along with prediction of unidirectional wave propagation at certain frequencies. Potential future research directions include extending the formulation to higher dimensions and wave propagation in other physical systems, as well as designing lattices with specific nonreciprocal mechanical wave propagation characteristics.

CHAPTER 7
TIME-DEPENDENT STRUCTURAL METAMATERIALS: EXPERIMENTAL VALIDATION

7.1 Overview

In the light of the interesting properties of time-modulated metamaterials discussed in chapter 5 and 6, the present chapter reports on a first step towards the practical implementation of broadband, time-modulation strategies of the elastic properties. Specifically, the chapter focuses on elastic waveguides with time-modulated stiffness featuring stop bands in the wavenumber domain. It is shown that such wavenumber stop bands, here referred to as "flat bands", result in the selective filtering of reflected waves at the interface between an homogeneous and time-modulated domains. The system is understood as a single port system, in which a broadband incident wave (input) results into a narrowband reflected wave (output) whose frequency content is centered at multiples of half of the modulation frequency ω_m. At the frequencies corresponding to flat bands, the group velocity of the waves in the modulated domain is zero, so their propagation is forbidden. As a result, such frequency components are reflected into the homogeneous domain. The location of the flat bands in the dispersion diagram is defined by the stiffness modulation frequency, therefore the filtering capabilities of the system can be easily tuned. The concept is first illustrated through analytical and numerical results. Then, an implementation of the proposed concept in an aluminum beam in transverse motion is presented. The approach is based on piezoelectric patches and switching negative capacitance shunts. The role of the negative capacitance shunts, connected in series with the piezoelectric patches, is to modify the equivalent stiffness of the resulting electro-mechanical system. A

switch is placed between each piezoelectric patch and the corresponding negative capacitance circuit. The softening effect is only induced when the switch is closed. Therefore, by periodically operating the switch, it is possible to obtain a structure with time-dependent effective stiffness. Finally, the chapter presents experimental results corresponding to the transient response of waves propagating along the beam measured by a scanning laser Doppler vibrometer. The measurements confirm not only that the switches work as expected, effectively inducing modulation of the effective stiffness of the system, but also that the reflected field is characterized by a narrowband frequency content defined by the chosen modulation scheme.

7.2 Theoretical background

An analytical model of an elastic, time-modulated waveguide is first presented, showing the existence of flat bands and their connection to the stiffness modulation frequency ω_m. The transverse motion of a beam with time-dependent material properties is considered, which is governed by the following equation:

$$R_g^2 E(t) \frac{\partial^4 w(x,t)}{\partial x^4} + \frac{\partial}{\partial t}\left[\rho(t) \frac{\partial w(x,t)}{\partial t}\right] = 0, \tag{7.1}$$

where A, I and $R_g = \sqrt{I/A}$ respectively denote the area, second moment and radius of gyration of the beam cross section, while E and ρ are the material Young's modulus and density. A time-dependent stiffness is introduced by assuming that the Young's modulus varies periodically in time, i.e. $E(t) = E(t + T_m)$, where $T_m = 2\pi/\omega_m$. A solution of the resulting equation of motion is sought in the form:

$$w(x,t) = e^{i(\omega t - \kappa x)} \sum_{n=-\infty}^{+\infty} \hat{w}_n e^{in\omega_m t}. \tag{7.2}$$

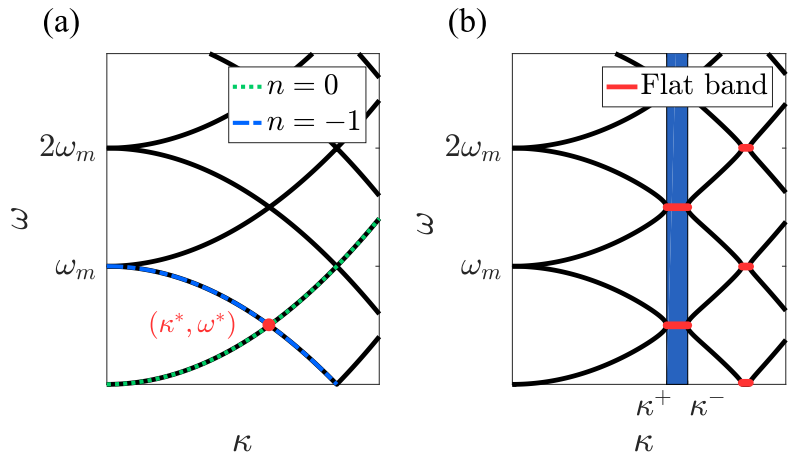

Figure 7.1: Dispersion diagrams for a beam in bending: homogeneous case (a), time-modulated with harmonic modulation (b). The interaction between the $n = 0$ and $n = -1$ order dispersion branches induces a flat band, in red, in a modulated system. Such flat band collapses to the point (κ^*, ω^*) for vanishing modulation amplitude. The approximate expression for the flat band, ranging from κ^+ to κ^-, is represented by the blue band.

For simplicity of the derivations to follow, an harmonic modulation is assumed, i.e.

$$E(t) = E_0 + E_m \cos(\omega_m t) = E_0(1 + \alpha_m \cos(\omega_m t)) \tag{7.3}$$

where $\alpha_m = E_m/E_0$ defines the amplitude of modulation.

The dispersion relation for the system is obtained by solving a quadratic eigenvalue problem (QEP) in ω upon imposing a wavenumber κ. The resulting dispersion diagrams for $\alpha_m \to 0$ and $\alpha_m \neq 0$ shown in Fig. 7.1 are ω_m-periodic in the frequency domain, and notably feature flat bands for finite α_m values. These were previously observed and denoted as κ bandgaps in photonic crystals with time-periodic dielectric properties [119]. In analogy with frequency bandgaps, or stop bands, these flat bands in the wavenumber domain are associated with a stationary oscillating component corresponding to a zero group velocity, and an exponentially growing component associated with parametric amplification. This is illustrated by imposing real values of wavenumber κ, and solving for the resulting complex frequency ω. Considering,

for example, the $n = 0$ and $n = -1$ orders only in Eq. 7.2, leads to the following characteristic equation:

$$(\omega^2 - \gamma\kappa^4)\Big[(\omega - \omega_m)^2 - \gamma\kappa^4\Big] - \Big(\frac{\alpha_m\gamma\kappa^4}{2}\Big)^2 = 0, \tag{7.4}$$

with $\gamma = c_0^2 R_g^2$ and $c_0 = \sqrt{E_0/\rho}$. For $\alpha_m \to 0$, the $n = 0$ and $n = -1$ order branches intersect at the point $\kappa^* = \sqrt{\omega_m/(2c_0 R_g)}$ and $\omega^* = \omega_m/2$. For the modulated systems ($\alpha_m \neq 0$), the solution of Eq. 7.4 is instead:

$$\omega = \frac{1}{2}\left[\omega_m - \sqrt{\omega_m^2 + 4\gamma\kappa^4 - 2\sqrt{\gamma\kappa^4(4\omega_m^2 + \alpha_m^2\gamma\kappa^4)}}\right]. \tag{7.5}$$

It follows that ω is complex if:

$$\omega_m^2 + 4\gamma\kappa^4 - 2\sqrt{\gamma\kappa^4(4\omega_m^2 + \alpha_m^2\gamma\kappa^4)} < 0, \tag{7.6}$$

which occurs for wavenumber values $\kappa \in [\kappa^+,\ \kappa^-]$, with:

$$\kappa^{\pm} = \sqrt[4]{\frac{\omega_m^2}{2\gamma(2 \pm \alpha_m)}} \tag{7.7}$$

In this wavenumber range, the corresponding frequency is complex, i.e. $\omega = \omega_r + i\omega_i$, where:

$$\omega_r = \frac{1}{2}\omega_m, \tag{7.8}$$

$$\omega_i = -\frac{1}{2}\sqrt{\omega_m^2 + 4\gamma\kappa^4 - 2\sqrt{\gamma\kappa^4(4\omega_m^2 + \alpha_m^2\gamma\kappa^4)}}. \tag{7.9}$$

The real part of the frequency thus remains constant with respect to the wavenumber, which suggests a stationary wave at a fixed frequency as described by a zero group

velocity, i.e.:

$$\frac{\partial \omega_r}{\partial \kappa} = 0. \tag{7.10}$$

Furthermore, it is noted that $\omega_i < 0$, hence waves with wavenumbers satisfying Eq. 7.7 are associated to an exponentially growing response in time.

The solution of the QEP obtained by imposing the solution in Eq. 7.2 leads to a family of branches that are identified by integers n. From the solution of the characteristic equation for various index orders and for $\alpha_m = 0$ one can show that these branches intersect at frequencies $\frac{|n-n'|}{2}\omega_m$, where n and n' denote two intersecting branches. These frequency values also identify the flat branches that occur when $\alpha_m \neq 0$.

7.3 Numerical analysis of broadband-to-narrowband conversion

Next, the behavior of a plane wave incident on an interface between a beam with constant properties and a modulated one is investigated. As discussed, it is conjectured that wave components at frequency $\omega_m/2$, and its integer multiples, do not propagate through the modulated medium as a result of the occurrence of flat bands. Thus, a broadband wave incoming from the time constant domain will be transmitted with the exception of the flat band frequency, which is reflected. Interestingly, the same phenomenon could be explained in terms of power conversion phenomena between the different harmonic components at the interface, as done for waves propagating from homogeneous to time-modulated domains in dispersionless rods undergoing longitudinal motion [120]. Considering the broadband signal as the input and the narrowband signal as the output of a single port device, time modulation leads to the narrow band filtering of the input signal. The filtering frequency of such system, depicted in Fig. 7.2, can be selected to produce different narrowband frequency outputs for the same broadband input through the selection of the modulation frequency ω_m. The

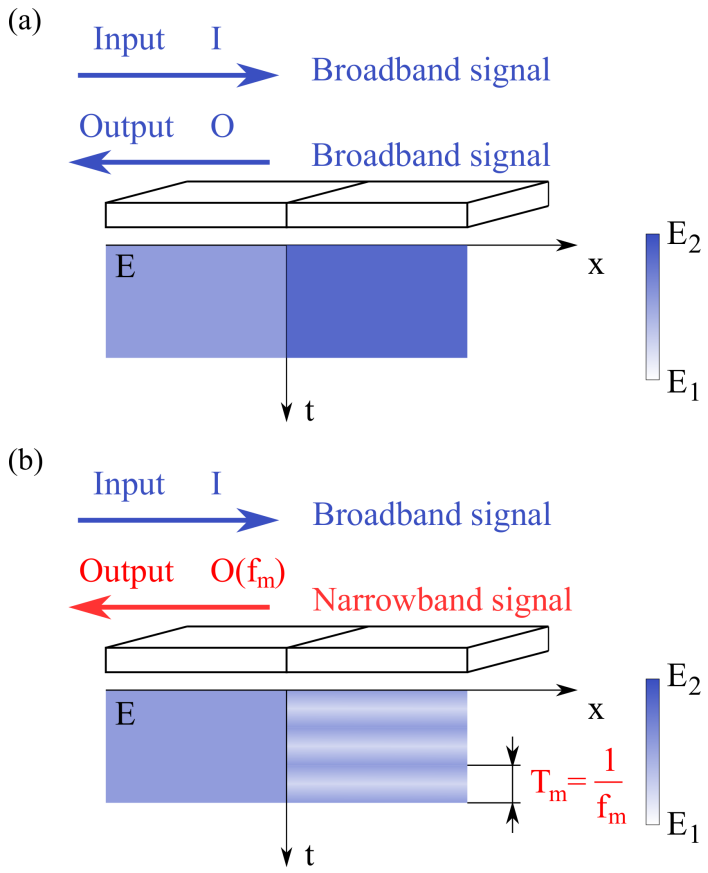

Figure 7.2: Broadband-to-narrowband conversion through time-modulation. Assuming the elastic moduli $E_2 > E_1$, a broadband wave impinging on the interface due to an abrupt change in elastic modulus in a piecewise homogeneous structure generates a broadband reflection (a). On the contrary, a narrowband output is induced by the same broadband signal input at the interface between an homogeneous and time-modulated domains (b), with the frequency of modulation $f_m = 1/T_m$.

concept is illustrated by evaluating the transient response of the waveguide with interface, which is computed through a finite-difference time-domain (FDTD) approach. In the simulations, we assume the time constant domain to be of length $L_h = 0.3$ m, while the modulated one is $L_m = 0.48$ m long. The cross-section of the beam is rectangular with $R_g = 8.67 \times 10^{-4}$ m. The density of the material is $\rho = 2700$ kg/m^3, while the Young's modulus is $E_0 = 69.9$ GPa. In the time modulated domain, the Young's Modulus obeys a square modulation law:

$$E(t) = E_0 + \frac{\alpha_m E_0}{2}\Bigg\{ \text{sgn}\Big[\cos(\omega_m t)\Big] - 1\Bigg\}, \tag{7.11}$$

with $\alpha_m = 0.2$ and sgn$(\cdot)$ sign function. A wave is injected in the system through a perturbation applied at the free end of the time constant beam which varies in time as a 4-cycle tone-burst of center frequency $f_{ext} = 5$ kHz. The frequency content of input $w_{in}(x_p, t)$ and output $w_{out}(x_p, t)$ are evaluated by probing a single location x_p close to the interface in the time constant domain. The corresponding Fourier transform shown in Fig. 7.3.a displays the frequency bandwidth of the input signal (black solid line). A comprehensive representation of the wave motion $w(x, t)$ along the waveguide is obtained through its representation in the frequency/wavenumber domain $\hat{\mathcal{W}}(\kappa, \omega)$, which is obtained through the application of a Fourier transformation in space and time. The contour plots in Fig. 7.3.b-d correspond to the magnitude $|\hat{\mathcal{W}}(\kappa, \omega)|$ of the resulting quantity and effectively locate the spectral content of the wave field along the theoretical dispersion branches (gray lines), which are superimposed for convenience. The contours in the $\kappa > 0$ region correspond to right propagating waves, while those in the $\kappa < 0$ half plane are associated with left traveling, hence reflected wave components. This representation hence effectively illustrates how broadband incident (right propagating) signal impinging at the interface is reflected (left propagating) as a narrowband signal at the frequency associated with half of the considered

modulation frequencies, in this case chosen as $f_m = 11, 12, 13$ kHz (see Fig. 7.3).

7.4 Implementation of time-modulation in an elastic waveguide

Time-modulation of the stiffness of the considered elastic waveguide by employing an array of piezoelectric transducers bonded to the beam and shunted through a suitable electrical impedance. The resulting electro-mechanical waveguide is known to have an effective modulus of elasticity that depends on the electric impedance of the shunting circuit [121, 122]. In the case of transverse motion of an elastic beam for example, the effect of the piezoelectric transducer on the stiffness can be described as a voltage-induced bending moment, in turn generated by the strain applied to the patch [123]. The actuation-induced bending moment can favor or oppose the motion, thus reducing or increasing the structure's effective stiffness. However, the use of the piezoelectric transducers alone marginally affects the dynamics of the structure, therefore they are often coupled to electrical circuits. For narrowband applications, resonant shunting circuits have been exploited to induce band gaps at frequencies defined by the resonant characteristics of the shunts [112]. For broadband applications, instead, negative capacitance circuits (NC) have been employed for vibration absorption [124]. Therefore, in order to achieve broadband filtering properties, in the implementation described herein a NC shunt in series with the piezoelectric transducer is used. The effect of the NC in series with the piezoelectric transducer is to reduce the effective stiffness of the structure. In this configuration, it is possible to identify two operation conditions, namely open and closed circuit. In the open circuit condition, the electrodes of the piezoelectric transducer are not connected, and the value of the transducer's elastic modulus is:

$$E_p^D = E_p^E/(1 - k_{31}^2) \tag{7.12}$$

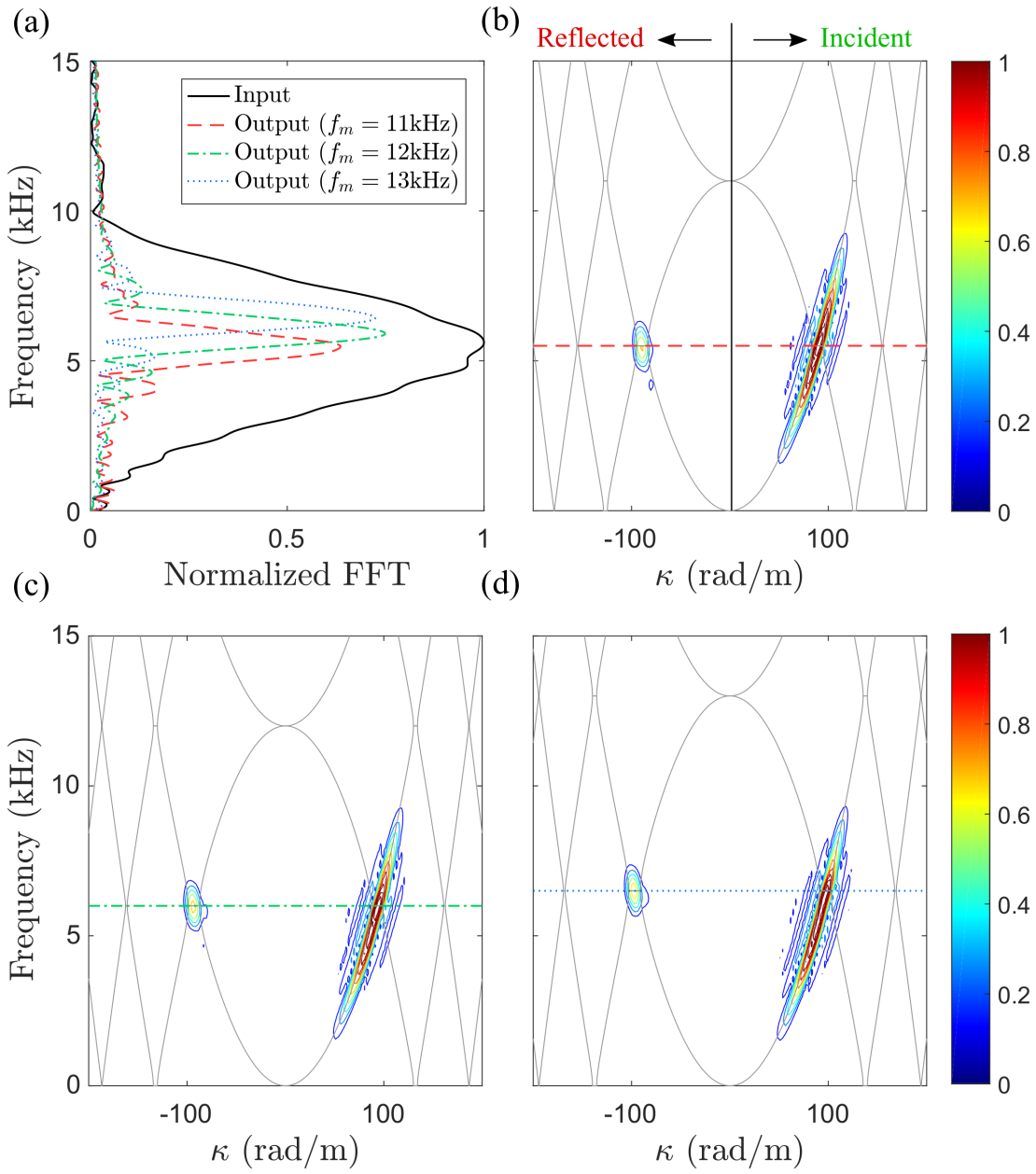

Figure 7.3: Response of the single port system obtained with a FDTD approach. For three different modulation frequencies, the same broadband input is converted into a different narrowband output (a). The Fourier transform's magnitude $|\hat{\mathcal{W}}(\kappa, \omega)|$ associated to the structure's response $w(x, t)$ shows narrowband frequency selection in reflected waves for broadband incident waves (b-d). Specifically, the reflected waves, which correspond to negative values of the wavenumber κ, have frequency content corresponding to the first flat band of the modulated structure at half of the frequency of modulation $f_m/2$, as predicted by the theoretical dispersion diagram (grey lines).

with E_p^E elastic modulus of the piezoelectric patch with short-circuited electrodes and k_{31} the relevant piezoelectric coupling coefficient. In the closed circuit condition, the NC shunt of capacitance $C_N = -C'$ produces a change in the piezoelectric material's elastic modulus, which is now given by:

$$E_p^{E^*} = E_p^E \frac{C' - C_p^T}{C' - C_p^S} \tag{7.13}$$

with C_p^T stress-free piezoelectric capacitance and $C_p^S = C_p^T(1 - k_{31}^2)$ strain-free piezoelectric capacitance. The value of capacitance C_N is chosen to reduce the effective stiffness of the shunted piezoelectric transducer $E_p^{E^*}$ below the short-circuited electrodes value E_p^E, so to obtain $E_p^{E^*} < E_p^D < E_p^E$. This is done by imposing $C' > C_p^T$, which also guarantees stability of the electro-mechanical system [125]. With respect to the circuit schematic shown in Fig. 7.4.a, the value of negative capacitance [126] is tuned by choosing the the resistors R_1 and R_2, and capacitor C according to the expression $C_N = -C' = -R_2/R_1C$ by trying to operate as close as possible to the stability limit $C' = C_p^T$, so to maximize the effective stiffness reduction provided by the shunt, and without inducing unstable behavior of the electro-mechanical system[125]. The resistor R_2 is implemented as the series sum of two resistors, one being equal to the resistor R_1, the other one being R_x. This second resistor is chosen to individually tune the negative capacitance circuits. The resistor R_0 prevents saturation of the capacitor, which would lead to instability [127, 126]. Finally, time-modulation of the system is implemented by periodically operating a switch that breaks the series connection between the piezoelectric transducer and the NC shunt, thus inducing the elastic modulus of the piezoelectric patch to vary between the close circuit configuration value $E_p^{E^*}$ and the open circuit configuration value E_p^D.

7.5 Experimental validation of broadband-to-narrowband conversion

The experimental validation of the frequency selective properties of time-modulated domains is now discussed. The test is performed on a slender aluminum beam ($E =$ 69.9 GPa, $\rho = 2700$ kg/m^3) with $h \times b$ rectangular cross section, $h = 0.003$ m being the cross-section height and $b = 0.030$ m its width. To achieve an effective stiffness change of the beam, 11 equally spaced pairs of piezoelectric patches are vacuum-bonded along the beam, as shown in Fig. 7.4. Each piezoelectric patch, with Young's modulus $E_p^E = 73$ GPa and density $\rho_p = 7800$ kg/m^3, is a $h_p \times b_p \times b_p$ thin plate, with $h_p = 0.001$ m and $b_p = 0.030$ m. The 11 piezoelectric patches are equally spaced, with a t_p gap between them equal to 0.015 m. For each couple, the piezoelectric patches are located on the opposite sides of the beam. Each patch is connected in series to a NC shunt, for a total of 22 NC circuits. A stable NC shunt is obtained with negative capacitance $C_N = -11$ nF and operational amplifier OPA445. All the circuital parameters are listed in Tab. 7.1. The measured stiffness reduction of the piezoelectric transducers, achieved by the NC shunt, is equal to 46 GPa, which is in good agreement with the theoretical value 49.3 GPa.

A square wave time-modulation of the stiffness with period T_m is induced into the structure by operating the switch. Such switching scheme induces a square stiffness law, thus time-modulating the effective stiffness with frequency ω_m.

The structure's response is measured through SLDV, as shown in Fig. 7.4. The measurement is collected for 2 ms at sampling rate $f_s = 128$ kHz. The scanned domain, which is $L_s = 0.78$ m long, is discretized through an equally spaced grid with 512 points, thus achieving a 0.0015 m spatial resolution. In order to reduce uncorrelated noise, for each of grid points, 20 repeats for each measurement are considered. The input $w_{in}^{exp}(x_p, t)$ and output $w_{out}^{exp}(x_p, t)$ are identified at the probe location x_p in the homogeneous domain placed right before the first piezoelectric patch. Three

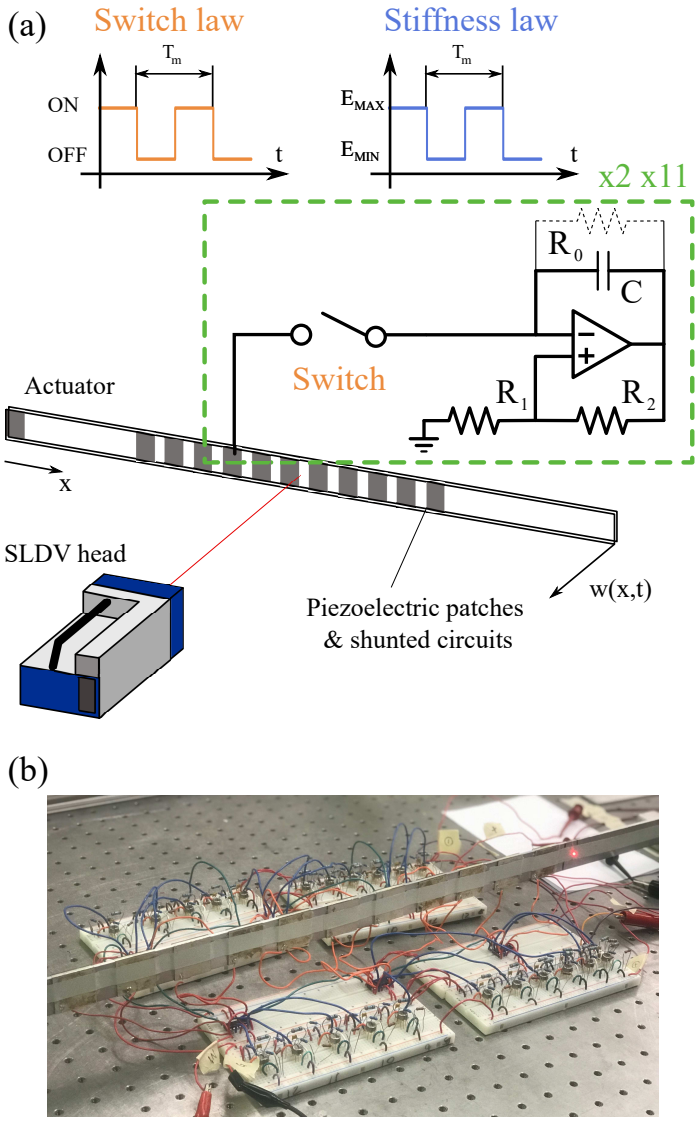

Figure 7.4: Experimental validation of time-modulation of the stiffness properties in a beam through negative capacitance shunts and switches. The beam is equipped with 11 pairs of piezoelectric patches, each connected to a negative capacitance (NC) circuit (a). A switch opens and closes the patch-NC circuit series with a periodic law, inducing the stiffness to vary between two values with period ω_m (b). The response $w(x,t)$ is measured by a scanning laser Doppler vibrometer (SLDV).

Quantity	Value	Unit
C	10	nF
R_0	1	$M\Omega$
R_1	10	$k\Omega$
R_2	$10 + R_x$	$k\Omega$
E_p^E	73	GPa
C_p^T	9.06	nF
k_{31}	0.32	$-$

Table 7.1: Parameters for negative capacitance circuits. The resistor R_x is chosen to individually tune each NC circuit and piezoelectric patch pair to obtain the same value for C_N

experiments are performed by exciting the same broadband input signal, centered at 5 kHz, then modulating the effective stiffness in a square fashion at frequency of modulation f_m equal to 11, 12 and 13 kHz. The analysis of the frequency spectrum of the incident and reflected waves (Fig. 7.5.a) confirms that the reflected waves have a narroband frequency content that is centered at frequency $f_m/2$, thus depends on the modulation frequency of the system. Analogously to the numerical case, the displacement field $w^{exp}(x,t)$ is transformed into the Fourier domain $\hat{\mathcal{W}}^{exp}(\kappa,\omega)$ and plot the contour levels of the magnitude $|\hat{\mathcal{W}}^{exp}(\kappa,\omega)|$ (Fig. 7.5.c-d) to identify the location of the energy content distribution of the measured field in the frequency-wavenumber domains. The experimental dispersion diagrams contour plots in Fig. 7.5.c-d show that, while the dispersion branch associated to the incident wave (or input) in the $\kappa > 0$ region remain the same in all the three experiments and match the theoretical dispersion diagram (grey solid lines), the energy of the reflected wave (or output), located in the $\kappa < 0$ region or the dispersion diagram, is narrowband. One can conclude that the system indeed behaves as a port, transforming the incident broadband signal into a narrowband signal. Furthermore, the location of the energy content of the output corresponds to the flat bands at $f_m/2$, in our experiments at 5.5, 6 and 6.5 kHz, in accordance to our simple theoretical model.

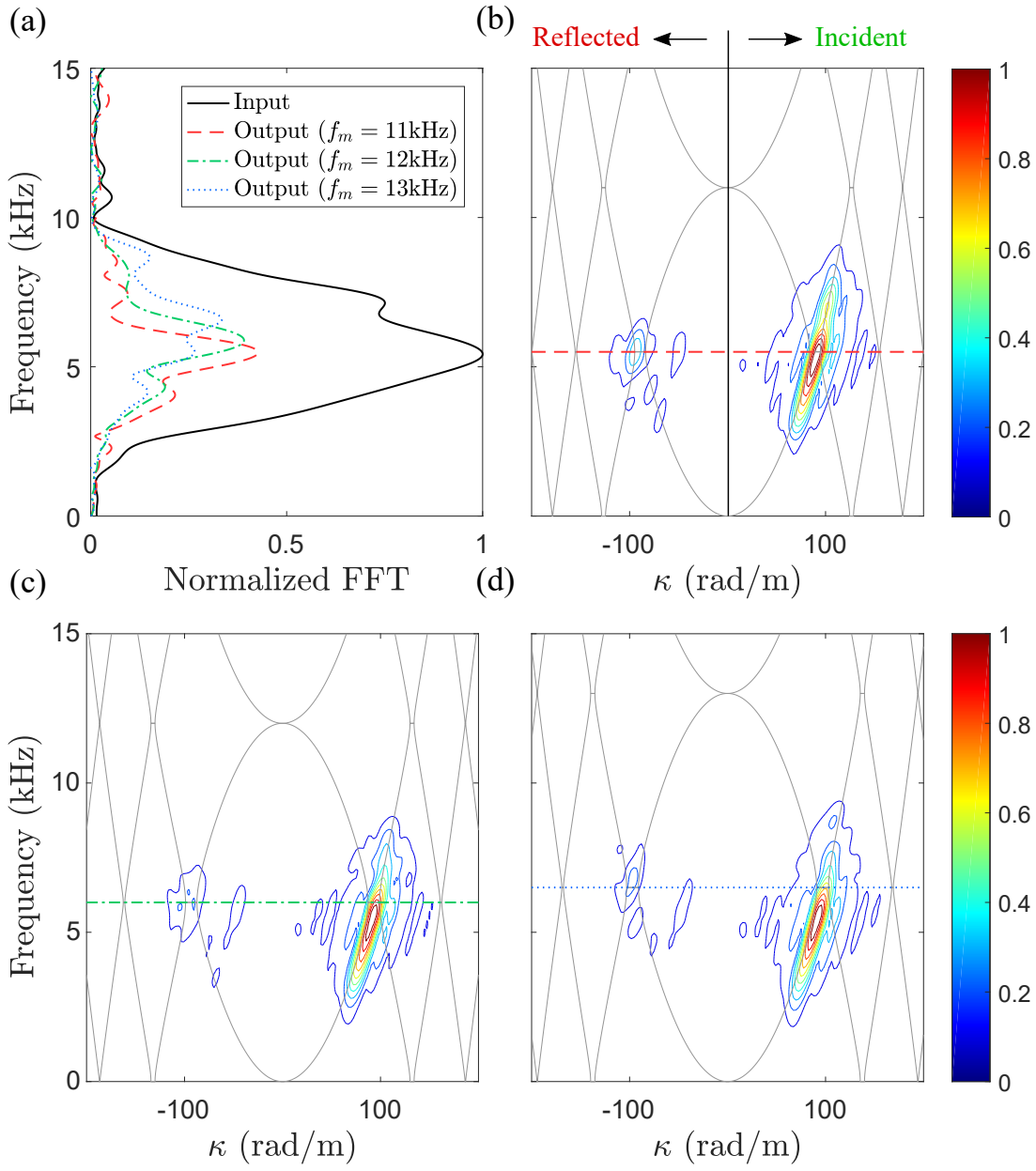

Figure 7.5: Measurement of the wave filtering properties in time-periodic beam with SLDV. The frequency spectrum of the reflected waves is centered at $f_m/2$, as expected for all three measurements (a). The Fourier transform's magnitude $|\hat{\mathcal{W}}^{exp}(\kappa, \omega)|$ of the structure's response $w^{exp}(x, t)$ in the modulated domain shows that the reflected wave depends on the modulation frequency, as predicted by the flat bands in the theoretical dispersion diagram (grey lines).

7.6 Conclusions

This chapter presented a study on a time-periodic elastic waveguide characterized by stop bands in the wavenumber domain. It is shown that, within such bands, the motion of the structure becomes stationary oscillating due to a zero group velocity, and an is associated to exponentially growing amplitude. Then, the theoretical model then is applied to analyze the interaction between a non-modulated and a time-modulated domain. It is shown that a broadband wave incident the interface between non-modulated and modulated domain, is reflected with narrowband frequency content centered at the flat bands. Next, a strategy to time-modulate the effective stiffness in an elastic waveguide is discussed. The time-modulation is obtained through piezoelectric transducers and shunted NC circuits. Experimental validation of the frequency filtering properties of the time-modulated domain confirm both the analytical and numerical results. The proposed strategy for time-modulating the elastic properties of mechanical systems may be extended to other time-periodic metamaterials, such as the ones described in chapter 5 and 6, in order to implement non-reciprocal devices.

CHAPTER 8
CONCLUSIONS AND FUTURE WORK

8.1 Overview

This chapter is divided into four sections. Following this overview, the work presented in the thesis is first summarized. Then, the key research contributions to the field of mechanical metamaterials are listed. Finally, the chapter presents possible investigation opportunities and closing remarks on the future of the field.

8.2 Summary

This thesis investigates structures with spatial and temporal modulation of the effective mechanical properties, contributing to the state-of-the-art of wave propagation control techniques by suggesting novel and systematic design criteria of structural elements.

The first part of the dissertation investigates the effects of periodic geometric undulations on the dispersion properties of 1D and 2D elastic structures. Periodic undulations correspond to initial curvature of beams and plates, which leads to the coupling of transverse and in-plane motion. Such coupling produces complete, modal and partial frequency band gaps along with directional wave motion. The effects of relevant geometric parameters defining the undulation, such as spatial period and undulation amplitude, are investigated through the application of the Plane Wave Expansion Method and a Finite Element-based analysis of dispersion. Experimental illustration of the band gap behavior of undulated beams, and numerical simulations of wave motion in plates serve as partial validations of the analytical predictions, and as demonstrations of the potential application of the concept for the design of

structural components and elastic waveguides with tailored band gap and directional properties. The analysis is then extended to undulated square structural lattices, which are 2D reticulates obtained by tessellating the plane with curved beam elements. The study considers both periodic undulated structures, in which the undulation is uniform throughout the structure as well as graded patterns, whereby the undulation is modulated within the lattice. Undulation is specifically considered in relation to its ability to induce mechanical anisotropy and to break the symmetry of the straight square lattice. Results show that wave motion is inhibited within specified frequency ranges owing to the generation of band gaps, and in specific directions as a result of the undulation-induced anisotropy. The experimental characterization of wave motion in lattice structures is currently of great interest due its relevance to the design of novel mechanical metamaterials with unique/unusual properties such as strongly directional behavior, negative refractive indexes and topologically protected wave motion. Assessment of these functionalities often requires the detection of highly spatially resolved in-plane wavefields, which for reticulated or porous structural assemblies is an open challenge. A Digital Image Correlation approach is implemented that tracks small displacements of the lattice nodes by centering image subsets about the lattice intersections. A high speed camera records the motion of the points by properly interleaving subsequent frames thus artificially enhancing the available sampling rate. This, along with an imaging stitching procedure, enables the capturing of a field of view that is sufficiently large for subsequent processing. The transient response of lattices is recorded in the form of full wavefields, which are processed to unveil features of wave motion. For a hexagonal lattice, time snapshots and frequency contours in the spatial Fourier domain are compared with numerical predictions to illustrate the accuracy of the recorded wavefields. The described novel optical technique is then applied to experimentally demonstrate the elastic wave filtering properties of graded undulated lattices. The progressive formation of frequency band gaps leads

to strong wave attenuation over a broad frequency range. The experimental investigation of wave transmission, conducted using a scanning laser Doppler vibrometer, and the DIC-based detection of full wavefields effectively illustrate this behavior.

The second part of the thesis focuses on periodic structures with time-periodicity of the mechanical properties. Specifically, longitudinal and transverse wave propagation in rods and beams with elastic properties that are periodically varying in space and time is first investigated. Spatio-temporal modulation of the elastic properties breaks mechanical reciprocity and induces one-way propagation. An analytic approach is employed to characterize the non-reciprocal behavior of the structures by analyzing the symmetry breaking of the dispersion spectrum, which results in the formation of directional band gaps and produces shifts of the First Brillouin Zone limits. The position and width of the directional band gaps are related to the modulation parameters. Moreover, the critical values of the modulation speed to maximize the non-reciprocal effect is identified. The theoretical predictions are verified by a finite element model of the modulated beams that computes the transient response of the structure. The two-dimensional Fourier transform of the predicted displacement fields are used to evaluate numerical band diagrams, showing excellent agreement between theoretical and numerical dispersion diagrams. The study is then extended to discrete one-dimensional chains of resonators connected by springs with modulated stiffness. Finally, the thesis presents a broadband-to-narrowband elastic wave filter that relies on time-modulation of the effective stiffness. For broadband waves impinging on the time-modulated domain of the system, narrowband reflected waves are induced due to the periodic effective stiffness change. Changing the modulation frequency tunes the response of the system, thus the frequency content of the reflected waves. An analytical model of the system shows that flat bands in the dispersion diagram with zero group velocity at integer multiples of half the modulation frequency, correspond to the peak of the reflected waves' frequency spectrum. The experimental

implementation of the stiffness modulation is achieved by using piezoelectric transducers and switchable negative capacitance shunts. When connected in series with the negative capacitance shunts, the piezoelectric transducers experience a reduction of stiffness compared to the open electrodes configuration. Then, periodically operating a switch in the series connection between the piezoelectric transducer and the negative capacitance shunts, a square-wave stiffness modulating scheme is achieved. Experimental results show that the reflected waves' frequency spectrum is predicted by the theoretical flat bands for different modulating frequencies.

8.3 Contributions

The work presented in this thesis provides the following contributions to the field of spatially and time-modulated structures:

- Introduction of periodically varying curvature in simple structural elements to control and filter elastic wave propagation. An analytic framework is proposed that relies on the structure's equations of motion to identify the critical geometric parameters responsible for band gap formation, and directional wave propagation.

- Extension to structural lattices of curvature-based modulation of the elastic properties. Periodic and graded lattice configurations are shown to exhibit dramatic change in wave propagation properties as undulation parameters and unit cell configuration vary.

- Experimental validation of the filtering properties of graded undulated lattices by means of a novel optical technique. The approach relies on high speed photography and digital image correlation to measure full wavefield and provide quantitative information on the interaction between the waves and the structure.

- Introduction of an analytical and numerical framework for the analysis of the dispersion properties of spatio-temporally modulated rods and beams, as well as discrete systems.

- Experimental implementation of a technique to modulate in time the effective stiffness of a mechanical system and evaluation of its wave filtering characteristics.

8.4 Future work

The envisioned future directions of research are discussed herein and presented in three different subsections: (i) periodic and graded undulated structures, (ii) extensions of the novel DIC-besed optical technique, (iii) time-modulated structures.

8.4.1 Periodic and graded undulated structures

From a theoretical point of view, the role of the curvature was investigated by assuming an already curved design. Since undulated patterns could be triggered by load-induced instabilities, a description of such effects on the dispersion properties of the structures could be analyzed by considering a general analytical model, where concentrated or distributed loads can be directly related, for instance, to the location of band gaps or highly directional modes in the dispersion diagram. The effective implementation of undulated lattice design cannot be achieved without taking into account also the static behavior of the structure. Intuitively, in the case of the square lattice configurations studied in this thesis, the undulation increases the compliance of the structure. In graded designs, the variation in compliance is continuous along the curvature gradation. Therefore, a study of the static homogenized properties of the undulated lattices, thus seen as their continuous counterparts, could be beneficial to obtain a more complete picture of their behavior.

8.4.2 Extensions of the novel DIC-based optical technique

In the present implementation, the suggested DIC-based optical technique for wavefield measurement is able to reliably measure the in-plane components of displacements. On the other hand, the much more mature 3D SLDVs are able to inform on all the component of displacement in the tested structure. While this did not represent a limitation with respect to the experimental validations presented in this thesis, the extension of the optical technique to 3D wavefield measurement would be extremely beneficial not only in the experimental study of periodic structures, but also in many other contexts, such as structural health monitoring and MEMS characterization. Another possible way to extend the DIC-based optical technique would be by to allow it to measure wave phenomena that involve large deformations. In the current form, the subset of pixel used for the correlation is fixed. As a result of that, as long as the motion is confined within such subset, the algorithm is able to successfully track it. In contrast when the displacements are larger than the size of the subset, the approach fails. An interesting problem that could be tackled with such an extension would be the investigation of waves due to impacts in soft recticulates, where the impact itself triggers a geometric transformation of the lattice, which in turn affects the way the energy propagates through the structure.

8.4.3 Time-modulated structures

While a first theoretical and experimental investigation of time-periodic structural elements has been presented in this thesis, among the problems that need to be addressed in the future is the evaluation of the energy required to achieve a time-dependent modulation of the mechanical properties. Different modulation strategies have to be compared and, ultimately, selected also based on their cost in terms of energy spent throughout the modulation process, since they might significantly differ for their energy efficiency. In the present work, time modulation of the effective

stiffness of studied structure has been realized in the form of a square wave modulation, by exploiting the differences in effective stiffness, induced by the switchable shunts, between open and closed circuit configurations. Since most of the theoretical studies on time-modulation relies on continuous modulating laws, which enable specific wave propagation properties, it would be advantageous to implement a continuous modulations of the elastic properties. Along these lines, an extension of the approach proposed in this thesis could be achieved by a continuously varying negative capacitance value. Probably the most interesting property of spatio-temporal periodic structure, namely one-way filtering capabilities due to non-reciprocal response, although extensively discussed, is yet to be demonstrated in mechanical systems. The main challenges to be faced are related to the number of unit cells required for the systems to affect wave propagation, as the number of modulation cycles experienced by the elastic waves is limited by time taken for the waves to travel through the system. Preliminary considerations on the minimum number of spatio-temporal unit cells required to achieve non-reciprocal wave propagation reveal that such number is larger than the number usually considered when designing spatially modulated periodic structures, thus imposing additional constraints to the design of spatio-temporal periodic structure.

As a final remark, given the growing understanding of periodic structures' fundamental mechanics, it is now time to transfer this knowledge into engineering practice. This could be done by promoting the abundance of theoretical notions, numerical techniques and experimental achievements outside the mechanical metamaterials community, perhaps with dedicated graduate level courses on the principles of this fascinating concept, similarly to what is being already done in photonics.

Appendices

APPENDIX A

DISPLACEMENT - STRESS RESULTANTS RELATIONS FOR UNDULATED PLATES

The membrane forces in Eq.s (2.15),(2.16) and (2.17) can be rewritten in terms of displacements u_1, u_2, and u_3 and local curvatures k_1 and k_2 as:

$$N_{11} = K\left[\frac{\partial u_1}{\partial x_1} + k_1 u_3 + \nu\left(\frac{\partial u_2}{\partial x_2} + k_2 u_3\right)\right] \tag{A.1}$$

$$N_{22} = K\left[\frac{\partial u_2}{\partial x_2} + k_2 u_3 + \nu\left(\frac{\partial u_1}{\partial x_1} + k_1 u_3\right)\right] \tag{A.2}$$

$$N_{12} = N_{21} = \frac{K(1-\nu)}{2}\left[\frac{\partial u_2}{\partial x_1} + \frac{\partial u_1}{\partial x_2}\right] \tag{A.3}$$

Similarly, the expressions of the bending moments write:

$$M_{11} = D\left[\frac{\partial k_1}{\partial x_1}u_1 + k_1\frac{\partial u_1}{\partial x_1} - \frac{\partial^2 u_3}{\partial x_1^2} + \nu\left(\frac{\partial k_2}{\partial x_2}u_2 + k_2\frac{\partial u_2}{\partial x_2} - \frac{\partial^2 u_3}{\partial x_2^2}\right)\right] \tag{A.4}$$

$$M_{22} = D\left[\frac{\partial k_2}{\partial x_2}u_2 + k_2\frac{\partial u_2}{\partial x_2} - \frac{\partial^2 u_3}{\partial x_2^2} + \nu\left(\frac{\partial k_1}{\partial x_1}u_1 + k_1\frac{\partial u_1}{\partial x_1} - \frac{\partial^2 u_3}{\partial x_1^2}\right)\right] \tag{A.5}$$

$$M_{12} = \frac{D(1-\nu)}{2}\left[\frac{\partial k_2}{\partial x_1}u_2 + k_2\frac{\partial u_2}{\partial x_1} + \frac{\partial k_1}{\partial x_2}u_1 + k_1\frac{\partial u_1}{\partial x_2} - 2\frac{\partial^2 u_3}{\partial x_1 \partial x_2}\right] \tag{A.6}$$

where $K = \frac{Eh}{1-\nu^2}$, $D = \frac{Eh^3}{12(1-\nu^2)}$, and $M_{21} = M_{12}$.

APPENDIX B

PWEM FORMULATION FOR UNDULATED PLATES

The full formulation of the EVP that is obtained by applying the PWEM for periodic undulated plates expressed by Eq.(2.35) is presented in this appendix. The three equations that can be obtained from plugging the expressions of displacements (2.34) and curvatures (2.29) into Eq. (2.15), (2.16) and (2.17) and after exploiting orthogonality write:

$$\begin{aligned} &P_{11}^{(0)}\hat{u_1}_{n,q} + \sum_{m,p,r,o} P_{11}^{(2)}\hat{u_1}_{n-m-r,q-p-o} + P_{12}^{(0)}\hat{u_2}_{n,q} + \sum_{m,p,r,o} P_{12}^{(2)}\hat{u_2}_{n-m-r,q-p-o} \\ &+ \sum_{m,p} P_{13}^{(1)}\hat{u_3}_{n-m,q-p} = \rho h\omega^2\hat{u_1}_{n,q} \end{aligned} \tag{B.1}$$

$$\begin{aligned} &P_{21}^{(0)}\hat{u_1}_{n,q} + \sum_{m,p,r,o} P_{21}^{(2)}\hat{u_1}_{n-m-r,q-p-o} + P_{22}^{(0)}\hat{u_2}_{n,q} + \sum_{m,p,r,o} P_{22}^{(2)}\hat{u_2}_{n-m-r,q-p-o} \\ &+ \sum_{m,p} P_{23}^{(1)}\hat{u_3}_{n-m,q-p} = \rho h\omega^2\hat{u_2}_{n,q} \end{aligned} \tag{B.2}$$

$$\begin{aligned} &\sum_{m,p} P_{31}^{(1)}\hat{u_1}_{n-m,q-p} + \sum_{m,p} P_{32}^{(1)}\hat{u_2}_{n-m,q-p} + P_{33}^{(0)}\hat{u_3}_{n,q} + \sum_{m,p,r,o} P_{33}^{(2)}\hat{u_3}_{n-m-r,q-p-o} \\ &= \rho h\omega^2\hat{u_3}_{n,q} \end{aligned} \tag{B.3}$$

where the coefficients $P_{ij}^{(0)}$,$P_{ij}^{(1)}$,$P_{ij}^{(2)}$, with $i,j = 1,2,3$, are defines as follows:

$$P_{11}^{(0)} = K\left\{\left[\frac{2\pi}{a}\left(\kappa_{01}+n\right)\right]^2 + \frac{1-\nu}{2}\left[\frac{2\pi}{a}\left(\kappa_{02}+q\right)\right]^2\right\} \tag{B.4}$$

$$P_{11}^{(2)} = \hat{k_{1m,p}} \hat{k_{1r,o}} D \left\{ \left[\frac{2\pi}{a} \left(\kappa_{01} + n - m \right) \right]^2 + \frac{1-\nu}{2} \left[\frac{2\pi}{a} \left(\kappa_{02} + q - p \right) \right]^2 \right\} \quad \text{(B.5)}$$

$$P_{12}^{(0)} = K \frac{1+\nu}{2} \left[\frac{2\pi}{a} \left(\kappa_{01} + n \right) \right] \left[\frac{2\pi}{a} \left(\kappa_{02} + q \right) \right] \quad \text{(B.6)}$$

$$P_{12}^{(2)} = \hat{k_{1m,p}} \hat{k_{2r,o}} D \frac{1+\mu}{2} \left[\frac{2\pi}{a} \left(\kappa_{01} + n - m \right) \right] \cdot \left[\frac{2\pi}{a} \left(\kappa_{02} + q - p \right) \right] \quad \text{(B.7)}$$

$$\begin{aligned} P_{13}^{(1)} = -j \Bigg\langle \hat{k_{1m,p}} \Bigg\{ & K \left[\frac{2\pi}{a} \left(\kappa_{01} + n \right) \right] + D \left[\frac{2\pi}{a} \left(\kappa_{01} + n - m \right) \right] \\ & \cdot \left\{ \left[\frac{2\pi}{a} \left(\kappa_{01} + n - m \right) \right]^2 + \left[\frac{2\pi}{a} \left(\kappa_{02} + q - p \right) \right]^2 \right\} \Bigg\} \\ & + \hat{k_{2m,p}} K \nu \left[\frac{2\pi}{a} \left(\kappa_{01} + n \right) \right] \Bigg\rangle \end{aligned} \quad \text{(B.8)}$$

$$P_{21}^{(0)} = K \frac{1+\nu}{2} \left[\frac{2\pi}{a} \left(\kappa_{01} + n \right) \right] \left[\frac{2\pi}{a} \left(\kappa_{02} + q \right) \right] \quad \text{(B.9)}$$

$$P_{21}^{(2)} = \hat{k_{1m,p}} \hat{k_{2r,o}} D \frac{1+\mu}{2} \left[\frac{2\pi}{a} \left(\kappa_{01} + n - r \right) \right] \cdot \left[\frac{2\pi}{a} \left(\kappa_{02} + q - o \right) \right] \quad \text{(B.10)}$$

$$P_{22}^{(0)} = K \left\{ \left[\frac{2\pi}{a} \left(\kappa_{02} + q \right) \right]^2 + \frac{1-\nu}{2} \left[\frac{2\pi}{a} \left(\kappa_{01} + n \right) \right]^2 \right\} \quad \text{(B.11)}$$

$$P_{22}^{(2)} = \hat{k}_{2m,p}\hat{k}_{2r,o}\, D\left\{ \left[\frac{2\pi}{a}\left(\kappa_{02}+q-p\right)\right]^2 + \frac{1-\nu}{2}\left[\frac{2\pi}{a}\left(\kappa_{01}+n-m\right)\right]^2 \right\} \quad \text{(B.12)}$$

$$\begin{aligned} P_{23}^{(1)} = -j\Bigg\langle \hat{k}_{2m,p}\Bigg\{ & K\left[\frac{2\pi}{a}\left(\kappa_{02}+q\right)\right] + D\left[\frac{2\pi}{a}\left(\kappa_{02}+q-p\right)\right] \\ & \cdot\left\{ \left[\frac{2\pi}{a}\left(\kappa_{01}+n-m\right)\right]^2 + \left[\frac{2\pi}{a}\left(\kappa_{02}+q-p\right)\right]^2 \right\}\Bigg\} \\ & + \hat{k}_{1m,p} K\nu\left[\frac{2\pi}{a}\left(\kappa_{02}+q\right)\right]\Bigg\rangle \end{aligned} \quad \text{(B.13)}$$

$$\begin{aligned} P_{31}^{(1)} = j\Bigg\langle \hat{k}_{1m,p}\Bigg\{ & K\left[\frac{2\pi}{a}\left(\kappa_{01}+n-m\right)\right] + D\left[\frac{2\pi}{a}\left(\kappa_{01}+n\right)\right] \\ & \cdot\left\{ \left[\frac{2\pi}{a}\left(\kappa_{01}+n\right)\right]^2 + \left[\frac{2\pi}{a}\left(\kappa_{02}+q\right)\right]^2 \right\}\Bigg\} \\ & + \hat{k}_{2m,p} K\nu\left[\frac{2\pi}{a}\left(\kappa_{01}+n-m\right)\right]\Bigg\rangle \end{aligned} \quad \text{(B.14)}$$

$$\begin{aligned} P_{32}^{(1)} = j\Bigg\langle \hat{k}_{2m,p}\Bigg\{ & K\left[\frac{2\pi}{a}\left(\kappa_{02}+q-p\right)\right] + D\left[\frac{2\pi}{a}\left(\kappa_{02}+q\right)\right] \\ & \cdot\left\{ \left[\frac{2\pi}{a}\left(\kappa_{01}+n\right)\right]^2 + \left[\frac{2\pi}{a}\left(\kappa_{02}+q\right)\right]^2 \right\}\Bigg\} \\ & + \hat{k}_{1m,p} K\nu\left[\frac{2\pi}{a}\left(\kappa_{02}+q-p\right)\right]\Bigg\rangle \end{aligned} \quad \text{(B.15)}$$

$$P_{33}^{(0)} = D\left\{ \left[\frac{2\pi}{a}\left(\kappa_{01}+n\right)\right]^2 + \left[\frac{2\pi}{a}\left(\kappa_{02}+q\right)\right]^2 \right\}^2 \quad \text{(B.16)}$$

$$P_{33}^{(1)} = \hat{k_1}_{m,p}\hat{k_1}_{r,o}K + \hat{k_2}_{m,p}\hat{k_2}_{r,o}K + \hat{k_1}_{m,p}\hat{k_2}_{r,o}2K\nu \tag{B.17}$$

where $n, q, m, p, r, o = -N, ..., N \in \mathbb{Z}$ and j being the imaginary unit. Truncation of the series defining u_1, u_2, u_3 and k_1, k_2 leads to including $2N + 1$ plane waves are considered, Eq.s (B.1), (B.2) and (B.3) and defines the EVP to be solved.

APPENDIX C

COEFFICIENTS OF THE QEP WITH FIRST ORDER WAVE EXPANSION FOR SPATIO-TEMPORAL BEAMS

The coefficients of Eq. 5.20 for a modulated beam in longitudinal motion write as follows:

$$L_{11} = \Omega^2 - 2\nu_m\Omega - \left[\left(\frac{\mu}{2\pi} - 1\right)^2 - \nu_m^2\right] \tag{C.1}$$

$$L_{12} = -\frac{\mu}{2\pi}\left(\frac{\mu}{2\pi} - 1\right)\frac{\alpha_m}{2} \tag{C.2}$$

$$L_{13} = 0 \tag{C.3}$$

$$L_{21} = -\frac{\mu}{2\pi}\left(\frac{\mu}{2\pi} - 1\right)\frac{\alpha_m}{2} \tag{C.4}$$

$$L_{22} = \Omega^2 - \left(\frac{\mu}{2\pi}\right)^2 \tag{C.5}$$

$$L_{23} = -\frac{\mu}{2\pi}\left(\frac{\mu}{2\pi} + 1\right)\frac{\alpha_m}{2} \tag{C.6}$$

$$L_{31} = 0 \tag{C.7}$$

$$L_{32} = -\frac{\mu}{2\pi}\left(\frac{\mu}{2\pi} + 1\right)\frac{\alpha_m}{2} \tag{C.8}$$

$$L_{33} = \Omega^2 + 2\nu_m\Omega - \left[\left(\frac{\mu}{2\pi} + 1\right)^2 - \nu_m^2\right] \tag{C.9}$$

Similarly, the coefficients of Eq. 5.47 for a modulated beam in transverse motion write as follows:

$$T_{11} = \Omega^2 - 2\nu_m\Omega - \left[\left(\frac{\mu}{2\pi} - 1\right)^4 \chi^2 - \nu_m^2\right] \tag{C.10}$$

$$T_{12} = -\left[\frac{\mu}{2\pi}\left(\frac{\mu}{2\pi} - 1\right)\right]^2 \frac{\alpha_m}{2} \tag{C.11}$$

$$T_{13} = 0 \tag{C.12}$$

$$T_{21} = -\left[\frac{\mu}{2\pi}\left(\frac{\mu}{2\pi} - 1\right)\right]^2 \frac{\alpha_m}{2} \tag{C.13}$$

$$T_{22} = \Omega^2 - \left(\frac{\mu}{2\pi}\right)^4 \chi^2 \tag{C.14}$$

$$T_{23} = -\left[\frac{\mu}{2\pi}\left(\frac{\mu}{2\pi} + 1\right)\right]^2 \frac{\alpha_m}{2} \tag{C.15}$$

$$T_{31} = 0 \tag{C.16}$$

$$T_{32} = -\left[\frac{\mu}{2\pi}\left(\frac{\mu}{2\pi} + 1\right)\right]^2 \frac{\alpha_m}{2} \tag{C.17}$$

$$T_{33} = \Omega^2 + 2\nu_m\Omega - \left[\left(\frac{\mu}{2\pi} + 1\right)^4 \chi^2 - \nu_m^2\right] \tag{C.18}$$

in which we define $\chi = R_g\kappa_m$.

REFERENCES

[1] M. I. Hussein, M. J. Leamy, and M. Ruzzene, "Dynamics of phononic materials and structures: Historical origins, recent progress, and future outlook," *Applied Mechanics Reviews*, vol. 66, no. 4, p. 040 802, 2014.

[2] I. Newton, *Philosophiae naturalis principia mathematica*. 1687.

[3] L. Brillouin, *Wave propagation in periodic structures: Electric filters and crystal lattices*, ser. Dover books and science. Dover Publications, 1953.

[4] C. Elachi, "Waves in active and passive periodic structures: A review," *Proceedings of the IEEE*, vol. 64, no. 12, pp. 1666–1698, 1976.

[5] M.-H. Lu, L. Feng, and Y.-F. Chen, "Phononic crystals and acoustic metamaterials," *Materials Today*, vol. 12, no. 12, pp. 34 –42, 2009.

[6] H. Xiang, Z. Shi, S. Wang, and Y. Mo, "Periodic materials-based vibration attenuation in layered foundations: Experimental validation," *Smart Materials and Structures*, vol. 21, no. 11, p. 112 003, 2012.

[7] J. Sanchez-Dehesa, V. M. Garcia-Chocano, D. Torrent, F. Cervera, S. Cabrera, and F. Simon, "Noise control by sonic crystal barriers made of recycled materials," *The Journal of the Acoustical Society of America*, vol. 129, no. 3, 2011.

[8] M. M. Sigalas, "Defect states of acoustic waves in a two-dimensional lattice of solid cylinders," *Journal of Applied Physics*, vol. 84, no. 6, 1998.

[9] Y. Pennec, B. Djafari-Rouhani, J. O. Vasseur, A. Khelif, and P. A. Deymier, "Tunable filtering and demultiplexing in phononic crystals with hollow cylinders," *Phys. Rev. E*, vol. 69, p. 046 608, 4 2004.

[10] V. Espinosa, V. J. Sanchez-Morcillo, K. Staliunas, I. Perez-Arjona, and J. Redondo, "Subdiffractive propagation of ultrasound in sonic crystals," *Phys. Rev. B*, vol. 76, p. 140 302, 14 2007.

[11] F. Cervera, L. Sanchis, J. V. Sanchez-Perez, R. Martinez-Sala, C. Rubio, F. Meseguer, C. Lopez, D. Caballero, and J. Sanchez-Dehesa, "Refractive acoustic devices for airborne sound," *Phys. Rev. Lett.*, vol. 88, p. 023 902, 2 2001.

[12] N Boechler, G Theocharis, and C Daraio, "Bifurcation-based acoustic switching and rectification," *Nature materials*, vol. 10, no. 9, 665668, 2011.

[13] S. Tol, F. L. Degertekin, and A. Erturk, "Phononic crystal luneburg lens for omnidirectional elastic wave focusing and energy harvesting," *Applied Physics Letters*, vol. 111, no. 1, p. 013 503, 2017.

[14] M. M. Sigalas, "Elastic wave band gaps and defect states in two-dimensional composites," *The Journal of the Acoustical Society of America*, vol. 101, no. 3, pp. 1256–1261, 1997. eprint: `https://doi.org/10.1121/1.418156`.

[15] S.-C. S. Lin, T. J. Huang, J.-H. Sun, and T.-T. Wu, "Gradient-index phononic crystals," *Phys. Rev. B*, vol. 79, p. 094 302, 9 2009.

[16] S. Tol, F. L. Degertekin, and A. Erturk, "Gradient-index phononic crystal lens-based enhancement of elastic wave energy harvesting," *Applied Physics Letters*, vol. 109, no. 6, p. 063 902, 2016.

[17] D. Mead, "Wave propagation in continuous periodic structures: Research contributions from southampton, 19641995," *Journal of Sound and Vibration*, vol. 190, no. 3, pp. 495 –524, 1996.

[18] ——, "Vibration response and wave propagation in periodic structures," *Journal of engineering for industry*, vol. 93, no. 3, pp. 783–792, 1971.

[19] D. Mead and S. Parthan, "Free wave propagation in two-dimensional periodic plates," *Journal of Sound and Vibration*, vol. 64, no. 3, pp. 325 –348, 1979.

[20] M. Åberg and P. Gudmundson, "The usage of standard finite element codes for computation of dispersion relations in materials with periodic microstructure," *The Journal of the Acoustical Society of America*, vol. 102, no. 4, pp. 2007–2013, 1997.

[21] G. A. Gazonas, D. S. Weile, R. Wildman, and A. Mohan, "Genetic algorithm optimization of phononic bandgap structures," *International Journal of Solids and Structures*, vol. 43, no. 18, pp. 5851 –5866, 2006.

[22] J. Christensen, M. Kadic, O. Kraft, and M. Wegener, "Vibrant times for mechanical metamaterials," *MRS Communications*, vol. 5, no. 3, 453462, 2015.

[23] N. A. Fleck, V. S. Deshpande, and M. F. Ashby, "Micro-architectured materials: Past, present and future," *Proceedings of the Royal Society of London A: Mathematical, Physical and Engineering Sciences*, vol. 466, no. 2121, pp. 2495–2516, 2010.

[24] L. R. Meza, G. P. Phlipot, C. M. Portela, A. Maggi, L. C. Montemayor, A. Comella, D. M. Kochmann, and J. R. Greer, "Reexamining the mechanical property space of three-dimensional lattice architectures," *Acta Materialia*, vol. 140, no. Supplement C, pp. 424 –432, 2017.

[25] L. C. Montemayor and J. R. Greer, "Mechanical response of hollow metallic nanolattices: Combining structural and material size effects," *Journal of Applied Mechanics*, vol. 82, no. 7, pp. 071 012–071012–10, 2015.

[26] V. Deshpande, N. Fleck, and M. Ashby, "Effective properties of the octet-truss lattice material," *Journal of the Mechanics and Physics of Solids*, vol. 49, no. 8, pp. 1747 –1769, 2001.

[27] M. R. O'Masta, L. Dong, L. St-Pierre, H. Wadley, and V. Deshpande, "The fracture toughness of octet-truss lattices," *Journal of the Mechanics and Physics of Solids*, vol. 98, no. Supplement C, pp. 271 –289, 2017.

[28] L. R. Meza, S. Das, and J. R. Greer, "Strong, lightweight, and recoverable three-dimensional ceramic nanolattices," *Science*, vol. 345, no. 6202, pp. 1322–1326, 2014.

[29] J. Bauer, A. Schroer, R. Schwaiger, and O. Kraft, "Approaching theoretical strength in glassy carbon nanolattices," *Nature Materials*, no. 15, 438443, 2016.

[30] A. Maggi, H. Li, and J. R. Greer, "Three-dimensional nano-architected scaffolds with tunable stiffness for efficient bone tissue growth," *Acta Biomaterialia*, vol. 63, no. Supplement C, pp. 294 –305, 2017.

[31] D. Mousanezhad, S. Babaee, H. Ebrahimi, R. Ghosh, A. S. Hamouda, K. Bertoldi, and A. Vaziri, "Hierarchical honeycomb auxetic metamaterials," *Scientific Reports*, vol. 5, p. 18 306, 2015.

[32] L. R. Meza, A. J. Zelhofer, N. Clarke, A. J. Mateos, D. M. Kochmann, and J. R. Greer, "Resilient 3d hierarchical architected metamaterials," *Proc. Natl. Acad. Sci. U.S.A.*, vol. 112, no. 37, pp. 11 502–11 507, 2015.

[33] F. Casadei and J. Rimoli, "Anisotropy-induced broadband stress wave steering in periodic lattices," *International Journal of Solids and Structures*, vol. 50, no. 9, 2013.

[34] A. S. Phani, J Woodhouse, and N. Fleck, "Wave propagation in two-dimensional periodic lattices," *The Journal of the Acoustical Society of America*, vol. 119, no. 4, pp. 1995–2005, 2006.

[35] A. Spadoni, M. Ruzzene, S. Gonella, and F. Scarpa, "Phononic properties of hexagonal chiral lattices," *Wave Motion*, vol. 46, no. 7, pp. 435 –450, 2009.

[36] Y.-F. Wang, Y.-S. Wang, and C. Zhang, "Bandgaps and directional properties of two-dimensional square beam-like zigzag lattices," *AIP Advances*, vol. 4, no. 12, p. 124 403, 2014.

[37] R. Ganesh and S. Gonella, "Experimental evidence of directivity-enhancing mechanisms in nonlinear lattices," *Applied Physics Letters*, vol. 110, no. 8, p. 084 101, 2017.

[38] P. Celli and S. Gonella, "Tunable directivity in metamaterials with reconfigurable cell symmetry," *Applied Physics Letters*, vol. 106, no. 9, p. 091 905, 2015.

[39] R. K. Pal, J. Rimoli, and M. Ruzzene, "Effect of large deformation pre-loads on the wave properties of hexagonal lattices," *Smart Mater. Struct.*, vol. 25, no. 5, p. 054 010, 2016.

[40] M. Schaeffer and M. Ruzzene, "Wave propagation in reconfigurable magneto-elastic kagome lattice structures," *Journal of Applied Physics*, vol. 117, no. 19, 2015.

[41] J. Meyer, A. Geim, M. Katsnelson, K. Novoselov, T. Booth, and S. Roth, "The structure of suspended graphene sheets," *Nature*, vol. 446, no. 7131, pp. 60–63, 2007.

[42] K. A. Seffen and S. V. Stott, "Surface texturing through cylinder buckling," *ASME Journal of Applied Mechanics*, 2014.

[43] S. Cai, D. Breid, A. Crosby, Z. Suo, and J. Hutchinson, "Periodic patterns and energy states of buckled films on compliant substrates," *Journal of the Mechanics and Physics of Solids*, vol. 59, no. 5, pp. 1094 –1114, 2011.

[44] K. Bertoldi and M. C. Boyce, "Wave propagation and instabilities in monolithic and periodically structured elastomeric materials undergoing large deformations," *Phys. Rev. B*, vol. 78, p. 184 107, 18 2008.

[45] P. Wang, J. Shim, and K. Bertoldi, "Effects of geometric and material nonlinearities on tunable band gaps and low-frequency directionality of phononic crystals," *Phys. Rev. B*, vol. 88, p. 014 304, 1 2013.

[46] F. Warmuth, M. Wormser, and C. Körner, "Single phase 3d phononic band gap material," *Scientific Reports*, vol. 7, p. 3843, 2017.

[47] L. D'Alessandro, E. Belloni, R. Ardito, A. Corigliano, and F. Braghin, "Modeling and experimental verification of an ultra-wide bandgap in 3d phononic crystal," *Applied Physics Letters*, vol. 109, no. 22, p. 221 907, 2016.

[48] P. Celli and S. Gonella, "Laser-enabled experimental wavefield reconstruction in two-dimensional phononic crystals," *Journal of Sound and Vibration*, vol. 333, no. 1, pp. 114 –123, 2014.

[49] R. Ganesh and S. Gonella, "Experimental evidence of directivity-enhancing mechanisms in nonlinear lattices," *Applied Physics Letters*, vol. 110, no. 8, p. 084 101, 2017.

[50] S. Rothberg, M. Allen, P. Castellini, D. D. Maio, J. Dirckx, D. Ewins, B. Halkon, P. Muyshondt, N. Paone, T. Ryan, H. Steger, E. Tomasini, S. Vanlanduit, and J. Vignola, "An international review of laser doppler vibrometry: Making light work of vibration measurement," *Optics and Lasers in Engineering*, vol. 99, pp. 11 –22, 2017, Laser Doppler vibrometry.

[51] B. Cazzolato, S. Wildy, J. Codrington, A. Kotousov, and M. Schuessler, "Scanning laser vibrometer for non-contact three-dimensional displacement and strain measurements."

[52] L. D. Landau and E. M. Lifshitz, *Electrodynamics of continuous media*. Pergamon Press, 1960.

[53] von Helmholtz H, *Treatise on physiological optics*. The Optical Society of America's Southall, 1924, vol. 1.

[54] A. D. Pierce, *Acoustics : An introduction to its physical principles and applications*. New York: McGraw-Hill Book Co., 1981.

[55] J. W.S. B. Rayleigh, *The theory of sound*. Macmillan, 1896, vol. 2.

[56] D Huang, L Tang, and R Cao, "Free vibration analysis of planar rotating rings by wave propagation," *J. Sound Vib.*, vol. 332, no. 20, pp. 4979 –4997, 2013.

[57] D Beli, S. P. Brando, and J. R. de Frana Arruda, "Vibration analysis of flexible rotating rings using a spectral element formulation," *J. Vib. Acoust.*, vol. 137, no. 4, 2015.

[58] L Onsager, "Reciprocal relations in irreversible processes. i.," *Phys. Rev.*, vol. 37, pp. 405–426, 4 1931.

[59] ——, "Reciprocal relations in irreversible processes. ii.," *Phys. Rev.*, vol. 38, pp. 2265–2279, 12 1931.

[60] H. B. G. Casimir, "On onsager's principle of microscopic reversibility," *Rev. Mod. Phys.*, vol. 17, pp. 343–350, 2-3 1945.

[61] R Fleury, D Sounas, M. R. Haberman, and A Alù, "Nonreciprocal acoustics," *Acoust. Today*, vol. 11, pp. 14–21, 3 2015.

[62] S. A. Cummer, J Christensen, and A Alù, "Controlling sound with acoustic metamaterials," *Nat. Rev. Mat.*, vol. 1, 2016.

[63] B Liang, B Yuan, and J Cheng, "Acoustic diode: Rectification of acoustic energy flux in one-dimensional systems," *Phys. Rev. Lett.*, vol. 103, p. 104 301, 10 2009.

[64] B Liang, X. S. Guo, J Tu, D Zhang, and J. C. Cheng, "An acoustic rectifier," *Nat. Mater.*, vol. 9, 989–992, 2010.

[65] Z Gu, J Hu, B Liang, X Zou, and J Cheng, "Broadband non-reciprocal transmission of sound with invariant frequency," *Sci. Rep.*, vol. 6, 2016.

[66] M. B. Zanjani, A. R. Davoyan, N Engheta, and J. R. Lukes, "Nems with broken t symmetry: Graphene based unidirectional acoustic transmission lines," *Sci. Rep.*, vol. 5, 2015.

[67] M. B. Zanjani, A. R. Davoyan, A. M. Mahmoud, N Engheta, and J. R. Lukes, "One-way phonon isolation in acoustic waveguides," *Appl. Phys. Lett.*, vol. 104, no. 8, 081905, 2014.

[68] R Fleury, D. L. Sounas, C. F. Sieck, M. R. Haberman, and A Alù, "Sound isolation and giant linear nonreciprocity in a compact acoustic circulator," *Science*, vol. 343, no. 6170, pp. 516–519, 2014.

[69] N Swinteck, S Matsuo, K Runge, J. O. Vasseur, P Lucas, and P. A. Deymier, "Bulk elastic waves with unidirectional backscattering-immune topological states in a time-dependent superlattice," *J. Appl. Phys.*, vol. 118, no. 6, 2015.

[70] Z Yu and S Fan., "Complete optical isolation created by indirect interband photonic transitions," *Nat. Photon.*, vol. 3, 2009.

[71] D. L. Sounas, C Caloz, and A Alù., "Giant non-reciprocity at the subwavelength scale using angular momentum-biased metamaterials," *Nat. Commun.*, vol. 4, 2013.

[72] D.-W. Wang, H.-T. Zhou, M.-J. Guo, J.-X. Zhang, J. Evers, and S.-Y. Zhu, "Optical diode made from a moving photonic crystal," *Phys. Rev. Lett.*, vol. 110, p. 093 901, 9 2013.

[73] Y Hadad, D. L. Sounas, and A Alù., "Space-time gradient metasurfaces," *Phys. Rev. B*, vol. 92, p. 100 304, 10 2015.

[74] J. C. Slater, "Interaction of waves in crystals," *Rev. Mod. Phys.*, vol. 30, pp. 197–222, 1 1958.

[75] J. C. Simon, "Action of a progressive disturbance on a guided electromagnetic wave," *IEEE Trans. Microw. Theory Tech.*, vol. 8, no. 1, pp. 18–29, 1960.

[76] A Hessel and A. A. Oliner, "Wave propagation in a medium with a progressive sinusoidal disturbance," *IEEE Trans. Microw. Theory Tech.*, vol. 9, no. 4, pp. 337–343, 1961.

[77] J. C. Cullen, "A travelling-wave parametric amplifier," *Nature*, vol. 181, p. 332, 1958.

[78] P. K. Tien and H Suhl, "A traveling-wave ferromagnetic amplifier," *Proc. IRE*, vol. 46, no. 4, pp. 700–706, 1958.

[79] E. S. Cassedy and A. A. Oliner, "Dispersion relations in time-space periodic media: Part i - stable interactions," *Proc. IRE*, vol. 51, no. 10, pp. 1342–1359, 1963.

[80] E. S. Cassedy, "Dispersion relations in time-space periodic media: Part ii - unstable interactions," *Proc. IRE*, vol. 55, no. 7, pp. 1154–1168, 1967.

[81] H. Nassar, X. Xu, A. Norris, and G. Huang, "Modulated phononic crystals: Non-reciprocal wave propagation and willis materials," *Journal of the Mechanics and Physics of Solids*, vol. 101, pp. 10 –29, 2017.

[82] J. Gump, I. Finkler, H. Xia, R. Sooryakumar, W. J. Bresser, and P. Boolchand, "Light-induced giant softening of network glasses observed near the mean-field rigidity transition," *Phys. Rev. Lett.*, vol. 92, p. 245 501, 24 2004.

[83] A. Bellino, A. Fasana, E. Gandino, L. Garibaldi, and S. Marchesiello, "A time-varying inertia pendulum: Analytical modelling and experimental identification," *Mechanical Systems and Signal Processing*, vol. 47, no. 1, pp. 120 –138, 2014.

[84] C. Cronne, J. O. Vasseur, O. B. Matar, M.-F. Ponge, P. A. Deymier, A.-C. Hladky-Hennion, and B. Dubus, "Brillouin scattering-like effect and non-reciprocal propagation of elastic waves due to spatio-temporal modulation of electrical boundary conditions in piezoelectric media," *Applied Physics Letters*, vol. 110, no. 6, p. 061 901, 2017.

[85] M. H. Ansari, M. A. Attarzadeh, M Nouh, and M. A. Karami, "Application of magnetoelastic materials in spatiotemporally modulated phononic crystals for nonreciprocal wave propagation," *Smart Materials and Structures*, vol. 27, no. 1, p. 015 030, 2018.

[86] A. Nanda and M. A. Karami, "One way sound propagation in a smart fluid," *ASME Conference on Smart Materials, Adaptive Structures and Intelligent Systems*, vol. 2, 2017.

[87] C. Kittel, *Introduction to solid state physics*. Wiley, 2004.

[88] A. Love, *A treatise on the mathematical theory of elasticity*, ser. Dover Books on Engineering Series. Dover Publications, 1944.

[89] W. Soedel, *Vibrations of shells and plates, second edition*, ser. Dekker Mechanical Engineering. Taylor & Francis, 1993.

[90] Z. Hou and B. M. Assouar, "Modeling of lamb wave propagation in plate with two-dimensional phononic crystal layer coated on uniform substrate using plane-wave-expansion method," *Physics Letters A*, vol. 372, no. 12, pp. 2091 –2097, 2008.

[91] Y. Xiao, J. Wen, and X. Wen, "Flexural wave band gaps in locally resonant thin plates with periodically attached springmass resonators," *Journal of Physics D: Applied Physics*, vol. 45, no. 19, p. 195 401, 2012.

[92] S. Hibbitt Karlsson, *Abaqus/standard analysis user's manual*. Dassault Systmes, 2012.

[93] Y. Lai, Y. Wu, P. Sheng, and Z.-Q. Zhang, "Hybrid elastic solids," *Nature Materials*, vol. 10, pp. 620–624, 2011.

[94] Y.-F. Wang, Y.-S. Wang, and C. Zhang, "Bandgaps and directional propagation of elastic waves in 2d square zigzag lattice structures," *Journal of Physics D: Applied Physics*, vol. 47, no. 48, p. 485 102, 2014.

[95] G. R. Cowper, "The Shear Coefficient in Timoshenko's Beam Theory," *Journal of Applied Mechanics*, vol. 33, p. 335, 1966.

[96] L. Gibson and M. Ashby, "Cellular Solids: Structure and Properties," 1999.

[97] D. Jurjo, C. Magluta, N. Roitman, and P. Gonçalves, "Experimental methodology for the dynamic analysis of slender structures based on digital image processing techniques," *Mech. Syst. Signal Pr.*, vol. 24, no. 5, pp. 1369 –1382, 2010.

[98] M. Schaeffer and M. Ruzzene, "Dynamic reconfiguration of magneto-elastic lattices," *C. R. Acad. Sci.*, vol. 343, no. 12, pp. 670 –679, 2015.

[99] M. Schaeffer, "Static and dynamic properties of reconfigurable magneto-elastic metastructures," PhD thesis, Georgia Institute of Technology, 2016.

[100] C Eberl, R. Thompson, and D. Gianola, "Free digital image correlation and tracking functions," 2010, (Date of access 09/09/2016).

[101] E. Jones, M. Silberstein, S. R. White, and N. R. Sottos, "In situ measurements of strains in composite battery electrodes during electrochemical cycling," *Exp. Mech.*, vol. 54, no. 6, pp. 971–985, 2014.

[102] E. Jones. (2013). Improved digital image correlation.

[103] S. Gonella and M. Ruzzene, "Analysis of in-plane wave propagation in hexagonal and re-entrant lattices," *Journal of Sound and Vibration*, vol. 312, no. 1–2, pp. 125 –139, 2008.

[104] G. Trainiti, J. Rimoli, and M. Ruzzene, "Wave propagation in undulated structural lattices," *Int. J. Solids Struct.*, vol. 9798, pp. 431 –444, 2016.

[105] M. Schaeffer, G. Trainiti, and M. Ruzzene, "Optical measurement of in-plane waves in mechanical metamaterials through digital image correlation," *Scientific Reports*, vol. 7, p. 42 437, 2017.

[106] A. T. Darnton and M. Ruzzene, "Optical measurement of guided waves," *The Journal of the Acoustical Society of America*, vol. 141, no. 5, EL465–EL469, 2017.

[107] F Tisseur and K Meerbergen, "The quadratic eigenvalue problem," *SIAM Review*, vol. 43, no. 2, pp. 235–286, 2001.

[108] W Alk and A Baz, "Active acoustic metamaterial with simultaneously programmable density and bulk modulus," *J. Vib. Acous.t*, vol. 135, no. 3, p. 031 001, 2013.

[109] L Yan, B Bao, D Guyomar, and M Lallart, "Periodic structure with interconnected nonlinear electrical networks," *J. Intell. Mater. Syst. Struct.*, 2016.

[110] L Meirovitch, *Principles and techniques of vibrations*. PrenticeHall, Englewood Cliffs, NJ, 1997.

[111] E. S. Cassedy, "Waves guided by a boundary with timespace periodic modulation," *Electrical Engineers, Proceedings of the Institution of*, vol. 112, no. 2, pp. 269–279, 1965.

[112] L Airoldi and M Ruzzene, "Design of tunable acoustic metamaterials through periodic arrays of resonant shunted piezos," *New J. Phys.*, vol. 13, no. 11, p. 113 010, 2011.

[113] V. V. Bolotin, "The dynamic stability of elastic systems. volume 2," 1964.

[114] N Swinteck, S Matsuo, K Runge, J. Vasseur, P Lucas, and P. Deymier, "Bulk elastic waves with unidirectional backscattering-immune topological states in a time-dependent superlattice," *Journal of Applied Physics*, vol. 118, p. 063 103, 2015.

[115] D. Polyzos and D. Fotiadis, "Derivation of Mindlin's first and second strain gradient elastic theory via simple lattice and continuum models," *International Journal of Solids and Structures*, vol. 49, pp. 470–480, 2012.

[116] E. Cassedy and A. Oliner, "Dispersion relations in time-space periodic media: Part I-Stable interactions," *Proceedings of the IEEE*, vol. 51, pp. 1342–1359, 1963.

[117] L Verlet, "Computer "experiments" on classical fluids. I. Thermodynamical properties of Lennard-Jones molecules," *Physical Review*, vol. 159, pp. 98–103, 1967.

[118] N. A. Estep, D. L. Sounas, J Soric, and A Alù, "Magnetic-free non-reciprocity and isolation based on parametrically modulated coupled-resonator loops," *Nat. Phys.*, vol. 10, no. 12, pp. 923–927, 2014.

[119] J. R. Zurita-Sánchez, P. Halevi, and J. C. Cervantes-González, "Reflection and transmission of a wave incident on a slab with a time-periodic dielectric function (t)," *Phys. Rev. A*, vol. 79, p. 053 821, 5 2009.

[120] K. Yi, M. Collet, and S. Karkar, "Frequency conversion induced by time-space modulated media," *Phys. Rev. B*, vol. 96, p. 104 110, 10 2017.

[121] R. L. Forward, "Electronic damping of vibrations in optical structures," *Appl. Opt.*, vol. 18, no. 5, pp. 690–697, 1979.

[122] N. Hagood and A. von Flotow, "Damping of structural vibrations with piezoelectric materials and passive electrical networks," *Journal of Sound and Vibration*, vol. 146, no. 2, pp. 243 –268, 1991.

[123] C. Fuller, S. Elliott, and P. Nelson, *Active control of vibration*. London: Academic Press, 1996, ISBN: 978-0-12-269440-0.

[124] S Behrens, A. J. Fleming, and S. O. R. Moheimani, "A broadband controller for shunt piezoelectric damping of structural vibration," *Smart Materials and Structures*, vol. 12, no. 1, p. 18, 2003.

[125] B de Marneffe and A Preumont, "Vibration damping with negative capacitance shunts: Theory and experiment," *Smart Materials and Structures*, vol. 17, no. 3, p. 035 015, 2008.

[126] B. S. Beck, K. A. Cunefare, and M. Collet, "The power output and efficiency of a negative capacitance shunt for vibration control of a flexural system," *Smart Materials and Structures*, vol. 22, no. 6, p. 065 009, 2013.

[127] A. Preumont, *Vibration control of active structures, an introduction*, ser. Solid Mechanics and Its Applications. Springer Netherlands, 2011.